Nanoscopic and Macroscopic Organization of Cationic Cyanine Dyes with Inorganic Layered Materials

無機層状結晶を利用したカチオン性シアニン色素の ナノおよびマクロスケールでの組織化

THESIS SUBMITTED TO WASEDA UNIVERSITY

Nobuyoshi MIYAMOTO

February, 2004

CONTENTS

CHAPTER 1.

CHAPTER 2.

ADSORPTION AND AGGREGATION OF A CATIONIC CYANINE DYE ON LAYERED SILICATES

CHAPTER 3.

UNI-DIRECTIONAL ORIENTATION OF CYANINE DYE AGGREGATES ON $K_4Nb_6O_{17}$ SINGLE CRYSTAL

CHAPTER 4.

VISIBLE LIGHT INDUCED ELECTRON TRANSFER AND LONG-LIVED CHARGE SEPARATED STATE IN CYANINE DYE/LAYERED TITANATE INTERCALATION COMPOUNDS..... 97

CHAPTER 5.

EXFOLIATION AND FILM PREPARATION OF A LAYERED TITANATE, Na₂Ti₃O₇, AND INTERCALATION OF PSEUDOISOCYANINE DYE

CHAPTER 6.

MACROSCOPIC AND SOFT ORGANIZATION OF PSEUDOISOCYANINE DYE WITH LYOTROPIC LIQUID CRYSTALS OBTAINED BY EXFOLIATION OF LAYERED NIOBATE

CHAPTER 7.

LIQUID CRYSTALLINE COLLOIDAL SYSTEM OBTAINED BY MIXING NIOBATE AND ALUMINOSILICATE NANOSHEETS....195

7.1. Introduction 196

7.2. Experimental 198

7.3. Results...200

7.4. Discussion 214

CHAPTER 1

INTRODUCTION

1. Introduction

1.1. General Introduction

Fabricating inorganic-organic nanocomposites containing photoactive species is of great interest for potential applications as optical devices, photoenergy conversion systems, etc. Among various methodologies to obtain nanocomposites, immobilization of photoactive species on or in layered solids is advantageous to organize small or very large species in controlled orientation and arrangement by utilizing the two-dimensional nanospace. However, precise control of the orientation and arrangement of the photoactive species by using inorganic layered materials is not yet straightforward. This thesis focuses on presenting new methodologies to organize photoactive species (the model dyes) both by nanoscopically and macroscopically by hybridizing with inorganic layered materials via guest-guest and guest-host interactions and morphological control of the host structure. Cyanine dyes are used as the model dyes, whose formation of large supramolecular aggregates via dye-dye interactions have been well-studied so far.

This thesis is composed of 8 chapters as follows.

Chapter 1 describes the background and objective of this thesis by showing the basic properties of inorganic layered materials and reviewing the previous studies of intercalation and exfoliation. The properties of cyanine dyes are also briefly reviewed.

In Chapters 2 – 4, variation of aggregation and orientation of cyanine dyes adsorbed to layered solids are investigated and the factors to control nanoscopic organization of the dye are revealed.

In Chapter 2, control of aggregation and adsorption of pseudoisocyanine dye in and on layered silicates are investigated. The dye was adsorbed to five kinds of clay minerals and layered polysilicate magadiite. Comparison of the visible absorption spectra revealed that the adsorbed dyes basically form J-aggregates, whereas the aggregation of the dye was suppressed (1) at lower dye loading, (2) by coadsorbing alkylammonium ions, and (3) by using layered silicates with small particle size. Further, the nanostructure of the dye aggregate was varied depending on the reaction

condition and the properties of the host.

Chapter 3 describes in-plane orientations of the dye aggregates on single crystals of layered niobate $K_4Nb_6O_{17}$. Polarized visible absorption spectra revealed that the dipoles of the dye aggregates (J- or herringbone-type aggregates) are uni-axially oriented along the crystallographic axes of $K_4Nb_6O_{17}$ over the whole crystal domain and that the orientation direction and the degree of orientation depended on the dye used. $K_4Nb_6O_{17}$ has an anisotropic surface with regularly arranged Nb-O$^-$ groups that can act as cation-exchanging sites; the periodicity of the arrangement of the sites along the *a*- and *c*-axes are different. The electrostatic interactions between the anionic sites and the positive charges of the dye cations were thought to cause the uni-directional orientation of the dye aggregates. The control of in-plane orientation of guest species in intercalation compounds has never been reported before. This methodology is applicable to a wide range of guest species, allowing fabrication of various supramolecular architectures with macroscopic anisotropy in a simple processing.

Chapter 4 demonstrates the visible-light-induced electron transfer in the intercalation compounds of cyanine dyes and layered titanates, $Cs_xTi_{2-x/4}\square_{x/4}O_4$ and $Na_2Ti_3O_7$. Visible absorption spectra showed that the cyanine dyes in the interlayer spaces formed J-aggregates. Emergence of the signals in ESR spectra upon visible-light irradiation to the samples as well as quenching of fluorescence of the intercalated dye aggregates in the interlayer spaces evidenced the electron transfer from the photo-excited J-aggregates, which is know as excellent photosensitizer, to the semiconducting titanate sheets. The photo-induced charge separated state was very stably kept; the apparent lifetimes of the charge separated states ranged from several minutes to 246 min, depending on the dye and the host. It is supposed that slow electron diffusion in the conduction band of the hosts and the peculiar nanostructure of the intercalation compounds is responsible to the stability of the charge separated state. Stable charge separation induced by visible light is an important step toward applications for light energy conversion and storage systems; the present system can be used as the material and model system (due to controlled nanostructure) for such applications.

Chapters 5 – 7 describe the control of macroscopic morphology of layered

solids by exfoliation and use of the host materials with controlled morphologies to organize cyanine dye both on the macroscopic and nanoscopic scales.

Chapter 5 describes exfoliation and restacking of layered titanate $Na_2Ti_3O_7$ as self-supporting multilayered films intercalated with pseudoisocyanine dye. Although layered materials with high layer charge density is generally difficult to be exfoliated due to strong binding between the sheets, ultrasonication and hydrothermal treatment were found to promote exfoliation in this system. The obtained film was intercalated with the dye as revealed by XRD, retaining the morphology. Polarized visible absorption spectra showed that the intercalated dye was macroscopically aligned along the film surface. The obtained films are applicable as optical devices and for detailed photochemical measurement of the intercalation compound.

Chapter 6 elucidates that exfoliated layered niobate $K_4Nb_6O_{17}$ forms lyotropic liquid crystals, where the exfoliated nanosheets are loosely held with orientational orderBy immobilizing a cyanine dye onto the loosely organized nanosheets, hierarchical and soft architectures containing the dye and the nanosheets were obtained. The sol containing the exfoliated niobate exhibited optical texturesand interference colors under crossed polarizers, indicating the formation of liquid crystalline phase. Gravity, rotational shear, and interfacial tension induced macroscopic orientation of the optical axis on sub-mm and cm scales. The sol was added with the dye and measured with polarized visible absorption spectra; the spectra showed that the dyes were adsorbed on the niobate sheet and are macroscopically oriented along the oriented nanosheets. Nanosheet dispersions with liquid crystalline property have scarcely been reported so far. Among those rare cases, the present system is characterized by the highly stable liquid crystallinity even at very low concentration as well as by semiconductivity and ion-exchange capability of the mesogenic nanosheets.

The later part of Chapter 6 clarifies the effect of lateral size of the nanosheet on the liquid crystallinity by preparing and examining the nanosheet colloids with controlled lateral sizes over very wide range (0.1 - 100 μm).. $K_4Nb_6O_{17}$ single crystal was used as starting material to yield the nanosheets with very large lateral size (up to 100 μm). Hydrothermal treatment of the crystals in aqueous solution of

propylammonium ions allowed successful exfoliation of the large crystal. By ultrasonicating the obtained nanosheet sol for different period, the nanosheets with controlled (reduced) lateral sizes were obtained. By estimating the phase transition concentrations (isotropic to biphasic and biphasic to liquid crystalline) of the nanosheet colloids with varied mean lateral sizes, it was revealed that the larger lateral size contributes to the formation of more stable liquid crystalline phases. This trend is basically rationalized by Onsager theory and is generalized to the nanosheet colloids of other layered materials.

Chapter 7 describes the organization of a cyanine dye in liquid crystalline nanosheet colloids composed of both montmorillonite and $K_4Nb_6O_{17}$. In visible absorption spectra, the dye added to a montmorillonite-niobate colloid showed the band similar to that observed in dye/montmorillonite system but not to that in dye/niobate system, indicating selective adsorption of the dye only onto montmorillonite in the double component nanosheet sol. The transfer of the dye from niobate sol to montmorillonite sol through a semipermeable membrane also supported the selective adsorption. Further, microscopic phase separation into niobate-rich and montmorillonite-rich phases was supposed to occur based on the XRD measurements of a dried sol. These results showed that the double component nanosheet colloids are potentially applicable as novel heterogeneous, anisotropic and soft nanohybrids with various functional species.

Chapter 8 shows conclusions of this thesis.

1.2. Inorganic Layered Materials and Intercalation

1.2.1. Overview

Inorganic layered materials are composed of stacking of nanometer-thick inorganic sheets, which are held together via electrostatic, van der Waals, or hydrogen bonding interactions. Due to the distinctive structural feature, inorganic layered solids undergo intercalation reaction (the insertion of guest species into the interlayer space of the host layered solids), leading to formation of so-called intercalation compounds (Figure 1). Intercalation reaction proceeds by (1) exchange of guest species with the species that were originally present in the interlayer space, or (2) sorption of molecules into the interlayer spaces via interactions of the guest species with layer surface or with the species originally existed in the interlayer space: formation of hydrogen and covalent bonds between the guest and host surface, formation of charge transfer complexes, hydrophobic interaction, etc. drive the reaction. By using an appropriate method, variety of guest species (solvents, ionic species, neutral molecules, polymers etc) can be intercalated in various host materials, leading to limitless variation of nanocomposite materials.
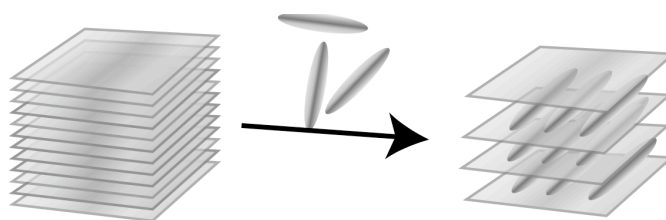
Figure 1. Schematic drawing of intercalation reaction.

Intercalation compounds are characterized by the novel features as follows:

(1) The guest species are orientationally and positionally organized along the defined two-dimensional host lattice, leading to modified properties of the guest species.

(2) Since the inorganic and organic parts are hybridized on nanometer scale, these

components can synergistically exhibit properties based on intimate interaction between host and guest and on the supramolecular structure.

(3) Extremely large surface area per weight and expandable interlayer space are suitable for application as adsorbates, catalysts, and support for catalysts.

(4) Wide variety of layered materials with different structure, morphology, charge density, composition, electric property, and magnetic property are available.

(5) Intercalated guest species possess high thermal and chemical stability due to blocking from oxygen etc. and rigid immobilization in the restricted nanospace.

(6) Two-dimensional interlayer spaces are usable as nanovessel with orientational and geometrical restrictions for chemical reactions, leading to e.g. syntheses of organic molecules in unusual selectivity, low-dimensional polymers, etc.

Table 1 shows class and example of typical layered materials used as the hosts of intercalation reaction. The structure, basic properties and intercalation reaction of the layered materials used in this study are described in the following sections. Another important feature of layered materials, exfoliation, will be described in Chapter 1.3.

Table 1.   Typical layered materials for intercalation.

layer charge	class	example
negative	2:1 clay mineral	montmorillonite, vermiculite, etc.
	transition metal oxides	$K_4Nb_6O_{17}$, $Na_2Ti_3O_7$, etc.
	Polysilicates	kanemite, octosilicate, magadiite, kenyite, makatite
	metal phosphates and phosphonates	α-$Zr(HPO_4)_2 \cdot 2H_2O$, γ-$Zr(PO_4)(H_2PO_4) \cdot 2H_2O$, etc.
positive	double hydroxides	hydrotalcite etc.
neutral	1:1 clay mineral	kaolinite
	metal oxide	MnO_2, MoO_3, V_2O_5, etc.
	Graphite	graphite, graphite oxide
	metal chalcogenides	MoS_2, WS_2, MoS_2, $CdPS_3$, $MnPS_3$, etc.
	metal halides and oxyhalides	$FeOCl$, $(RNH_3)_2PbI_4$, etc.

1.2.2. Smectite Clays

Smectite clay minerals are most widely known and historically studied class of layered materials. Figure 2 represents the schematic structure of a smectite clay, montmorillonite. The aluminosilicate layer of montmorillonite is composed of corner-sharing SiO_4 tetrahedral layers sandwiched by edge-sharing $Al(O, OH)_6$ octahedral layers. Due to this tetrahedral-octahedral-tetrahedral structure, smectite clays are termed as 2:1 clay minerals. Isomorphous substitution of the central metallic atoms of the octahedra and tetrahedra with lower valency atoms, e.g. Si^{4+} with Al^{3+}, Al^{3+} with Mg^{2+} and Fe^{2+}, and Mg^{2+} with Li^+, bares net negative charge inside the layer. To compensate the negative charge, metal cations such as Na^+ and Ca^+ are present in the interlayer spaces. These interlayer cations are easily swelled by polar solvents and exchangeable with other cations, allowing this material to undergo intercalation reactions easily with various cationic guest species.

Other than montmorillonite, several kind of smectite clays and its analogues (vermiculites and micas), which differ in ideal chemical composition and the type of isomorphous substitution, are known to possess intercalation capability (Table 2). Most of these clay minerals occur naturally in earth soils, whereas the composition, isomorphous substitution, impurity level, and crystallinity of the clays differ depending on the production areas. Synthetic clay minerals, which are suited for chemical experiments due to lower impurity content, are also available. The layer charge density is related to reactivity for intercalation as well as to ion exchange capacity: larger charge density leads to stronger binding of adjacent clay sheets, resulting in lower reactivity for intercalation.

Exchangeable cations
nH₂O

○Oxygens ⊖Hydroxyls ● Aluminum, iron, magnesium
○and ● Silicon, occasionally aluminum
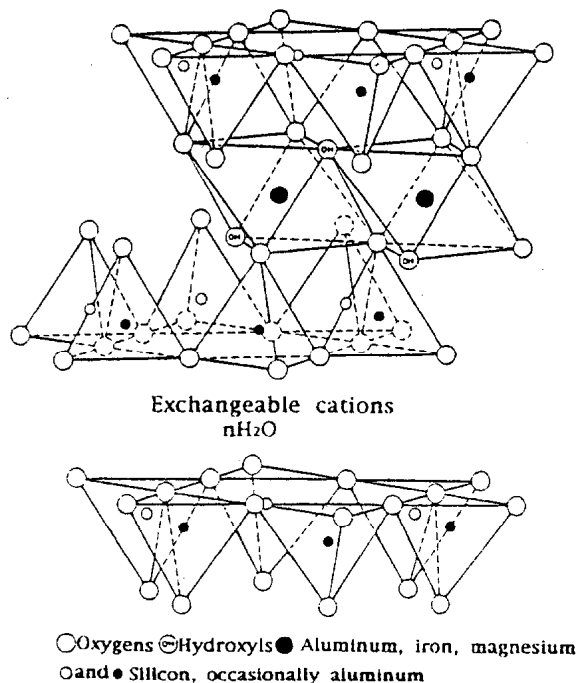
Figure 2. Schematic structure of montmorillonite.

Table 2. Typical 2:1 type clay minerals with intercalation capability.

classification	layer charge / e^- per (Si,Al)$_4$O$_{10}$	clay mineral	isomorphous substitution	ideal composition
smectites	0.2-0.6	montmorillonite	octahedral	$Na_x(Al, Mg)_2Si_4O_{10}(OH)_2$
		saponite	tetrahedral	$Na_xMg_3(Si, Al)_4O_{10}(OH)_2$
		hectorite	octahedral	$Na_x(Mg, Li)_3Si_4O_{10}(F,OH)_2$
		beidellite	tetrahedral	$Na_xAl_2(Si, Al)_4O_{10}(OH)_2$
vermiculite	0.6-0.9	vermiculite	both	$Na_x(Mg, Fe^{2+},Al)_{2-3}(Al, Si)_4O_{10}(OH)_2$
micas	0.6-1.0	taeniolite etc.	octahedral	$K(Mg, Li)_{2-3}(Al, Si)_4O_{10}(O,F,OH)_2$

1.2.3. Layered Polysilicates

Layered polysilicates (Table 3) are the class of layered solids with the layers made up only of SiO_4 tetrahedra. These materials occur in natural soil or are synthesized by hydrothermal heating of the mixture of e.g. SiO_2, NaOH and water. The crystal structure of makatite,[1] kanemite,[2] and octosilicate[3] have been determined as shown in Figure 3; however the structures of other layered polysilicates such as magadiite and kenyaite are still unknown and some model structures have been proposed based on ^{29}Si, ^{1}H and ^{23}Na NMR and the chemical compositions.[4,5]

Exchangeable alkali metal cations such as Na^+ and K^+ are present as the salt of $\equiv Si\text{-}O^-$ group of the silicate layer, although isomorphous substitution is not present inside the layers of layered polysilicates in contrast with smectite clays. Acid treatment of these materials leads layered polysilicic acids with silanol groups in the interlayer spaces. The metal cations and protons are exchangeable with other cations to form intercalation compounds; however, the reactivity is relatively low compared to smectite clays due to higher layer charge density. Preintercalation of alkylammonium ions such as dodecyltrimethylammonium cation was found to promote intercalation of some bulky guest species that are not directly intercalated. Other than ion exchange, polar organic molecules are also intercalated by forming hydrogen bond with interlayer silanol groups.[6] Silylation[7-10] and esterification[11] of interlayer silanol groups also lead intercalation compound with covalent bond between host and guest species. The obtained intercalation compounds are applicable as adsorbents[12,13] and precursor of mesoporous materials.[14,15]

Table 3. Layered polysilicates and their chemical compositions.

Silicate	Chemical composition
Makatite	$Na_2O \cdot 4SiO_2 \cdot 5H_2O$
Kanemite	$Na_2O \cdot 4SiO_2 \cdot 7H_2O$
Octosilicate	$Na_2O \cdot 8SiO_2 \cdot 9H_2O$
Magadiite	$Na_2O \cdot 14SiO_2 \cdot 10H_2O$
Kenyaite	$Na_2O \cdot 22SiO_2 \cdot 10H_2O$

(a)   (b)   (c)
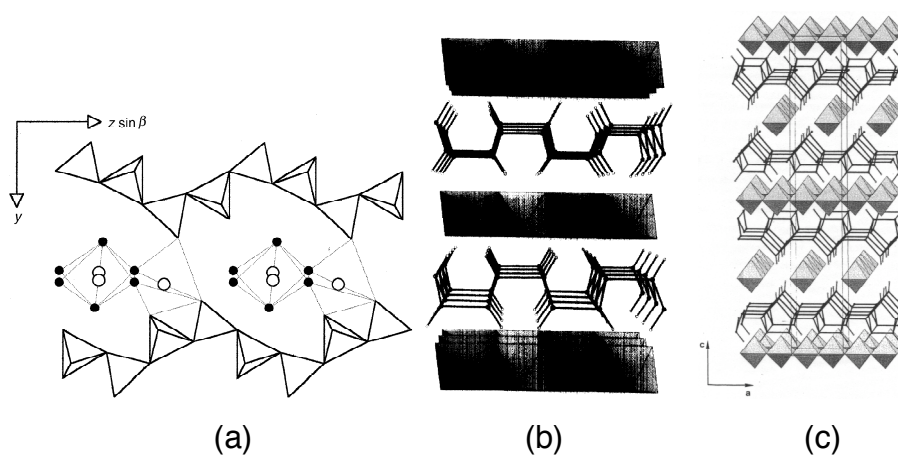
Figure 3. Schematic structures of layered polysilicates: (a) makatite,[1] (b) kanemite[2] and (c) octosilicate.[3] SiO_4 tetrahedra, water, oxygen atoms (small filled circles) and sodium ions (large unfilled circles) are shown in (a).   (b) and (c) are the skeletal models of the silicate layer with the sodium/hydrate water octahedral.

1.2.4. Layered Niobates and Titanates

Structure and Synthesis

To date, various kinds of layered transition metal oxides were synthesized and their intercalation capability as well as electric and optical properties were investigated. Among such materials, layered niobates and titanates are most intensively studied due to their novel semiconducting nature and structural and compositional variety. The structures of selected layered titanates and niobates are shown in Figure 4.
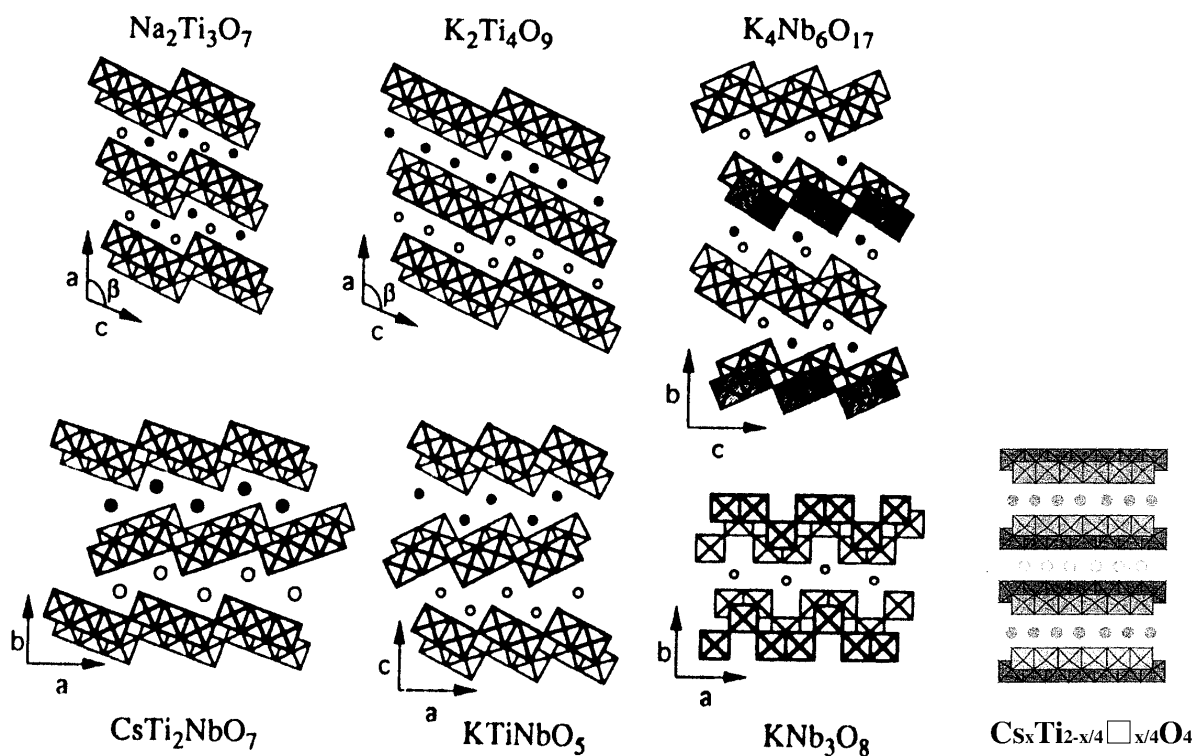
Figure 4. Schematic structures of typical layered titanates and niobates. Hatched squares represent NbO_6 or TiO_6 octahedra, and filled/empty circles represent alkali-metal ions at different positions.

Layered titanates and niobates are synthesized by solid-state reactions.[16-18]   For example, $Na_2Ti_3O_7$ is synthesized by heating a mixture of Na_2CO_3 and TiO_2 in the molar ratio of 1.1 : 3 at 900 °C for 24 h, and then for another 24 h after grinding.   These materials are also synthesized under relatively mild conditions (e.g. hydrothermal heating of an aqueous mixture of starting materials);[19-21] the soft-chemical route would merit for large scale synthesis.   On the other hand, although the layered solids are obtained as polycrystalline state in most cases, some of the materials such as $K_4Nb_6O_{17}$[22-24] and $Cs_xTi_{2-x/4}\square_{x/4}O_4$[25] are grown as large single crystals by slowly cooling down the melted mixture of the materials (e.g. Nb_2O_5 and K_2CO_3 for the niobates) in flux.   The single crystal of KNb_3O_8[24] was grown from the melt by Czochralski method.

Semiconductivity

Layered titanates and niobates are characterized by their semiconducting nature which leads to novel photocatalytic[26, 27] and luminescent properties.[28-32,27,33,34]   In the UV-spectra of the layered titanates and niobates, band-gap absorptions are observed at around < 350 nm, showing that the materials are intrinsic semiconductor with large bandgap energies similar to the well-known bulk semiconductor TiO_2.   Although experimental estimation of the conduction band edge energy is difficult, Kim et al. theoretically estimated the energy for layered niobates and titanates.   The estimated band gap and the conduction band edge energies are shown in Table 4 with those for anatase TiO_2 and bulk Nb_2O_5 for comparison.

Domen et al. found that layered niobate $K_4Nb_6O_{17}$[36,37] catalyze overall decomposition of water into H_2 and O_2 under UV-irradiation.   The photocatalytic activity for water decomposition was also reported for $Na_2Ti_3O_7$, $K_2Ti_2O_5$, $K_2Ti_4O_9$ and $K_2Ti_6O_{13}$,[38,26,27] although, sacrificing agent such as methanol was necessary and only H_2 evolved in these cases.   Due to the semiconductivity of the host lattice, the electrons in valence band are excited by UV-light to conduction band, followed by migration to active sites to reduce H_2O to H_2.   The photocatalytic activity was largely improved by loading clusters of Ni[39,40] or Pt[41] in the interlayer space since these clusters work as active sites for the reaction.   Deposition of CdS,[42] Fe_2O_3,[43] and TiO_2[44] in the interlayer

spaces also improved the photocatalytic properties.

Another property that originates from the semiconducting nature is luminescence one. Kudo et al. investigated in detail the luminescence property of layered titanates and niobates. Layered titanates ($K_2Ti_2O_5$, $Na_2Ti_3O_7$, $K_2Ti_4O_9$)[28] and niobates ($K_4Nb_6O_{17}$ and KNb_3O_8)[29] emitted blue light (around 400 – 500 nm) at 77 K by band gap excitation. Remarkably, KNb_3O_8 and $K_2Ti_2O_5$ were luminescent even at room temperature, which is rare case for bulk materials.[45] The luminescent property was tunable by ion-exchange of the interlayer spaces.[46] The luminescent intensity of $K_4Nb_6O_{17}$ became lower and the luminescence maximum wavelength red-shifted by exchanging the interlayer K^+ with H^+. The change in luminescence property was accompanied by the change in Raman spectra. These results indicated that the state of Nb-O bond was modified upon cation exchange, resulting in the change in the energy state of niobate layers.

Table 4. Band gaps energy (E_g) and conduction band edge energies at the point of zero charge (E_{Cs}^0) for titanates and niobates.[35]

	E_g / eV	E_{Cs}^0 / V vs NHE
TiO_2 (anatase)	3.22	-0.30
Nb_2O_5(bulk)	3.0	-0.55
$Na_2Ti_3O_7$	3.47	-0.96
$K_2Ti_4O_9$	3.48	-0.98
$KTiNbO_5$	3.50	-0.79
$CsTi_2NbO_7$	3.67	-0.83
KNb_3O_8	3.53	-0.45
$K4Nb_6O_{17}$	3.52	-0.76
$H_2Ti_3O_7$	3.27	0.015
$H_2Ti_4O_9$	3.25	-0.044
$HTiNbO_5$	3.47	0.021
HTi_2NbO_7	3.37	-0.054
HNb_3O_8	3.58	-0.073
$K_2H_2Nb_6O_{17}$	3.45	-0.265

Intercalation

The interlayer metal cations of the layered titanates and niobates are exchangeable with other cations to yield a variety of intercalation compounds. In early days, ion exchange with proton,[17, 47] metal ions,[48] alkylammonium[49-55] and pyridinium ions,[56] was investigated. These fundamental studies revealed that the intercalation reaction of layered titanates and niobates proceeded by ion-exchange of the interlayer cations and/or acid-base reaction with surface $–O^-H^+$ group with basic guest. Although the reactivity for intercalation is generally low due to relatively higher charge density of the sheet than e.g. smectite clays, various guest species are intercalated by preintercalation of basic guests such as alkylammonium ions, followed by replacing the preintercalated species with the target ionic guests.

Due to the semiconducting property and intercalation capability, layered titanates and niobates are suitable to fabricate photoactive nanohybrid systems.[57] Therefore, these materials have been intercalated or adsorbed with various photofunctional species such as methylviologen,[58-63] tris(2,2'-bipyridine)ruthenium(II) complex cation,[26,35,64 ,65,66] porphyrins,[67-69] methylene blue,[70] and rare earth metal cations.[30,71] Some of the details on the application of these photoactive intercalation compounds for the model system of electron and/or energy transfer will be described in Chapter 1.4.

Surface Derivatization

Recently, silylation of the surface -OH group of layered niobates and titanates was reported. Ide et al. reported[72] silylation of $K_2Ti_4O_9$ by the reaction of octylammonium-$K_2Ti_4O_9$ with a mixture of n-alkyltrimethoxysilane. Elemental analysis, XRD, thermogravimetry, infrared spectra, and ^{29}Si MAS NMR spectra evidenced the presence of organosilyl groups in the interlayer space. The silylation was also confirmed by the fact that the organosilyl gropus was stably held and not removed by treatment with acetone, chloroform, hydrochloric acid, or aqueous ammonia.

On the other hand, Bruzaud et al. reported grafting of poly(dimethylsilixane) to

$HTiNbO_5$ by in situ intercalative polymerization of cyclosiloxane in the presence of tetramethylammonium- or tetrabutylammnonium-exchanged $HTiNbO_5$.[73] Although no definitive proof of silylation was presented, XRD, elemental analysis and infrared spectra probed the presence of poly(dimethylsilixane) in the composite. Ligation of 3-aminopropylsilane onto butylammonium-exchanged $HCa_2Nb_3O_{10}$ was also reported; however no detailed characterization is provided in the report except for confirmation by ninhydrin reaction.[74]

1.3. Exfoliation of Inorganic Layered Materials

1.3.1. Overview

Inorganic layered materials swell by intercalation of solvent molecules into their expandable interlayer space; infinite swelling of the interlayer space leads to *exfoliation* (or delamination) of layered materials to individual inorganic nanosheets (Figure 5). The obtained nanosheets are regarded as peculiar macromolecular species characterized by (1) extremely large aspect ratio with large lateral size up to several μm and uniform thickness of several nm, (2) electric, optical and magnetic properties and defined structure with high crystallinity, which originate from the intrinsic property of host materials, and (3) capability of supramolecularly organizing guest species on the sheet. These features open applications of the inorganic nanosheets as modules for fabricating nanohybrid solids with controlled morphology and novel colloidal systems. This section describes the methods and applications of exfoliation of inorganic layered materials.
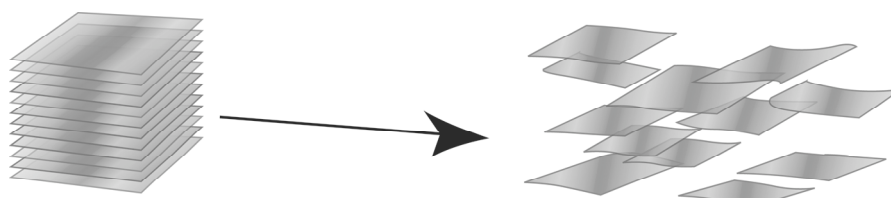
Figure 5. Schematic drawing of exfoliation of layered crystals.

1.3.2. Materials and Methods

Spontaneous Exfoliation by Dispersing in Solvents

Layered clay minerals such as montmorillonite, saponite and hectorite are easily exfoliated by dispersing in water, due to high affinity of interlayer cation (normally Na^+ and Ca^{2+}) with water and weak attractive interactions between the adjacent layers with low layer charge density. Due to the ease of preparation and high chemical stability of the aluminosilicate layers, the colloids of exfoliated clays have extensively been studied: due to peculiar properties such as rheological one, colloidal dispersion of exfoliated layered clay minerals have attracted scientific interests and been

used for versatile industrial applications.

In 1970s, a layered metal chalcogenides such as TiS_2,[75] TaS_2 and NbS_2[76] were found to be exfoliated by dispersing in solvents with high dielectric constants (e.g. formamide and N-methyl formamide). Exfoliation of NbS_2,[77] MoS_2[78-80] and WS_2[81] were also studied lately. Although the exfoliated metal chalcogenides were used to prepare catalysts and intercalation compounds with large guest species that are not topochemically intercalated, the drawback is that the layers themselves are chemically unstable in the presence of water or oxygen.

Exfoliation by Modifying the Interlayer Environment

Exchanging of the interlayer metal cations with alkylammonium ions, such as tetrabutylammonium, propylammonium, butylammonium and ethylammonium, was found to be a convenient way to exfoliate various layered materials in water: exfoliation of layered solids such as niobates,[82-87,67,88-92] titanates,[93-104] zirconium phosphates,[105,83,106-109,67] MnO_2,[110,111], $H_2W_2O_7$,[112] $MnPS_3$,[113] $CdPS_3$[113] and ruthenium oxide[114] have been conducted by this method. The intercalation of alkylammonium serves to expand the interlayer space as well as to give higher affinity of the interlayer space with solvents, so that the solvent molecules can easily penetrate into the interlayer space.

Detailed studies of the process and condition of exfoliation have been made for some systems. Sasaki et al. studied the exfoliation of the layered titanate $Cs_xTi_{2-x/4}\square_{x/4}O_4$ as the function of the concentration of tetrabuthylammonium cation by measuring XRD patterns of wet colloids obtained by treating the titanate with the aqueous alkylammonium.[93, 94, 97] Fully exfoliated state was obtained at intermediate alkylammonium contents. When the amount of the alkylammonium ions was not large enough to cover the surface of the titanate sheet, the system did not keep exfoliated state but tetrabutylammonium- and proton-exchanged forms of the titanate emerged as shown by XRD measurement. At higher alkylammonium contents, the system was no longer in exfoliated state but in osmotic swelling state. The observed results would be rationalized as follows: although certain amount of alkylammonium is necessary to

modify the accessibility of water molecules into interlayer spaces, excess amount of alkylammonium ions (higher ionic strength of the system) serves to screen electrostatic repulsion force between the nanosheets, leading to destabilization of exfoliated state.

Just like the use of cationic exfoliating agent for exfoliation of anionic layers, anionic surfactant (dodecylsulfate) were used to delaminate layered double hydroxides, whose layers are positively charged, in butanol.[115, 116] Amino acid anion (glycine)[117] and alkoxide anion[118] were also used for exfoliation of layered double hydroxides in formamide and water, respectively.

Instead of using ionic species as exfoliating reagent, surface modification of layered solids with covalently bonded species were also reported. Ide et al. showed that a layered titanate modified with organosilanes were dispersed in toluene, methanol and chloroform.[72] Mitamura et al. reported that layered silicate magadiite was dispersed in toluene after esterification of the surface with butanol.[11] Such methodology would be advantageous to gain nanosheets with higher thermal and chemical stability.

Exfoliation of graphite oxide is another example of surface modification with covalently bonded species. Aromatic carbons of the graphite layers are oxidized to –OH and –COOH groups. Although graphite is dispersed neither in water nor organic solvents,[119] the oxidized forms of graphite are spontaneously exfoliated in water due to high hydrophilicity.[120-123] Notably, graphite oxide is recovered to graphite chemically or electrochemically.[120]

1.3.3. Applications
1.3.3.1. Multilayered films
Casting and Spin Coating Depositions

Since the exfoliated layered solids possess highly anisotropic shape, highly oriented multilayered films with a nanostructure are obtained by simply casting or spin-coating the sols that contain nanosheets. The thin films have been prepared by this method with the layered materials such as MPS_3 (M = Mn, Cd),[113] $K_4Nb_6O_{17}$,[124,98] $Cs_xTi_{2-x/4}\square_{x/4}O_4$,[96,98-101, 103] and smectite clays.[125-130] Due to the large anisotropy of the

nanosheets, the restacked nanosheets tend to be oriented along the surface of substrates as exemplified by observation by AFM and TEM, and by polarized spectroscopies (IR[131] or UV-visible[130]) performed on the film intercalated with chromophores. Since the films thus obtained are highly transparent and anisotropic, in contrast with the powders with the same composite and nanostructure, these films are suitable to use as photo devices by incorporating photofunctional species: the applications as non-linear optical[127,113] and photo chemical hole burning[125] materials have been reported.

Layer-by-Layer Deposition

Kleinfeld and Ferguson[132-135] reported stepwise formation of multilayered films by alternate adsorption of a cationic polyelectrolyte PDDA (poly(diallyldimethyl-ammonium chloride)) and exfoliated nanosheets of Laponite (synthetic layered clay mineral, hectorite); the methodology is now recognized as 'layer-by-layer deposition'. Figure 6 represent the deposition process presented in the report: first, aqueous solution of PDDA was dropped on the substrate (hydroxylated silicon wafer), followed by rinse with water and drying. Subsequently, aqueous dispersion of Laponite was dropped, rinsed and dried. Repeating this cycle 200 times resulted in the films with thickness of 0.2 μm. Constant increase of ellipsometric thickness with increasing number of the cycles and observation of the 00l reflections by X-ray diffraction evidenced the formation of multilayered structure. Layer-by-layer film deposition has been applied to wide range of materials: layer-by-layer films containing α-Zr(HOPO$_3$)$_2$,[83,136,67] niobates (KTiNbO$_5$, KCa$_2$Nb$_3$O$_{10}$ and KCa$_2$NaNb$_4$O$_{13}$),[108,87,67] titanate,[137-139] as well as layered clay minerals[140-144] were fabricated.
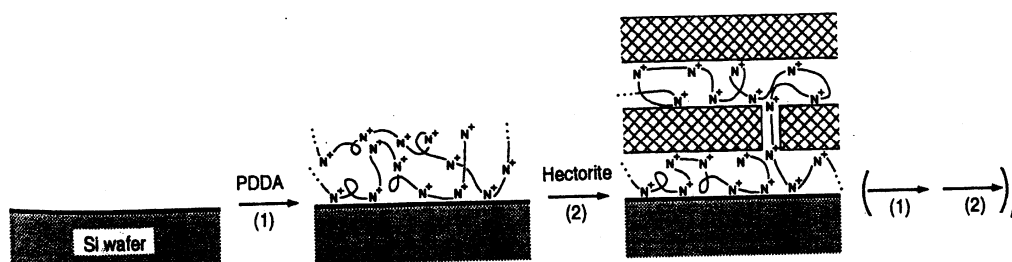
Figure 6. Layer-by-layer deposition of PDDA-Laponite film.[132]

The great merit of layer-by-layer film deposition is potential for fabricating heterogeneous stacking of various components in desired sequence, as proposed by Kellar et al.[83] (Figure 7a). For example, the heterostructure was obtained by sequential deposition of anionic nanosheets of α-ZrP and $K_2Nb_6O_{17}^{2-}$ with a polycation PAH ((poly(allylamine)hydrochloride); increment of the ellipsometric thickness corresponded to the thickness of each components (Figure 7b), indicating the formation of the heterogeneous superstructure.

By heterogeneously assembling electron acceptor, sensitizing dyes, and nanosheets of titanoniobate or zirconium phosphate, the model system of photo-induced electron transfer was fabricated.[136, 145, 146] As another example of applications, Cassagneau et al. fabricated high density (1232 mAh g^{-1} of graphitic carbon) rechargeable lithium ion battery cathode composed of heterogeneously stuck polyethyleneoxide, PDDA, and garaphite oxide.

(a)   (b)
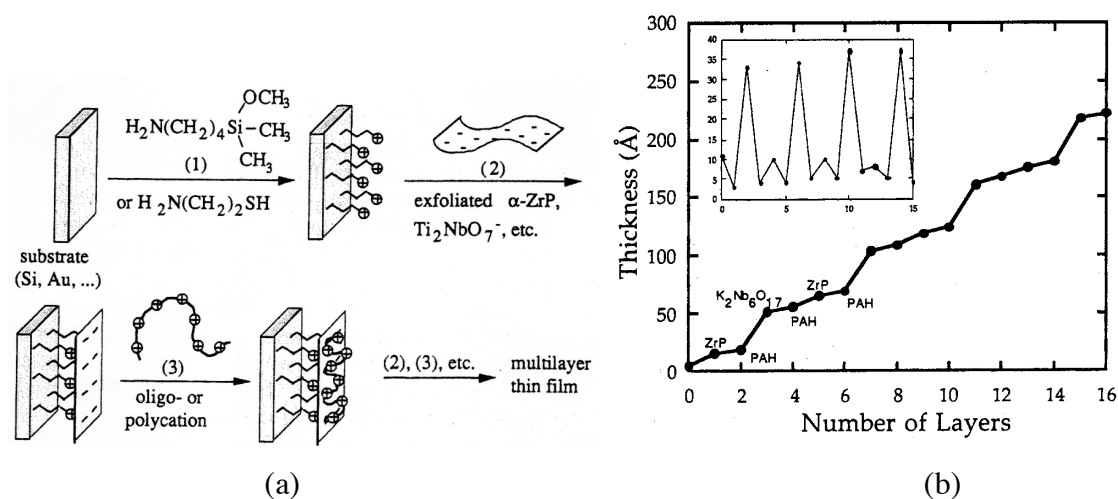
Figure 7. (a) Sequential adsorption scheme for producing multilayer films by alternate adsorption of inorganic two-dimensional anions and oligomeric or polymeric cations. (b) Ellipsometric data for the α-ZrP/PAH/$K_2Nb_6O_{17}^{2-}$/PAH heterostructure; Layer thicknesses were calculated using a film refractive index of 1.54. The inset shows the first derivative of the thickness for each adsorption step. Small and large peaks in the inset correspond to α-ZrP and $K_2Nb_6O_{17}^{2-}$ adsorption steps, respectively; points in between are PAH adsorption. [83]

Electrophoretic Deposition

Multilayered films are also deposited electrophoretically by making use of the charge of the exfoliated nanosheets. The advantage of this technique compared to the casting and layer-by-layer depositions is high uniformity of resulting film, easiness in thickness control, applicability to large scale deposition, and deposition to complex shaped substrate.

Sugimoto et al. reported electrophoretic deposition of exfoliated $H_2Ti_4O_9$ nanosheets (Figure 8).[104] The counter cations of the titanate, the exfoliating agent tetrabutylammonium cations, are collected around the cathode, whereas the negatively charged nanosheets are deposited onto the anode, resulting in the formation of $H_2T_4O_9$ film as confirmed by XRD. In contrast, the electrophoretic deposition of the films from the suspended fine powders of $Cs_xTi_{2-x/4}\square_{x/4}O_4$[147] and $K_4Nb_6O_{17}$,[148] which are not completely exfoliated, results in the film of alkylammonium-intercalated forms. Thermal treatment of the deposited films led to an oriented $TiO_2(B)$ film, which is valuable due to electrochemical and catalytic properties compared to other TiO_2 polymorphs, with the *(0k0)* planes lying perpendicular to the substrate.
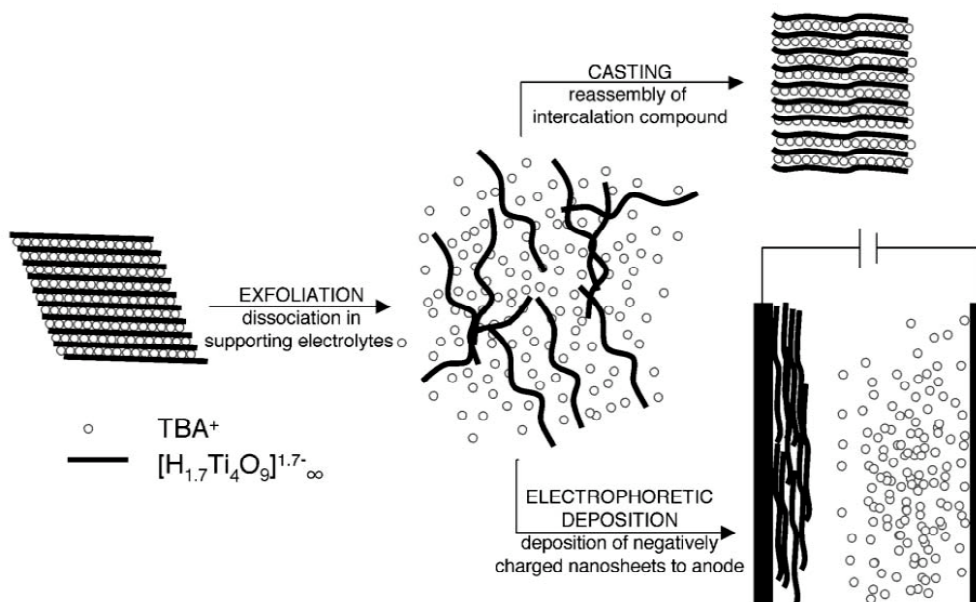
Figure 8. Schematic of the exfoliation and deposition of $H_2Ti_4O_9$ H_2O.

1.3.3.2. Porous solids

The nanosheets obtained by exfoliation are also usable as building units of porous materials. Sasaki et al. reported fabrication of porous titanium dioxide powders by reassembling exfoliated layered titanate $Cs_xTi_{2-x/4}\square_{x/4}O_4$ (Figure 9).[95] The sol containing the titanate nanosheets was freeze-dried to yield "voluminous white solid with cotton-like appearance". Heating this solid at 400 - 700 °C resulted in destruction of the lamellar structure; by removal of interlayer tetrabutylammonium ions and H_2O molecules, the material was recrystallized into titanium dioxide with pores. The final product was a flaky powder with the BET surface area of 47 - 104 $m^2\,g^{-1}$ and mode pore size of 23 - 51 nm depending on the temperature of heating.
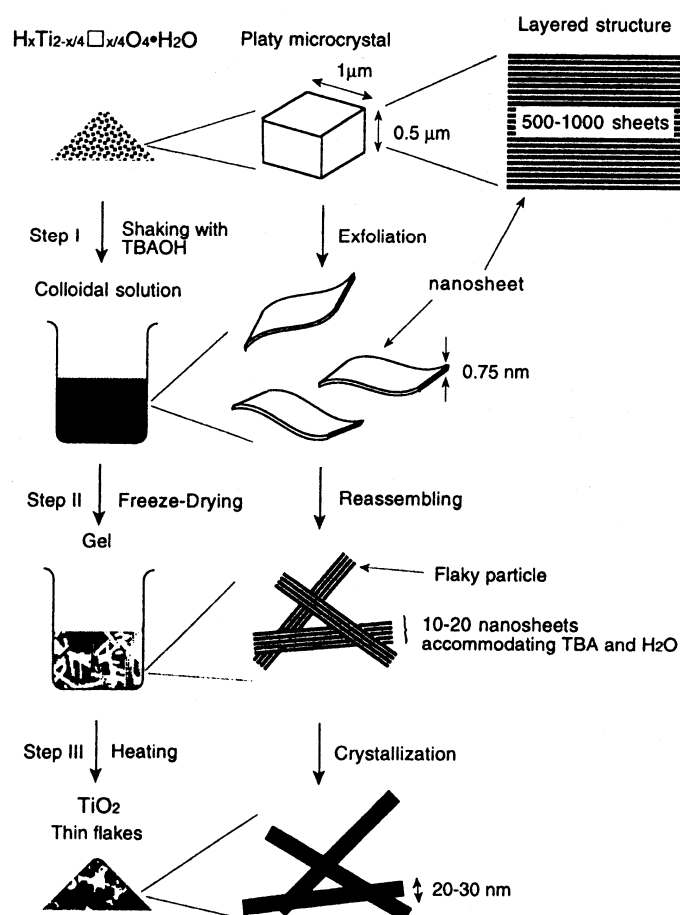
Figure 9. Schematic illustration of synthetic process of the titanium dioxide thin flakes.[95]

Reassembling of exfoliated nanosheets with pillars also leads to porous solids. Exfoliated nanosheets of $Cs_xTi_{2-x/4}\square_{x/4}O_4$[149] and $K_4Nb_6O_{17}$[84-86] were reassembled with pillars of metal oxide fine particles in the interlayer spaces; the potential use of these materials as photocatalysts were examined in these reports. Even without freeze drying and pillaring, acidification of $HTiNbO_5$ nanosheet colloids also lead to aggregation and precipitation of the powders, which worked as stronger solid acid catalyst than the bulk solid of $HTiNbO_5$.[150]

Another strategy of fabricating porous solids from exfoliated nanosheets makes use of curling of the nanosheets due to the flexibility of the sheets. Saupe et al. found that exfoliated niobate nanosheets are curled into well-defined tubules, which are useable as building units of porous materials.[88] The formation of tubules was observed by TEM; the nanosheets tended to be curled at higher colloid concentration and lower pH. It was also inferred that curling occurred only when the niobate is exfoliated to single layers as evidenced by AFM. From these observations, it was suggested that the curling is driven by the inherent asymmetricity of the exfoliated nanosheets (one side is less sterically crowded than the other). Drying the colloid containing the tubules resulted in porous powders with the BET surface area of 37 m^2 g^{-1} and mean pore size of 10 nm, which was comparable to the diameter of the tubules observed by TEM.

Camerel et al.[151] extended the concept of Saupe et al. in a unique way to obtain mesoporous niobate-aluminosilicate composite with unidirectionally oriented pores (Figure 10 and 11). The colloid of tubules was added with the solutions of aluminum sulfate and sodium silicates, followed by hydrothermal treatment. The tubules were self-organized with their main axis in same directions due to the formation of nematic liquid crystalline state driven by excluded volume effect between the tubules. The obtained composite possessed BET surface area of 102 m^2 g^{-1} and mean pore size of 14.6 nm, indicating that the method presented is valuable for synthesizing composite mesoporous materials.

Most recently, nematic liquid crystalline phase of V_2O_5 nanosheet ribbons (the details of the liquid crystalline nature of V_2O_5 system is described in the following section) was used as a template, not as a module, to fabricate mesoporous composite

with aligned pores on the cm scale.[151] Hydrolysis of tetramethoxysilane in the presence of liquid crystalline V_2O_5 sol yielded inorganic-inorganic composites; after removing V_2O_5, the composite exhibited slit-like mesopores (the cross-sectional dimensions of 2 × 20 nm) and a specific surface area of 207 m^2g^{-1}. Applying weak magnetic field (0.85 T) during preparation yielded large single domain (cm-scale) with unidirectional channel director.
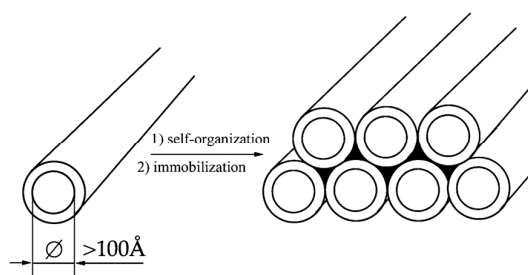
Figure 10. Schematic representation of a novel route to the synthesis of mesoporous materials by self-assembling of tubular structures. The black zones between cylinders represent a glue, here an aluminosilicate.
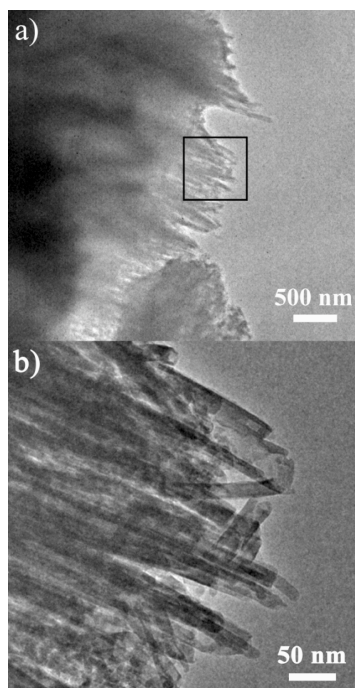
Figure 11. (a) TEM image of the composite material aluminosilicate–niobium oxide tubules. (b) Zoom of the border of a grain showing the frozen nematic-like organization of tubules along the edge of this composite material.

1.3.3.3. Lyotropic Liquid Crystals

Recently, dispersions of nanosheets obtained by exfoliation of layered solids are attracting recurrent interests as novel class of lyotropic liquid crystals. It is generally known that a dispersion of anisotropic particles form liquid crystalline phases at higher concentrations; this type of liquid crystals, whose formation is induced by concentration change, is termed as lyotropic liquid crystals, being distinguished from thermotropic ones. Organic materials such as surfactant micelle solutions and dispersions of a stiff polymer (DNA, TMV, etc.) are known as typical examples of lyotropic liquid crystals. In contrast, liquid crystalline dispersions of inorganic particles is of great interest due to high chemical stability and electric and optical properties of the inorganic particles.[152-154] Exfoliated nanosheets are regarded as fascinating class of liquid crystalline inorganic dispersions with structural and compositional varieties, defined crystal structures, a large anisotropy of the sheets, and modifiable layer surfaces according to the techniques developed for intercalation chemistry. These features are valuable in view of the potential applications of the lyotropic liquid crystals as optical, magnetic and electric devices,[153,155,74] templates for porous materials,[156,151] soft matrices of functional molecules,[157] etc.

On the other hand, the mechanism of formation of lyotropic liquid crystals has been theoretically investigated for long period. In 1940s, Onsager showed that lyotropic liquid crystallinity of colloidally dispersed anisotropic particles (rods and plates) is rationalized by excluded-volume effects working among the particles:[158-162] the anisotropic colloids transit from isotropic to liquid crystalline state when the loss of orientational entropy is outweighed by gain in excluded-volume (packing) entropy. On this basis, the liquid crystalline state is favored at higher concentration and larger aspect ratio of the particles. The simulation[163-166] studies have verified that colloidally dispersed anisotropic particles (rods and plates) generally form lyotropic liquid crystals. Large number of colloidally dispersed rods such as viruses,[167] chain polymers,[168,162] DNA,[169,170] surfactant micelles and inorganic nanoparticles[152,153,155] have been found to form liquid crystals. However, only a limited number of colloidal plates[171-174] have been reported so far. Thus, the nanosheet dispersions derived from layered solids are

also attractive as novel model systems for theoretical investigations.

As the first example of liquid crystalline nanosheet colloid, colloidally dispersed V_2O_5 nano-ribbons were discovered in 1920s[175] and have been investigated by several groups.[176-180] The optical textures such as schlieren one observed under crossed polarizers with polarized microscope (Figure 12) as well as the small-angle x-ray scattering data of the sol evidenced the formation of nematic liquid crystalline phases. Further, the liquid crystalline V_2O_5 sol was shown to be macroscopically oriented by magnetic[181] or electric fields.[179]
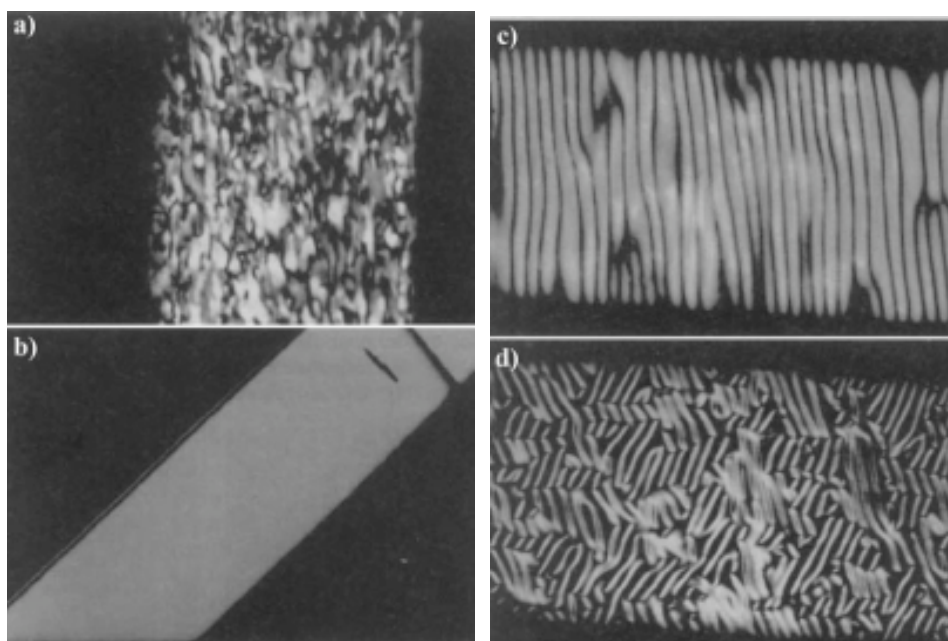
Figure 12. Texture photographs in polarized light of transient hydrodynamic instabilities induced by a sudden change of the magnetic field orientation: (a) starting from a powder sample; (b) the magnetic field is applied along the main capillary axis; (c) the magnetic field direction is now perpendicular to the main capillary axis, but still in the plane of the figure. In consecutive stripes, the ribbons point in two different but symmetrical directions with respect to the polarizer-analyzer directions, giving rise to a zigzag pattern; (d) the magnetic field direction is now perpendicular to the plane of the figure. The dark regions are areas where the ribbons are perpendicular to the plane of the figure whereas the bright regions are areas where the ribbons still lie in the plane of the figure.

Desvaux et al. showed a novel application of liquid crystalline V_2O_5 sol as anisotropic medium for NMR spectroscopy.[180] dissolved biomolecules such as oligosaccharide is aligned in the medium, leading to structural restraints that help to determine the structure of the biomolecules by NMR spectroscopy. Compared to other organic media for the same purpose, this system is advantageous in that the medium is highly stable over wide temperature range, and that no isotope labeling of a sample is required.

The liquid crystallinity of clay minerals has also been known for long;[182-185] however, the liquid crystallinity is observed only with gelation of the colloids so that detailed study of the clay liquid crystals is not straightforward. Gabriel et al. studied the liquid crystallinity of the colloids of montmorillonite and hectorite clays as the function of salt and clay concentrations[183] by careful preparation and observation of the sol and gel samples (Figure 13).

Although only V_2O_5 and clays had been known as liquid crystalline nanosheet dispersion systems for long, some novel systems were recently found. $H_3Sb_3P_2O_{14}$ was reported as the first example of lamellar liquid crystal,[154] in contrast to nematic ones. This system is also characterized by the magnetic responsibility as has been reported for V_2O_5 system. Chapter 6 of this thesis describes another novel example of liquid crystalline nanosheet colloid composed of exfoliated layered niobate $K_4Nb_6O_{17}$.[157] This is the first case that the particle size is controlled over very wide range. Also, this system is characterized by the photoactivity and capability of forming hybrid, which would lead to novel soft materials. Exfoliated layered niobates KNb_3O_8 and $KTiNbO_5$ and layered double hydroxides[186] were also recently reported as another examples of liquid crystalline nanosheet colloids.
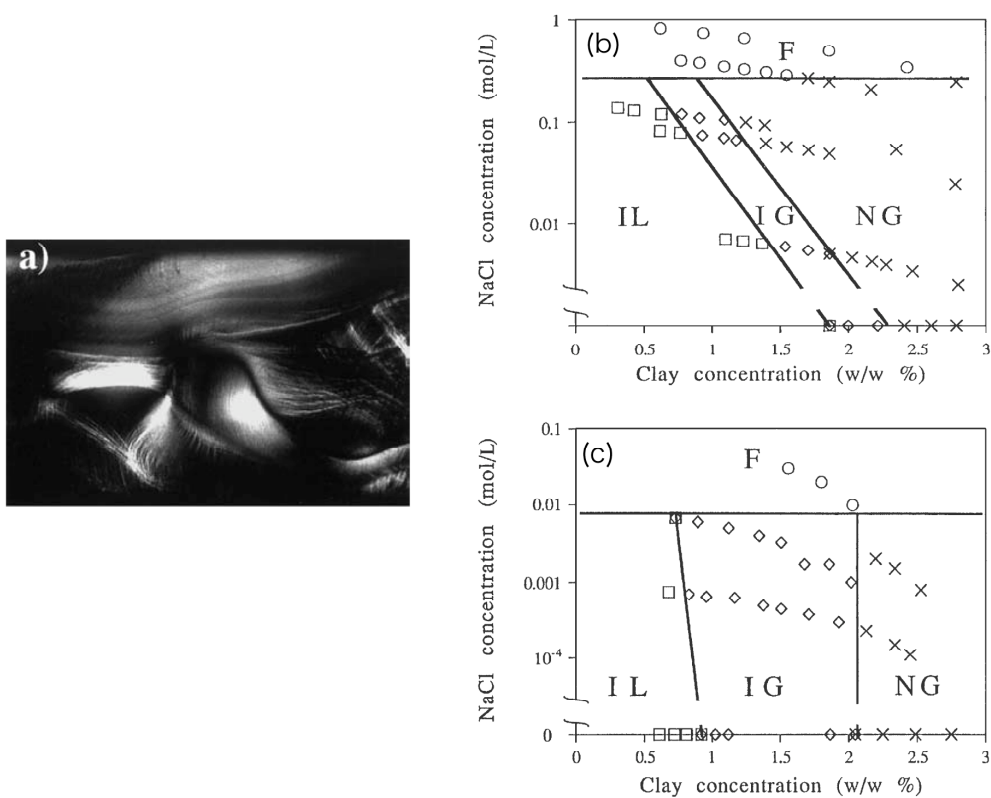
Figure 13. (a) Microscopic observations in polarized light of the textures of the aqueous Bentonite suspension ([clay] = 0.044 g/cm^3). Phase diagrams of (b) Bentonite and (c) Laponite clay suspensions: (*circles*, F) Flocculated samples; (*squares*, IL) isotropic liquid samples (*lozenges*, IG) isotropic gel samples; (*crosses*, NG) nematic gel.

1.4. Photofunctional Nanohybrids from Inorganic Layered Materials

1.4.1. Overview and Examples

Fabricating supramolecular assemblies of photoactive species is of great interest since the property of photoactive species is tuned by the interaction between the species and their arrangement and orientations.   Whereas self-assembling of appropriately designed molecules as Langmuir-Blodgett films, micelles, vesicles, and single crystals is a way to fabricate the desired architectures, organizing the photoactive species on or inside defined matrixes or templates is promising alternatives.   Whereas organic materials such as cellulose and DNA are used as the matrixes, using inorganic materials is advantageous because inorganic components synergistically exert novel properties such as high mechanical and chemical strength and electric properties.   Among various inorganic matrixes such as sol-gel glasses, zeolites and mesoporous solids, inorganic layered materials are capable of organizing any size of guest species with distinctive two-dimensional anisotropy as already shown in Chapter 1.2.   Therefore, as one of the smartest application of intercalation chemistry, organizing photoactive species in the interlayer spaces has been investigated in the last decade.   Whereas novel applications of such methodology for non-linear optical, photochemical hole burning, photochromic and luminescence materials have been reviewed previously,[187,188] this section focuses on photoinduced electron and/or energy transfer systems, which would lead novel photoenergy conversion and storage systems.

1.4.2. Photoinduced Electron Transfer from Hosts to Viologens

Viologens are useful spectroscopic probes for electron transfer reaction since they undergo reversible reduction/oxidation reaction, and the one-electron reduced species is well-characterized by blue-color or the characteristic absorption bands in visible spectrum at around 400 and 600 nm.   Also, viologens are used as electron relays.   Therefore, viologens were immobilized in layered solids such as clay minerals,[189-194] titanate,[58] niobates,[59-63] zirconium phosphate[195-197] and V_2O_5[198] as well as in zeolites, surfactant micells and vesicles, and photochemical behavior of the

composites was investigated in view of fabricating solar energy conversion and storage systems.

Miyata et al. reported[58] photo-induced electron transfer between the semiconducting host layer and methylviologen. Upon UV-light irradiation, viologen radicals were formed as confirmed by ESR and visible absorption spectroscopies.   The results indicated that the titanate layer act as electron donor: the photoexcited titanate sheet transfer electron to methylviologen, resulting in reduction of methylviologen to radical cation species.   Nakato et al. systematically investigated the intercalation and photoinduced charge separation between methylviologen and various layered semiconducting solids such as $HTiNbO_5$,[59,63] $K_4Nb_6O_{17}$, HNb_3O_8[60,61,63] and $HA_2Nb_3O_{10}$ (A = Ca, Sr).[62]   By comparing these systems, it was discussed that the nanostructures of the compounds and the cationic species coexisting with viologen in the interlayer space affect the stability of the photo-generated $MV^{+\bullet}$.

Vermeulen et al. reported long-lived charge separation induced by light irradiation in layered compounds composed of alternating layers of viologen and zirconium phosphate (Figure 14).[195-197]   In this system, halide ions, which coexist with the viologen in the interlayer spaces, worked as an electron acceptor, whereas the formation of viologen radical was initiated by excitation of the viologen followed by charge transfer from halide ions.   The photoexcitation of viologen at the initial stage was evidenced by the similarity of the action spectra to the absorption spectrum of viologen in the system.   The role of halide ions as the electron acceptor was deduced from the strong dependence of the relative photoreduction rate of the viologen on halogen: 1 : 0.82 : 0.67 for Cl, Br and I, respectively.   The generated radicals were stably kept for days and hours under anaerobic and aerobic conditions, respectively.   It was proposed that the unusual stability of the charge-separated state arises from structural features which allow for delocalization of the radical and shielding from molecular oxygen.   This speculation was also partly supported by the fact that in the film samples, which were not as tightly packed as microcrystalline samples, the generated viologen radical was much less stable.[196]

Long-lived viologen radical cation was also formed in the interlayer spaces of

smectite clays by photo irradiation.[194]   It was claimed, in this report, that lone pair of Si-O-Al oxygens, which occurred due to isomorphous substitution of the Si^{4+} with Al^{3+} in the tetrahedral sites of the framework of smectite clays, act as electron donor (Figure 15); similar mechanism had been also proposed for zeolites with similar surface structure.   Remarkably, the radical cation of the viologen generated in synthetic hectorite clay was very stable in air giving the half-life of 4 month.
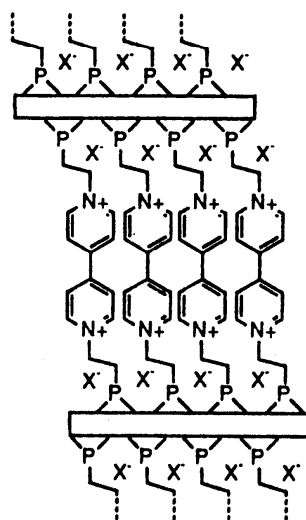
Figure 14.   Schematic structure of the viologen-zirconium phosphate complex.
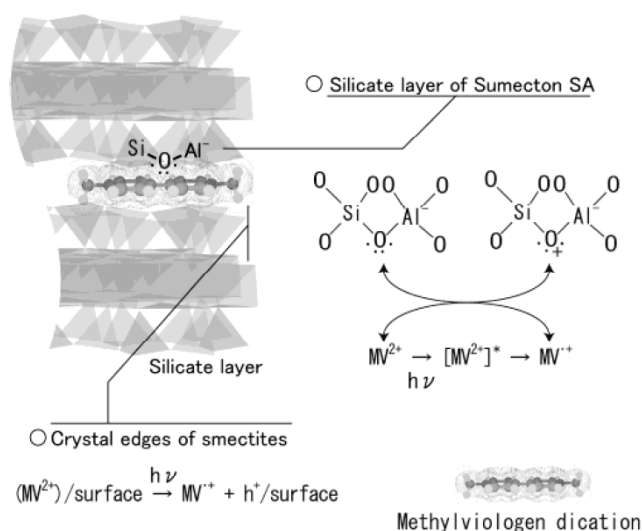
Figure 15.   Proposed electron-donating sites of smectite.

1.4.3. Photoinduced Energy/Electron Transfer from a
Sensitizing Dye to Host Layer

<u>**Ruthenium Polypyridine Complexes**</u>

Complexation of sensitizing dyes with layered semiconducting materials is worth investigating for the application as sensitized photocatalyst as well as for model system of electron transfer reactions in heterogeneous media. Ruthenium polypyridine complexes such as tris(2,2'-bipyridine)ruthenium(II) complex (abbreviated as $[Ru(bpy)_3]^{2+}$) are most widely used as photosensitizer and spectroscopic probe due to high chemical stability and characteristic metal-to-ligand charge transfer (MLCT) absorption and long-lived luminescence from triplet state. Whereas the ruthenium complexes were intercalated in various layered solids in order to probe the state of the interlayer spaces, photo-induced electron/energy transfer to host layers have been investigated by some groups.

Kim et al. reported sensitization of proton-exchanged $K_4Nb_6O_{17}$ by adsorbing $Ru\text{-}L_3^{2+}$ (L = 2,2'-bipyridyl-4,4'-dicarboxyalate) on external surfaces of the layered niobate (Figure 16).[26] In the laser flash photolysis/transient diffuse reflectance measurements on the suspension of proton-exchanged $K_4Nb_6O_{17}$ adsorbed with RuL_3^{2+}, bleaching of MLCT absorption at 460 - 470 nm and biphasic decay of the bleached band was observed, indicating formation of Ru^{3+}-semiconducotr charge-separated state. When KI is added to the suspension, the beaching at 460-470 nm was not observed and a positive transient at 380 nm, attributed to $I_2^{\bullet-}$, was observed. Thus the reaction sequence was inferred as:

$$*RuL_3^{2+} \rightarrow RuL_3^{3+} + e^- \text{conduction band}$$
$$RuL_3^{3+} + I^- \rightarrow RuL_3^{2+} + I^{\bullet}$$
$$I^{\bullet} + I^- \rightarrow I_2^{\bullet-}$$
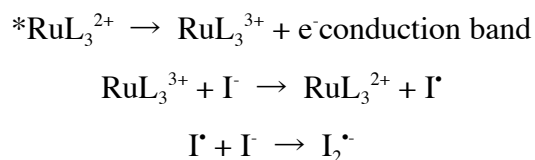
By loading platinum clusters in the interlayer space, the material evolved H_2 by visible-light irradiation for the production of H_2 and I_3^- in aqueous iodide solutions.

Similar dye-sensitized hydrogen evolution was also observed for other layered

niobates and titanoniobates (KNb_3O_8, $KTiNbO5$ and $CsTi_2NbO_7$) with some difference in the rate of hydrogen evolution, whereas the layered titanates ($Na_2Ti_3O_7$ and $K_2Ti_4O_9$) were inactive in the photocatalytic reaction.[35] The absence of photocatalytic activity in titanate systems were rationalized by the more negative conduction band edge potentials of the titanates compared to that of hydrogen/water formal potential. The structural difference of the materials, which cause difference in accessibility of electron donor and interlayer conductivity, was also thought to be the reason for that difference. In this system, some optimization of the catalytic activity was reported afterward.[65]

Figure 16. Schematic drawing and potential energy diagram of RuL_3^{2+}-sensitized layered metal oxide semiconductor systems for HI photolysis.

The photo-induced electron/energy transfer was also examined for the ruthenium complex intercalated between layered semiconductors. Nakato et al. [64] intercalated $Ru(bpy)_3^{2+}$ in $K_4Nb_6O_{17}$, $HTiNbO_5$ and $H_2Ti_4O_9$ and found that fluorescence lifetimes of intercalated $Ru(bpy)_3^{2+}$ are shorter than in aqueous solution of $Ru(bpy)_3^{2+}$; this result indicate that the guest-to-host electron/energy transfer probably took place. The microstructure and coexisting species affected the luminescence lifetime. Comparison of racemic and enantiometric $Ru(bpy)_3^{2+}$ as sensitizer would also give information of the effect of microenvironment of the intercalated $Ru(bpy)_3^{2+}$ on the sensitization process.[199]

Furube et al. examined $Ru(bpy)_3^{2+}/K_4Nb_6O_{17}$ system by femtosecond transient absorption spectroscopy.[66] The excitation of the compound at 400 nm resulted in bleaching of ground-state absorption of the dye accompanied by very weak transient absorption at the wavelength of > 550 nm, which would be ascribed as the tail of the band (centered at around 370 nm) originated from excited state of $Ru(bpy)_3^{2+}$ (triplet state). Very short life times of these transient states (around 1 ns) compared to that observed in aqueous $Ru(bpy)_3^{2+}$ (670 ns) suggested the electron transfer from photoexcited $Ru(bpy)_3^{2+}$ to the niobate sheet. Based on the fluorescence decay results and the lifetimes of the transient absorption bands fitted as double-exponential decay, the dynamics of the system upon photoexcitation were inferred (Figure 17); however, further confirmation would be necessary to confirm the proposed schematic diagram.
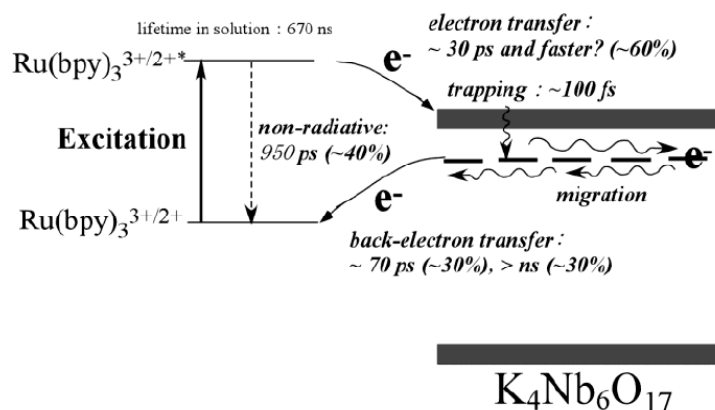
Figure 17. Proposed dynamics of $K_4Nb_6O_{17}$ intercalated with $Ru(bpy)_3^{2+}$ excited by a 400 nm fs pulse is illustrated with the schematic energy diagram.

Porphyrins

Porphyrins and phthalocyanines are typical antenna dyes, which is analogous to chlorophyll derivatives in natural photosynthetic systems of green leaf. Complexation of porphyrin derivatives with various layered materials has been conducted.[200,201,67,68,202,69,203]   In some cases, photoinduced electron transfer between the sheets and the dyes have been examined aiming at applications as photoenergy conversion and its model systems.

Kaschak et al. fabricated "energy transfer cascade" films by sequentially stacking electron acceptor (viologen), exfoliated nanosheets of zirconium phosphate or titanoniobate, and sensitizing dyes (coumarin- and fluorescein-derivatized polymers and porphyrin derivatives), by layer-by-layer assembly technique.[67]   UV-visible absorption and emission spectroscopy showed that the overall energy/electron transfer reaction occurs with approximate quantum yields of 0.47.   The yield was even higher (0.61) when $HTiNbO_5$ was used instead of α-ZrP (Figure 18).   It was supposed that semiconducting $HTiNbO_5$ sheets play an active role in relaying the electron from photoexcited dye to the viologen electron acceptor.

Yamaguchi et al. intercalated tetrakis(4-carboxyphenil)porphyrinato zinc(II) (Zn(II)TCPP) into the interlayer spaces of $K_4Nb_6O_{17}$.[68]   In the fluorescence lifetime measurement, short life-time component which would be ascribed to electron transfer from the dye to host layer was observed, along with the hydrogen evolution upon visible light irradiation in the presence of KI.   These features were observed only in the system synthesized from proton-exchanged form of $K_4Nb_6O_{17}$, whose conduction band energy is more positive than the $K_4Nb_6O_{17}$, supporting occurrence of the electron injection process.

Tong et al. reported visible-light induced charge-separation in the composite film of tetrakis(N-methylpyridinium-4-yl)porphyin ($TMPyP^{4+}$), titanoniobate $TiNbO_5^-$, and methyl viologen.[69, 203]   The film was obtained by casting and drying the aqueous suspension of viologen/$TiNbO_5$ intercalation compound, followed by casting and drying the suspension of $TMPyP^{4+}$/$TiNbO_5$ intercalation compound onto the same film. Irradiation of visible light to this composite film caused the formation of

methylviologen. The action spectrum coincided with the visible spectrum of the intercalated porphyrin. These results indicate the electron transfer from excited TMPyP^{4+} to methyl viologen. This electron transfer event was supposedly mediated by the titanate sheets since TMPyP^{4+} and methyl viologen are spatially separated.
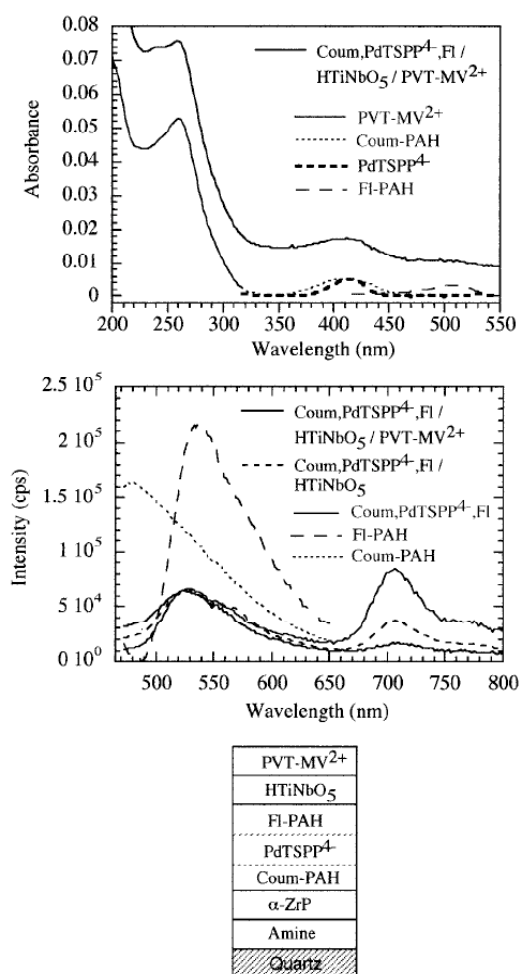
Figure 18. Absorption (top) and emission (middle, $I_{ex} = 450$ nm) spectra of an energy/electron transfer assembly and its schematic model structure (bottom).[67]

Other Electron Donors

Krishna et al. reported the photo-induced formation of very stable radical cations of N,N,N',N'-tetramethylbenzidine[204] and alkylphenothazines[205] adsorbed to the external surface of layered α-zirconium phosphate. The framework of zirconium phosphate was thought to be the electron acceptor. In the alkylphenothazine systems, the half-life of the generated charge separated states varied from a few days to several weeks at room temperature with increasing alkyl chain length of alkylphenothizines; the variation in half-life was ascribed to larger inductive effect for the longer alkyl chain.

1.5. Cyanine dyes

1.5.1. Structures and Properties

Cyanine dyes, which are family of polymethine dyes, are attracting wide range of interests due to its fascinating photochemical properties, distinctive aggregation behavior and important technological application as photosensitizers of silverhalide-based photographic systems.   As exemplified in Figure 19, cyanine dyes are made up of a polymethine resonant chain (Figure 19 upper left denoted as streptocyaine cation) whose ends are linked to heterocyclic groups.
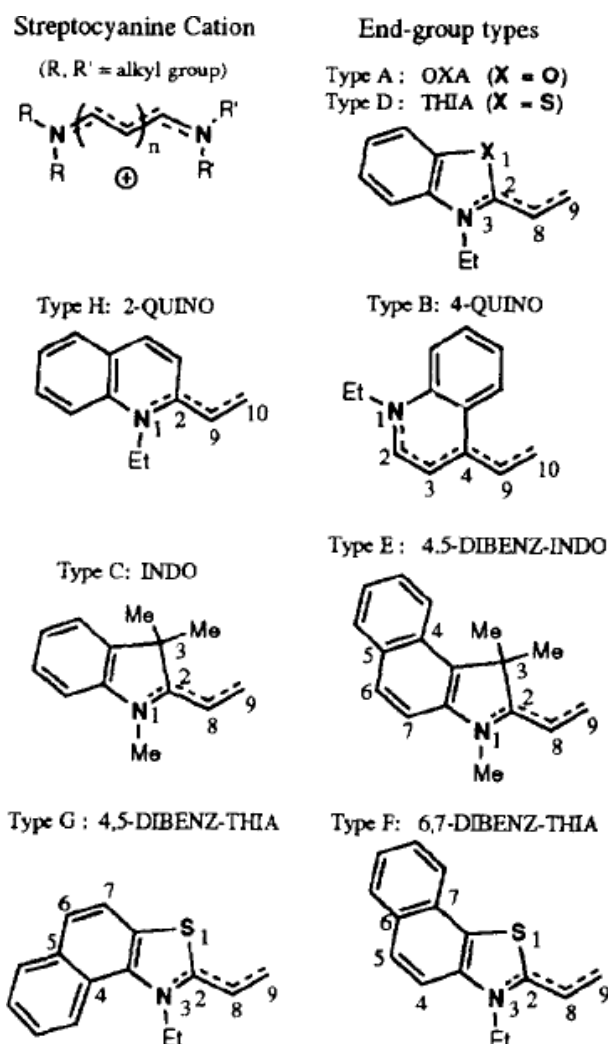
Figure 19.   The formula of the streptocyanines and of 8 end-group types in cyanine dyes.

The absorption maximum of the dye varies depending on the molecular structure. Figure 20 shows that the absorption maxima ($S_0 S_1$ transition) and other transitions of cyanine dyes are linearly dependent on the methine chain length and are also strongly dependent on the heterocyclic moieties. Furthermore, the properties of the dye (aggregation behavior, chemical stability, etc.) have also been tuned by introducing substituents onto the heterocycles or methine chain.
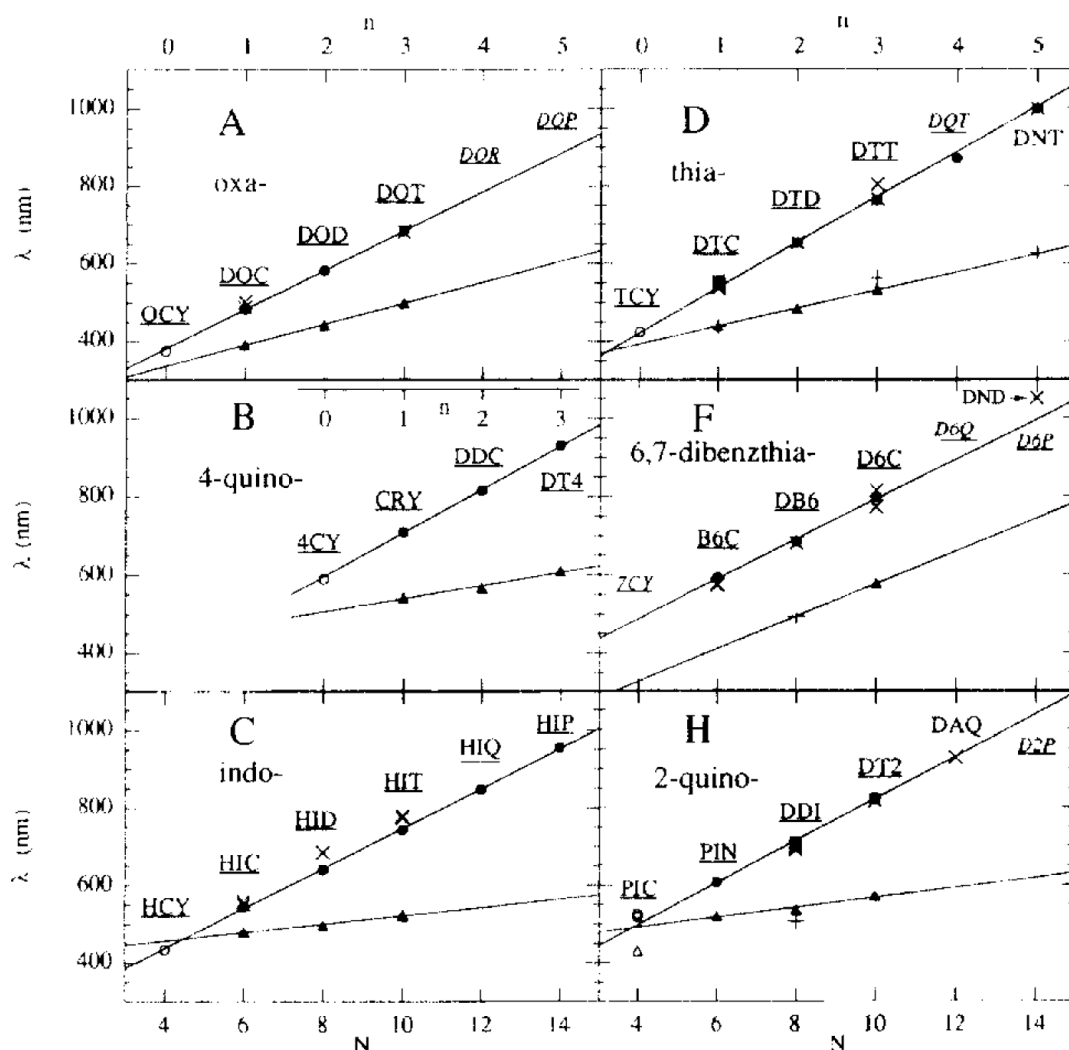
Figure 20. Plot of measured $S_1 S_n$ (triangles) and $S_0 S_1$ (circles) transition band maxima for cyanines (empty marks) and carbocyanine (filled marks) dyes showing the linear shift dependence in a wavelength scale within each endgroup types A to H, which corresponds to those in Figure 20. Unsubstituted chain dye codes are underlined. The substituted dyes are represented by (+) for $S_1 S_n$ and (x) for $S_0 S_1$ bands but are not labeled. Only filled triangles and circles (unsubstituted carbocyanines) are used for the fits.[206]

Estimation of LUMO level of the dyes is important to understand the photo processes in sensitized photographic and electron transfer systems. The energy level of LUMO, E_{LUMO}, was estimated according to the relationship[211]

$$E_{\text{LUMO}} \text{ (eV)} = -E_{\text{red}} \text{ (V vs SCE)} - 4.38.$$

where, E_R is electrochemically measured redox potentials of the dyes. Table 5 shows an example of published E_{red} values measured by phase-selective second-harmonic ac voltammetry[207].

Table 5. Comparison of formal potential $E^{o'}$ for cyanine dyes. [207]

No.	Dye Structure	$E^{o'}_{red}$ [a]	E_{lit} [b]	ΔE [c]	$E^{o'}_{ox}$	E_{lit}	ΔE
1		-1.506	-1.50	6	+0.662	+0.58	82
2		-1.445	-1.38	65	+1.370	>1.2	—
3		-1.310	-1.26	50	+1.020	+0.94	80
4		-1.295	-1.10	195	+0.994	+0.90	94
5		-1.280	-1.35	-70	+0.634	+0.54	94
6		-1.172	-1.13	38	+0.756	+0.76	4
7		-1.157	-1.04	117	+1.107	+1.06	27
8		-1.148	-1.09	58	+1.213	+1.00	213
9		-1.128	-1.03	98	+1.113	+0.99	123
10		-1.125	-1.10	25	+0.897	+0.76	137
11		-1.120	-1.20	-80	+0.902	+0.76	142
12		-1.118	-1.07	48	+1.222	+1.00	222
13		-1.117	-1.08	37	+1.314	+1.36	-46
14		-1.107	-1.15	-43	+0.901	+0.76	141
15		-1.090	-1.02	70	+0.743	+0.76	-17
16		-1.068	-1.12	-52	+0.77[d]	+0.62	150
17		-1.060	-1.00	60	+0.902	+0.78	152
18		-1.048	-1.05	-2	+0.902	+0.73	172
19		-1.045	-1.16	-115	+0.697	+0.49	207
20		-1.035	-1.11	-75	+0.757	+0.58	177
21		-1.014	-1.02	-6	+0.898	+0.62	278
22		-1.013	-1.06	-47	+0.976	+0.87	106
23		-1.000	-1.06	-60	+1.088	+0.88	208
24		-0.943	-0.86	83	+0.976	+0.85	126
25		-0.928	-0.86	68	+0.886	+0.77	116
26		-0.921	-0.89	31	+0.938	+0.82	118
27		-0.92[de]	-0.90	20	+1.015	+0.95	65
28		-0.885	-0.83	55	+0.630	+0.48	150
29		-0.884	-0.98	-96	+0.513	+0.28	283
30		-0.860	-0.99	-130	+0.55[d]	+0.19	360
31		-0.820	-0.87	-50	+0.775	+0.68	95
32		-0.808	-0.63	178	+1.145	—	—
33		-0.795	-0.55	245	+0.790	+0.72	70
34		-0.780	-0.79	-10	+1.096	+1.00	96
35		-0.725	-0.69	35	+1.441	+1.33	111
36		-0.689	-0.81	-121	+1.184	+0.95	234
37		-0.666	-0.64	26	+1.621	+1.54	81
38		-0.663	-0.41	253	+1.430	+1.61	-180
39		-0.661	-0.32	341	+1.49[d]	+1.77	-280
40		-0.650	-0.54	110	+1.515	+1.50	15
41		-0.646	-0.65	-4	+1.211	+0.77	441
42		-0.580	-0.45	130	+1.252	+1.09	162
43		-0.517	-0.25	267	+1.260	+1.34	-110
44		-0.490	-0.20	290	+1.305	+1.46	-155
45		-0.482	-1.08	-595	+1.294	+0.41	884
46		-1.000	—	—	+0.453	—	—

[a] $E^{o'}$ represents the "reversible" one-electron redox potential obtained by second-harmonic ac voltammetry. All potentials were measured in duplicate runs versus the NaCl saturated calomel electrode and converted to the Ag/AgCl reference electrode by adding 40 mV.
[b] E_{lit} values were obtained from the literlatures[208-210]
[c] $\Delta E = | E^{o'}| - | E_{lit} |$
[d] Owing to complicated follow-up chemistry, the second-harmonic ac response for this dye was poorly defined and limited accuracy to the nearest 0.01-0.02 V
[e] Dye insoluble in CH_3CH; potentials were measured in CH_2Cl_2/0.10M TBABF$_4$ and referred to the same reference redox system used in CH_3CN. Values listed for this dye may not be consistent with others in Table 5.

1.5.2. Aggregation

Cyanine dyes form large two-dimensional supramolecular aggregates under certain conditions such as in concentrated solutions. The structures of the aggregates are known as two-dimensional ones: the ideal models of J-, H- and herringbone-type aggregates are shown in Figure 21. These models have been verified by X-ray[212-214] diffraction of dye crystals, electron diffraction of LB-films[215-221] and observation of the dye aggregate by scanning tunneling microscopy[222,223] and scanning force microscopy.[224]

J-aggregate   H-aggregate   herringbone-aggregate
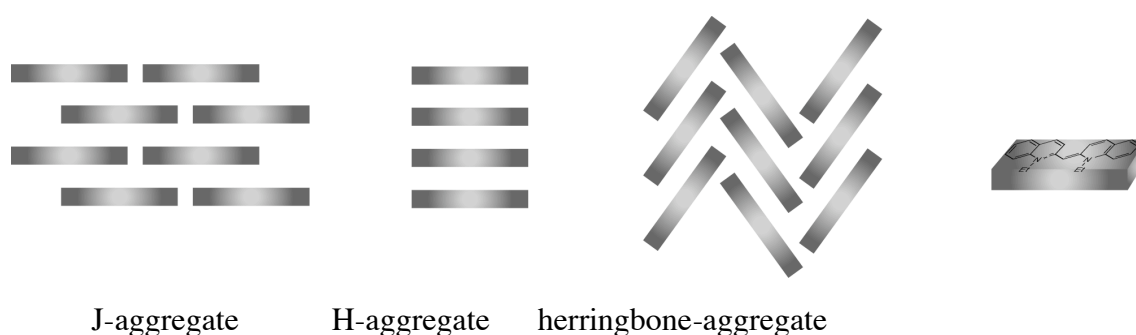
Figure 21.   Ideal model of cyanine dye aggregates

The aggregation behavior of the dye depends on various factors. Basically, the type of the aggregates depends on the molecular structure; interaction between adjacent heterocyclic rings drives the aggregation behavior. The effects of added salt, pH, pressure, temperature and absorption on formation of aggregates have also been investigated. However, there remains difficulty and lack of knowledge to control the number of the dye molecules in the aggregates, nanostructure (e.g. slip angle) of the aggregates, and aggregate formation in or on matrixes.

Upon aggregation, photochemical properties of cyanine dyes are largely modified. It is known that J-aggregates shows characteristic sharp absorption band relative to a monomer band, whereas H-aggregates show a broad band at shorter wavelength region relative to monomer band. Molecular exciton theory[225, 226] accounts for the variation of the absorption spectrum of the dye upon formation of H- and J-

aggregates. According to the theory, the energy difference between the aggregate transition and the monomer one, ΔV, is expressed by

$$\Delta V = 2h^{-1}(n\text{-}1)/n <M^2>/r^3 \ (1\text{-}3\cos^2\alpha)$$

where h is the Plank's constant, n the number of dye molecules in the aggregate, r the distance between the molecules, α the angle between the long axes of the molecules and the aggregate axis, and $<M^2>$ the transition dipole moment which is proportional to the molar extinction coefficient of the monomer. Figure 22 schematically shows the variation in transition energy upon aggregation based on the theory, or the equation. Thus the energy of the allowed transition is larger than $E_{TR}(M)$ for H-aggregate and is smaller for J-aggregate.
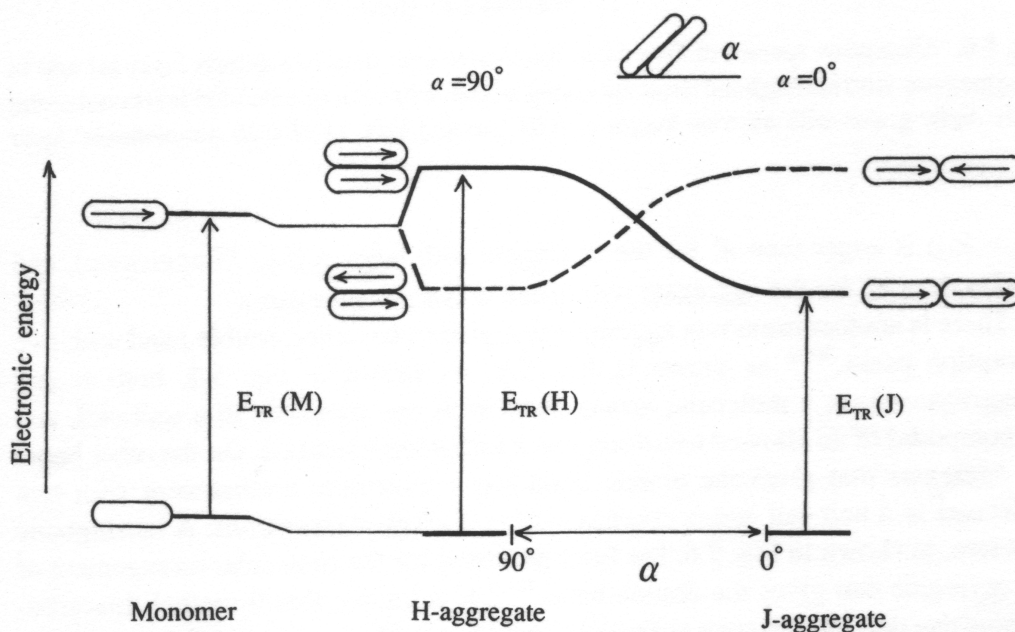
Figure 22. Schematic representation of the electronic transitions in a monomer, H-aggregate, and J-aggregate on the basis of the interaction between molecular excitons in aggregates, where α is the slip angle between molecules in an aggregate, and $E_{TR}(M)$, $E_{TR}(H)$, and $E_{TR}(J)$ are the transition energies of a monomer, H-aggregate, and J-aggregate, respectively.

Herringbone-type aggregates show so-called Davydov splitting characterized by the appearance of double bands that are red- and blue-shifted relative to a monomer band and are polarized perpendicularly to each other. The double band in herringbone-type aggregate is also accounted for by molecular exciton theory.

Other than the variation in absorption spectra, the dye aggregates, especially J-aggregates, show distinctive photochemical properties due to delocalization of excitons over the aggregates. Resonance fluorescence is characteristic of J-aggregates: due to delocalization of excitons, fluorescence with very small stokes shift (several nm) and very short life time (order of ps) is observed. Efficient third order optical non-linearity was observed in J-aggregate of pseudoisocyanine; the low-dimensional excitons in the J-aggregates were thought to be responsible to the property.[227] The application of J-aggregates of cyanine dyes for photochemical hole burning materials was also investigated.[228-230] Further, excellent photosensitizing properties of cyanine dyes are only observed in J-aggregated states; the delocalization of excitons over the aggregate should be responsible to the property, although detailed mechanism is not known.

1.6. References

(1) H. Annehed, L. Fälth, F. J. Lincoln, *Z. Kristallogr.,* **159**, 203 (1982).

(2) H. Gies, B. Marler, S. Vortmann, U. Oberhagemann, P. Bayat, K. Krink, J. Rius, I. Wolf, C. Fyfe, *Micropor. Mesopor. Mater.,* **21**, 183 (1998).

(3) S. Vortmann, J. Rius, S. Siegmann, H. Gies, *J. Phys. Chem. B,* **101**, 1292 (1997).

(4) A. Brandt, W. Schwieger, K.-H. Bergk, *Cryst. Res. Tecnol,* **23**, 1201 (1988).

(5) G. G. Almond, R. K. Harris, K. R. Franklin, *J. Mater. Chem.,* **7**, 681 (1997).

(6) G. Lagaly, K. Beneke, A. Weiss, *Am. Miner.,* **60**, 650 (1975).

(7) E. Ruiz-Hitzky, J. M. Rojo, *Nature,* **287**, 28 (1980).

(8) K. Isoda, K. Kuroda, M. Ogawa, *Chem. Mater.,* **12**, 1702 (2000).

(9) A. Shimojima, D. Mochizuki, K. Kuroda, *Chem. Mater.,* **13**, 3603 (2001).

(10) D. Mochizuki, A. Shimojima, K. Kuroda, *J. Am. Chem. Soc.,* **124**, 12082 (2002).

(11) Y. Mitamura, Y. Komori, S. Hayashi, Y. Sugahara, K. Kuroda, *Chem. Mater.,* **13**, 3747 (2001).

(12) M. Ogawa, S. Okutomo, K.Kuroda, *J. Am. Chem. Soc.,* **120**, 7361 (1998).

(13) I. Fujita, K. Kuroda, M. Ogawa, *Chem. Mater.,* **15**, 3134 (2003).

(14) T. Yanagisawa, T. Shimizu, K. Kuroda, C. Kato, *Bull. Chem. Soc. Jpn.,* **63**, 988 (1990).

(15) T. Kimura, T. Kamata, M. Fujiwara, Y. Takano, M. Kaneda, Y. Sakamoto, O. Terasaki, Y. Sugahara, K. Kuroda, *Angew. Chem. Int. Ed.,* **39**, 3855 (2000).

(16) S. Andersson, A. D. Wadsley, *Acta. Crystallogr.,* **14**, 1245 (1961).

(17) H. Izawa, S. Kikkawa, M. Koizumi, *J. Phys. Chem.,* **86**, 5023 (1982).

(18) I. E. Grey, I. C. Madsen, J. A. Watts, L. A. Bursil, J. Kwiatkowska, *J. Solid State Chem.,* **58**, 350 (1985).

(19) S. Uchida, Y. Inoue, Y. Fujishiro, T. Sato, *J. Mater. Sci.,* **33**, 5125 (1998).

(20) D. Li, J. Yang, L. Zhang, X. Wang, L. Lu, X. Yang, *J. Mater. Chem.,* **12**, 1796 (2002).

(21) N. Masaki, S. Uchida, T. Sato, *J. Mater. Chem.,* **12**, 305 (2002).

(22) M. Kestigian, F. D. Leipziger, J. R. Carter, F. G. Garabedian, *J. Am. Ceram. Soc.,*

49, 517 (1966).

(23) H. Hirano, T. Fukuda, *Jpn. J. Appl. Phys.,* **7**, 1413 (1968).

(24) K. Nassau, J. W. Shiever, J. L. Bernstein, *J. Electrochem. Soc.,* **116**, 348 (1969).

(25) T. Tanaka, Y. Ebina, K. Takada, K. Kurashima, T. Sasaki, *Chem. Mater.,* **15**, 3564 (2003).

(26) Y. I. Kim, S. Salim, M. J. Huq, T. E. Mallouk, *J. Am. Chem. Soc.,* **113**, 9561 (1991).

(27) A. Kudo, T. Kondo, *J. Mater. Chem.,* **7**, 777 (1997).

(28) A. Kudo, T. Sakata, *J. Mater. Chem.,* **3**, 1081 (1993).

(29) A. Kudo, T. Sakata, *Chem. Lett.,* 2179 (1994).

(30) A. Kudo, T. Sakata, *J. Phys. Chem.,* **99**, 15963 (1995).

(31) A. Kudo, *Chem. Mater.,* **9**, 664 (1997).

(32) A. Kudo, E. Kaneko, *J. Mater. Sci. Lett.,* **16**, 224 (1997).

(33) A. Kudo, E. Kaneko, *Micropor. Mesopor. Mater.,* **21**, 615 (1998).

(34) A. Kudo, T. Shibata, H. Kato, *Chem. Lett.,* 959 (1999).

(35) Y. I. Kim, S. J. Atherton, E. S. Brigham, T. E. Mallouk, *J. Phys. Chem.,* **97**, 11802 (1993).

(36) K. Domen, A. Kudo, M. Shibata, A. Tanaka, K. Maruya, T. Onishi, *J. Chem. Soc., Chem. Commun.,* 1706 (1986).

(37) K. Domen, A. Kudo, A. Shiozaki, A. Tanaka, K. Maruya, T. Onishi, *J. Chem. Soc., Chem. Commun.,* 356 (1986).

(38) M. Shibata, A. Kudo, A. Tanaka, K. Domen, K. Maruya, T. Onishi, *Chem. Lett.,* **80**, 4403 (1987).

(39) A. Kudo, A. Tanaka, K. Domen, K. Maruya, T. Onishi, *J. Catal.,* **111**, 67 (1988).

(40) A. Kudo, K. Sayama, A. Tanaka, K. Domen, K. Maruya, T. Onishi, *J. Catal,* **120**, 337 (1989).

(41) K. Sayama, A. Tanaka, K. Domen, K. Maruya, T. Onishi, *Catal. Lett,* **4**, 217 (1990).

(42) J. Yoshimura, A. Tanaka, J. N. Kondo, K. Domen, *Bull. Chem. Soc. Jpn.,* **68**, 2439 (1995).

(43) T. Sato, Y. Yamamoto, Y. Fujishiro, S. Uchida, *J. Chem. Soc., Faraday Trans.,* **92**,

5089 (1996).

(44) S. Uchida, Y. Yamamoto, Y. Fujishiro, A. Watanabe, O. Ito, T. Sato, *J. Chem. Soc., Faraday Trans*, **93**, 3229 (1997).

(45) J. Alarcon, G. Blasse, *Phys. Status Solidi A,* **135**, 627 (1993).

(46) A. Kudo, T. Sakata, *J. Phys. Chem.,* **100**, 17323 (1996).

(47) T. Sasaki, Y. Komatsu, Y. Fujiki, *Chem. Mater.,* **4**, 894 (1992).

(48) N. Kinomura, N. Kumada, F. Muto, *J. Chem. Soc., Dalton Trans*., 2349 (1985).

(49) G. Lagaly, K. Beneke, *J. Inorg. Nucl. Chem.,* **38**, 1513 (1976).

(50) S. Kikkawa, M. Koizumi, *Mater. Res. Bull.,* **15**, 533 (1980).

(51) H. Rebbah, M. M. Borel, B. Raveau, *Mater. Res. Bull.,* **15**, 317 (1980).

(52) H. Izawa, S. Kikkawa, M. Koizumi, *Polyhedron,* **2**, 741 (1983).

(53) A. Grandin, M. M. Borel, B. Raveau, *Mater. Res. Bull.*, **20**, 1279 (1985).

(54) J.-F. Lambert, Z. Deng, J.-B. d'Espinose, J. J. Fripiat, *J. Colloid Interface Sci.,* **132**, 337 (1989).

(55) C. Airoldi, L. M. Nunes, R. F. d. Farias, *Mater. Res. Bull.,* **35**, 2081 (2000).

(56) T. Sasaki, F. Izumi, M. Watanabe, *Chem. Mater.,* **8**, 777 (1996).

(57) T. Nakato, K. Kuroda, *Eur. J. Solid State Inorg. Chem.,* **32**, 809 (1995).

(58) H. Miyata, Y. Sugahara, K. Kuroda, C. Kato, *J. Chem. Soc., Faraday Trans. 1,* **84**, 2677 (1988).

(59) T. Nakato, H. Miyata, K. Kuroda, C. Kato, *React. Solids,* **6**, 231 (1988).

(60) T. Nakato, K. Kuroda, C. Kato, *J. Chem. Soc., Chem. Comm*., 1144 (1989).

(61) T. Nakato, K. Kuroda, C. Kato, *Chem. Mater.,* **4**, 128 (1992).

(62) T. Nakato, K. Ito, K. Kuroda, C. Kato, *Micropor. Mater.,* **1**, 283 (1993).

(63) T. Nakato, K. Kuroda, C. Kato, *Catal. Today,* **16**, 471 (1993).

(64) T. Nakato, K. Kusunoki, K. Yoshizawa, K. Kuroda, M. Kaneko, *J. Phys. Chem.,* **99**, 17896 (1995).

(65) G. B. Saupe, T. E. Mallouk, W. Kim, R. H. Schmehl, *J. Phys. Chem. B,* **101**, 2508 (1997).

(66) A. Furube, T. Shiozawa, A. Ishikawa, A. Wada, K. Domen, C. Hirose, *J. Phys. Chem. B,* **106**, 3065 (2002).

(67) D. M. Kaschak, J. T. Lean, C. C. Waraksa, G. B. Saupe, H. Usami, T. E. Mallouk, *J. Am. Chem. Soc.,* **121**, 3435 (1999).

(68) Y. Yamaguchi, T. Yui, S. Takagi, T. Shimada, H. Inoue, *Chem. Lett*., 644 (2001).

(69) Z. Tong, T. Shichi, K. Oshika, K. Takagi, *Chem. Lett*., **9**, 876 (2002).

(70) T. Nakato, *J. Incl. Phenom. Mol. Recog. Chem.,* **13**, 249 (1992).

(71) A. Kudo, E. Kaneko, *Chem. Commun*., 349 (1997).

(72) Y. Ide, M. Ogawa, *Chem. Commun*., 1262 (2003).

(73) S. Bruzaud, G. Levesque, *Chem. Mater.,* **14**, 2421 (2002).

(74) F. E. Osterloh, *J. Am. Chem. Soc.,* **124**, 6248 (2002).

(75) A. Lerf, R. Schöllhorn, *Inorg. Chem.,* **16**, 2950 (1977).

(76) D. W. Murphy, G. W. Hull, *J. Chem. Phys.,* **62**, 973 (1975).

(77) C. Liu, O. Singh, P. Joensen, A. E. Curzon, R. F. Frindt, *Thin Solid Films,* **113**, 165 (1984).

(78) P. Joensen, R. G. Frindt, S. R. Morrison, *Mater. Res. Bull.,* **21**, 457 (1986).

(79) D. Yang, S. J. Sandoval, W. M. R. Divigalpitiya, J. C. Irwin, R. F. Frindt, *Phys. Rev. B,* **43**, 12053 (1991).

(80) D. Yang, R. F. Frindt, *J. Phys. Chem. Solids,* **57**, 1113 (1996).

(81) V. Petkov, S. J. L. Billinge, J. Heising, M. G. Kanatzidis, *J. Am. Chem. Soc.,* **122**, 11571 (2000).

(82) M. M. J. Treacy, S. B. Rice, A. J. Jacobson, J. T. Lewandowski, *Chem. Mater,* **2**, 279 (1990).

(83) S. W. Keller, H.-N. Kim, T. E. Mallouk, *J. Am. Chem. Soc.,* **116**, 8817 (1994).

(84) K. Domen, Y. Ebina, S. Ikeda, A. Tanaka, J. N. Kondo, K. Maruya, *Catal. Today,* **28**, 167 (1996).

(85) R. Abe, K. Shinohara, A. Tanaka, M. Hara, J. N. Kondo, K. Domen, *Chem. Mater.,* **9**, 2179 (1997).

(86) R. Abe, K. Shinohara, A. Tanaka, M. Hara, J. N. Kondo, K. Domen, *J. Mater. Res.,* **13**, 861 (1998).

(87) M. Fang, C. H. Kim, G. B. Saupe, H.-N. Kim, C. C. Waraksa, T. Miwa, A. Fujishima, T. E. Mallouk, *Chem. Mater.,* **11**, 1526 (1999).

(88) G. B. Saupe, C. C. Waraksa, H.-N. Kim, Y. J. Han, D. M. Kaschak, D. M. Skinner, T. E. Mallouk, *Chem. Mater.,* **12**, 1556 (2000).

(89) R. E. Schaak, T. E. Mallouk, *Chem. Mater.,* **12**, 3427 (2000).

(90) R. E. Schaak, T. E. Mallouk, *Chem. Mater.,* **12**, 2513 (2000).

(91) Y.-S. Han, I. Park, J.-H. Choy, *J. Mater. Chem.,* **11**, 1277 (2001).

(92) N. Miyamoto, H. Yamamoto, R. Kaito, K. Kuroda, *Chem. Commun.*, 2378 (2002).

(93) T. Sasaki, M. Watanabe, H. Hashizume, H. Yamada, H. Nakazawa, *J. Am. Chem. Soc.*, **118**, 8329 (1996).

(94) T. Sasaki, M. Watanabe, H. Hashizume, H. Yamada, H. Nakazawa, *J. Chem. Soc., Chem. Commun.*, 229 (1996).

(95) T. Sasaki, S. Nakano, S. Yamauchi, M. Watanabe, *Chem. Mater.,* **9**, 602 (1997).

(96) R. Abe, K. Shinohara, A. Tanaka, M. Hara, J. N. Kondo, K. Domen, *Chem. Mater.,* **10**, 329 (1998).

(97) T. Sasaki, M. Watanabe, *J. Am. Chem. Soc.*, **120**, 4682 (1998).

(98) R. Abe, S. Ikeda, J. N. Kondo, M. Hara, K. Domen, *Thin Solid Films*, **343-344**, 156 (1999).

(99) T. Sumida, R. Abe, M. Hara, J. N. Kondo, K. Domen, *Electrochem.,* **67**, 1224 (1999).

(100) M. Koinuma, Y. Matsumoto, T. Sumida, K. Domen, *Electrochem. Solid-State Lett.*, **3**, 481 (2000).

(101) T. Sumida, R. Abe, M. Hara, J. N. Kondo, K. Domen, *J. Mater. Res.,* **15**, 2587 (2000).

(102) J.-Y. Kim, I. Chung, J.-H. Choy, *Chem. Mater.,* **13**, 2759 (2001).

(103) T. Sumida, Y. Takahara, R. Abe, M. Hara, J. N. Kondo, K. Domen, M. Kakihana, M. Yoshimura, *Phys. Chem. Chem. Phys.,* **3**, 640 (2001).

(104) W. Sugimoto, O. Terabayashi, Y. Murakami, Y. Takatsu, *J. Mater. Chem.*, **12**, 3814 (2002).

(105) G. Alberti, M. Casciola, U. Costantino, *J. Colloid Interface Sci.,* **107**, 256 (1985).

(106) G. Alberti, C. Dionigi, E. Giontella, S. Murcia-Mascarós, R. Vavani, *J. Colloid Interface Sci.,* **188**, 27 (1997).

(107) G. Alberti, E. Giontella, S. Murcia-Mascarós, *Inorg. Chem.*, **36**, 2844 (1997).

(108) H.-N. Kim, S. W. Keller, T. E. Mallouk, *Chem. Mater.*, **9**, 1414 (1997).

(109) D. M. Kaschak, S. A. Johnson, D. E. Hooks, H.-N. Kim, M. D. Ward, T. E. Mallouk, *J. Am. Chem. Soc.*, **120**, 10887 (1998).

(110) Z. Liu, K. Ooi, H. Kanoh, W. Tang, T. Tomida, *Langmuir*, **16**, 4154 (2000).

(111) Y. Omomo, T. Sasaki, L. Wang, M. Watanabe, *J. Am. Chem. Soc.*, **125**, 3568 (2003).

(112) R. E. Schaak, T. E. Mallouk, *Chem. Commun.*, **2002**, 706 (2002).

(113) I. Lagadic, P. G. Lacroix, R. Clément, *Chem. Mater.*, **9**, 2004 (1999).

(114) W. Sugimoto, H. Iwata, Y. Yasunaga, Y. Murakami, Y. Takasu, *Angew. Chem., Int. Ed.*, **42**, 4092 (2003).

(115) M. Adachi-Pagano, C. Forano, J.-P. Besse, *Chem. Commun.*, 91 (2000).

(116) F. Leroux, M. Adachi-Pagano, M. Intissar, S. Chauvére, C. Forano, J.-P. Besse, *J. Mater. Chem.*, **11**, 105 (2001).

(117) T. Hibino, W. J. Jones, *J. Mater. Chem.*, **11**, 1321 (2001).

(118) E. Gardner, K. M. Huntoon, T. J. Pinnavaia, *Adv. Mater.*, **13**, 1263 (2002).

(119) B. C. Brodie, *Liebigs Ann. Chem.*, **114**, 6 (1860).

(120) N. A. Kotov, I. Dékány, J. H. Fendler, *Adv. Mater.*, **8**, 637 (1996).

(121) T. Cassagneau, J. H. Fendler, *Adv. Mater.*, **10**, 877 (1998).

(122) N. I. Kovtyukhova, P. J. Ollivier, B. R. Martin, T. E. Mallouk, S. A. Chizhik, E. V. Buzaneva, A. D. Gorchinskiy, *Chem. Mater.*, **11**, 771 (1999).

(123) Z. Liu, Z. S. Wang, X. Yang, K. Ooi, *Langmuir*, **18**, 4926 (2002).

(124) R. Abe, M. Hara, J. N. Kondo, K. Domen, *Chem. Mater.*, **10**, 1647 (1998).

(125) M. Ogawa, T. Handa, K. Kuroda, C. Kato, T. Tani, *J. Phys. Chem.*, **96**, 8116 (1992).

(126) M. Isayama, K. Sakata, T. Kunitake, *Chem. Lett.*, 1283 (1993).

(127) M. Ogawa, M. Takahashi, K. Kuroda, *Chem. Mater.*, **6**, 715 (1994).

(128) M. Isayama, K. Nomiyama, T. Kunitake, *Adv. Mater.*, **8**, 641 (1996).

(129) M. Ogawa, N. Kanaoka, K. Kuroda, *Langmuir*, **14**, 6969 (1998).

(130) K. Sonobe, K. Kikuta, K. Takagi, *Chem. Mater*, **11**, 1089 (1999).

(131) K. Suga, J. F. Rusling, *Langmuir,* **9**, 3649 (1993).

(132) E. R. Kleinfeld, G. S. Ferguson, *Science,* **265**, 370 (1994).

(133) G. S. Ferguson, E. R. Kleinfeld, *Adv. Mater.,* **7**, 414 (1995).

(134) E. R. Kleinfeld, G. S. Ferguson, *Chem. Mater.,* **7**, 2327 (1995).

(135) E. R. Kleinfeld, G. S. Ferguson, *Chem. Mater.,* **8**, 1575 (1996).

(136) D. M. Kaschak, T. E. Mallouk, *J. Am. Chem. Soc.,* **118**, 4222 (1996).

(137) T. Sasaki, Y. Ebina, T. Tanaka, M. Harada, M. Watanabe, G. Decher, *Chem. Mater.,* **13**, 4661 (2001).

(138) T. Sasaki, Y. Ebina, K. Fukuda, T. Tanaka, M. Harada, M. Watanabe, *Chem. Mater.,* **14**, 3524 (2002).

(139) Z. S. Wang, T. Sasaki, M. Muramatsu, Y. Ebina, T. Tanaka, L. Z. Wang, M. Watanabe, *Chem. Mater.,* **15**, 807 (2003).

(140) Y. Lvov, K. Ariga, I. Ichinose, T. Kunitake, *J. Am. Chem. Soc.,* **117**, 6117 (1995).

(141) Y. Lvov, K. Ariga, I. Ichinose, T. Kunitake, *Langmuir,* **12**, 3038 (1996).

(142) N. A. Kotov, T. Haraszti, L. Turi, G. Zavala, R. E. Geer, I. Dékány, J. H. Fendler, *J. Am. Chem. Soc.,* **119**, 6821 (1997).

(143) N. A. Kotov, S. Magonov, E. Tropsha, *Chem. Mater.,* **10**, 886 (1998).

(144) B. van Duffel, R. A. Schoonheydt, *Langmuir,* **15**, 7520 (1999).

(145) D. W. Kim, A. Blumstein, J. Kumar, S. K. Tripathy, *Chem. Mater.,* **13**, 243 (2001).

(146) D. W. Kim, A. Blumstein, S. K. Tripathy, *Chem. Mater.,* **13**, 1916 (2001).

(147) Y. Matsumoto, A. Funatsu, D. Matsuo, U. Unal, *J. Phys. Chem. B,* **105**, 10893 (2001).

(148) M. Koinuma, H. Seki, Y. Matsumoto, *J. Electroanal. Chem.,* **531**, 81 (2002).

(149) J.-H. Choy, H.-C. Lee, H. Jung, H. Kim, H. Boo, *Chem. Mater.,* **14**, 2468 (2002).

(150) A. Takagaki, M. Sugisawa, D. Lu, J. N. Kondo, M. Hara, K. Domen, S. Hayashi, *J. Am. Chem. Soc.,* **125**, 5479 (2003).

(151) F. Camerel, J.-C. P. Gabriel, P. Btail, *Adv. Funct. Mater.,* **13**, 377 (2003).

(152) A. S. Sonin, *J. Mater. Chem.,* **8**, 2557 (1998).

(153) J.-C. P. Gabriel, P. Davidson, *Adv. Mater.,* **12**, 9 (2000).

(154) J.-C. P. Gabriel, F. Camerel, B. J. Lemaire, H. Desvaux, P. Davidson, P. Batail,

Nature, **413**, 504 (2001).

(155) L. Li, J. Walda, L. Manna, A. P. Alivisatos, *Nano Lett.*, **2**, 557 (2002).

(156) F. Camerel, J.-C. P. Gabriel, P. Batail, *Chem. Commun.*, 1926 (2002).

(157) N. Miyamoto, T. Nakato, *Adv. Mater.,* **14**, 1267 (2002).

(158) L. Onsager, *Ann. NY Acad. Sci.,* **51**, 627 (1949).

(159) P. A. Forsyth, S. Marcelja, D. J. Mitchell, B. W. Ninham, *J. Chem. Soc., Faraday Trans 2,* **73**, 84 (1977).

(160) P. A. Forsyth, S. Marcelja, D. J. Mitchell, B. W. Ninham, *Adv. Colloid Interface Sci.,* **9**, 37 (1978).

(161) G. J. Vroege, H. N. W. Lekkerkerker, *Rep. Prog. Phys.,* **55**, 1241 (1992).

(162) T. Sato, A. Teramoto, *Adv. Polymer Sci.,* **126**, 85 (1996).

(163) D. Frenkel, R. Eppenga, *Phys. Rev. Lett.,* **52**, 1089 (1982).

(164) D. Frenkel, B. M. Mulder, *Mol. Phys.,* **55**, 1171 (1985).

(165) J. A. C. Veerman, D. Frenkel, *Phys. Rev. A,* **45**, 5632 (1992).

(166) M. Bates, D. Frenkel, *J. Chem. Phys.,* **110**, 6553 (1999).

(167) F. C. Bawden, N. W. Pirie, J. D. Bernal, I. Fankuchen, *Nature,* **138**, 1051 (1936).

(168) A. Ciferri, Ed., *Liquid Crystallinity in Polymers* (VCH publishers, Inc., New York, 1991).

(169) T. E. Strzelecka, M. W. Davidson, R. L. Rill, *Nature,* **331**, 457 (1988).

(170) F. Livolant, A. M. Levelut, J. Doucet, J. P. Benoit, *Nature,* **339**, 724 (1989).

(171) A. B. D. Brown, S. M. Clarke, A. R. Rennie, *Langmuir,* **14**, 3192 (1998).

(172) F. M. van der Kooij, H. N. W. Lekkerkerker, *J. Phys. Chem. B,* **102**, 7829 (1998).

(173) A. B. D. Brown, C. Ferrero, T. Narayanan, A. R. Rennie, *Eur. Phys. J. B,* **11**, 481 (1999).

(174) F. M. van der Kooij, K. Kassapidou, H. N. W. Lekkerkerker, *Nature,* **406**, 868 (2000).

(175) V. H. Zocher, *Anorg. Allg. Chem.,* **147**, 91 (1925).

(176) P. Davidson, A. Garreau, J. Livage, *Liquid Crystals,* **16**, 905 (1994).

(177) P. Davidson, C. Bourgaux, L. Schoutteten, P. Sergot, C. Williams, J. Livage, *J. Phys. II France,* **5**, 1577 (1995).

(178) O. Pelletier, C. Bourgaux, O. Diat, P. Davidson, J. Livage, *Eur. Phys. J. B,* **12**, 541 (1999).

(179) S. Lamarque-Forget, O. Pelletier, I. Dozov, P. Davidson, P. Martinot-Lagarde, J. Livage, *Adv. Mater.,* **12**, 1267 (2000).

(180) H. Desvaux, J.-C. P. Gabriel, P. Berthault, F. Camerel, *Angew. Chem. Int. Ed.,* **40**, 373 (2001).

(181) X. Commeinhes, P. Davidson, C. Bourgaux, J. Livage, *Adv. Mater.,* **9**, 900 (1997).

(182) I. Langmuir, *J. Chem. Phys.,* **6**, 873 (1938).

(183) J.-C. P. Gabriel, C. Sanchez, P. Davidson, *J. Phys. Chem.,* **100**, 11139 (1996).

(184) A. Mourchid, E. Lécolier, H. van Damme, P. Levitz, *Langmuir,* **14**, 4718 (1998).

(185) B. J. Lemaire, P. Panine, J. C. P. Gabriel, P. Davidson, *Europhys. Lett.,* **69**, 55 (2002).

(186) S. Liu, J. Zhang, N. Wang, W. Liu, C. Zhang, D. Sun, *Chem. Mater.,* **15**, 3240 (2003).

(187) J. K. Thomas, *Chem. Rev.,* **93**, 301 (1993).

(188) M. Ogawa, K. Kuroda, *Chem. Rev.,* **95**, 399 (1995).

(189) C. Detellier, G. Villemure, *Inor. Chim. Acta.,* **86**, 19 (1984).

(190) G. Villemure, C. Detellier, A. G. Szabo, *J. Am. Chem. Soc.,* **108**, 4658 (1986).

(191) H. Miyata, Y. Sugahara, K. Kuroda, C. Kato, *J. Chem. Soc., Faraday Trans. 1.,* **83**, 1851 (1987).

(192) G. Villemure, G. Bazan, H. Kodama, A. G. Szabo, C. Detellier, *Appl. Clay Sci.,* **2**, 241 (1987).

(193) G. Villemure, C. Detellier, A. G. Szabo, *Langmuir,* **7**, 1215 (1991).

(194) N. Kakegawa, T. Kondo, M. Ogawa, *Langmuir,* **19**, 3578 (2003).

(195) L. A. Vermeulen, M. E. Thompson, *Nature,* **358**, 656 (1992).

(196) L. A. Vermeulen, J. L. Snover, L. S. Sapochak, M. E. Thompson, *J. Am. Chem. Soc.,* **115**, 11767 (1993).

(197) L. A. Vermeulen, M. E. Thompson, *Chem. Mater.,* **6**, 77 (1994).

(198) A. Bose, P. He, C. Liu, B. D. Ellman, R. J. Twieg, S. D. Huang, *J. Am. Chem. Soc.,* **124**, 4 (2002).

(199) K. Yao, S. Nishimura, Y. Imai, H. Wang, T. Ma, E. Abe, H. Tateyama, A. Yamagishi, *Langmuir,* **19**, 321 (2003).

(200) T. Nakato, Y. Iwata, K. Kuroda, M. Kaneko, C. Kato, *J. Chem. Soc., Dalton Trans.,* 1405 (1993).

(201) M. A. Bizeto, D. L. A. De Faria, V. R. L. Constantino, *J. Mater. Sci. Lett.,* **18**, 643 (1999).

(202) M. A. Bizeto, D. L. A. De Faria, V. R. L. Constantino, *J. Mater. Sci.,* **37**, 265 (2002).

(203) Z. Tong, T. Shichi, K. Takagi, *J. Phys. Chem. B,* **106**, 13306 (2002).

(204) R. M. Krishna, L. Kevan, *Micropor. Mesopor. Mater.,* **32**, 169 (1999).

(205) R. M. Krishna, V. Kurshev, L. Kevan, *Phys. Chem. Chem. Phys.,* **1**, 2833 (1999).

(206) Y. H. Meyer, M. Pittman, P. Plaza, *J. Photochem. Photobiol. A,* **114**, 1 (1998).

(207) J. R. Lenhard, *J. Imaging Sci.,* **30**, 27 (1986).

(208) T. Penner, P. B. Gilman, Jr., *Photogr. Sci. Eng.,* **19**, 102 (1975).

(209) P. B. Gilman, Jr., *Pure Appl. Chem.,* **49**, 357 (1977).

(210) P. B. Gilman, Jr., *Photogr. Sci. Eng.,* **23**, 71 (1983).

(211) T. Tani, *Photogr. Sci. Eng.,* **14**, 72 (1970).

(212) J. Wheatley, *J. Chem. Soc.,* **1959**, 3245 (1959).

(213) H. Yoshioka, K. Nakatsu, *Chem. Phys. Lett.,* **11**, 255 (1971).

(214) K. Nakatsu, H. Yoshida, T. Aoki, *Chem. Lett.,* **1972**, 339 (1972).

(215) C. Duschl, W. Frey, W. Knoll, *Thin Solid Films,* **160**, 251 (1988).

(216) S. Kirstein, H. Möhwald, *Chem. Phys. Lett.,* **154**, 303 (1989).

(217) S. Kirstein, H. Möhwald, *Chem. Phys. Lett.,* **189**, 408 (1992).

(218) V. N. Bliznyuk, S. Kirstein, H. Möhwald, *J. Phys. Chem.,* **97**, 569 (1993).

(219) V. N. Bliznyuk, H. Möhwald, *Thin Solid Films,* **261**, 275 (1995).

(220) S. Kirstein, H. Möhwald, *J. Chem. Phys.,* **103**, 826 (1995).

(221) S. Kirstein, R. Steitz, R. Garbella, H. Möhwald, *J. Chem. Phys.,* **103**, 818 (1995).

(222) M. Kawasaki, H. Ishii, *Chem. Lett.,* **1994**, 1079 (1994).

(223) M. Kawasaki, H. Ishii, *J. Imaging Sci. Technol.,* **39**, 210 (1995).

(224) L. Wolthaus, A. Schaper, D. Möbius, *Chem. Phys. Lett.,* **225**, 322 (1994).

(225) E. D. McRae, M. Kasha, *J. Chem. Phys.,* **28**, 721 (1958).

(226) A. S. Davydov, *Theory of Molecular Excitons* (Pleum, New York, 1971).

(227) Y. Wang, *J. Opt. Soc. Am. B,* **8**, 981 (1991).

(228) R. Hirschmann, W. Kohler, J. Friedrich, E. Daltrozzo, *Chem. Phys. Lett.,* **151**, 60 (1988).

(229) K. Misawa, S. Machiba, K. Horie, T. Kobayashi, *Chem. Phys. Lett.,* **240**, 210 (1995).

(230) M. Lindrum, I. Y. Chan, *J. Chem. Phys.,* **104**, 5359 (1996).

CHAPTER 2

ADSORPTION AND AGGREGATION OF A CATIONIC CYANINE DYE ON LAYERED SILICATES

2.1. Adsorption and Aggregation of a Cationic Cyanine Dye on Layered Clay Minerals

2.1.1. Introduction

Inorganic layered materials such as clay minerals are expected as media to build up highly organized inorganic-organic nanostructures utilizing their two dimensional surfaces. Ogawa et al. have synthesized photochemical hole burning[1] and nonlinear optical[2] materials by using clay minerals as organizing media of photoactive species. On designing such photofunctional materials, elucidating the factors to affect the organizing manner of guest species is indispensable. Because the spectroscopic features of organic dyes adsorbed on clays change reflecting the states of the dyes, the distribution and location of guest species on a clay surface have been investigated using various organic dyes as spectroscopic probes.[3,4] It has been suggested that the states of dyes are controlled by surface charge density, type of isomorphous substitution and particle size of clays[5-8] as well as coadsorbing species.[9]

1,1'-Diethyl-2,2'-cyanine (pseudoisocyanine abbreviated as PIC; Scheme 1) form a specific aggregate, so called J-aggregate, in a highly concentrated solution. J-aggregation is also observed when the dye is adsorbed to silver halides,[10] polymers,[11] colloidal silica,[12] etc. J-aggregate of cyanine dye has attracted much attention for its applications for spectral sensitization of photographic processes[13] and its useful optical properties.[14]
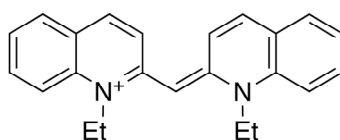
Scheme 1. 1,1'-Diethyl-2,2'-cyanine (pseudoisocyanine abbreviated as PIC)

Ogawa et al. have investigated the adsorption and aggregation of PIC cations on montmorillonite and saponite for aqueous suspensions and cast films.[15]   The aggregation states of PIC were controlled by the selection of the clay.   The change in the state of adsorbed cyanine dyes during the evaporation of solvent has also been revealed.   In this chapter, the effect of clays on the states of PIC is discussed in further details by comparing the absorption spectra of PIC adsorbed onto Na-fluor-tetrasilicic mica, Na-hectorites, Na-montmorillonite and Na-saponite.   The effect of solvent and coadsorbed cations is also investigated.   The detailed studies on the controlling factors responsible for the states of PIC on clay minerals offer notable information for organizing photoactive species in a more precise manner.

2.1.2. Experimental

<u>Materials</u>

Synthetic Na-saponite (Sumecton SA supplied from Kunimine Industries Co.), synthetic Na-hectorite (SWN supplied from Coop Chemical Co. and Laponite RD supplied from Laporte Industries Co.), synthetic Na-fluor-tetrasilicic mica (TSM; supplied from Topy Industries Co.) and natural Na-montmorillonite (Kunipia F supplied from Kunimine Industries Co.) were used as host materials.   TSM was used after removing non-expandable impurities by dispersion and sedimentation.   The cation exchange capacities (CEC) of montmorillonite, TSM, SWN, Laponite and saponite are 119, 100, 100, 73 and 71 mequiv/100g of host, respectively.   Tetramethylammonium (abbreviated as TMA)-montmorillonite was obtained by an ion exchange reaction of Na-montmorillonite with an aqueous solution of TMA bromide.   TMA bromide (Tokyo Kasei Ind. Co. (extra pure grade)) and ethylene glycol (WAKO Pure Chemical Ind. Co. (extra pure grade)) were used without further purification.   PICBr was purchased from Nippon Kanko Shikiso Co., and used as received.

<u>Sample Preparation and Characterization</u>

Aqueous clay suspensions (1 g dm^{-3}) were obtained by dispersing powders of clays in water and stirring for 2 days at room temperature.   Stable aqueous PIC/clay

suspensions were obtained typically by adding 80 dm^{-3} of an aqueous solution of PICBr (6.25×10^{-6} mol dm^{-3}) to 20 dm^{-3} of the clay suspension (1 g dm^{-3}).   The PICBr/clay ratio was thus set to 2.5 mmol / 100 g clay (PIC concentration is 5×10^{-6} mol dm^{-3}) since the suspension tended to flocculate at higher PIC/clay ratios.   Ethylene glycol and water/ethylene glycol mixtures were also used as solvents.   The mixture was stirred for a day before measurements for equilibration and the visible absorption spectra of the suspensions were recorded on a Shimadzu UV-3100PC spectrophotometer. Fluorescence spectra were recorded on a Hitachi F-4500 spectrofluorophotometer.

2.1.3. Results and Discussion

Effect of the Type of Clay Minerals

The difference in the states of adsorbed PIC was revealed between clays with larger particle sizes (montmorillonite and TSM) and smaller particle sizes (saponite, SWN and Laponite).   The absorption spectra of the aqueous mixtures containing 20 mg of clays and 100 ml of 5×10^{-6} mol dm^{-3} PIC Br (the amount of PIC is 2.5 mmol / 100 g clay) are shown in Figure 1.   Because no residual PIC was detected in the supernatant after centrifugation (1 h at 20000 rpm) of the suspensions, it was confirmed that the spectra reflects the states of the PIC adsorbed on the clays.   In the PIC/SWN (Figure 1a), PIC/Laponite (Figure 1b) and PIC/saponite (Figure 1c) systems, the absorption bands were observed at 527 nm, 526 nm, and 525 nm, respectively, accompanied by vibronic satellite bands or shoulders in shorter wavelengths.   Because these bands are only slightly red-shifted relative to the band observed for a dilute aqueous solution of PICBr (523 nm), they are attributable to monomeric PIC.   In contrast, new absorption bands emerged at 565 nm in the PIC/TSM system (Figure 1d) and 566 nm in the PIC/montmorillonite system (Figure 1e).   These new bands were largely red-shifted relative to the monomer band and accompanied fluorescence at about 569 nm for both the systems.   These absorption and luminescence bands are characteristic to the J-aggregate of PIC.[16,13]   Thus, the adsorbed PIC cations formed J-aggregates on TSM and montmorillonite, while they were distributed molecularly on SWN, Laponite and saponite.

A diameter of saponite particles is evidenced to be smaller than 0.01 μm, determined by light scattering, whereas the estimated diameter of montmorillonite was larger than 1 μm. The surface area of circular platelet with the diameter of 0.01 μm is 79 nm^2 for one side. Assuming the edge-on adsorption of a PIC cation on a silicate surface and the molecular size of PIC, one PIC cation occupy 0.69 nm^2 of the silicate surface[17]. Therefore, the maximum number of PIC cations on one surface of a particle is calculated to be about 110. Although the number of the dyes in J-aggregate has not been accurately determined (reported numbers are ranged from 4 to over 1000 [13,18-21]), it is reasonable to suppose that such small particles like Laponite, SWN and saponite can not offer enough spaces for the formation of J-aggregates. These results, in turn, can indicate that the J-aggregate of PIC is so large that the aggregation behavior was affected by the particle size of the clays.
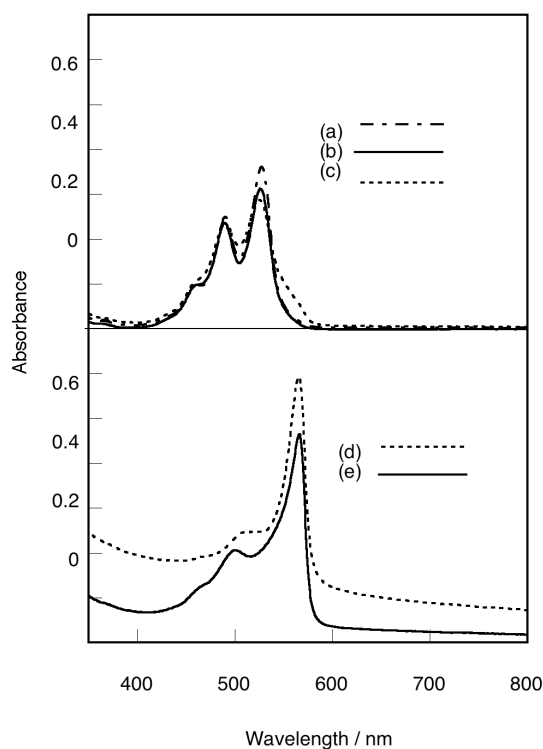
Figure 1. Absorption spectra of the mixtures containing 20 mg of (a) Na-SWN , (b) Na-Laponite, (c) Na-saponite, (d) Na-TSM and (e) Na-montmorillonite and 100 ml of 5 × 10^{-6} mol dm^{-3} PICBr aqueous solutions (the amount of PIC is 2.5 mmol/100g clay).

61

On the other hand, the differences in the CEC values or types of isomorphous substitution have been described in previous studies as possible factors to control the states of adsorbed guest species.[5,7,8] The present results, however, exclude these possibilities. In spite of the comparable CEC values of TSM and SWN (about 100 mmol/100 g clay), the spectroscopic features were different between the PIC/TSM and PIC/SWN systems: J-band appeared in the PIC/TSM system (Figure 1d), but not in the PIC/SWN system (Figure 1a). The type of isomorphous substitution is not likely to affect the states of PIC, neither. No significant effects on the spectra of the suspensions were observed among the clays with tetrahedral substitution (saponite) and octahedral substitution (Laponite and SWN): these absorption spectra in the PIC/saponite (Figure 1c), PIC/SWN (Figure 1a) and PIC/Laponite (Figure 1b) systems similarly exhibited the bands that are attributed to the monomeric PIC distributed on the silicate surface. Thus, the effect of CEC and types of isomorphous substitution is ruled out and the difference in the particle size of clays is considered to be the major factor to control the state of the PIC in the present systems.

Effect of coadsorbed cations

The J-aggregation of PIC was also controlled by coadsorbing cations. Figure 2 illustrates the absorption spectra of PIC/TMA-montmorillonite and PIC/Na-montmorillonite systems. In the PIC/TMA-montmorillonite system (Figure 2b), the monomer band at 529 nm and its vibrational bands as well as the J-band at 570 nm appeared, while only the J-band was observed in the PIC/Na-montmorillonite system (Figure 2a). Thus, the aggregation of PIC was partially suppressed by the coadsorption of TMA.

Dyes aggregate by dye-dye interactions due to the van der Waals force between dyes and/or the energy stabilization caused by the delocalization of π-electrons in dye aggregates. The aggregation states of dyes are of importance since the spectroscopic and photophysical properties depend on them. The aggregations of dyes such as γ-stilbazolium,[22] and spiropyrans[23] on the clays has been controlled by varying the length of alkyl chain in the coadsorbing alkylammoniums or dyes. The

coadsorption of neutral species such as poly(N-vinyl-2-pyrrolidone) was also effective for the disaggregation of Ru(bpy)$_3$$^{2+}$ cations on the silicate surface.[24] Thus, the dyes and coadsorbing species are mixed due to the high affinity between them, resulting in the dilution and disaggregation of dyes.   The suppression of aggregation of PIC is also interpreted as the guest-guest interaction due to the high affinity between PIC and TMA and the reduction of the interaction between adjacent PIC cations.
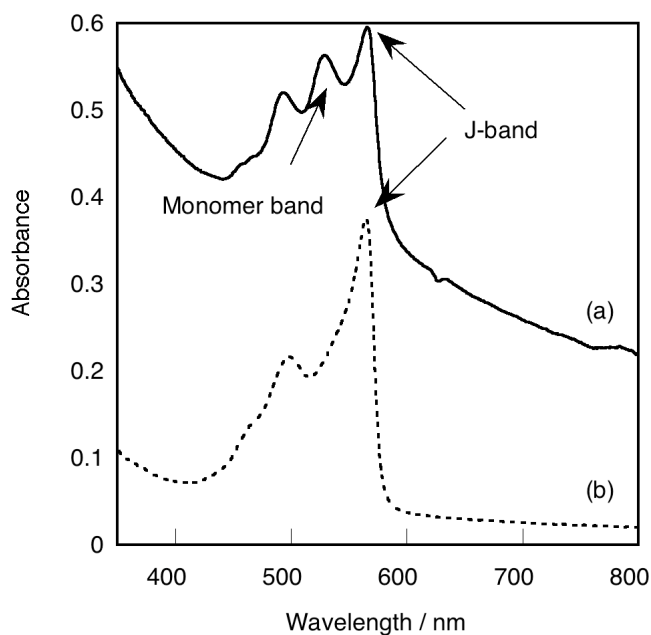
Figure 2.   Absorption spectra of the mixtures containing 20 mg of (a) TMA-montmorillonite system and (b) Na-montmorillonite and 100 ml of 5 × 10^{-6} mol dm^{-3} PICBr aqueous solutions (the amount of PIC is 2.5 mmol/100g clay).

Effect of solvent

The use of ethylene glycol or ethylene glycol-water mixture as solvent for the PIC/montmorillonite suspension resulted in deformation of the aggregates. In the visible absorption spectra, the PIC/montmorillonite suspension in ethylene glycol exhibited a monomer band at 527 nm (Figure 3a); a dilute solution of PIC in ethylene glycol also showed a monomer band at 527 nm. In contrast, the J-band (567 nm) was predominant in the aqueous suspension of PIC/montmorillonite (Figure 3d). Thus, it is supposed that the dissociation of J-aggregates in ethylene glycol was caused by high affinity of ethylene glycol with PIC. PIC cations on the clay surface are supposedly surrounded by ethylene glycol molecules and are mainly present in a monomeric state.
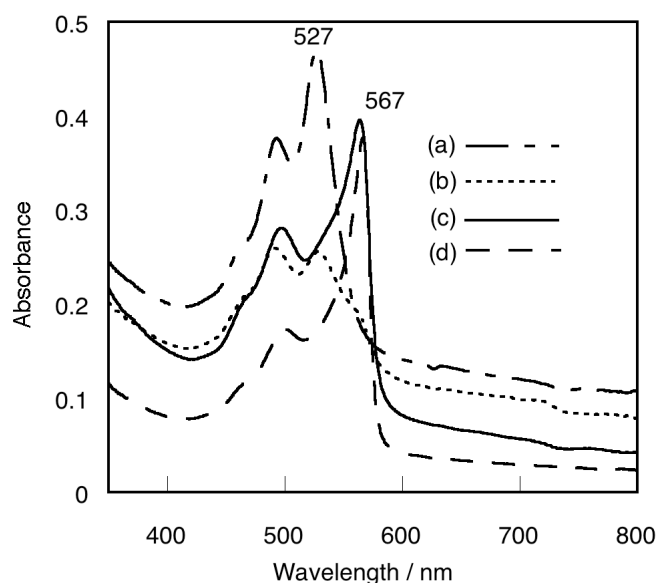
Figure 3. Absorption spectra of the mixtures containing 20 mg of montmorillonite and 5×10^{-6} mol dm^{-3} PICBr solutions (the amount of PIC is 2.5 mmol/100g clay); the ratios of ethylene glycol to water in the solvents are (a) 100 %, (b) 80%, (c) 60% and (d) 0%.

Interestingly, PIC/montmorillonite suspensions in the mixture of water and ethylene glycol displayed both J-band and monomer band.(Figures 3b and 3c)   The contribution of the J-band and the monomer band in the spectra varied, corresponding to the composition of the solvent.   This result indicates that two domains, where the PIC cations are adsorbed as monomers in one water-rich domain and J-aggregate in another ethylene glycol-rich domain, are present.   Assuming the equilibrium between J-aggregate and monomer,[21] it is also probable that the increasing ratio of ethylene glycol in the homogeneous mixture enhanced the ability of solvent to suppress the aggregation of PIC because of an alteration of the net property of the solvent such as polarity. Accordingly, the equilibrium between monomer and J-aggregate shifted toward monomer.

2.1.4. Conclusion

The adsorption and aggregation of PIC on various clays in the suspensions have been investigated.   Particle size of clays was considered to be a major factor to control the states of PIC in these systems.   On the other hand, the dissociation of J-aggregate was observed when TMA-exchanged clay was employed as the host material or ethylene glycol as the solvent.   Thus, the aggregation of PIC was effectively controlled by the interactions between PIC cations and the surrounding species as well as the nature of clays.

2.1.5. References

(1) M. Ogawa, T. Handa, K. Kuroda, C. Kato, T. Tani, *J. Phys. Chem.*, **96**, 8116 (1992).

(2) M. Ogawa, M. Takahashi, K. Kuroda, *Chem. Mater.*, **6**, 715 (1994).

(3) J. K. Thomas, *Acc. Chem. Res.*, **21**, 275 (1988).

(4) M. Ogawa, K. Kuroda, *Chem. Rev.*, **95**, 399 (1995).

(5) Z. Grauer, G. L. Grauer, D. Avnir, S. Yariv, *J. Chem. Soc., Faraday Trans. 1,* **83**, 1685 (1987).

(6) J. Cenens, R. A. Schoonheydt, *Clays Clay Miner.*, **36**, 214 (1988).

(7) C. B. Sunwar, H. Bose, *J. Colloid and Interface Sci.*, **136**, 54 (1990).

(8) F. L. Arbeloa, M. J. T. Estévez, T. L. Arbeloa, I. L. Arbeloa, *Clay Minerals*, **32**, 97 (1997).

(9) M. Ogawa, K. Kuroda, *Bull. Chem. Soc. Jpn.*, **70**, 2593 (1997).

(10) J. E. Maskasky, *J. Imaging Sci.*, **35**, 29 (1991).

(11) T. Kunisawa, T. Sato, Y. Yonezawa, *Mol. Cryst. Liq. Cryst.*, **294**, 169 (1997).

(12) M. Watanabe, M. Herren, M. Morita, *J. Lumin.*, **58**, 198 (1994).

(13) A. H. Herz, *Photogr. Sci. Eng.,* **18**, 323 (1974).

(14) D. Möbius, *Adv. Mater.,* **7**, 437 (1995).

(15) M. Ogawa, R. Kawai, K. Kuroda, *J. Phys. Chem.*, **100**, 16218 (1996).

(16) E. E. Jelley, *Nature*, 1009 (1936).

(17) V. Czikkely, H. D. Forsterling, H. Kuhn, *Chem. Phys. Lett.*, **6**, 11 (1970).

(18) Y. Yonezawa, D. Möbius, H. Kuhn, *J. Appl. Phys.,* **62**, 2022 (1987).

(19) A. A. Muenter, D. V. Brumbaugh, J. Apolito, L. A. Horn, F. C. Spano, S. Mukamel, *J. Phys. Chem.*, **96**, 2783 (1992).

(20) T. Tani, T. Suzumoto, K. Kemnitz, K. Yoshihara, *J. Phys. Chem.*, **96**, 2778 (1992).

(21) T. Tanaka, T. Matsubara, *J. Imaging Sci. Technol.*, **38**, 495 (1994).

(22) H. Usami, K. Takagi, Y. Sawaki, *Bull. Chem. Soc. Jpn.,* **64**, 3395 (1991).

(23) H. Tomioka, T. J. Itoh, *J. Chem. Soc., Chem. Commun.*, 532 (1991).

(24) M. Ogawa, M. Inagaki, N. Kodama, K. Kuroda, C. Kato, *J. Phys. Chem.,* **97**, 3819 (1993).

2.2. Intercalation of a cationic cyanine dye into the layer silicate magadiite

2.2.1. Introduction

Supramolecular assemblies have extensively been investigated aiming at mimicries of life systems and constructing new classes of porous materials and novel photofunctional and electronic materials.[1]   Among many supramolecular assemblies, J-aggregates of cyanine dyes have been investigated since the discovery by Jelley and Scheibe in 1936.   J-aggregates are characterized by the appearance of an excitonic absorption band in the visible absorption spectra at longer wavelengths relative to the monomer band and by a resonance fluorescence with a very small Stokes shift.[2,3]   J-aggregates of cyanine dyes exhibit useful photofunctions such as sensitizing and third order non-linear optical properties.[4,5]   Therefore, formation of the aggregates and control of the microstructures of the aggregates have been of great interest.[6-8]

Host-guest interactions in a two-dimensional interlayer space are useful to control microstructure of molecular assemblies.[11-13]   The previous chapter showed that the aggregation of 1,1'-diethyl-2,2'-cyanine (pseudoisocyanine, abbreviated as PIC) on the surface of smectite clays[9,10] depends on the nature of clay, coadsorbed species and solvent.   However, the states of PIC found in these systems were those 'typical' in other systems.[14-16]   In this chapter, magadiite[17] is used as the host material for the intercalation of PIC to further modify the aggregation state of PIC.   Magadiite is a layer silicate with the ideal composition $Na_2Si_{14}O_{29} \bullet nH_2O$ and possesses cation exchange capacity.[18-20]   The cation exchange capacity is higher than smectite clays.

2.2.2. Experimental

Host materials

Na-magadiite was synthesized by the method described by Kosuge et al.[21]   A mixture of colloidal silica, sodium hydroxide and water in the molar ratio of 1.00: 0.23: 18.2 was sealed in a Teflon-lined autoclave and was hydrothermally treated at 150 $^{\circ}$C

for 48 h.   The formation of Na-magadiite was confirmed by X-ray diffraction (XRD) analysis.   The XRD pattern (Figure 1a) was in accordance with the JCPDS data (No. 42-1350).

Dodecyl, tetradecyl and hexadecyltrimethylammonium cations (abbreviated as $C_{12}TMA$, $C_{14}TMA$ and $C_{16}TMA$, respectively) were intercalated by the method reported previously.[19]   The conditions were slightly modified.   Na-magadiite was stirred in aqueous solutions of the alkylammonium chlorides (0.1 mol dm^{-3}) for 5 days at room temperature, followed by washing with acetone.   The basal spacing increased from 1.55 nm to 2.79, 3.01 and 3.12 nm for $C_{12}TMA$-, $C_{14}TMA$- and $C_{16}TMA$-magadiites. The adsorbed amount of $C_{12}TMA$, $C_{14}TMA$ and $C_{16}TMA$ were 1.8, 1.7, 1.6 mol CnTMA per a mol $Si_{14}O_{29}$ (the formula unit of magadiite).   The IR absorption bands, such as the C-H stretching mode at around 2900 cm^{-1}, also confirmed the formation of CnTMA-magadiites (Figure 2a for $C_{12}TMA$-magadiite).   H-magadiite was obtained by acid treatment of Na-magadiite with 0.2 mol dm^{-3}-HCl for one day at room temperature, followed by washing with acetone.   The basal spacing of H-magadiite was 1.12 nm, in accordance with the previous reports.[18,19,22]

Intercalation of PIC

The powders of Na-magadiite and $C_{12}TMA$-magadiite were dispersed in a PICBr aqueous solution (5 × 10^{-4} mol dm^{-3}) and stirred for 6 days at 60 °C.   The PIC/$Si_{14}O_{29}$ molar ratio was set to 1.8 for the Na-magadiite system and was varied from 0.2 to 2.4 for the $C_{12}TMA$-magadiite system.   The adsorbed amount of the dye varied depending on the initial PIC/$Si_{14}O_{29}$ molar ratio (Table 1).   After the reaction, a solid product was separated by centrifugation, followed by washing with acetone until the supernatant became colorless and drying under ambient atmosphere.   It must be noted that the intercalation of PIC did not proceed when acetone or ethanol was used instead of water for the reaction of $C_{12}TMA$-magadiite as confirmed by XRD and IR spectra. $C_{14}TMA$-magadiite, $C_{16}TMA$-magadiite and H-magadiite were also used as host materials and were allowed to react under the same conditions.   The initial molar ratios of PIC/$Si_{14}O_{29}$ were 0.9 for $C_{14}TMA$- and $C_{16}TMA$-magadiites and 0.2 for H-magadiite.

Table 1. The samples in this study

sample	amount of PIC adsorbed	basal spacing	gallery height***
	/ mol per formula unit of magadiite	/ nm	/ nm
PIC/H-magadiite	0.08 *	1.34	0.22
PIC/Na-magadiite	0.44 *	1.63	0.51
PIC/C$_{12}$TMA-magadiite-0.2	0.15 **	3.02	1.90
PIC/C$_{12}$TMA-magadiite-0.4	0.30 **	2.87	1.75
PIC/C$_{12}$TMA-magadiite-1.0	0.79 *	2.10	0.98
PIC/C$_{12}$TMA-magadiite-2.4	0.82 *	2.05	0.93

* from CHN analysis

** the concentration changes of PICBr solution before and after adsorption

*** obtained by subtracting the basal spacing of dehydrated H-magadiite (1.12 nm)

Characterization

XRD patterns were obtained with a Mac Science MXP^3 diffractometer with monochromated CuKα radiation at the tube voltage of 40 kV and the tube current of 30 mA. Infrared (IR) spectra of KBr pellets were recorded on a Perkin-Elmer FT-IR 1640 spectrometer. The adsorbed amounts of PICBr and CnTMA cations were determined by CHN analysis (Perkin-Elmer PE-2400II). When both PIC$^+$ and CnTMA$^+$ were present in the product, the compositions were determined by the concentration change of the PICBr solution before and after the reaction measured by UV-Vis spectroscopy on a Shimadzu UV-3100PC spectrophotometer. The UV-Vis spectra of the products (powders) were measured by dispersing the powders in water and ultrasonicating to obtain homogeneous aqueous suspensions. The fluorescence spectra were recorded on a Hitachi F-4500 spectrofluorophotometer.

2.2.3. Results

The reaction of PIC with Na-magadiite

XRD and compositional analyses confirm that PIC was intercalated in magadiite by

ion-exchange reaction of PIC with Na-magadiite.   The XRD pattern of the product (orange powders; denoted as PIC/Na-magadiite) is shown in Figure 1c.   Although the basal spacing of the product (1.63 nm) is slightly shrunk from that of Na-magadiite (1.56 nm), the gallery height (calculated as 1.63 - 1.12 = 0.51 nm by subtracting the basal spacing of H-magadiite.[18,19,22]) is large enough for PIC to be intercalated.   The compositional analysis also confirms the intercalation of PIC; the amount of adsorbed PIC was 0.44 mol per a mol of $Si_{14}O_{29}$.   No Further changes were found when the reaction was repeated with fresh PIC Br solution.
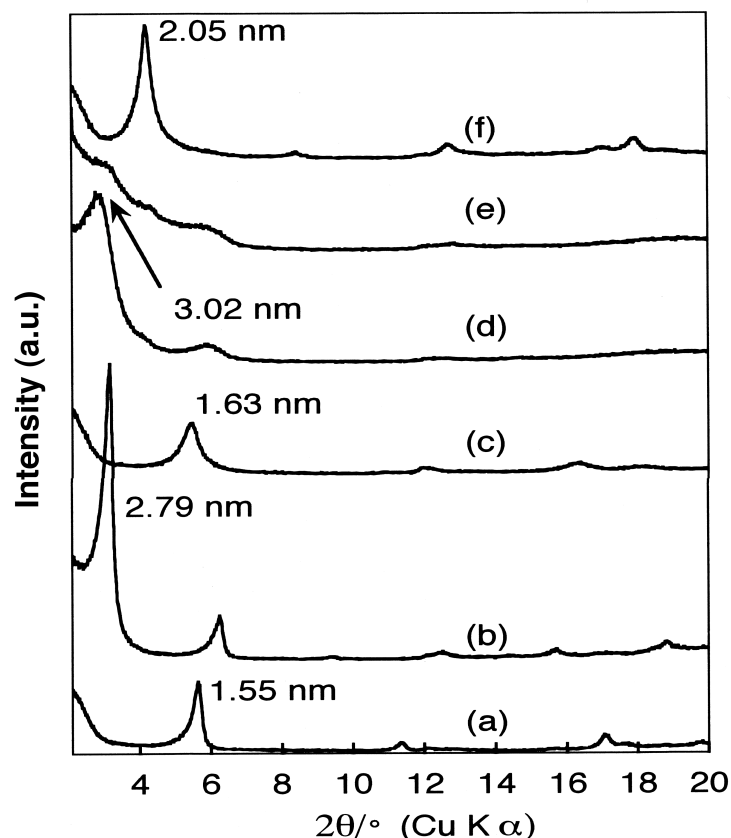
Figure 1.   XRD patterns of (a) Na-magadiite, (b) C_{12}TMA-magadiite, (c) PIC/Na-magadiite, (d) PIC/C_{12}TMAmagadiite-0.2.

The reaction of PIC with alkylammonium-exchanged magadiites

Intercalation compounds of PIC with magadiite were also obtained by using C_{12}TMA-magadiite as the starting material. The products were red colored powders. The basal spacing of the product with the initial PIC/$Si_{14}O_{29}$ ratio of 2.4 (hereafter denoted as PIC/C_{12}TMA-magadiite-2.4) was 2.05 nm (Figure 1f), and it was smaller than that of the host C_{12}TMA-magadiite (2.79 nm). The gallery height was large enough for PIC to be intercalated. In the IR spectrum (Figure 2b), the absorption bands of the ring-stretching modes were observed at 1300 - 1600 cm^{-1}, whereas the C-H stretching bands of C_{12}TMA at around 2900 cm^{-1} almost disappeared. The adsorbed amount was 0.82 mol per a mol $Si_{14}O_{29}$, and the value was larger than that of the product from Na-magadiite.
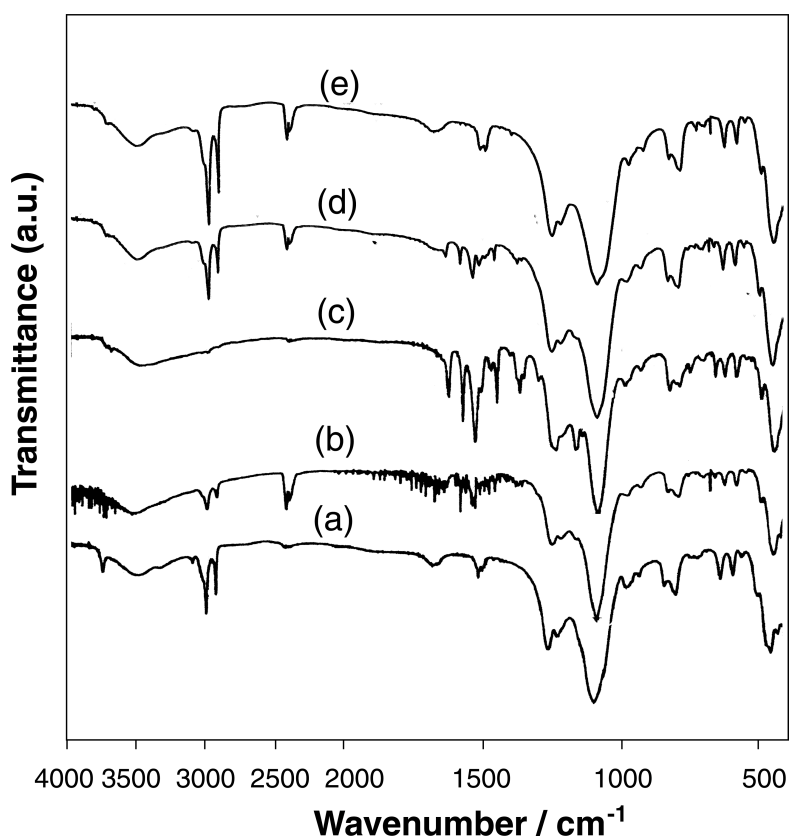
Figure 2. IR spectra of (a) C_{12}TMA-magadiite, (b) PIC/C_{12}TMAmagadiite-0.4, (e) PIC/C_{12}TMA-magadiite-2.4, and (d) PIC/C_{14}TMA-magadiite and (e) PIC/C_{16}TMA-magadiite.

When the initial ratio $PIC/Si_{14}O_{29}$ was small (0.2; denoted as $PIC/C_{12}TMA$-magadiite-0.2), the XRD peaks were broadened (Figure 1d), indicating that the arrangement and the distribution of the guest species are not uniform.   The peak was centered at d = 3.02 nm, which was larger than that of $C_{12}TMA$-magadiite by 0.23 nm. The IR bands of both $C_{12}TMA$ and PIC were observed in these products (Figure 2c), although the band of $C_{12}TMA$ was smaller than that in $C_{12}TMA$-magadiite.   When the initial $PIC/Si_{14}O_{29}$ ratio was 0.4, a biphasic compound was obtained, characterized by two broad diffraction peaks at d = 2.87 and 2.05 nm (Figure 1e).   Thus, $C_{12}TMA^+$ remained in the interlayer space due to incomplete ion-exchange.

When PIC was reacted with $C_{16}TMA$-magadiite, the XRD pattern did not change.   The adsorbed amount of PIC was not determined by the concentration change of the solution due to the detector limit.   No IR bands of PIC were observed (Figure 2e), while the IR bands of $C_{16}TMA$ were observed, indicating that the adsorbed amount of PIC is very small.   When $C_{14}TMA$-magadiite was used, the basal spacing did not change but the diffraction peaks were broadened.   Both IR absorption bands of $C_{14}TMA$ and PIC were observed (Figure 2d).   The adsorbed amount of PIC was 0.49 mol per a mol $Si_{14}O_{29}$ and this was smaller than that in $PIC/C_{12}TMA$-magadiite-1.0 system (0.79 mol per a mol $Si_{14}O_{29}$).

The reaction of PIC with H-magadiite

The basal spacing of H-magadiite increased from 1.12 nm to 1.34 nm after the treatment with PIC Br solution.   However, this is not indicative of the intercalation of PIC, since the gallery height of at least 0.4 nm is required for PIC to be intercalated and the amount of PIC adsorbed was very small (0.08 mol per a mol $Si_{14}O_{29}$).   The observed increase in the basal spacing must be ascribed to the intercalation of water molecules.[22]   PIC is supposedly adsorbed on the external surface of H-magadiite.

Visible absorption and fluorescence spectra of the products

The visible absorption spectra of PIC changed upon adsorption to magadiite, indicating the variation of the state of PIC upon adsorption.   PIC/H-magadiite

dispersed in water showed an absorption band at 530 nm with its vibronic satellite band at 492 nm (Figure 3f). In PIC/Na-magadiite (Figure 3e) and PIC/C_{12}TMA-magadiite-2.4 (Figure 3d), broad absorption bands were observed at 541 nm and 557 nm, respectively, with satellite bands at lower wavelengths. Thus, the observed absorption maxima are red-shifted by 7-32 nm upon adsorption from that of PIC monomer observed in dilute (5×10^{-5} mol dm^{-3}) PICBr aqueous solution (Figure 3a), depending on the starting material used. These results are in contrast with the PIC/clay systems described in the previous Chapter 2.1: PIC was present as monomer on hectorite, giving the absorption maximum at 523 nm (Figure 3b), and as J-aggregate on montmorillonite, characterized by the sharp band at 566 nm (Figure 3c).[10]
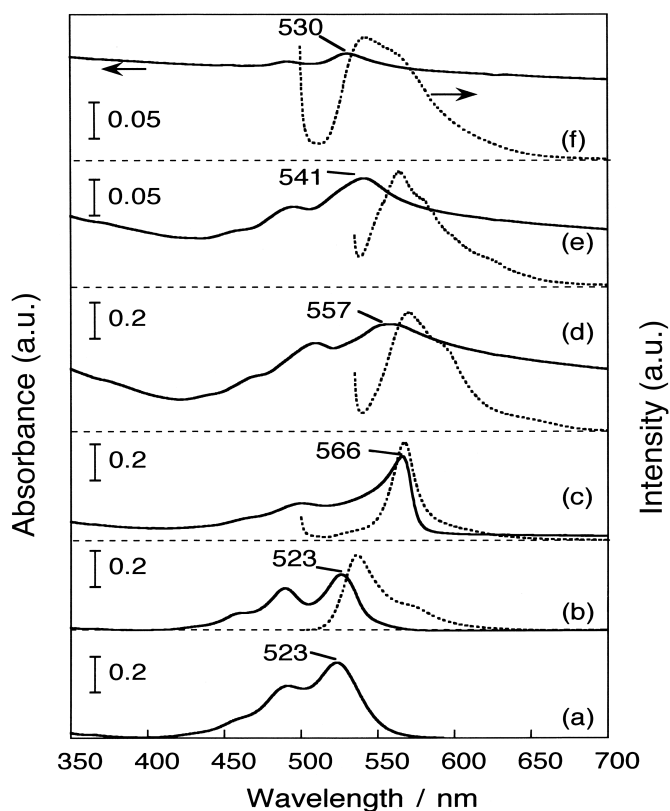
Figure 3. Absorption (solid lines) and fluorescence (dotted lines) spectra of (a) the aqueous solution of PICBr (5×10^{-5} mol dm^{-3}) and the aqueous suspensions of (b) PIC/hectorite, (c) PIC/montmorillonite, (d) PIC/C_{12}TMA-magadiite-2.4, (e) PIC/Na-magadiite, and (f) PIC/H-magadiite. The excitation wavelengths are 490 nm (for (b), (c) and (f)) and 525 nm (for (d) and (e)).

The fluorescence spectra also indicate the variation of the state of PIC upon adsorption. The bands were observed at 570 nm, 564 nm and 540 nm in PIC/C_{12}TMA-magadiite-2.4, PIC/Na-magadiite and PIC/H-magadiite (dotted lines in Figure 3), while no emission was observed for an aqueous PIC Br solution (5×10^{-5} mol dm^{-3}).

The amount of adsorbed PIC also affects the state of the PIC. PIC/C_{12}TMA-magadiite-0.2 (Figure 4a) showed the absorption band at 527 nm, which is ascribable to monomeric PIC, as well as the band at 545 nm, which would be ascribed to an aggregate. In contrast, at higher PIC loadings, only the bands at longer wavelength are observed at 553 and 557 nm for PIC/C_{12}TMA-magadiite-0.4 (Figure 4b) and -2.4, respectively.
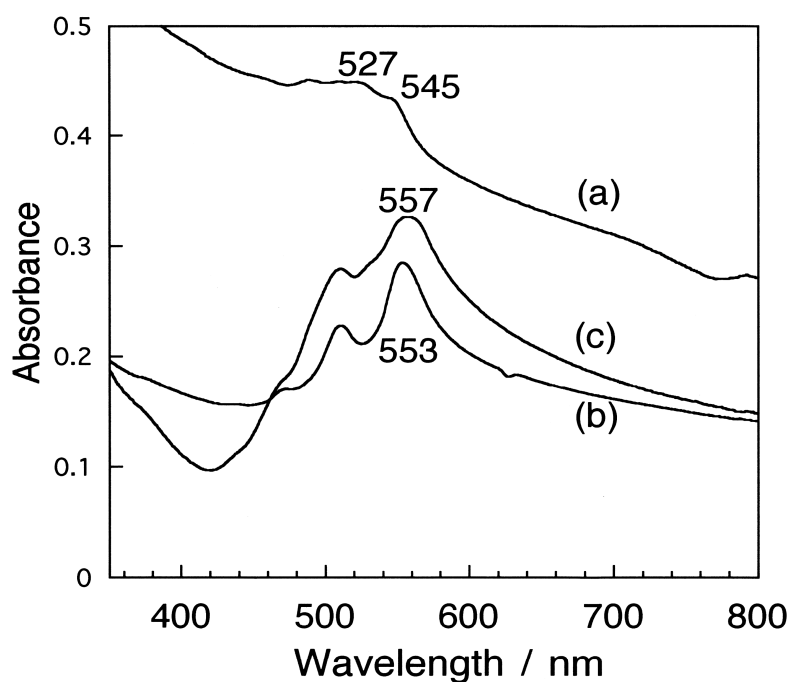
Figure 4. Absorption spectra of the aqueous suspensions of (a) PIC/C_{12}TMA-magadiite-0.2, (b) PIC/C_{12}TMA-magadiite-0.4 and (c) PIC/C_{12}TMA-magadiite-2.4. The spectrum (c) is same as in Figure 3d.

2.2.4. Discussion

Intercalation Reactivity of Magadiite with PIC

The XRD, chemical analytical and spectroscopic results revealed the intercalation of PIC into magadiite by ion-exchange when Na-magadiite and C_{12}TMA-magadiite were used as host materials.   It is known that intercalation is not so easy for magadiite and only limited guest species are intercalated by ion-exchange. Guest–exchange[23] (pre-intercalation with easily intercalating species and replacing them by other species) or utilization of a crown ether[24] were effective ways for intercalation of bulky guest species such as tris(2,2'-bipyridine)ruthenium(II) complex cations. Interestingly, the reactivity for intercalation of PIC was reduced with increasing chain length of CnTMA-magadiites.   The van der Waals interaction between the alkyl chains reduces the amount of PIC adsorbed.

The Controlled Arrangement of PIC in the Interlayer Spaces of Magadiite

The arrangement of PIC in the interlayer space is derived from the basal spacing and the size of PIC (ca. 0.4 nm × 0.8 nm × 1.6 nm).   In PIC/C_{12}TMA-magadiite-2.4 with the gallery height of 0.93 nm, the possible arrangement of PIC in the interlayer space is monomolecular with the molecular plane perpendicular to the silicate layer or a bimolecular layer arrangement with the molecular plain parallel to the silicate layer.   On the other hand, the basal spacing of 0.51 nm in PIC/Na-magadiite indicates a monomolecular arrangement with the molecular plane inclined to the silicate layer by less than 40°.

The PIC orientation is also discussed based on the visible spectra: the spectra reveal an anomalous state of PIC in the interlayer space.   For PIC/C_{12}TMA-magadiite-2.4, the absorption maxima were largely shifted toward longer wavelengths (557 nm) compared with the monomer band (523 nm).   It is well established that PIC forms specific J-aggregates on AgBr [14,16] and clay minerals,[9,10] showing the absorption bands at 571 - 579 nm and 566 nm for AgBr and montmorillonite, respectively.   The absorption bands observed in PIC/C_{12}TMA-magadiite-2.4 would also be caused by PIC aggregation.   However, the microstructure of the aggregates are supposedly different

from that of typical J-aggregates on AgBr since the spectral shifts are smaller.

The emission spectrum of PIC/C_{12}TMA-magadiite-2.4 (dotted lines in Figure 3d) also indicates the different character of the aggregate from typical ones. A Stokes shift (the difference in wavelength of absorption and fluorescence maxima) of 15 nm was larger than observed for typical J-aggregates. The Stokes shift observed for typical J-aggregates (the PIC adsorbed on montmorillonite) is only a few nm (Figure 3c) as a result of a rapid propagation of an exciton through out the aggregate.[25]

The spectral shifts in absorption bands upon aggregation of the dye cations are approximated by the molecular exciton theory of McRae and Kasha.[26] The energy difference between the aggregate transition and the monomer one, ΔV, is expressed by

$$\Delta V = 2h^{-1}(n\text{-}1) / n <M^2> / r^3 (1\text{-}3\cos^2\alpha)$$

where h is the Plank's constant, n is the number of dye molecules in the aggregate, r is the distance between the molecules, α, is the angle between the long axes of the molecules and the aggregate axis and $<M^2>$ is the transition dipole moment which is proportional to the molar extinction coefficient of the monomer. On the basis of this theory, smaller spectral shifts are attributed to larger values of r and α and smaller values of n. Thus, the smaller spectral shifts observed here can be interpreted by (1) modification of the microstructure of the aggregate (represented by r and α) and/or (2) reduction of the size of the aggregates (represented by n). (1) is more plausible because the surface of the silicate layer is fully covered by PIC cations. The microstructure may be modified by the strong interaction of PIC with magadiite layer.

The UV-visible spectroscopic results of PIC/H-magadiite can be a proof of the strong interaction between the silicate layer of magadiite and PIC. The spectral shift of the monomer band is related to the adsorption on the silicate layer. The shift was larger than observed in PIC/hectorite (2-4 nm),[10] indicating stronger interactions between PIC and magadiite. The emission band observed in PIC/H-magadiite also proves the strong interaction between the silicate layer of magadiite and the PIC. It is known that a monomeric PIC in solutions does not emit fluorescence because the

excited dye is easily inactivated through non-radiative processes.[27,28]   The observed emission from monomeric PIC adsorbed on H-magadiite may be caused by strong interaction between the silicate layer and PIC by electrostatic interaction.   The fluorescence from a monomeric PIC was also observed when PIC was adsorbed on hectorite (Figure 3b).

The aggregation state of PIC was affected by coexisting of $C_{12}TMA^+$.   The UV-visible absorption bands due to PIC aggregates were also found in PIC/C_{12}TMA-magadiite-0.2 and –0.4.   Although it was shown that both PIC^+ and $C_{12}TMA^+$ were present in the interlayer spaces based on XRD and IR, it is probable that PIC was segregated due to the strong tendency of PIC to form aggregates.   Although the formation of the aggregate was revealed, UV-visible spectra showed that the aggregate size is affected by the presence of $C_{12}TMA^+$.   The spectral shift decreased with decreasing adsorption of PIC^+.   This observation may be caused by a smaller aggregate size.   Evidently, the alkyl chains reduce the average size of the aggregates.   The size of the aggregates has been controlled by varying the conditions such as temperature[7] and pressure[8] as well as by dilution with similar molecule[6]   As mentioned in Chapter 2.1., the aggregation of PIC on montmorillonite was partially suppressed by the presence of tetramethylammonium cations.[10]

On the other hand, the state of the PIC was also different in the PIC/Na-magadite system, i.e. when PIC was coexisted with Na^+.   The absorption band at 541 nm (Figure 3e) would indicates formation of PIC aggregates.   However, the spectral shift is smaller than that of PIC/C_{12}TMA-magadiite-2.4, indicating a different microstructure of the aggregate.   The PIC cations in the interlayer space are more largely inclined in PIC/Na-magadiite as inferred from the smaller basal spacing measured by XRD; the difference in the microstructure could lead to the difference in spectral shift.   The difference in the adsorbed amount would also result in modified microstructure.

The aggregation of cyanine dyes is mainly dominated by the molecular structure.[25]   For example, PIC forms a J-aggregate in concentrated solutions, while the homologous dye with a longer methine chain bridging the two quinoline rings (1,1'-

diethyl-2,2'-carbocyanine) forms H- or herringbone aggregates. For optimization of electronic and optical properties of functional organic molecules, the control of molecular arrangements as well as the molecular design is indispensable. An alternative way to control the microstructure by interactions with the surface of layered compounds presented here is of great importance.

2.2.5. Conclusions

PIC was intercalated into magadiite by ion-exchange of Na-magadiite and $C_{12}TMA$-exchanged magadiite.   The intercalated PIC ions formed aggregates in both systems.   The microstructure was different from the typical structure observed in other systems such as PIC on AgBr.   The PIC aggregates formed in PIC/Na-magadiite and PIC/$C_{12}TMA$-magadiite-2.4 showed different microstructures.   The microstructure of the PIC aggregates was also controlled in the interlayer spaces when alkylammonium cations coexisted.

2.2.6. References

(1) J.-M. Lehn, *Supramolecular Chemistry: Concepts and Perspectives*. (Wiley-VCH, Weinheim, 1995).

(2) E. E. Jelley, *Nature*, 1009 (1936).

(3) G. Scheibe, *Angew. Chem.,* **49**, 563 (1936).

(4) T. Tani, *J. Imaging Sci.,* **64**, 143 (1990).

(5) Y. Wang, *J. Opt. Soc. Am. B*, **8**, 981 (1991).

(6) A. A. Muenter, D. V. Brumbaugh, J. Apolito, L. A. Horn, F. C. Spano, S. Mukamel, *J. Phys. Chem.,* **96**, 2783 (1992).

(7) T. Tanaka, T. Matsubara, *J. Imaging Sci. Technol.,* **38**, 495 (1994).

(8) M. Lindrum, I. Y. Chan, *J. Chem. Phys.,* **104**, 5359 (1996).

(9) M. Ogawa, R. Kawai, K. Kuroda, *J. Phys. Chem.,* **100**, 16218 (1996).

(10) N. Miyamoto, R. Kawai, K. Kuroda, M. Ogawa, *Appl. Clay. Sci.,* **16**, 161 (2000).

(11) M. S. Whittingham, A. J. Jacobson, *Intercalation Chemistry.* M. S. Whittingham, A. J. Jacobson, Eds. (Academic Press, New York, 1982).

(12) J. K. Thomas, *Acc. Chem. Res.,* **21**, 275 (1988).

(13) M. Ogawa, K. Kuroda, *Chem. Rev.,* **95**, 399 (1995).

(14) Tani, *Photogr. Sci. Eng.,* **16**, 163 (1972).

(15) H. Stiel, S. Daehne, K. Teuchner, *J. Lumin.,* **39**, 351 (1988).

(16) J. E. Maskasky, *J. Imaging Sci.,* **35**, 29 (1991).

(17) H. P. Eugster, *Science,* **157**, 1177 (1967).

(18) G. Lagaly, K. Beneke, A. Weiss, *Am. Miner.,* **60**, 642 (1975).

(19) G. Lagaly, K. Beneke, A. Weiss, *Am. Miner.,* **60**, 650 (1975).

(20) J. S. Dailey, T. J. Pinnavaia, *J. Inclusion Phenom. Mol. Recogn. Chem.,* **13**, 47 (1992).

(21) K. Kosuge, A. Yamazaki, A. Tsunashima, R. Otsuka, *J. Ceram. Soc. Jpn.,* **100**, 326 (1992).

(22) J. M. Rojo, E. Ruiz-Hitzky, J. Sanz, *Inorg. Chem.,* **27**, 2785 (1988).

(23) M. Ogawa, N. Maeda, *Clay Miner.,* **33** (1998).

(24) M. Ogawa, Y. Takizawa, *Chem. Mater.,* **11**, 30 (1999).

(25) A. H. Herz, *Adv. Colloid Interface Sci.*, **8**, 237 (1977).

(26) E. D. McRae, M. Kasha, *J. Chem. Phys.*, **28**, 721 (1958).

(27) L. J. E. Hofer, R. J. Grabenstetter, E. O. Wiig, *J. Am. Chem. Soc.*, **72**, 203 (1950).

(28) C. J. Tredwell, C. M. Kealy, *Chem. Phys.*, **43**, 307 (1979).

CHAPTER 3

UNI-DIRECTIONAL ORIENTATION OF CYANINE DYE AGGREGATES ON $K_4Nb_6O_{17}$ SINGLE CRYSTAL

3. Uni-Directional Orientation of Cyanine Dye Aggregates on $K_4Nb_6O_{17}$ Single Crystal

3.1. Introduction

Organized molecular assemblies with defined geometry are of great interest from scientific and technological viewpoints. Such systems have been constructed by 'crystal engineering'[1] or self-assembly of Langmuir-Blodgett films, micelles, vesicles through molecular design, as well as by immobilization of molecular component on organic (DNA, cellulose, dendrimer, etc.) and inorganic matrixes (layered solids, zeolites, etc.) Immobilization of an organic molecule within low-dimensional inorganic framework is a promising methodology.[2-4] Among possible inorganic matrices, layered materials are advantageous to fabricate multi-layered structures, 'intercalation compounds', with expandable interlayer distance. Oriented thin films of layered materials were constructed to exploit the anisotropic nature and to use the intercalation compounds as optical and electronic devices[5-7] However, there remains difficulty to control in-plane orientation of the components.

Here, supramolecular structures with three-dimensional anisotropy are fabricated by taking advantage of the in-plane anisotropy of the layered niobate $K_4Nb_6O_{17}$[8-10] (Figure 1a). Cyanine dyes (Scheme 1) were adsorbed on single crystals of $K_4Nb_6O_{17}$ and the orientations of the dyes were revealed by polarized spectra. Cyanine dyes were used as probes to examine the orientation and the aggregation, since the dyes form low-dimensional aggregates whose arrangements, e.g. J-, H- and herringbone aggregates and orientations are identified by polarized UV-visible spectra.[11]

3.2. Experimental

Sample Preparation

Single crystals of $K_4Nb_6O_{17}$ were grown by a flux-method reported previously.[8,9] The powders of Nb_2O_5 and K_2CO_3 were mixed in the molar ratio of 1.0: 1.1. The mixture was placed in a Pt crucible (10 cm in diameter and 5 cm in depth for 10 - 30 g of the mixture), and heated to 1150 ℃ at the rate of 5 ℃ min^{-1}. After heating at 1150

°C for 10 h, the mixture was slowly cooled down to 800 °C at the rate of 0.3 °C min^{-1} and to RT at the rate of 5 °C min^{-1}. Typically, ca. 4 g of $K_4Nb_6O_{17}$ crystals was obtained from 30 g of the mixture. The crystal was cleaved along *ac*-plane and cut along *a*- and *c*-axes[9] into platy rectangular solids with the size of several mm^2 and the thickness of ca 0.1 mm (Figure 1b). The formation of $K_4Nb_6O_{17}$ was confirmed by XRD analysis.

The crystals were allowed to react with solutions of the dyes (1:1 mixture of water and ethanol). Typically, 0.003-0.008 g of the $K_4Nb_6O_{17}$ crystal and 8 dm^{-3} of the dye solution (6.25×10^{-4} mol dm^{-3}) were sealed in a screw capped glass tube and allowed to stand for 5-6 days at 60 °C, followed by washing the colored crystal with acetone or ethanol. Although many cracks stemmed on the crystals after the reactions, the rectangular shapes of the host crystals were retained so that crystallographic directions were refined by XRD analysis.

n = 0,1, 2 for dye-1, -2, -3   Et = ethyl
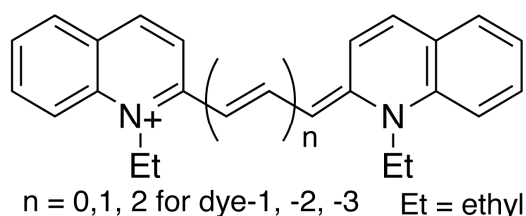
Scheme 1. Dyes used in this study

(a)   (b)
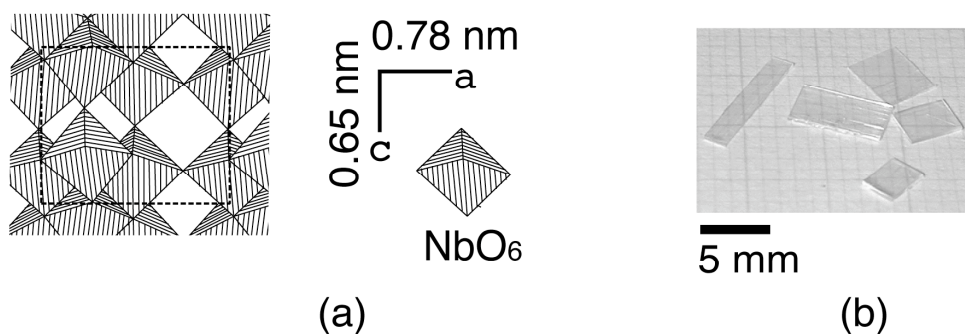
Figure 1. (a) The surface structure of $K_4Nb_6O_{17}$ cleaved from 'interlayer I' and (b) photograph of single crystals of $K_4Nb_6O_{17}$.

Characterizations

The XRD patterns of the $K_4Nb_6O_{17}$ crystals before and after the adsorption of the dyes were recorded on a Mac Science MXP[3] diffractometer with monochromated CuKα radiation (the tube voltage and current are 40 kV and 30 mA). The crystals were fixed in the sample chamber by using a double-faced tape and the XRD patterns were measured from three orthogonal edges to refine the crystallographic directions of the crystals (Figure 2).
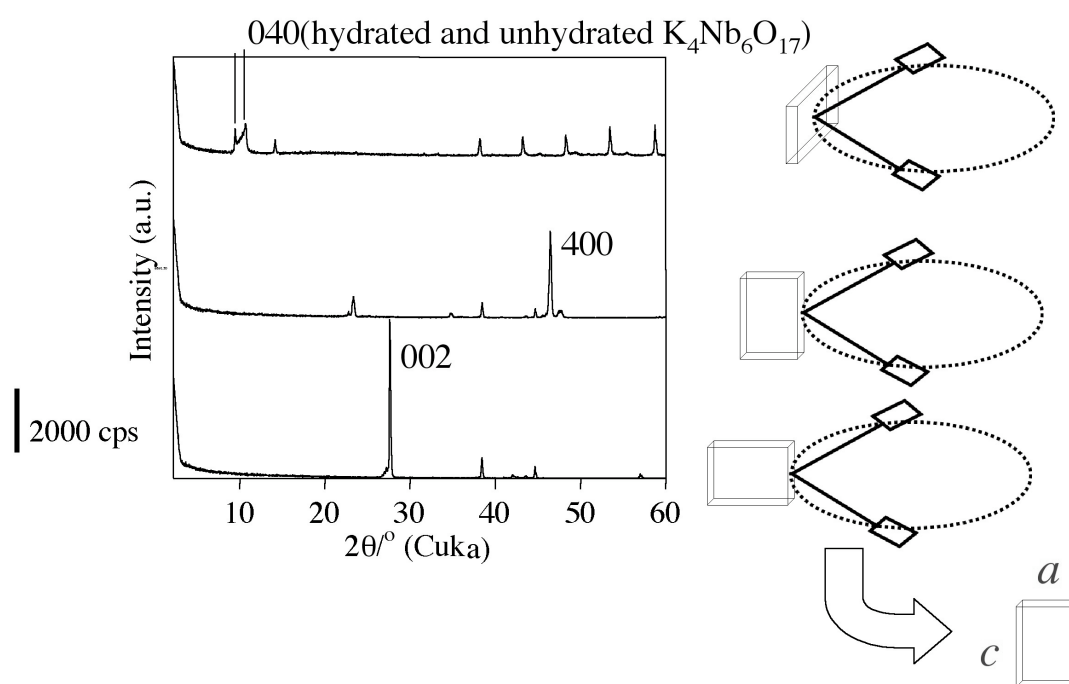
Figure 2. Refinement of the crystallographic axis of the single crystalline $K_4Nb_6O_{17}$ by XRD measurement on different surfaces.

The visible absorption spectra were measured with a Shimadzu UV-2500PC spectrophotometer attached with a polarizer (Figure 3). A colored crystal was fixed in the sample chamber, whereas the polarizer was rotated so that the angle α between the fixed *c*-axis of the crystal and the polarized direction of the incident light was varied. A depolarizer was placed between the incident light and the sample to obtain non-polarized light for the measurement. Also, the spectra were measured without the sample at each α; these back-ground spectra were subtracted from the spectra of the samples to cancel the polarized properties of the photomultiplier and polarizers. In the measurements of **dye-3** systems, the obtained spectra were considerably noisy due to the scattering and interference of the incident light caused by the cracks on the sample. Since the noises could not be removed experimentally, smoothing calculation was applied by calculating average of 69 points around the objective point; the obtain spectra were clear enough for the discussion without losing any accuracy. Polarized fluorescence spectra were recorded on a Hitachi F-4500 spectrofluorophotometer with the depolarizer and polarizer between the incident light; no polarizer was placed between the sample and photomultiplier. It must be noted that the sample is not set parallel to the polarizer for the fluorescence measurement in contrast with the setup for absorption spectra.
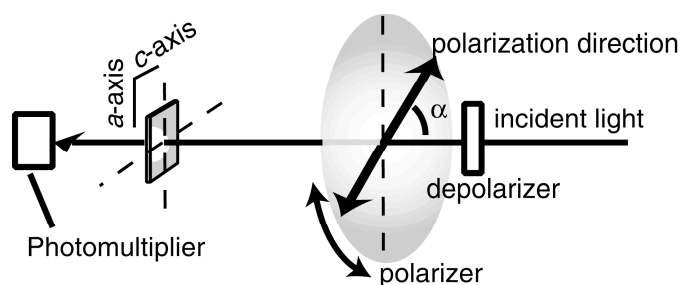
Figure 3. Experimental setup for polarized absorption spectroscopic measurement.

3.3. Results and Discussion

Aggregation and Orientation of 1,1'-diethyl-2,2'-cyanine on the Niobate Crystal

The polarized absorption spectra of **dye-1** adsorbed on $K_4Nb_6O_{17}$ are shown in Figure 4, where α represents the angle between the polarization direction and the *c*-axis of the crystal.   The absorption bands were centered at around 580 nm, which is red-shifted from that of the monomer band at 525 nm observed in a dilute aqueous solution of **dye-1**.   In the fluorescence spectrum (Figure 4, dotted line), the fluorescence band was centered at 595 nm.   The spectroscopic observations indicate that **dye-1** form J-aggregates.[11]   The monomer bands were absent in the spectra, indicating that most of **dye-1** were present as J-aggregates.
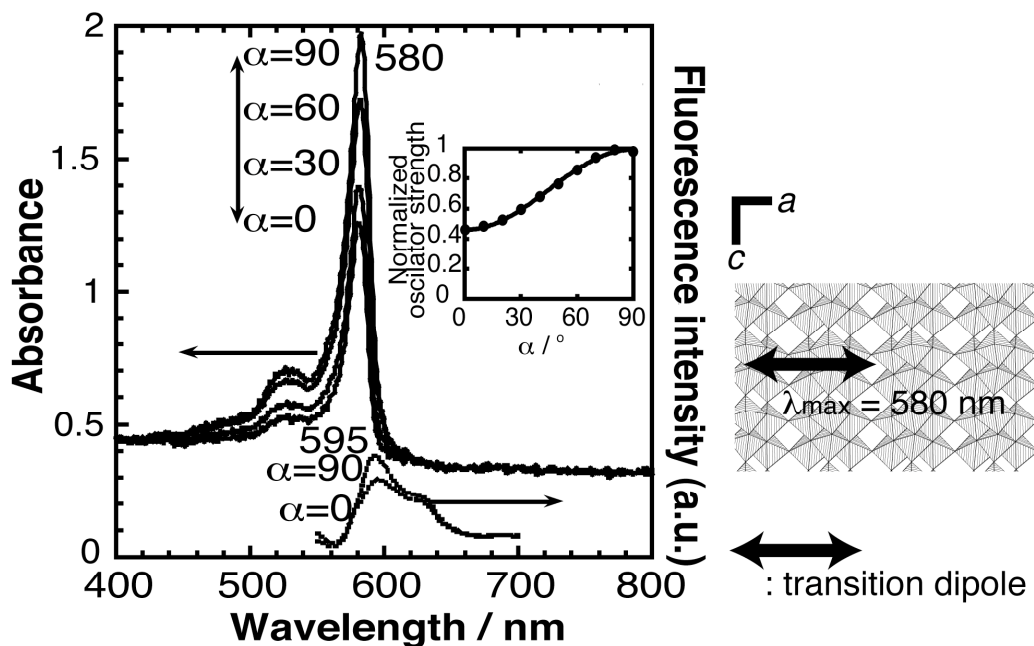
Figure 4.   Polarized absorption (solid lines) and fluorescence (dotted lines) spectra of **dye-1** adsorbed on $K_4Nb_6O_{17}$.   The inset represents normalized variation of oscillator strength at α.   The solid line is the theoretical curve.   Orientation of the transition dipole of the dye on $K_4Nb_6O_{17}$ is shown beside the spectra.

The absorbance and the fluorescence intensity varied depending on α, while the wavelengths of the absorption maxima were almost constant. The oscillator strength at α (f_a) was calculated by integrating the polarized spectrum at α over energy after removing background. Normalized variation of f_a with α is shown in the inset of Figure 4. Supposing that the dipoles of the J-aggregate were preferentially oriented along $\alpha = 90$ °, f_a is expressed by $f_a = (f_{90} - f_0) \sin^2\alpha + f_0$. The plot in Figure 4 coincided with the theoretical curve (solid line in the figure). The dipoles of the J-aggregates is parallel to the long axis of the dye cations.[12] Thus it was revealed that the dipoles of the J-aggregates and the long axis of the dye cations were oriented preferentially, although not perfectly, along the a-axis of $Nb_6O_{17}^{4-}$ sheets (Figure 4). The difference of the fluorescence intensities at $\alpha = 0$ and $\alpha = 90$ was smaller than the difference in the absorbance. This incompatibility is due to (1) the difference in the experimental setup and (2) the more complicated process for fluorescence.

It seems that the dye aggregates not only on the external surfaces but also in the interlayer spaces, although no remarkable change was found in the XRD patterns after the reactions in any present samples. Ogawa et al. have reported the formation of dye aggregates in the interlayer spaces of clays.[13] Adsorption of the dye aggregate in the interlayer spaces in the present system is plausible since (1) the basal spacing was expanded when microcrystalline $K_4Nb_6O_{17}$ was reacted with the dye and (2) every pieces obtained by slicing the colored samples along ac-plane, was similarly colored as exemplified by the photograph for the **dye-2** system (Figure 5).
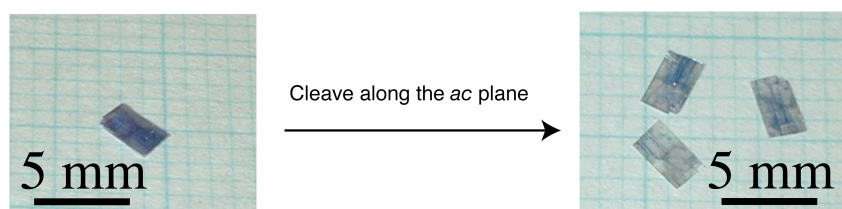
Figure 5. The photograph of $K_4Nb_6O_{17}$ crystals adsorbed with **dye-2.**

The adsorbed amount of **dye-1** was roughly estimated from the absorbance in the UV-visible spectra (A = up to 2), molar extinction coefficient of the J-aggregate ($\varepsilon = 2.6 \times 10^4$ mol^{-1}m^2),[12] the volume per 1 mol of $K_4Nb_6O_{17}$ ($V = 2.5 \times 10^{-4}$ m^{3}mol^{-1})[10] and the thickness of the sample (L = ca. 1×10^{-4} m).   The amount (= $V A / \varepsilon / L$) was estimated to be up to 2×10^{-4} molecules per the unit cell of $K_4Nb_6O_{17}$.   Because the amount is so small and the PICBr salt on the surface was washed off, it is plausible that the dye cations were adsorbed as a monolayer on the niobate sheet, rather than as PICBr salt.   Optical microscopic observation showed that the dye adsorption proceeded from edges and cracks so that the adsorption was inhomogeneous.

Aggregation and Orientation of 1,1'-diethyl-2,2'-carbocyanine and 1,1'-diethyl-2,2'-dicarbocyanine on the Niobate Crystal

Anisotropic absorption spectra were also observed when **dye-2** and **dye–3** were employed.   The polarized spectra of the **dye-2** system are shown in Figure 6a. At $\alpha = 0$ °, the absorption bands were observed at 648 nm and 604 nm.   These bands were red-shifted relative to the monomer band (600 nm).   At $\alpha = 90$ °, these bands were replaced by a new band at 502 nm.

The polarized spectra of the **dye-3** system are shown in Figure 6b.   It is remarkable that the orientation direction in the **dye-3** system is rotated by 90 ° compared to the **dye-2** system, although the spectra resemble to those of the **dye-2** system.   At α = 90 °, the absorption band was observed at 835 nm, which was red-shifted from the monomer band of this dye (700 nm).   As α decreases, this band gradually disappeared and a blue-shifted band emerged at 618 nm.

Possible interpretation for the spectra is the formation of herringbone-type aggregates with the stacking column direction parallel to the *a*- and *c*-axes for **dye-2** and **dye-3**, respectively.   Based on extended molecular exciton theory, herringbone-type aggregates show so-called 'Davydov splitting'.[14,15]   This is identified by the absorption bands which are red- and blue-shifted relative to a monomer band and are polarized perpendicularly to each other, as observed in the present **dye-2** and **dye-3** systems.
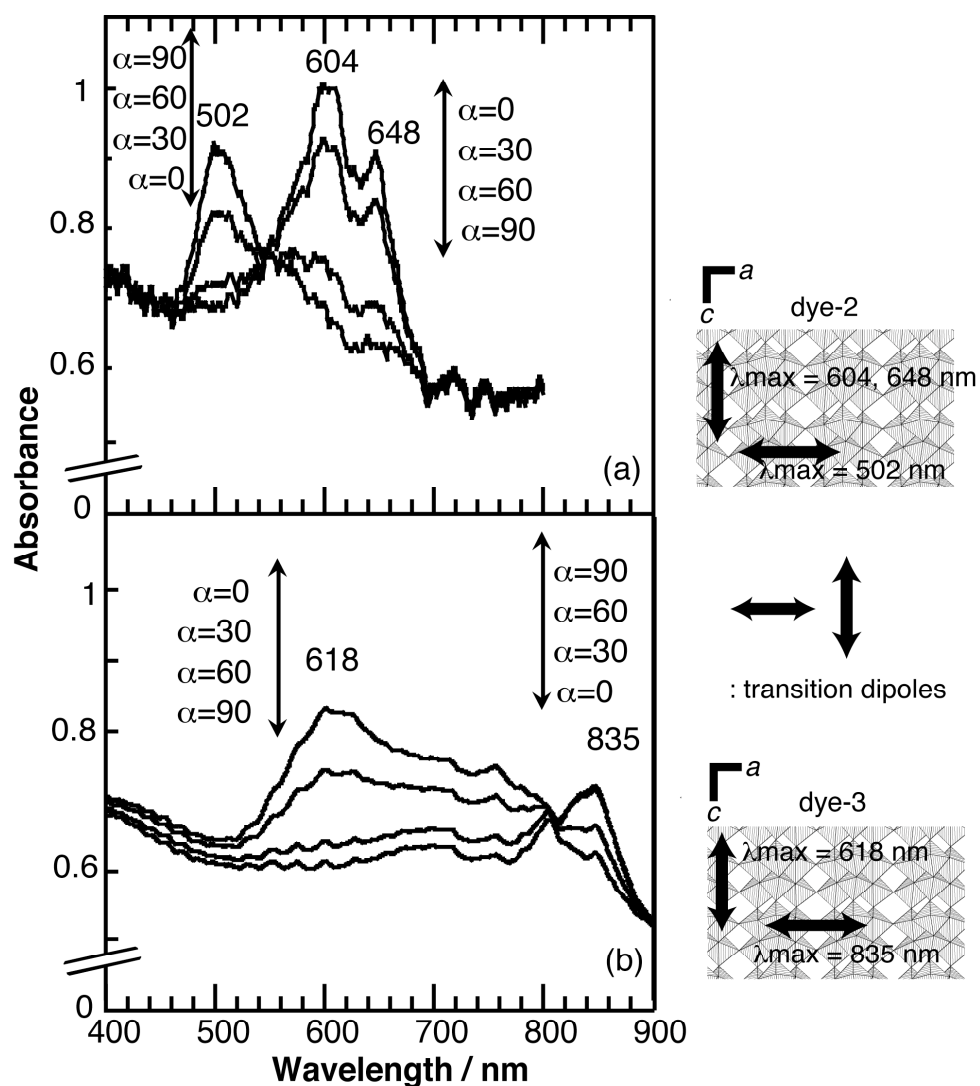
Figure 6. Polarized absorption spectra of (a) dye-2 and (b) dye-3 adsorbed on $K_4Nb_6O_{17}$. Orientations of the transition dipoles of the dyes on $K_4Nb_6O_{17}$ are shown beside the spectra. The spectra (b) were obtained after smoothing calculation.

Dichroism of the Samples

Dichroism (red/colorless, blue/red and green/colorless for **dye-1**, **dye-2** and **dye-3**, respectively) of the samples was observed by naked-eyes under polarized illuminations (Figure 7). Together with the spectroscopic results, it was evident that the aggregates of the cyanine dyes were oriented along crystallographic axes of $K_4Nb_6O_{17}$ over the whole crystal domain.

1 mm
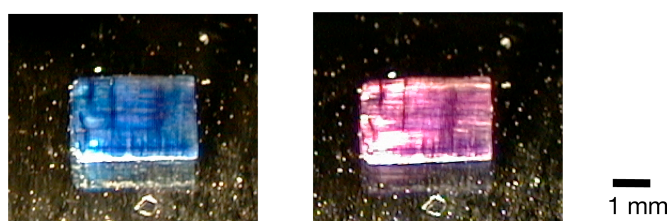
Figure 7. The photograph of $K_4Nb_6O_{17}$ crystal adsorbed with **dye-2** under polarized illuminations (left) parallel and (right) perpendicular to the c-axis of the niobate.

The Machanism of the Uni-directional Orientation

$K_4Nb_6O_{17}$ have an anisotropic surface (Figure 1a) with regularly arranged NbO^- groups which can act as cation exchange sites. The electrostatic interactions between the anionic sites and the positive charges on the dye cations should be responsible to the uni-directional orientation of the dye aggregates. Although the mechanism may be similar to those claimed in the reports on epitaxial growth of dye aggregates on $AgBr$[16] and mica,[17] the surface of $K_4Nb_6O_{17}$ is one-fold symmetric and anionic unlike those cases. It is possible that the periodic distance of the anionic sites matched (1) with the distance between the localized positive charges on the odd methine carbon of the dye cation[18,19] or (2) with the distance between adjacent dyes induced by cooperation of adsorption with aggregation since the microstructures of the aggregates are strongly directed by dye-dye interaction. Systematic studies with various guests and hosts and detailed spectroscopic characterization will clarify the mechanism further.

3.4. Conclusion

Supramolecular structures with three-dimensional anisotropy were fabricated by taking advantage of the in-plane anisotropy of $K_4Nb_6O_{17}$[8-10] (Figure 1a). Polarized spectra as well as dichroism observed under polarized illuminations revealed that J-aggregate of dye-1 and herringbone-type aggregates of dye-2 and –3 were uni-directionally oriented along crystallographic axes of $K_4Nb_6O_{17}$ over the whole crystal surface of $K_4Nb_6O_{17}$. Optical properties of dye aggregates are of great interest as model systems of low-dimensional excitons, which bring about useful optical properties.[11,20] The present system with well-defined geometry is preferable for detailed studies on photophysics of dye aggregates using polarized light.[21] The present success in uni-directional control of the dye orientation inside the matrix may lead to future three-dimensional supramolecular devices.

3.5. References

(1) G. R. Desiraju, *Chem. Commun.*, 1475 (1997).

(2) G. A. Ozin, *Adv. Mater.*, **4**, 612 (1992).

(3) M. Ogawa; K. Kuroda, *Chem. Rev.,* **95**, 399 (1995).

(4) J. -F. Nicoud, *Science,* **263**, 636 (1994).

(5) M. Ogawa, M. Takahashi, K. Kuroda, *Chem. Mater.*, **6**, 715 (1994).

(6) R. Abe, M. Hara, J. N. Kondo, K. Domen, *Chem. Mater.*, **10**, 1647 (1998).

(7) (a) M. Fang, C. H. Kim, G. B. Saupe, H. –N. Kim, C. C. Waraksa, T. Miwa, A. Fujishima, T. E. Mallouk, *Chem. Mater.,* **11,** 1526 (1999).   (b) H. -N. Kim, S. W. Keller, T. E. Mallouk, *Chem. Mater.*, **9,** 1414 (1997).   (c) S. W. Keller, H. -N. Kim, T. E. Mallouk, *J. Am. Chem. Soc.,* **116**, 8817 (1994).

(8) M. Gasperin, M.T. L. Bihan, *J. Solid State Chem.*, **43**, 346 (1982).

(9) K. Nassau, J. W. Shiever, J. L. Bernstein, *J. Electrochem. Soc.,* **116**, 348 (1969).

(10) G. B. Saupe, C. C. Waraksa, H. -N. Kim, Y. J. Han, D. M. Kaschk, D. M. Skinner, T. E. Mallouk, *Chem. Mater.*, **12**, 1556 (2000).

(11) T. Kobayashi, *J-aggregates*; World Scientific Publishing: Singapore (1996).

(12) E. Daltrozzo, G. Schiebe, K. Gschwind, F. Haimerl, *Photogr. Sci. Eng.*, **18**, 441 (1974).

(13) M. Ogawa, R. Kawai, K. Kuroda, *J. Phys. Chem.* **100**, 16218 (1996).

(14) A. S. Davydov, *Theory of Molecular Excitons*; Pleum: New York, (1971).

(15) S. Kirstein, H. Möhwald, *Adv. Mater.*, **7**, 460 (1995).

(16) J. E. Maskasky, *Langmuir*, **7**, 407 (1991).

(17) M. Li, A. Wang, G. Mao, L. Dähne, *J. Phys. Chem. B*, **103**, 11161 (1999).

(18) R. Radeglia, E. Gey, T. Steiger, S. Kulpe, R. Lück, M. Ruthenberg, M. Stierl, *J. Prakt. Chem.,* **316**, 766 (1974).

(19) Y. Ferré, H. Larlvé, E.-J. Vincent, *Phtogr. Sci. Eng.,* **18**, 457 (1974).

(20) T. Tani, in *Photographic sensitivity -Theory and mechanism.* (Oxford, New York, 1995)

(21) (a) L. Dähne, *J. Am. Chem. Soc.,* **117**, 12855 (1995).   (b) S. Kirstein, H. Möhwald, *J. Chem. Phys.,* **103**, 826 (1995).   (c) K. Misawa, S. Machida, K. Horie, T.

Kobayashi, T. *J. Lumin*. **60**, 812 (1994). (d) K. Saito, K. Ikegami, S. Kuroda, M. Saito, Y. Tabe, M. Sugi, *J. Appl. Phys*. **68**, 1968 (1990).

CHAPTER 4

VISIBLE LIGHT INDUCED ELECTRON TRANSFER AND LONG-LIVED CHARGE SEPARATED STATE IN CYANINE DYE/LAYERED TITANATE INTERCALATION COMPOUNDS

4. Visible light induced electron transfer and long-lived charge separated state in cyanine dye/layered titanate intercalation compounds

4.1. Introduction

Hybridization of wide-bandgap semiconductors with sensitizing dyes is a promising way to modify the materials to be responsive to visible lights. Dye-sensitized solar cells and photocatalysts have been investigated aiming at utilizing the whole spectral range of solar light in the energy conversion systems. There have been so many publications on exploring new sensitizing dyes and complexations to construct hybrid materials. Microcrystalline semiconductor solar cells with ruthenium-polypyridine complexes as sensitizers are known examples.[1] Materials with controlled and defined nanostructures are valuable for fundamental studies of the photo processes in dye-sensitized semiconductor systems to optimize the materials performance.

Because several inorganic layered solids are usable to fabricate defined and organized multi-layered structures with guest species in a nanometer scale by intercalation,[2-4] the combination of sensitizing dyes with inorganic layered semiconducting solids is promising for fabricating desired electron-transfer systems. Layered titanates are suitable for such purposes because of their ion-exchange capability[5,6] and semiconductivity.[7,8] A series of layered titanates with variable chemical compositions and structures are available, so that systematic studies on the physicochemical properties have been possible.[7,9-24]

UV-light induced electron-transfer in the intercalation compounds of viologens with layered semiconductors (layered niobates and titanate)[9-11,13,15] was reported previously. Visible-light induced guest-to-host electron transfer was also reported. Tris(2,2'-bipyridine)ruthenium(II) complex cation (abbreviated as $[Ru(bpy)_3]^{2+}$)[18,23] was intercalated in the interlayer spaces of layered titanates and niobates, and the guest-to-host electron transfer induced by visible light was demonstrated, based on the fluorescence quenching. $[Ru(bpy)_3]^{2+}$ was also adsorbed on the external surfaces of layered niobates and titanates[7, 12, 20] and the sensitized photocatalytic properties were

investigated. Porphyrins have also been used as sensitizers.[21,22,24] However, long lived charge separated state of intercalation compounds induced by visible light has never been achieved, whereas the formation of unusually long-lived charge separated state was reported for $K_2La_2Ti_3O_{10}$ or the titanate doped with Pr^{3+}, Tb^{3+} ($\sim$ 10 min)[16] and for layered titanates and niobates intercalated with methylviologen ($>$ 1h).[9-11,13,15] $[Ru(bpy)_3]^{2+}$ and cationic porphyrins tend to aggregate when adsorbed to layered solids,[4] and the excited state of the dyes change upon aggregation. Therefore, the sensitizers were incorporated as monomers in the reported systems. However, certain kind of dyes such as covalently linked polynuclear complexes[25,26] and self-assembled dye aggregates[27,28] are known to show excellent sensitizing properties. The use of these dye aggregates as sensitizers in intercalation compounds would open up further variation and better properties.

In this chapter, preparation and photochemical characterization of cyanine dye/layered titanate intercalation compounds are described; the dye formed so-called J-aggregates in the interlayer space and acted as sensitizers. The guest-to-host electron transfer was induced by visible light and unusually long-lived charge separated state was achieved in these compounds. The layered titanates, $Na_2Ti_3O_7$ and $Cs_xTi_{2-x/4}\square_{x/4}O_4$ (Scheme 1) were used as the host materials. Two cyanine dyes (Scheme 2), 1,1'-diethyl-2,2'-cyanine (**dye-1**) and 5,5'-dichloro-3,3',9-triethyl-thiacarbocyanine (**dye-2**), were employed as the guest species because they form J-aggregates and are widely used as excellent sensitizers in silver bromide based photographic systems.[27,28]

4.2. Experimental

Materials

1,1'-diethyl-2,2'-cyanine bromide (**dye-1**, purity 99.9 %) and 5,5'-dichloro-3,3',9-triethyl-thiacarbocyanine iodide (**dye-2**, purity 97.8 %) were purchased from Hayashibara Biochemical Laboratories, Inc. and were used without further purification. The layered titanates were synthesized according to the reported solid-state reactions.[29,5,30] $Na_2Ti_3O_7$[29,5] was synthesized by heating a mixture of Na_2CO_3 and TiO_2 (anatase) in the molar ratio of 1.1 : 3 at 900 °C for 24 h, and then for another 24 h after

grinding. $Cs_xTi_{2-x/4}\square_{x/4}O_4$[30,31] was synthesized by heating a mixture of Cs_2CO_3 and TiO_2 in the molar ratio of 1 : 5.2 at 800 °C for 20 h.   The formation of the layered titanates was confirmed by XRD; most of the peaks coincided with those in the literatures.[5,31] Natural Na-montmorillonite (product of Tsukinuno mine, Japan; JCSS-3101, reference clay sample supplied from The Clay Science Society of Japan; cation exchange capacity is 119 meq/100 g clay) was used as received.
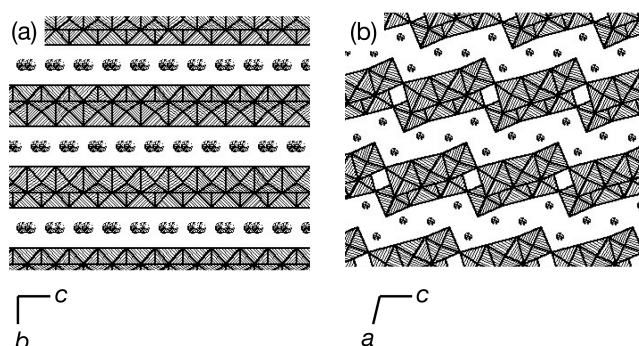
Scheme 1.   The layered titanates used in this study: (a) $Cs_xTi_{2-x/4}\square_{x/4}O_4$, and (b) $Na_2Ti_3O_7$.

1,1'-diethyl-2,2'-cyanine bromide (**dye-1**)

5,5'-dichloro-3,3',9-triethyl-thiacarbo cyanine bromide (**dye-2**)
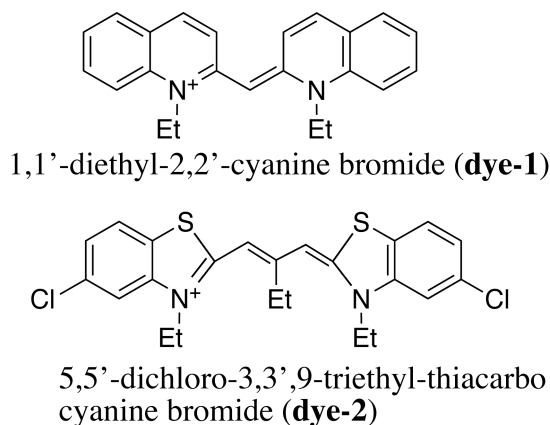
Scheme 2.   Dyes used in this study.

Intercalation of Alkylammonium Ions

Proton-exchanged layered titanates (H/Ti_3O_7 and $H/Ti_{2-x/4}\square_{x/4}O_4$) were obtained by the procedures similar to those reported previously.[5,31] The host materials were dispersed in 1 mol dm^{-3}-HCl in the ratios of 10 g host dm^{-3} for $Na_2Ti_3O_7$ and 50 g host dm^{-3} for $Cs_xTi_{2-x/4}\square_{x/4}O_4$, and the mixtures were magnetically stirred for 3 days at room temperature. Hydrochloric acid was replaced with fresh ones every day. The powder XRD patterns of the proton-exchanged forms were similar to those reported previously, showing the successful proton exchange.[5,31]

Intercalation of propylammonium and hexylammonium ions into H/Ti_3O_7 was conducted by a two-step reaction. H/Ti_3O_7 was sealed in a glass ampoule with an aqueous solution of methylamine (40 vol.- %) and was allowed to react at 60 °C for 6 days to obtain a methylammonium/Ti_3O_7 intercalation compound. The methylammonium/Ti_3O_7 was allowed to react with an aqueous solution of propylamine (50 vol.- %) or hexylamine (50 vol.- %) at 60 °C for 6 days to yield propylammonium/Ti_3O_7 and hexylammonium/Ti_3O_7 intercalation compounds. Propylammonium/$Ti_{2-x/4}\square_{x/4}O_4$ was synthesized by the reaction of an aqueous solution of propylamine (50 vol.- %) with $H/Ti_{2-x/4}\square_{x/4}O_4$ at 60 °C for 6 d. For all the reactions, excess amounts of the alkylammonium ions (the molar ratio of alkylammonium/H in titanates = 20) were used and the products were washed repeatedly with acetone to remove residual alkylamines.

Intercalation of the Dyes

Dye-1/Ti_3O_7 intercalation compound was synthesized by the reaction of the propylammonium/Ti_3O_7 intercalation compound with an aqueous solution of **dye-1** (5×10^{-5} mol dm^{-3}) at 60 °C for 6 days in a glass ampoule. **Dye-2**/Ti_3O_7 was obtained by the reaction of hexylammonium/Ti_3O_7 with a **dye-2** solution (5×10^{-5} mol dm^{-3}) in the mixture of methanol and water (50 vol.- %). **Dye-1**/$Ti_{2-x/4}\square_{x/4}O_4$ and **dye-2**/$Ti_{2-x/4}\square_{x/4}O_4$ were synthesized by the reactions of the dye solutions with propylammonium/$Ti_{2-x/4}\square_{x/4}O_4$ under the same condition. The molar ratios of dye/[Ti_3O_7] and dye/[$Ti_{2-x/4}\square_{x/4}O_4$] in the mixtures were set to 0.3 - 0.45. The reaction

with larger amounts of the dyes did not lead to further increase in the adsorbed amounts of the dyes, indicating that the intercalation reaction proceeded to the point where the available interlayer space is fully occupied by the dye rather than quantitatively. Intercalation of **dye-1** and **dye-2** into Na-montmorillonite was conducted by dispersing the host in the dye solutions and stirring the mixture at room temperature for 1 d.   All the samples were washed with acetone to remove residual dyes until the supernatant after centrifugation became colorless.

Characterizations

XRD patterns of the powder samples were measured on a Mac Science MXP[3] diffractometer with monochromated CuKα radiation at the tube voltage of 40 kV and the current of 30 mA.   CHN analysis was performed to determine the adsorbed amounts of the alkylammonium ions and the dyes in the products with a Perkin Elmer PE-2400II instrument.   The UV-visible spectra were measured with a Shimadzu UV-2500PC spectrophotometer for aqueous suspensions containing 0.2 g dm^{-3} of the powder samples.   Fluorescence spectra of the suspensions were measured on a Hitachi FS-4500 fluorophotometer.   The excitation wavelengths were 490 and 590 nm for the **dye-1** and **dye-2** systems, respectively.   Light induced ESR spectra were taken with a JEOL JES-PX1060 electron spin resonance spectrometer under the irradiations of UV and visible lights to the powder samples.   The powders were placed in the bottom of a glass tube and stored in dark before the measurements in order to avoid the generation of radicals by environmental illuminations.   The ESR spectra were also measured under controlled temperature, using a JEOL JES-FA300 electron spin resonance spectrometer attached with an ES-DVT4 temperature controller.   The UV and visible lights were irradiated with a USHIO 100 W Xe-Lamp through a band-pass filter, HOYA U-340 (the transmittance centered at 350 nm) and a sharp-cut filter, HOYA L42 (cut-off wavelength is 420 nm), respectively.

4.3. Results

Syntheses of the Intercalation Compounds

The formation of the intermediates, alkylammonium-exchanged forms, was confirmed by XRD and elemental analyses. The basal spacings of propylammonium/Ti_3O_7, hexylammonium/Ti_3O_7 and propylammonium /$Ti_{2-x/4}\square_{x/4}O_4$ were 1.24 nm (Figure 1b), 2.07 nm (Figure 1d), and 1.03 nm (Figure 2b), respectively, and the values were expanded from those of the proton-exchanged forms (0.79 nm (Figure 1a) for H/Ti_3O_7 and 0.94 nm for H/$Ti_{2-x/4}\square_{x/4}O_4$ (Figure 2a)), indicating the formation of the alkylammonium-titanates intercalation compounds. The amounts of the intercalated alkylammonium ions were 0.31, 0.67 and 0.52 molecules per the formula units of the titanates for propylammonium /Ti_3O_7, hexylammonium/Ti_3O_7, and propylammonium /$Ti_{2-x/4}\square_{x/4}O_4$, respectively.

It must be noted that the reaction of H/Ti_3O_7 with propylammonium solution yielded incompletely exchanged propylammonium/Ti_3O_7 with remaining H/Ti_3O_7 phase even when the reactions were prolonged to 3 weeks or repeated. In contrast, the reaction of H/Ti_3O_7 with methylammonium solution proceeded almost completely and the following reaction of methylammonium/Ti_3O_7 with propylammonium solution yielded propylammonium/Ti_3O_7 containing with no remaining H/Ti_3O_7. The difference in pK_b values between the organoamines can be a factor to determine the reactivity because the reactions of H/Ti_3O_7 with organoamines proceed in terms of the acid-base reaction. However, the pK_b values are not considerably different (4.5 $\times 10^{-4}$ and 4.1 $\times 10^{-4}$ for methylamine and propylamine, respectively), so it is probable that smaller methylammonium more easily penetrates into the interlayer space than propylammonium.

The XRD patterns of the dye/layered titanate intercalation compounds show that, after the reactions with the dyes, the d-values were varied to 1.70 nm (Figure 1c), 1.63 nm (Figure 1e), 1.57 nm (Figure 2c) and 1.71 nm (Figure 2d) for **dye-1**/Ti_3O_7, **dye-2**/Ti_3O_7, **dye-1**/$Ti_{2-x/4}\square_{x/4}O_4$ and **dye-2**/$Ti_{2-x/4}\square_{x/4}O_4$, respectively, indicating the successful formation of the intercalation compounds. Supposing that all the C atoms are derived from the dyes (i.e. all the alkylammonium cations were displaced by the

dyes and protons), the amounts of the adsorbed dyes were determined to be 0.20, 0.13, 0.23 and 0.14 molecules per the formula units of the hosts (or 69, 60, 89, and 45 mmol/100g of the samples), for **dye-1**/Ti_3O_7, **dye-2**/Ti_3O_7, **dye-1**/$Ti_{2-x/4}\square_{x/4}O_4$, and **dye-2**/$Ti_{2-x/4}\square_{x/4}O_4$, respectively.

Pre-intercalation of alkylammonium ion is necessary for intercalation of the dyes in all the systems. **Dye-1** was not intercalated to $Na_2Ti_3O_7$, H/Ti_3O_7, and methylammonium/Ti_3O_7; the use of the intermediate, propylammonium/Ti_3O_7, led the successful intercalation.[32] The use of intermediate also promoted the intercalation of the dyes into $Cs_xTi_{2-x/4}\square_{x/4}O_4$; the intercalation of **dye-1** and **dye-2** into $Cs_x/Ti_{2-x/4}\square_{x/4}O_4$ was successful when propylammonium/$Ti_{2-x/4}\square_{x/4}O_4$ was used as the host material, while they were not intercalated directly into $Cs_xTi_{2-x/4}\square_{x/4}O_4$ and $H/Ti_{2-x/4}\square_{x/4}O_4$. Intercalation of **dye-2** into $Na_2Ti_3O_7$ was achieved only when hexylammonium/Ti_3O_7 was used as the intermediate. The intercalation was unsuccessful when propylammonium/Ti_3O_7 was used. Higher hydrophobicity and sufficient expansion of the interlayer space are thought to be responsible for the reactivities.

The formation of the **dye-1**/montmorillonite and **dye-2**/montmorillonite intercalation compounds was shown by XRD and CHN analyses. The basal spacing increased from 1.3 nm (Na-montmorillonite) to 1.7 nm and 1.6 nm for the **dye-1** and **dye-2** systems, respectively; the value for **dye-1** is in accordance with the reported value, indicating the intercalation of the dye.[33] The adsorbed amounts of the dyes were determined to be 80 and 39 mmol per 100g of the **dye-1/** and **dye-2**/montmorillonite intercalation compounds, respectively.
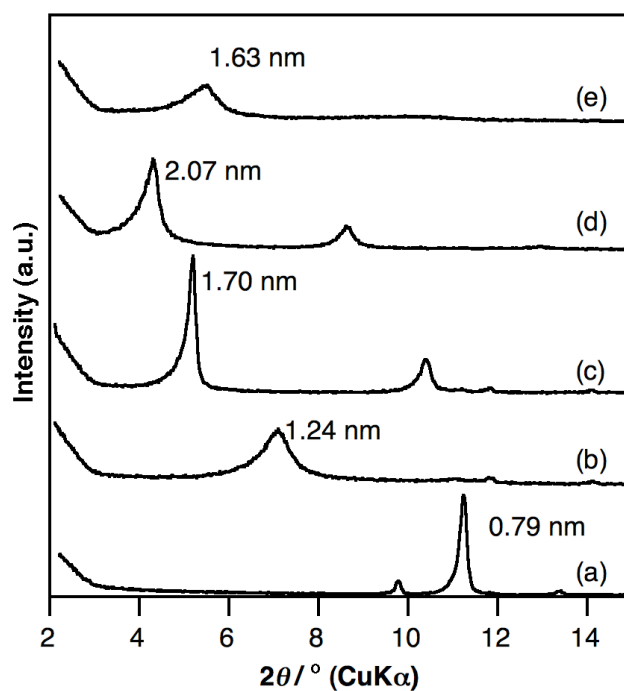
Figure 1. XRD patterns of (a) H/Ti_3O_7, (b) propylammonium/Ti_3O_7, (c) **dye-1**/Ti_3O_7, (d) hexylammonium /Ti_3O_7 and (e) **dye-2**/Ti_3O_7.
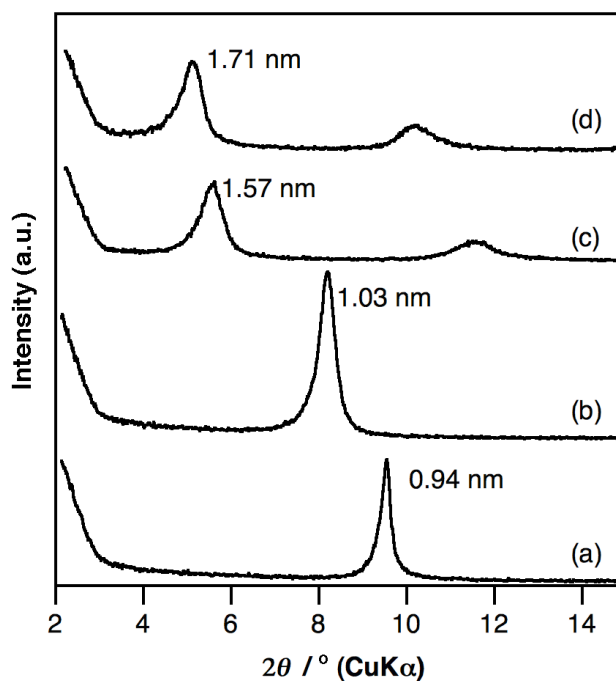
Figure 2. XRD patterns of (a) $H/Ti_{2-x/4}\square_{x/4}O_4$, (b) propylammonium/$Ti_{2-x/4}\square_{x/4}O_4$, (c) **dye-1**/$Ti_{2-x/4}\square_{x/4}O_4$ and (d) **dye-2**/$Ti_{2-x/4}\square_{x/4}O_4$.

UV-Visible Spectra

The UV-visible absorption spectra revealed the formation of J-aggregates of the dyes in the interlayer spaces of the intercalation compounds.   In the spectra of **dye-1**/Ti_3O_7 (Figure 3a), **dye-1**/$Ti_{2-x/4}\square_{x/4}O_4$ (Figure 3b) and **dye-1**/montmorillonite (Figure 3c), the sharp absorption bands were observed at around 579, 583 and 576 nm, respectively, which were remarkably red-shifted relative to the monomer band (523 nm) observed in a dilute (5 $\times 10^{-5}$ mol dm^{-3}) aqueous solution of **dye-1**.   It is well established that J-aggregates of cyanine dyes show red-shifted absorption bands relative to the monomer bands due to exciton coupling.[28]   The observed red-shifted bands (Figures 3a-c) are attributed to the J-aggregates of **dye-1**.   Also, weak fluorescence bands were observed at around 590 nm as shown later in Figure 5, confirming the formation of J-aggregates.

The formation of J-aggregates of **dye-2** in the interlayer spaces was also proved by the UV-visible spectra.   While the monomer band is observed at 553 nm in a dilute (4 $\times 10^{-6}$ mol dm^{-3}) methanol solution of the dye, the absorption maxima were observed at relatively longer wavelengths (648, 625 and 626 nm for **dye-2**/Ti_3O_7 (Figure 4a), **dye**-2/$Ti_{2-x/4}\square_{x/4}O_4$ (Figure 4b) and **dye-2**/montmorillonite (Figure 4c), respectively), indicating the formation of J-aggregates.
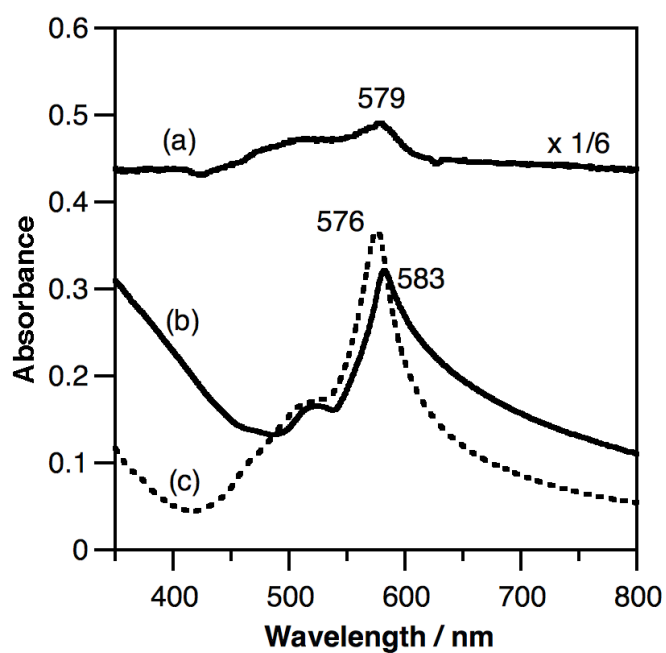
Figure 3. Visible absorption spectra of aqueous suspensions of (a) **dye-1**/Ti_3O_7, (b) **dye-1**/$Ti_{2-x/4}\square_{x/4}O_4$, and (c) **dye-1**/montmorillonite.
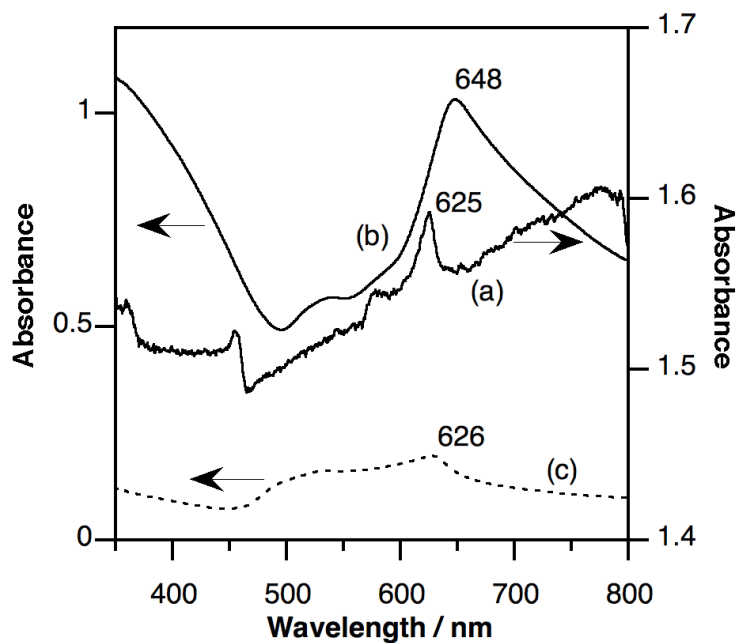
Figure 4. Visible absorption spectra of aqueous suspensions of (a) **dye-2**/Ti_3O_7, (b) **dye-2**/$Ti_{2-x/4}\square_{x/4}O_4$, and (c) **dye-2**/montmorillonite.

Figure 5 shows the fluorescence spectra of **dye-1**/Ti_3O_7, **dye-1**/$Ti_{2-x/4}\square_{x/4}O_4$ and **dye-1**/motmorillonite.   The observed band around 587 nm (Figure 5a and b) and 580 nm (Figure 5c) are ascribed to the resonance emission from the J-aggregates. Remarkably, the fluorescence intensities were much weaker for **dye-1**/Ti_3O_7 and **dye-1**/$Ti_{2-x/4}\square_{x/4}O_4$ compared to **dye-1**/motmorillonite, indicating that the fluorescence was quenched in the titanate systems.   In the **dye-2** systems, the fluorescence from the J-aggregates was observed only for **dye-2**/montmorillonite at 633 nm (Figure 6c), while the fluorescence was thoroughly quenched for the **dye-2**/Ti_3O_7 and **dye-2**/$Ti_{2-x/4}\square_{x/4}O_4$ systems (Figures 6a and b).

It must be noted that fluorescence spectra are normally altered at higher concentrations by re-absorption of the fluorescence and scattering of excitation and fluorescence lights.   The spectra shown above were measured at the sufficiently low concentrations where such effects were negligible; the spectra of the suspensions with varied concentrations were preliminary measured to check the effects (Figure 7).   The concentrations of the dyes used for the measurement of Figures 5 and 6 were in sufficiently narrow ranges (1.4×10^{-4} and 1.8×10^{-4} mol dm^{-3} for the **dye-1** systems and 0.8×10^{-4} and 1.2×10^{-4} mol dm^{-3} for the **dye-2** systems), allowing us to compare the fluorescence intensities.
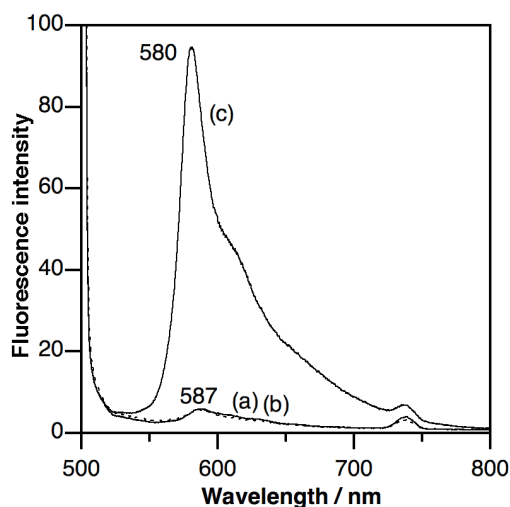
Figure 5.   Fluorescence spectra of (a) **dye-1**/Ti_3O_7, (b) **dye-1**/$Ti_{2-x/4}\square_{x/4}O_4$, and (c) **dye-1**/montmorillonite.
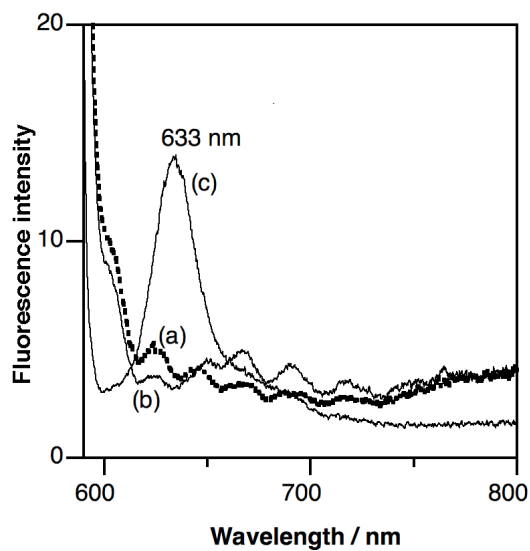
Figure 6. Fluorescence spectra of (a) **dye-2**/Ti_3O_7, (b) **dye-2**/$Ti_{2-x/4}\square_{x/4}O_4$, and (c) **dye-2**/montmorillonite.
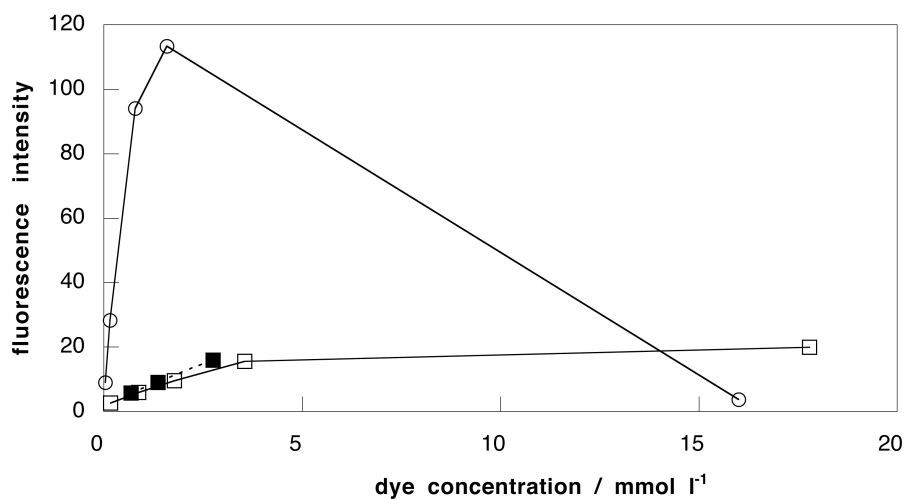
Figure 7. Relationship between the dye concentration and fluorescence intensity observed in (open rectangle) **dye-1**/$Ti_{2-x/4}\square_{x/4}O_4$, (filled rectangle) **dye-1**/Ti_3O_7 and (open circle) **dye-1**/motnmorillonite.

Visible Light-Induced ESR Signals

The ESR spectra of **dye-1**/Ti_3O_7 and **dye-1**/$Ti_{2-x/4}\square_{x/4}O_4$ before and after the visible light irradiation are shown in Figure 8. In both the systems, the ESR signals emerged upon the irradiation of the visible light. The ESR signal observed for the **dye-1**/$Ti_{2-x/4}\square_{x/4}O_4$ system (Figure 8d) was isotropic with g-value of 2.002, while the signal was anisotropic with the peaks at g = 2.028, 2.009, and 2.002 for the **dye-1**/Ti_3O_7 system (Figure 8b). The g-values are typical of free radicals of organic species, and light-induced ESR signals[34-37] of various cyanine dye/AgBr systems had been observed and studied in detail. Therefore, the signals observed here are ascribed to dication radicals of cyanine dyes. The difference in the shapes of the spectra is thought to reflect different nanostructures of the intercalation compounds. The visible-light induced ESR signals were also observed for the **dye-2** systems (Figure 9). The spectra for the **dye-2** systems were almost isotropic with the g-values of 2.002, similar to the one observed for the **dye-1**/$Ti_{2-x/4}\square_{x/4}O_4$ system.

In contrast to the above results, light induced ESR signal was not observed for the compounds without the dyes (H/Ti_3O_7, H/$Ti_{2-x/4}\square_{x/4}O_4$, propylammonium /$Ti_3O_7$ and propylammonium/$Ti_{2-x/4}\square_{x/4}O_4$) and for **dye-1**/ and **dye-2**/montmorillonite intercalation compounds. ESR signal was not observed for crystals of **dye-1** and **dye-2**. The UV light irradiation, instead of the visible light, gave only very small responses in the ESR spectra for all the dye/titanate systems.
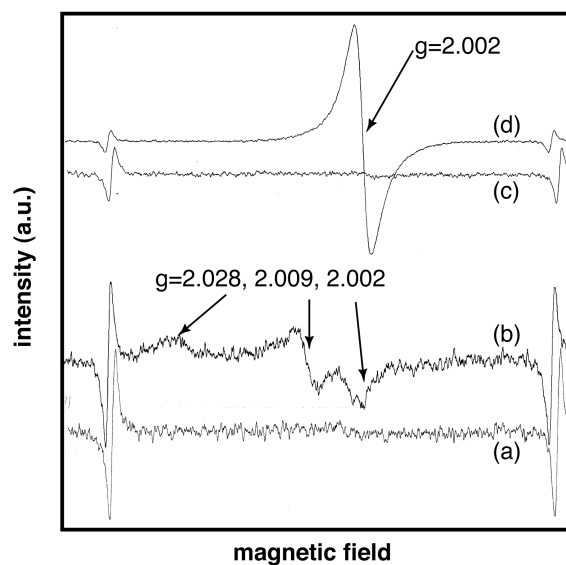
Figure 8. ESR spectra of (a)(b) **dye-1**/Ti_3O_7 and (c)(d) **dye-1**/$Ti_{2-x/4}\square_{x/4}O_4$. The spectra were measured (a)(c) before and (b)(d) after the irradiation of visible light.
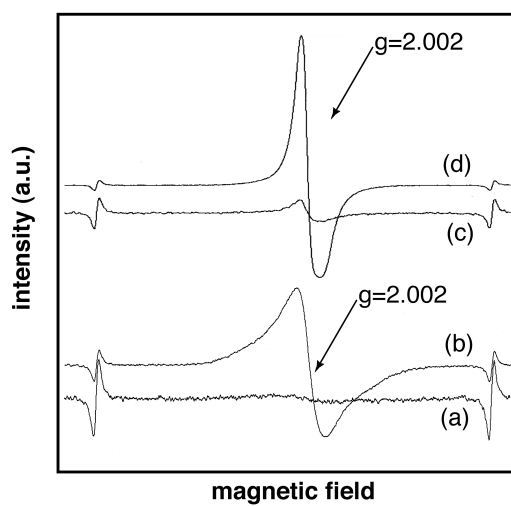
Figure 9. ESR spectra of (a)(b) **dye-2**/Ti_3O_7 and (c)(d) **dye-2**/$Ti_{2-x/4}\square_{x/4}O_4$. The spectra were measured (a)(c) before and (b)(d) after the irradiation of visible light.

111

The ESR signals began to grow just after the beginning of the irradiation and the intensity increased up to the saturation points after 15-30 min. After terminating the irradiation, the signals immediately began to decay. The decay curves of the ESR signals in the **dye-1**/Ti_3O_7, **dye-2**/Ti_3O_7, **dye-1**/$Ti_{2-x/4}\square_{x/4}O_4$, and **dye-2**/$Ti_{2-x/4}\square_{x/4}O_4$ systems are shown in Figure 10a, b, c, and d as semi-log plots. By fitting the decay curves as single-exponential or double-exponential decay, the apparent lifetimes of the charge separated states were estimated as shown in Table 1. The apparent lifetimes ranged from several minutes to hours (246 min), depending on the dye and the host: the charge separated state was more stable in the **dye-2** systems than **dye-1** systems and in the $Cs_xTi_{2-x/4}\square_{x/4}O_4$ systems than in the Ti_3O_7 systems. An N_2 purged sample was also tested for the **dye-2**/Ti_3O_7, but no remarkable difference was found in the spectrum and the decay curve is comparable to that for the sample in air.

The decay rate of the ESR signals varied depending on the temperature. Figure 11 shows the relationship (Arrhenius plot) between the temperature and the decay rate of the ESR signal intensity determined for the **dye-1**/$Ti_{2-x/4}\square_{x/4}O_4$ system. The apparent decay rate significantly dropped at lower temperature.
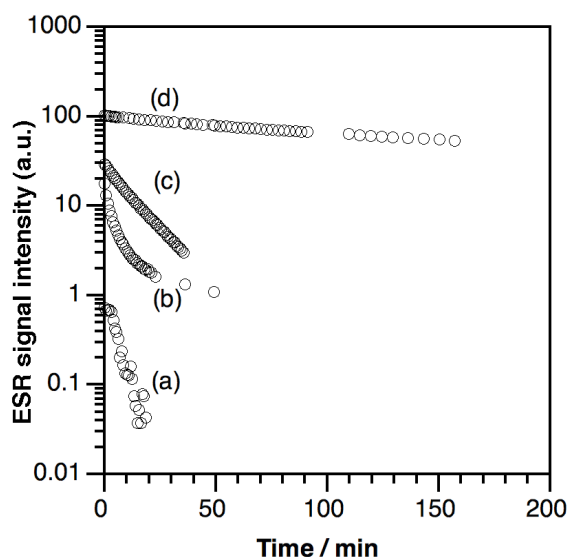
Figure 10. Decay curves of the ESR signal intensities of (a) **dye-1**/Ti_3O_7, (b) **dye-2**/Ti_3O_7, (c) **dye-1**/$Ti_{2-x/4}\square_{x/4}O_4$, and (d) **dye-2**/$Ti_{2-x/4}\square_{x/4}O_4$.

Table 1. The average life-time of the charge separated states.

sample	lifetime / min
dye-1/Ti_3O_7	6
dye-2/Ti_3O_7	22 (27 %), 2 (73 %)
dye-1/$Ti_{2-x/4}\square_{x/4}O_4$	17
dye-2/$Ti_{2-x/4}\square_{x/4}O_4$	246
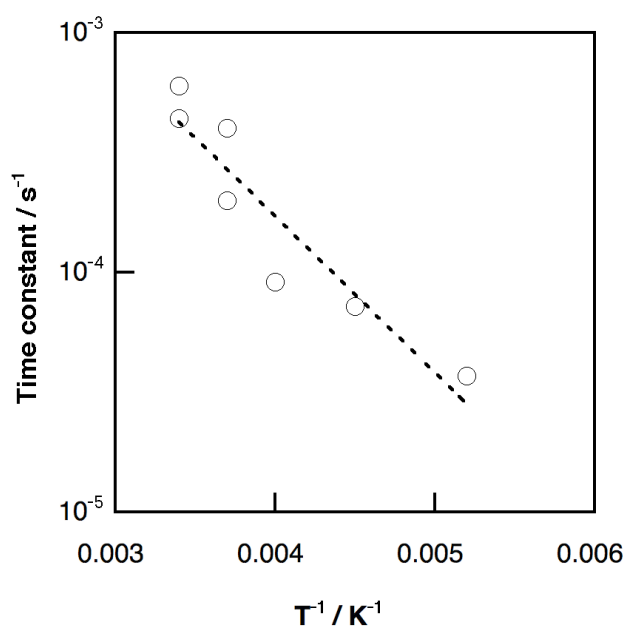
Figure 11. Relationship between reciprocal temperature and time constant of the decay of the ESR signal intensity after terminating visible light irradiation to dye-1/$Ti_{2-x/4}\square_{x/4}O_4$.

4.4. Discussion

The Nanostructures of the Products

The nanostructures of the products are inferred from the XRD data, UV-visible spectra, elemental analyses, and the sizes of the dyes. The gallery height of **dye-1**/$Ti_{2-x/4}\square_{x/4}O_4$ is calculated to be 0.91 nm by subtracting the basal spacing of dehydrated $H/Ti_{2-x/4}\square_{x/4}O_4$ (0.66 nm) from the observed basal spacing (1.57 nm). Since the size of the dye is $0.4 \times 1.5 \times 0.8$ nm^3, two structural models are possible: one is the model where the dye is present as a single molecular layer with its shorter axis of the molecular plane almost perpendicular to the titanate sheet, and the other is the model where the dye is present as a bilayer with its molecular plane parallel to the titanate sheet. Since **dye-1** is present as J-aggregate, as has been revealed by the UV-visible spectra, the single layer model is more plausible; J-aggregate of cyanine dyes are thought to possess a two dimensional brick-stone structure where the dyes are stacked with the molecular planes flat to each other.[28] Assuming this orientation, the area occupied by the dye is estimated to be 0.24 nm^2 per the unit of $Ti_{2-x/4}\square_{x/4}O_4$. This value is comparable to the available surface area of the titanate, 0.23 nm^2 per the unit of $Ti_{2-x/4}\square_{x/4}O_4$ (= $2Zac$ = $2 \times 1 \times 0.383$ nm $\times$ 0.296 nm, where a and c are the lattice parameters of the titanate[30], Z (=1) is the number of $Ti_{2-x/4}\square_{x/4}O_4$ included in a unit cell), indicating that the dyes almost fully cover the interlayer surface. It is supposed that the incompatibility between the gallery height (0.91 nm) of the intercalation compound and the height of **dye-1** (0.8 nm) is due to the nanostructure of the dye aggregate; in the J-aggregate, the side chains are not on the same side, while the quinoline rings are overlapping,[38] resulting in the larger thickness of the aggregate layer than the height of a single dye molecule.

In the case of **dye-2**/$Ti_{2-x/4}\square_{x/4}O_4$, the intercalated amount of **dye-2** was smaller than that of **dye-1**; this is partly due to the larger size of **dye-2** ($0.3 \times 2.0 \times 0.8$ nm^3) than **dye-1**. However, the surface coverage is only 70 % if the orientation of the dye is assumed to be similar to the **dye-1** system. Judging from the fact that no larger amount of dye-2 was adsorbed by the reaction with larger amounts of the dye, the intercalation reaction should have proceeded to the point where the available interlayer

space is fully covered by the dye.   Supposing that the dye fully covered the layer surface, the shorter molecular plane of **dye-2** is thought to be inclined by about 50° to the host layer.

Similar nanostructures are also inferred for **dye-1**/Ti_3O_7 and **dye-2**/Ti_3O_7.   The gallery height is difficult to estimate for these systems since the layer is not a flat plate (Scheme 1b).   The gallery heights are roughly estimated as 0.91 and 0.84 nm, by subtracting the basal spacing of H/Ti_3O_7 (0.79 nm) from those of the products. Assuming that the available surface area on the titanate (0.35 nm^2 per the unit of Ti_3O_7 (= $2bc$ / Z = 2 × 0.38 nm × 0.91 nm / 2, where b and c are the lattice parameters of the titanate[29] and Z (= 2) is the number of Ti_3O_7 included in a unit cell)) is fully covered with the monomolecular layer of the dye, **dye-1** is packed with its shorter molecular axis almost perpendicular to the sheet, while **dye-2** is present with its shorter molecular axis inclined at ca. 60°, both forming J-aggregates.

The nanostructures of the dye aggregates can also affect the surface structure of the hosts.   As described in Chapter 3, the surface structure of a layered niobate $K_4Nb_6O_{17}$ affects the nanostructure and the orientation of the aggregate of **dye-1**.[39]   The difference in the layer structures between Ti_3O_7 and $Ti_{2-x/4}\square_{x/4}O_4$, exemplified in Scheme 1, can affect the nanostructure of the dye aggregate in the interlayers.   The anisotropy of the ESR spectra observed for the **dye-1**/Ti_3O_7 system can be caused by such differences.   The difference in the absorption maxima of the J-aggregates between the dye/Ti_3O_7 and dye/$Ti_{2-x/4}\square_{x/4}O_4$ systems is attributed to the difference in the size and the nanostructure (slip angle in the stacking of dye) of the dye according to the molecular exciton theory.[40]

Visible-Light Induced Electron-Transfer

The fluorescence quenching and visible-light induced ESR signal strongly prove the visible light induced electron-transfer from the J-aggregates of the dyes to the semiconducting host layers in all the dye/layered titanate intercalation compounds. The following photoprocesses are inferred for the present systems: the dye in the interlayer is firstly (1) excited by visible light and (2) the excited dye^{+*} is deactivated by

fluorescence or (3) undergoes electron transfer reaction to host layer to generate the conduction band electron, denoted as e^-_{CB}, followed by (4) recombination:

Excitation of a dye: $dye^+ + h\nu \rightarrow dye^{+*}$ (1)

Fluorescence: $dye^{+*} \rightarrow dye^+ + fluorescence$ (2)

Electron transfer: $dye^{+*} + host \rightarrow dye^{2+\cdot} + e^-_{CB}$ (3)

Recombination : $dye^{2+\cdot} + e^-_{CB} \rightarrow dye^+$ (4)
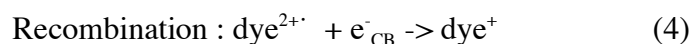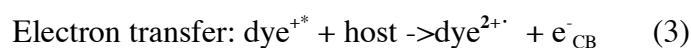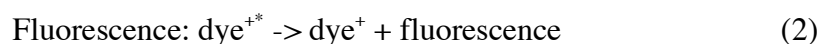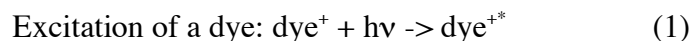
In all the present dye/titanate systems, the ESR signals emerged with visible light irradiation, not by UV-light, clearly proving the formation of $dye^{2+\cdot}$ by the processes (1) and (3), whereas the quenching of the fluorescence is interpreted as the result of the competence of fluorescence (2) with electron transfer (3).   In contrast, only the processes (1) and (2) took place in the montmorillonite systems because the excited dye can not electrically interact with the insulating aluminosilicate layers, so that neither fluorescence quenching nor ESR signals were observed.   The present study thus showed a clear proof for the electron transfer from the cyanine dye J-aggregate to the semiconducting host layers.   To our knowledge, this is the first case of proving light induced electron transfer between layered semiconductors and intercalated dye aggregates.

The electron transfer from the cyanine dyes to the titanate layers is energetically feasible.   Although accurate potentials of the conduction band edge of the dye-intercalated titanates are unknown, it should be around the theoretically predicted values of $H_2Ti_3O_7$ (-3.54 eV vs vacuum) and $Na_2Ti_3O_7$ (-4.52 eV vs vacuum) in the literature.[12]   On the other hand, the LUMO levels E_{LUMO} of **dye-1** and **dye-2** are estimated as -3.21 and –3.32 eV vs vacuum according to the electrochemically measured redox potentials E_R of the dyes[41] and the relationship[42]

$$E_{LUMO} \text{ (eV)} = - E_R \text{ (V vs SCE)} – 4.38.$$

Thus, the excited electrons in the LUMO of the dyes are allowed to be transferred to the conduction band of the titanate, which is energetically lower than E_{LUMO} of the dye.   Many reports on visible light induced electron transfer from cyanine dye J-aggregates to TiO_2, SnO_2 and ZnO[43] as well as to $AgBr$[27] also support the occurrence of the electron transfer in the present system.

Long-Lived Charge Separated States

The kinetics of the recombination processes is discussed from the decay curves of the ESR signal intensities (Figure 10), since the ESR signal intensity is proportional to the concentration of dye^{2+}.   Although the recombination kinetics must be rather complex than single or double exponential, the roughly estimated lifetimes shown in Table 1 indicate the high stability of the charge separated states.

Stabilization of charge separated state has been reported in some intercalation compounds containing donors or acceptors in the interlayer spaces of the semiconducting layered materials.   Stabilization of methyl viologen radical dications, which were generated by photoinduced electron transfer between host and guest, were rationalized by blocking of approaching O_2, which can mediate the recombination, to the radicals.[9-11,44,13,15,45,46]   However, in the present system, no remarkable difference was found in the recombination rates in N_2 and air.   On the other hand, layered perovskite doped with rare earth ions exhibited luminescence even after irradiation was terminated,[16] indicating long-lived charge separated state.   In that report, the slow recombination was interpreted as the slow migration of the conduction band electron due to the presence of trap sites in the host.

It is supposed that the stable charge separated state observed in this study is caused by slow electron diffusion in the host layers due to the presence of trapping sites of electrons; impurities and vacant sites of the titanate should work as the trapping sites. Because the recombination rate was much slower in the $Ti_{2-x/4}\square_{x/4}O_4$ systems than in the Ti_3O_7 systems, it is inferred that the vacant sites in $Ti_{2-x/4}\square_{x/4}O_4$ acted as the trap sites to slow the diffusion of the conduction band electrons.   Apparent activation energy of the back reaction is estimated from the slope of the Arrhenius plot (Figure 11) to be around

0.1 eV.   The small activation energy can support the presence of such trap sites.[16]   The nanostructure of the composites can also play an important role in the photoprocess. The higher stability found for the **dye-2** systems than the **dye-1** systems would be explained by the different nanostructures of the composites as well as the difference in the energy levels of these dyes.

The J-aggregated state of the intercalated cyanine dyes should also be responsible to the long-lived charge separation.   The charge left in the dye after the electron injection is regarded as a positive hole which slowly migrate in J-aggregate.[36] The migration of the positive hole would enhance spatial separation of the charges between the titanate sheet and the dye, leading to the slow back reaction.   On the other hand, fast injection of the positive holes into the valence band occurs in some cyanine dye/AgBr systems when HOMO level of the dye is higher than the valence band of AgBr;[36] however this process does not occur in the present systems, since the valence band edges of the titanates are far below the HOMO level of the dye.

4.5. Conclusions

Long-lived charge separated state induced by visible light via guest-to-host electron transfer was revealed in cyanine dye/layered titanate intercalation compounds, where the J-aggregates of the cyanine dyes acted as sensitizers. The apparent lifetimes of the charge separated states ranged from several minutes to 246 min, depending on the dye and the host. The stability of the charge separated state is rationalized by slow electron diffusion in the conduction band of the hosts as well as the nanostructure of the intercalation compounds.

Taking advantage of the further modifiable two-dimensional nanostructure of the intercalation compounds by coadsorbing other functional species in the interlayer space, the present system would be applicable as a good model system for sensitized photoenergy conversion. Further systematic study on the preparation of dye/layered titanate and niobates intercalation compounds and their optical properties are worth conducting.

4.6. References

(1) A. Hagfeldt, M. Grätzel, *Acc. Chem. Res.,* **33**, 269 (2000).

(2) M. S. Whittingham, A. J. Jacobson, *Intercalation Chemistry.* M. S. Whittingham, A. J. Jacobson, Eds. (Academic Press, New York, 1982).

(3) G. A. Ozin, *Adv. Mater.,* **4**, 612 (1992).

(4) M. Ogawa, K. Kuroda, *Chem. Rev.,* **95**, 399 (1995).

(5) H. Izawa, S. Kikkawa, M. Koizumi, *J. Phys. Chem.,* **86**, 5023 (1982).

(6) H. Izawa, S. Kikkawa, M. Koizumi, *Polyhedron,* **2**, 741 (1983).

(7) Y. I. Kim, S. Salim, M. J. Huq, T. E. Mallouk, *J. Am. Chem. Soc.,* **113**, 9561 (1991).

(8) A. Kudo, T. Kondo, *J. Mater. Chem.,* **7**, 777 (1997).

(9) H. Miyata, Y. Sugahara, K. Kuroda, C. Kato, *J. Chem. Soc., Faraday Trans. 1,* **84**, 2677 (1988).

(10) T. Nakato, K. Kuroda, C. Kato, *J. Chem. Soc., Chem. Comm.*, 1144 (1989).

(11) T. Nakato, K. Kuroda, C. Kato, *Chem. Mater.,* **4**, 128 (1992).

(12) Y. I. Kim, S. J. Atherton, E. S. Brigham, T. E. Mallouk, *J. Phys. Chem.,* **97**, 11802 (1993).

(13) T. Nakato, K. Ito, K. Kuroda, C. Kato, *Micropor. Mater.,* **1**, 283 (1993).

(14) T. Nakato, Y. Iwata, K. Kuroda, M. Kaneko, C. Kato, *J. Chem. Soc., Dalton Trans.*, 1405 (1993).

(15) T. Nakato, K. Kuroda, C. Kato, *Catal. Today,* **16**, 471 (1993).

(16) A. Kudo, T. Sakata, *J. Phys. Chem.,* **99**, 15963 (1995).

(17) T. Nakato, K. Kuroda, *Eur. J. Solid State Inorg. Chem.,* **32**, 809 (1995).

(18) T. Nakato, K. Kusunoki, K. Yoshizawa, K. Kuroda, M. Kaneko, *J. Phys. Chem.,* **99**, 17896 (1995).

(19) A. Kudo, E. Kaneko, *Chem. Commun.*, 349 (1997).

(20) G. B. Saupe, T. E. Mallouk, W. Kim, R. H. Schmehl, *J. Phys. Chem. B,* **101**, 2508 (1997).

(21) D. M. Kaschak, J. T. Lean, C. C. Waraksa, G. B. Saupe, H. Usami, T. E. Mallouk, *J. Am. Chem. Soc.,* **121**, 3435 (1999).

(22) Y. Yamaguchi, T. Yui, S. Takagi, T. Shimada, H. Inoue, *Chem. Lett.*, 644 (2001).

(23) A. Furube, T. Shiozawa, A. Ishikawa, A. Wada, K. Domen, C. Hirose, *J. Phys. Chem. B,* **106**, 3065 (2002).

(24) Z. Tong, T. Shichi, K. Oshika, K. Takagi, *Chem. Lett.,* **9**, 876 (2002).

(25) R. Amadelli, R. Argazzi, C. A. Bignozzi, F. Scandola, *J. Am. Chem. Soc.,* **112**, 7099 (1990).

(26) B. O'Regan, M. Grätzel, *Nature,* **353**, 737 (1991).

(27) T. Tani, in *Photographic sensitivity -Theory and mechanism.* (Oxford, New York, 1995) pp. 111.

(28) T. Kobayashi, *J-aggregates* (World Scientific Publishing, Singapore, 1996).

(29) S. Andersson, A. D. Wadsley, *Acta. Crystallogr.,* **14**, 1245 (1961).

(30) I. E. Grey, I. C. Madsen, J. A. Watts, L. A. Bursil, J. Kwiatkowska, *J. Solid State Chem.,* **58**, 350 (1985).

(31) T. Sasaki, M. Watanabe, Y. Michiue, Y. Komatsu, F. Izumi, S. Takenouchi, *Chem. Mater.,* **7**, 1001 (1995).

(32) N. Miyamoto, K. Kuroda, M. Ogawa, *Mol. Cryst. Liq. Cryst.,* **341**, 259 (2000).

(33) M. Ogawa, R. Kawai, K. Kuroda, *J. Phys. Chem.,* **100**, 16218 (1996).

(34) W. C. Needler, R. L. Griffitg, W. West, *Nature,* **191**, 902 (1961).

(35) T. Tani, *Photogr. Sci. Eng.,* **19**, 356 (1975).

(36) T. Tani, *J. Imaging Sci.,* **30**, 41 (1986).

(37) T. Tani, *J. Appl. Phys.,* **62**, 2456 (1987).

(38) H. Yoshioka, K. Nakatsu, *Chem. Phys. Lett.,* **11**, 255 (1971).

(39) N. Miyamoto, K. Kuroda, M. Ogawa, *J. Am. Chem. Soc.,* **123**, 6949 (2001).

(40) E. D. McRae, M. Kasha, *J. Chem. Phys.,* **28**, 721 (1958).

(41) J. R. Lenhard, *J. Imaging Sci.,* **30**, 27 (1986).

(42) T. Tani, *Photogr. Sci. Eng.,* **14**, 72 (1970).

(43) Y. Yonezawa, H. Kurokawa, S. Ito, M. Yamamoto, *J. Soc. Photogr. Sci. Technol. Jpn.,* **55**, 169 (1992).

(44) L. A. Vermeulen, M. E. Thompson, *Nature,* **358**, 656 (1992).

(45) L. A. Vermeulen, J. L. Snover, L. S. Sapochak, M. E. Thompson, *J. Am. Chem. Soc.,* **115**, 11767 (1993).

(46) L. A. Vermeulen, M. E. Thompson, *Chem. Mater.,* **6**, 77 (1994).

CHAPTER 5

EXFOLIATION AND FILM PREPARATION OF A LAYERED TITANATE, $Na_2Ti_3O_7$, AND INTERCALATION OF PSEUDOISOCYANINE DYE

5. Exfoliation and film preparation of a layered titanate, $Na_2Ti_3O_7$, and intercalation of pseudoisocyanine dye

5.1. Introduction

Fabrication of functional supramolecular structures utilizing inorganic framework is of great interest both from scientific and practical standpoints.[1,2] The interlayer spaces of layered inorganic solids are suitable for constructing well-organized molecular assemblies through intercalation.[2,3] Layered titanates are attractive host materials for such purpose due to their semiconducting[4,5] and ion-exchange properties.[6-14] Photo-induced electron transfer between titanate sheets and methylviologen,[7] rare earth ions,[11] cyanine dyes,[15] and $Ru(bpy)_3^{2+}$[16,9] have been investigated so far. In those studies, the samples were obtained and characterized as fine powders. For the detailed spectroscopic and electronic characterizations and for their applications as electronic and optical devices,[17-20] the hierarchical design of the nanostructures and the macroscopic morphology is a basic prerequisite. Film is an ideal morphology for such purposes.

Casting a suspension on a substrate is a promising method to prepare films of intercalation compounds. Swelling (or exfoliation) of layered solids into single or small number of layers is the first step to convert layered materials into thin films. However, the materials that can be exfoliated had been limited to those with excellent swelling property such as smectite clay minerals.[21,22] Ion-exchange of the interlayer ions with tetrabutylammonium ions was shown to be a way to promote exfoliation of layered materials such as $KTiNbO_5$,[23] $K_4Nb_6O_{17}$,[24] $Cs_xTi_{2-x/4}\square_{x/4}O_4$ ($\square$ = vacancy, x = 0.7),[25-31] α-$Zr(HPO_4)_2$,[32-34] layered perovskites.[23,35-37] Other than these materials, exfoliation of variety of layered materials have also been reported to date:[38] for example, layered chalcogenides,[39] graphite oxide,[40] layered double hydroxides,[41] tungstates,[42] manganese oxide,[43] and ruthenium oxides.[44] Using the exfoliated layered solids as a module, single and multilayered films were fabricated by "layer-by-layer" deposition from layered perovskites,[23,35,36] titanate,[29-31] and α-$Zr(HPO_4)$[32-34] as well as of a clay

mineral.[22]   Multilayered films were also obtained by casting or spin coating colloidal sols of layered titanates[45,46] and niobates[47,46,20] on substrates.   The latter method is useful to obtain relatively thick multilayered structures in one-step method, whereas layer-by-layer method may lead more complicated supramolecular structures such as a multi-component energy/electron transfer cascade.[17]

The degree of exfoliation, which is an important factor, has been examined by AFM and TEM observations,[23,24] measuring average thickness of the "layer-by-layer" films by ellipsometry,[32,22] in-situ XRD of the colloidal suspensions[25,28] and UV-visible spectroscopy of the suspensions.[28]   However, it is still difficult to characterize the degree of exfoliation properly and to control exfoliation of various layered solids effectively.   Therefore, the dispersion and film deposition of various layered solids are further worth investigating.

In this study, layered titanate $Na_2Ti_3O_7$ (Scheme 1) was swelled and exfoliated to single layers, then thin films of the titanate were fabricated as self-standing and supported films by restacking the exfoliated titanate sheets.   The degree of exfoliation was effectively controlled by ultrasonication and hydrothermal treatment of the suspension.   We finally fabricated a supramolecular composite film with alternating layers of two-dimensional semiconductor, the titanate, and J-aggregate of a cyanine dye by intercalating the dye into the pre-deposited propylammonium-exchanged $Na_2Ti_3O_7$ film. $Na_2Ti_3O_7$ has larger particle size, larger surface charge density and different crystal structure compared to the layered titanate $H_xTi_{2-x/4}\square_{x/4}O_4$ whose exfoliation and film preparation has most extensively been investigated among layered titanates.   J-aggregates of cyanine dyes are well known as an excellent sensitizer[48] and have been formed in the interlayer spaces of $K_4Nb_6O_{17}$,[49] $Na_2Ti_3O_7$,[13] layered clay minerals,[50,51] and layered silicate.[52]

1,1'-diethyl-2,2'-cyanine bromide (PIC)
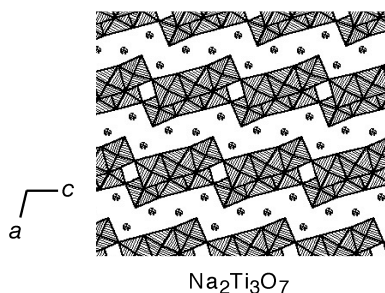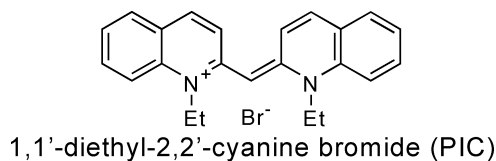
$Na_2Ti_3O_7$

Scheme 1 Schematic structures of the dye and the titanate.

5.2. Experimental

Starting Materials

$Na_2Ti_3O_7$ was synthesized by calcining a mixture of Na_2CO_3 and TiO_2 (anatase) in a molar ratio of 1.1 : 3 at 900 °C for 24 h, according to the literatures.[53,6] The calcination was repeated two times. 1,1'-Diethyl-2,2'-cyanine bromide (pseudoisocyanine, abbreviated as PIC hereafter; Scheme 1; purity 99.9 %) was purchased from Hayashibara Biochemical Laboratories, Inc. and was used without further purification.

Intercalation of Alkylammonium Ions

Proton-exchanged form of $Na_2Ti_3O_7$[6] was obtained by suspending 10 g dm^{-3} of $Na_2Ti_3O_7$ in 1 mol dm^{-3} HCl and stirring the mixture for 3 d. 1 mol dm^{-3} HCl was replaced daily. The formation of the host materials were confirmed by XRD, which showed the pattern similar to those reported previously.[53,6] The proton-exchanged $Na_2Ti_3O_7$ thus obtained was sealed in a glass ampoule with an aqueous solution of methylamine (40 vol.- %) and the mixture was allowed to react at 60 °C for 6 days to yield a methylammonium/Ti_3O_7 intercalation compound as identified by XRD. The

methylammonium/Ti_3O_7 intercalation compound was allowed to react with an aqueous solution of propylamine (50 vol.- %) at 60 °C for 6 days to yield a propylammonium/Ti_3O_7 intercalation compound (denoted as PA/Ti_3O_7 hereafter). Excess amounts of the alkylammonium ions (20 and 40 mol of methylammonium and propylammonium per a mol of $[Ti_3O_7]^{2-}$) were used for the reactions. Intercalation of propylammonium ions was thus conducted in two steps because pre-intercalation of methylammonium was effective to completely remove the unreacted host material (proton-exchanged $Na_2Ti_3O_7$).[13] The formation of PA/Ti_3O_7 was confirmed by XRD and CHN analysis. The amount of propylammonium ions in PA/Ti_3O_7 was 0.56 mol per a mol of $[Ti_3O_7]^{2-}$; the rest of the layer charge is supposed to be compensated by proton. The basal spacing was in the range of 1.1 - 1.2 nm depending on the hydration of the interlayer space; the basal spacing is large enough for propylammonium to be present in the interlayer space.

<u>Exfoliation of PA/Ti_3O_7</u>

The colloidal sol containing exfoliated titanate sheets was obtained by dispersing and swelling powders of PA/Ti_3O_7 in water (2 g dm^{-3} or 6.7×10^{-3} mol dm^{-3} of Ti_3O_7) followed by ultrasonication for 1 h and centrifugation at 4000 rpm for 15 min to remove precipitates (non-exfoliated PA/Ti_3O_7). This titanate sol was used for preparing all the films described in this study. To check the effect of ultrasonication and hydrothermal treatment on the degree of exfoliation, the sols were also obtained with reduced ultrasonication period (10 min) and/or with hydrothermal treatment (150 °C, 1 h) before centrifugation. It must be noted that prolonged hydrothermal treatments (3 h and 1 days) resulted in partial (3 h) and complete (1 days) transformation of the material into anatase TiO_2 as identified by XRD; the condition (150 °C, 1h) was employed to avoid such structural transformation.

<u>Preparation of the Films and Intercalation of the Dye</u>

The titanate sol was cast on substrates (quartz glass or mica) drop by drop with

a syringe; by storing the substrate covered with the sol at room temperature for 2 - 3 days, the sol was completely dried and the film was formed. Although the deposition method is very simple, we should note that rapid drying of the film, e.g. at 60 ºC, results in rougher surface morphology as observed by SEM. A self-supporting film was obtained by casting the titanate sol on a Teflon-substrate and subsequent peeling off from the substrate by soaking in acetone. PIC was intercalated into the supported and unsupported films by soaking the films in an aqueous solution of PICBr (5×10^{-4} mol dm^{-3}) at 60 °C for several days, followed by washing with acetone.

<u>Characterizations</u>

X-ray diffraction (XRD) patterns of powders and films were obtained by a Mac Science MXP^3 diffractometer with monochromated CuKα radiation at the tube voltage of 40 kV and the current of 30 mA. CHN analysis of PA/Ti$_3$O$_7$ powders was performed by a Perkin Elmer PE-2400II instrument. UV-visible spectra of the titanate sols and the films deposited on quartz glass supports were measured on a Shimadzu UV-2500PC spectrophotometer. UV-visible spectra of the powders were measured in a diffuse reflection mode on the same spectrophotometer attached with an integral sphere. SEM images of films were taken by a HITACHI S450S microscope. AFM images of the films deposited on mica substrates and the titanate sheets individually deposited on the substrates were taken with a Nanoscope III apparatus (Digital Instruments) operated in contact mode, using silicon nitride cantilevers and scanning at 1 Hz with 512 lines per image resolution and 0.1 - 0.2 V set-point. The amounts of Ti in the titanate sols after centrifugation were determined by ICP analysis by using a Nippon-Jarrell-Ash ICAP-575 Mark II apparatus. ICP analysis was also performed on the sols filtrated with a 0.2 μm pored membrane filter.

5.3. Results and Discussion

__Formation of PA/Ti$_3$O$_7$ films__

By exfoliating and restacking the PA/Ti$_3$O$_7$ powders on a quartz glass substrate, a transparent thin film was obtained.   The photograph of the supported film formed on the substrate is shown in Figure 1a.   In the SEM image of the supported film (Figure 1d), a monolithic domain with the thickness of ca. 1 μm is observed on the substrate. The PA/Ti$_3$O$_7$ film was also obtained as self-standing films, whose photographs are shown in Figures 1b and 1c.

Although the macroscopic morphology is largely modified from microcrystalline powders to thin films, the nanostructure of the layered titanate was retained in the restacked film as confirmed by the XRD measurement.   In the XRD pattern of the film (Figure 2a), *100* reflection was observed at d = 1.1 nm, accompanying a weak *200* reflection at d = 0.5 nm.   The basal spacing of the film is consistent with that of PA/Ti$_3$O$_7$ fine powders, indicating that the thin film possesses a layered structure similar to that of the powders of PA/Ti$_3$O$_7$: the Ti$_3$O$_7^{2-}$ sheets and propylammonium ions are stacked alternately on the substrate.   Although we have not examined the composition of the film, we presume it same as the powder since the film was obtained by simply suspending the powder in water and subsequent evaporation. Reassembling of the film as the alkylammonium-intercalated form is a reasonable result since propylammonium is present as counter cation of the negatively charged titanate sheet in the sol.
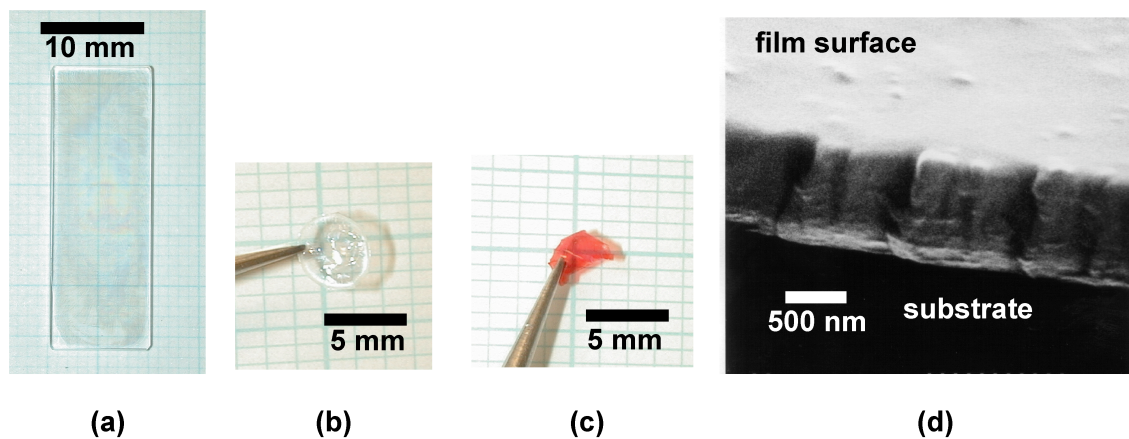
Figure 1. The photographs of (a) supported and (b) unsupported films of PA/Ti_3O_7 and (c) an unsupported film intercalated with PIC. (d) The SEM image of the PA/Ti_3O_7 film formed on glass substrate.
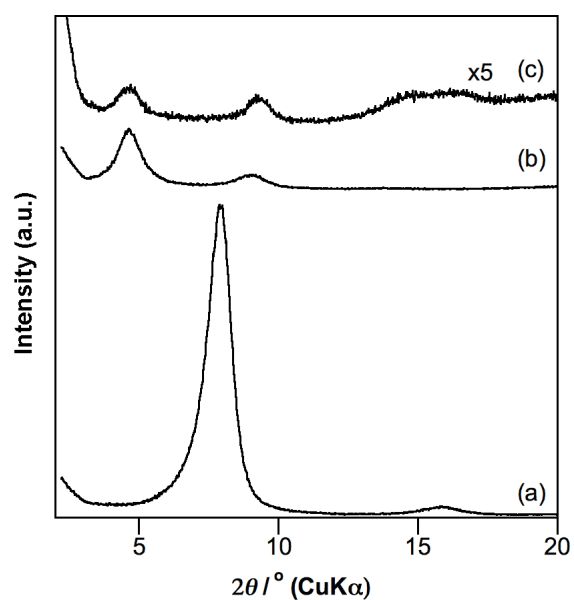
Figure 2. XRD patterns of (a) a supported film of PA/Ti_3O_7 and (b) supported and (c) unsupported films intercalated with PIC.

The AFM observation of the film demonstrated that the films are composed of highly exfoliated titanate sheets restacked flat on the substrate. Figure 3a shows the AFM differential image of the film deposited on a mica substrate. Rectangular sheets are stacked parallel to the substrate with their edges in random directions. The rectangular shape of the sheets proves that the sheets are derived from exfoliated PA/Ti_3O_7 fine powders since the original powders are rectangular microcrystals. The section analysis (the upper part of Figure 3a) showed that the surface of the film was very smooth (the difference in the lowest and highest points is < 20 nm); the observation is in consistent with the SEM observation (Figure 1d) which also indicated the smoothness of the film surface.
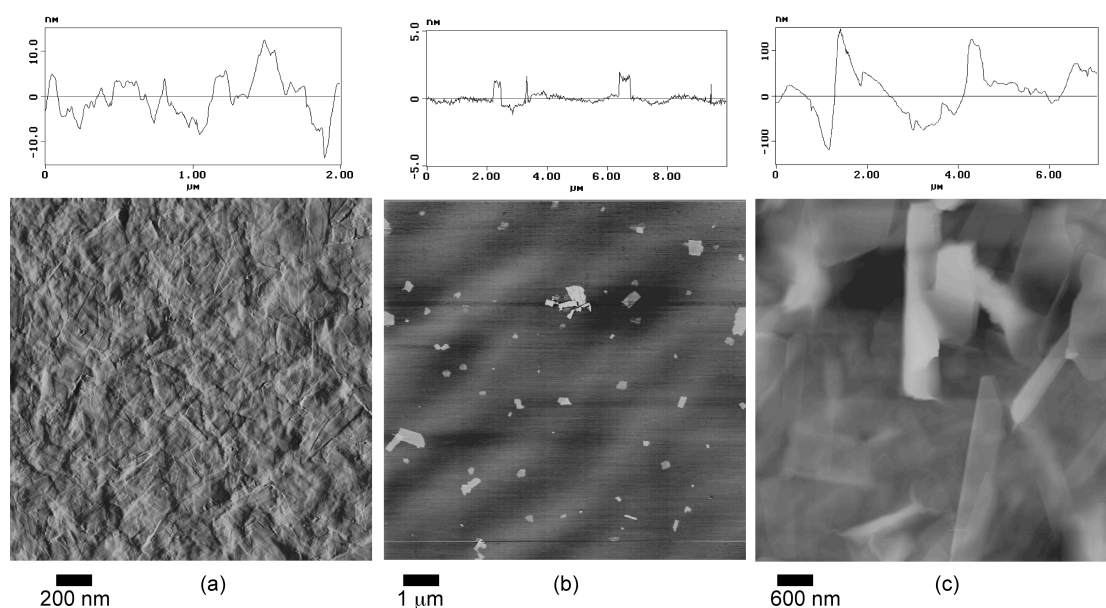
Figure 3. AFM images of (a) PA/Ti_3O_7 film (differential image), (b) the individual titanate sheets on mica substrate (height scan image) and (c) PA/Ti_3O_7 film prepared from the titanate sol before centrifugation (height scan image). The results of section analyses are shown on the upper part of the images.

The thickness of the titanate sheets consisting the film was estimated by observing individual titanate sheets by casting and drying a dilute (1 % of the sol used for the film preparation) titanate sol. In the AFM image (height scan; Figure 3b), the individual titanate sheets are observed without stacking or aggregating. The section analysis (the upper part of Figure 3b) showed that the thickness of the titanate sheets was ca. 1 nm, which corresponds to the thickness of $[Ti_3O_7]^{2-}$ sheet (0.98 nm) estimated from the known crystal structure.[41] The thicknesses of the exfoliated sheets of $HTiNbO_5$ [23] and $K_4Nb_6O_{17}$[24] have been estimated by AFM, indicating that these materials are exfoliated to single layers. The present result indicates that $Na_2TI_3O_7$ was exfoliated to single layers.

The UV-visible spectra of the titanate sol, in which a blue-shift of the bandgap absorption was observed, also support the high degree of exfoliation of the layered titanate. Figures 4a and c compare the UV-visible spectra of the titanate sol and powders of PA/Ti_3O_7. The absorption maximum was observed at around 263 nm for the titanate sol (Figure 4a), whereas the maximum is at around 293 nm for the powders (Figure 4c). The blue-shift of the absorption maximum relative to that of powders indicates the increase of the bandgap energy of the titanate in the sol than in the form of fine powders. The variation in bandgap energy is explained in terms of size quantization effect: the bandgap energy of a semiconductor increases when its size is reduced to nm order. In the case of two-dimensional semiconductor, it was reported that the bandgap energy is dominated by the thickness, while the lateral size is less concerned.[54,55]

Interestingly, the blue-shift of the absorption maximum was observed even after the titanate sheets in the sol were restacked into a thin film. We should expect that the electrical and optical properties of the restacked films are similar to that of the powders, since they are regarded as similar multi-layered solids. However, the absorption maximum of the restacked film was observed at 263 nm (Figure 4b), which was blue-shifted relative to that of the powders (293 nm; Figure 4c) and was similar to that of the sol (263 nm). We suppose that the incompatibility arise from the anisotropy

in the transition moment of the titanate sheets between the directions perpendicular and parallel to the sheet (*bc*-plane of the crystal); the anisotropy in the reflection spectrum is also reported in the single crystal of layered semiconductor $(C_{10}H_{21}NH_3)_2PbI_4$.[56] Since the titanate sheet is flat on the substrate and the film is set perpendicular to the incident light for the measurement, the spectrum of the film reflect only the transition moment parallel to the titanate sheet. In contrast, the spectrum of the powder is the sum of the transition moments of all the directions.
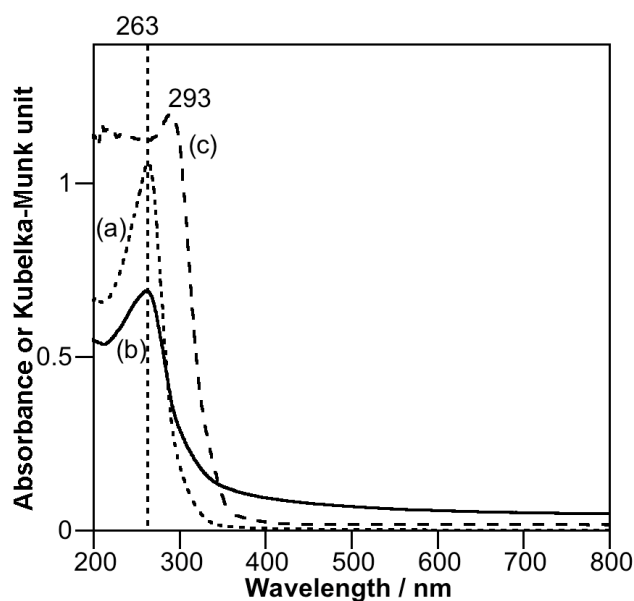
Figure 4. UV-visible absorption spectra of (a) the titanate sol used for the film preparation (diluted to 1 vol.- % for the measurement), (b) PA/Ti_3O_7 film, and (c) PA/Ti_3O_7 powders. The spectrum (c) was obtained by Kubelka-Munk correlation over the diffuse reflection spectrum measured by using integrating sphere.

The obtained film was transparent in the visible wavelength region; the transparency is favorable for detailed spectroscopic measurements and optical application of composite films obtained by intercalation of photofunctional species. The visible spectrum of the film (Figure 4b) as well as the photograph (Figure 1a) exemplifies the transparency of the film: for example, Figure 4b indicates that the absorbance of the film at 800 nm is 0.048, which corresponds to the transmittance of 90 %.   We suppose that the fine morphology of the film (as exemplified in the AFM image (Figure 2a)), which should arise from the high degree of exfoliation of the titanate in the sol, is responsible to the transparency of the films.   In the AFM image of an opaque film obtained by casting and drying the titanate sol before centrifugation, the surface was rough with the difference of 100 nm (Figure 3c) due to the presence of non-exfoliated particles.   The large non-exfoliated particles should scatter transmitting light so that the film becomes opaque.   The centrifugation process effectively removed non-exfoliated particles which interfere the formation of the transparent film.

Although centrifugation is effective to remove non-exfoliated particles, increasing the degree of exfoliation is favorable to obtain the transparent film in higher yield because a significantly large part of the initially loaded titanate is removed as a deposit by centrifugation; it was found that ultrasonication is effective to promote exfoliation.   The amounts of the titanate retained in the titanate sol after centrifugation was estimated by ICP analysis.   Whereas 6.7×10^{-3} mol dm^{-3} of Ti$_3$O$_7$ was initially loaded in the system, ICP analysis showed that 62 % of the loaded titanate (4.3×10^{-3} mol dm^{-3} of Ti$_3$O$_7$) was retained in the supernatant, when the sol was ultrasonicated for 1 h before centrifugation.   In contrast, only 11 % of the loaded titanate was retained with 10 min of ultrasonication.   Thus, ultrasonication was effective to promote exfoliation of the titanate.   We suppose that ultrasonication caused dispersion of the aggregated particles of the titanate so that more titanate particles were effectively exfoliated.

Hydrothermal treatment of the suspension was also effective to promote exfoliation, probably due to kinetically and/or thermodynamically promoted hydration of the interlayer space.   With the hydrothermal treatment (150 ºC, 1h) of the titanate

sol ultrasonicated for 10 min, 32 % of the loaded titanate was retained after centrifugation. Since no Ti atoms were present in the sol filtrated with a 2 μm pored membrane filter, the titanate is not dissolved into water by the hydrothermal treatment. The hydrothermal treatment after the ultrasonication of 1 h resulted in the retention of 81 % of the loaded titanate (5.6×10^{-3} of mol dm^{-3}) after centrifugation; however, the filtrated sol also contained a considerable amount of Ti (3.0×10^{-3} mol dm^{-3} of Ti$_3$), indicating that a part of the titanate was dissolved into water in this case. Although the film prepared from this sol (with 1 h of ultrasonication and hydrothermal treatment) showed no difference compared to that in Figure 2a, prolonged hydrothermal treatment (3 h and 1 day) resulted in partial (3 h) and complete (1 day) transformation of the material into anatase TiO$_2$ as identified by XRD.

It must be noted that no remarkable differences were found in the XRD patterns, UV-visible spectra and morphologies (AFM and SEM) of the films prepared from the suspension obtained under different conditions. Although ultrasonication could cause reduction of the lateral size the titanate sheets upon ultrasonication, we did not observe such the reduction by AFM in the present case: the observed lateral size was in the range of 0.1-1 μm regardless of ultrasonication time. Partitioning by centrifugation can be a reason for this since the particles with the lateral size of around 3 μm are observed in the AFM image (Figure 3c) of the film deposited without centrifugation. We expect that the present methodologies to promote exfoliation are applicable to other layered materials. Exfoliation of a single crystal material by this method have recently been reported.[57]

Intercalation of PIC

The obtained thin film retained cation exchange property of the original powders of PA/Ti$_3$O$_7$; a thin film of PIC/Ti$_3$O$_7$ intercalation compound was successfully obtained by the reaction of the pre-deposited film with an aqueous solution of PIC, retaining the morphology and transparency of the film. Remarkably, the intercalation was also successful even with the self-supporting film (Figure 1c), which is more fragile

than the supported.   We have already reported the synthesis of PIC/Ti$_3$O$_7$ intercalation compound in a powder form.[13]   However, the conversion of the powders of PIC/Ti$_3$O$_7$ intercalation compound into thin film was not successful because the intercalation compound was not dispersed in solvents.

The increase in basal spacing measured by XRD clearly proved intercalation of the dye into the interlayer space of the titanate film.   Figure 2b and c show the XRD patterns of the supported and unsupported PIC/Ti$_3$O$_7$ films.   The basal spacing increased to 1.8 nm from that of the PA/Ti$_3$O$_7$ film (1.1 nm; Figure 2a).   The basal spacing (1.8 nm) is similar to that of powders of PIC/Ti$_3$O$_7$ intercalation compound,[13] indicating successful intercalation of the dye into the interlayer space of the titanate film. It must be noted that the intercalated film sometimes contain unreacted phase (propylammonium-intercalated form) identified by XRD, and is sometimes inhomogeneously colored, indicating partial retention of propylammonium. Optimizing the condition of intercalation to the film is valuable for detailed characterization of the film and applications.

The UV-visible spectrum of the PIC/Ti$_3$O$_7$ film revealed the formation of J-aggregates of the dye in the interlayer space.   The UV-visible spectra of the film before and after the intercalation of PIC are shown in Figures 5a and b.   After intercalation, the absorption band due to PIC emerged at 570 nm, which is largely red-shifted from the monomer band (525 nm) observed in a dilute (5×10^{-5} mol dm^{-3}) aqueous solution of PICBr (Figure 5c).   Since the band around 570 nm is ascribable to J-aggregate of PIC,[48] the dye is present as J-aggregates in the interlayer space.   On the other hand, the absorption maximum due to the bandgap of the titanate sheets was only slightly blue-shifted by the intercalation of the dye (from 257 nm to 252 nm, as are revealed in Figures 5a and b, respectively), indicating that the electric property of the host layer is not significantly affected by the intercalation of the dye.
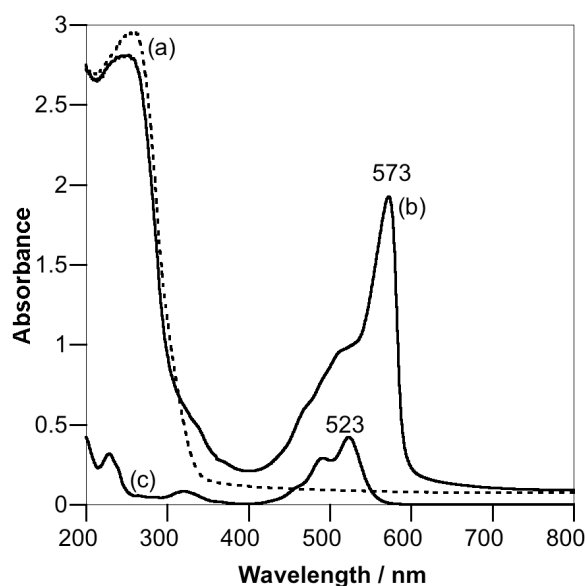
Figure 5. UV-visible absorption spectra of (a) PA/Ti$_3$O$_7$-film, (b) PIC/Ti$_3$O$_7$-film, and (c) aqueous solution of PICBr (5×10^{-5} mol dm^{-3}).

The nanostructure of the composite film is discussed from the basal spacing and the structure of the dye aggregate. The gallery height was estimated to be 1.0 nm by subtracting the basal spacing of dehydrated proton-exchanged Na$_2$Ti$_3$O$_7$ (0.8 nm)[6] from the observed basal spacing (1.8 nm). Based on the gallery height and the size of PIC (ca. 0.4 nm × 1.5 nm × 0.8 nm based on the molecular structure at lowest energy configuration obtained on Chem3D software), one can derive two models of PIC orientation in the interlayer space: one is the model where the dye is present as a single molecular layer with the short axis of the molecular plane almost perpendicular to the host layer, and the other is the model where the dye is present as a double layer with the molecular plane parallel to the host layer. Since the J-aggregate of PIC has a two-dimensional "brick stone" structure where the molecular planes stack parallel to each other,[48] the single molecular layer model is more plausible. Supposing this arrangement, the long axis of PIC, the direction of the dipole of PIC, lies parallel to the

titanate sheet.

Based on the nanostructure of the intercalation compound discussed above and on the macroscopic orientation of the titanate sheets (flat on the substrate), the dipole of PIC is expectedly macroscopically oriented parallel to the film surface.   To estimate the macroscopic orientation of PIC, polarized visible spectra of the PIC/Ti$_3$O$_7$ film (supported) were measured.   When the film was set almost parallel (inclined by 5°) to the incident light (Figure 6a), a strong anisotropy was observed in the J-band, as is exemplified by the large difference in absorbance between a = 0 and 90.   In contrast, the band was isotropic (the spectra was independent of a) when the film was set perpendicularly (Figure 6b).   It is clearly revealed that the long axis of PIC, which corresponds to the transition moment of the dye, was oriented flat to the substrate. Thus the macroscopic orientation and transparency of the composite film, in contrast with the powder samples, were utilized to obtain clear visible spectra and to examine the anisotropy of the material.

The successful preparation of PIC/K$_4$Nb$_6$O$_{17}$ single crystal hybrid, which is suitable for detailed spectroscopic characterization, was already described in Chapter 3 of this thesis.[49]   However, materials obtained as single crystals are limited so far.   The present method is applicable to various materials which are obtained only as fine powders.
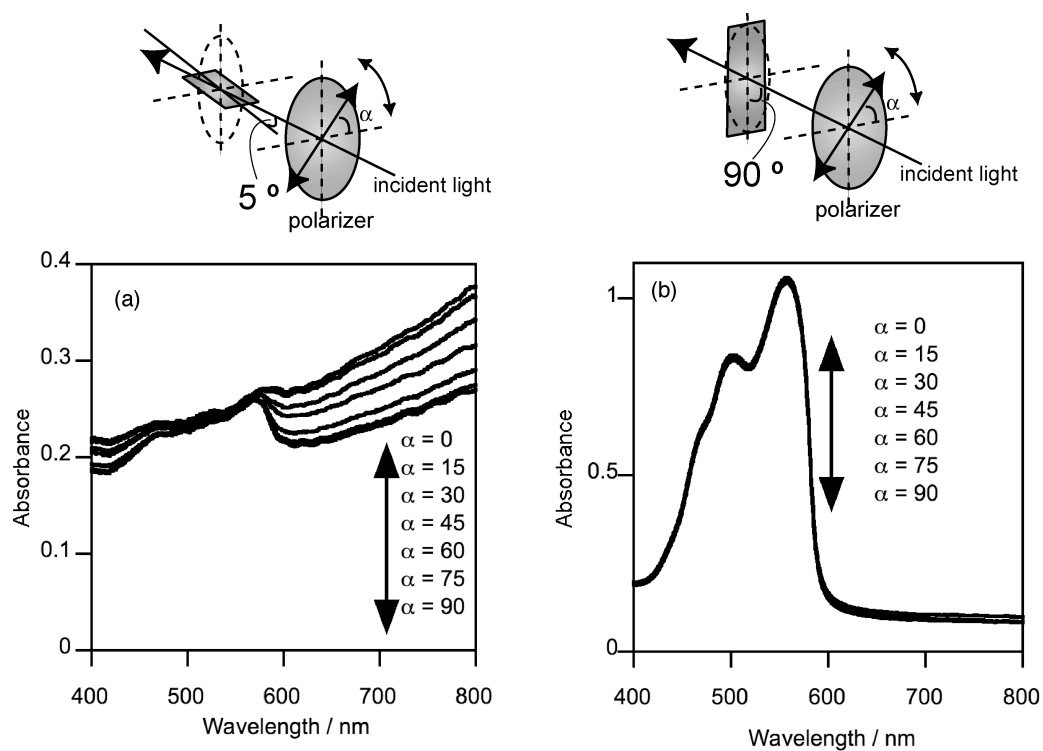
Figure 6. The polarized visible spectra of a PIC/Ti_3O_7-film. The angle between the substrate plane and the incident light was set to (a) 5 ° and (b) 90 ° by rotating the film. The symbol a represents the angle between the polarization direction of the incident light and the rotation axis of the film.

5.4. Conclusions

Transparent thin films of the layered titanate $Na_2Ti_3O_7$ ion-exchanged with propylammonium were fabricated with and without substrate supports through exfoliation and restacking of the powders of propylammonium/Ti_3O_7 intercalation compound. Hydrothermal treatment and ultrasonication were effective to promote exfoliation of the layered solid; this methodology will be applicable to other layered solids that are difficult to be exfoliated. The transparent thin film of propylamonium/Ti_3O_7 intercalation compound is valuable as a host for functional molecules such as dye due to its expandable two-dimensional nanospace and macroscopic anisotropy. Taking advantage of the ion-exchange capability of the film, a cationic cyanine dye (PIC) was successfully intercalated into the film as J-aggregates, retaining the morphology and transparency of the film. The obtained multilayer composite of the J-aggregate and the semiconducting titanate layers is applicable for model systems of energy and electron transfer as well as for optical and electronic devices.

5.5. References

(1) G. A. Ozin, *Adv. Mater.,* **4**, 612 (1992).

(2) M. Ogawa, K. Kuroda, *Chem. Rev.,* **95**, 399 (1995).

(3) M. S. Whittingham, A. J. Jacobson, *Intercalation Chemistry.* M. S. Whittingham, A. J. Jacobson, Eds. (Academic Press, New York, 1982).

(4) K. Domen, A. Kudo, A. Shiozaki, A. Tanaka, K. Maruya, T. Onishi, *J. Chem. Soc., Chem. Commun.*, 356 (1986).

(5) A. Kudo, T. Kondo, *J. Mater. Chem.,* **7**, 777 (1997).

(6) H. Izawa, S. Kikkawa, M. Koizumi, *J. Phys. Chem.,* **86**, 5023 (1982).

(7) H. Miyata, Y. Sugahara, K. Kuroda, C. Kato, *J. Chem. Soc., Faraday Trans. 1,* **84**, 2677 (1988).

(8) T. Nakato, Y. Iwata, K. Kuroda, M. Kaneko, C. Kato, *J. Chem. Soc., Dalton Trans.*, 1405 (1993).

(9) T. Nakato, K. Kusunoki, K. Yoshizawa, K. Kuroda, M. Kaneko, *J. Phys. Chem.,* **99**, 17896 (1995).

(10) T. Sasaki, M. Watanabe, Y. Michiue, Y. Komatsu, F. Izumi, S. Takenouchi, *Chem. Mater.,* **7**, 1001 (1995).

(11) A. Kudo, E. Kaneko, *Chem. Commun.*, 349 (1997).

(12) M. Ogawa, Y. Takizawa, *Chem. Mater.,* **11**, 30 (1999).

(13) N. Miyamoto, K. Kuroda, M. Ogawa, *Mol. Cryst. Liq. Cryst.*, **341**, 259 (2000).

(14) R. Kaito, N. Miyamoto, K. Kuroda, M. Ogawa, *J. Mater. Chem.,* **12**, 1 (2002).

(15) N. Miyamoto, K. Kuroda, M. Ogawa, *J. Phys. Chem. B*, in press.

(16) Y. I. Kim, S. Salim, M. J. Huq, T. E. Mallouk, *J. Am. Chem. Soc.,* **113**, 9561 (1991).

(17) D. M. Kaschak, J. T. Lean, C. C. Waraksa, G. B. Saupe, H. Usami, T. E. Mallouk, *J. Am. Chem. Soc.,* **121**, 3435 (1999).

(18) D. W. Kim, A. Blumstein, J. Kumar, S. K. Tripathy, *Chem. Mater.,* **13**, 243 (2001).

(19) D. W. Kim, A. Blumstein, S. K. Tripathy, *Chem. Mater.,* **13**, 1916 (2001).

(20) A. Furube, T. Shiozawa, A. Ishikawa, A. Wada, K. Domen, C. Hirose, *J. Phys. Chem. B,* **106**, 3065 (2002).

(21) H. van Olphen, *An Introduction to Clay Colloid Chemistry, 2nd ed.* (Krieger, Malabar, FL, 1977).

(22) E. R. Kleinfeld, G. S. Ferguson, *Science,* **265**, 370 (1994).

(23) M. Fang, C. H. Kim, G. B. Saupe, H.-N. Kim, C. C. Waraksa, T. Miwa, A. Fujishima, T. E. Mallouk, *Chem. Mater.,* **11**, 1526 (1999).

(24) G. B. Saupe, C. C. Waraksa, H.-N. Kim, Y. J. Han, D. M. Kaschak, D. M. Skinner, T. E. Mallouk, *Chem. Mater.,* **12**, 1556 (2000).

(25) T. Sasaki, M. Watanabe, H. Hashizume, H. Yamada, H. Nakazawa, *J. Am. Chem. Soc.,* **118**, 8329 (1996).

(26) T. Sasaki, M. Watanabe, H. Hashizume, H. Yamada, H. Nakazawa, *J. Chem. Soc., Chem. Commun.*, 229 (1996).

(27) T. Sasaki, S. Nakano, S. Yamauchi, M. Watanabe, *Chem. Mater.,* **9**, 602 (1997).

(28) T. Sasaki, M. Watanabe, *J. Am. Chem. Soc.*, **120**, 4682 (1998).

(29) T. Sasaki, Y. Ebina, T. Tanaka, M. Harada, M. Watanabe, G. Decher, *Chem. Mater.,* **13**, 4661 (2001).

(30) T. Sasaki, Y. Ebina, K. Fukuda, T. Tanaka, M. Harada, M. Watanabe, *Chem. Mater.,* **14**, 3524 (2002).

(31) Z. S. Wang, T. Sasaki, M. Muramatsu, Y. Ebina, T. Tanaka, L. Z. Wang, M. Watanabe, *Chem. Mater.,* **15**, 807 (2003).

(32) S. W. Keller, H.-N. Kim, T. E. Mallouk, *J. Am. Chem. Soc.*, **116**, 8817 (1994).

(33) H.-N. Kim, S. W. Keller, T. E. Mallouk, *Chem. Mater.*, **9**, 1414 (1997).

(34) D. M. Kaschak, S. A. Johnson, D. E. Hooks, H.-N. Kim, M. D. Ward, T. E. Mallouk, *J. Am. Chem. Soc.,* **120**, 10887 (1998).

(35) R. E. Schaak, T. E. Mallouk, *Chem. Mater.,* **12**, 3427 (2000).

(36) R. E. Schaak, T. E. Mallouk, *Chem. Mater.,* **12**, 2513 (2000).

(37) Y.-S. Han, I. Park, J.-H. Choy, *J. Mater. Chem.,* **11**, 1277 (2001).

(38) A. J. Jacobson, in *Comprehensive supramolecular chemistry* G. Alberti, T. Bein, Eds. (Pergamon, Oxford, 1996), vol. 7, pp. 315.

(39) D. W. Murphy, G. W. H. Jr., *J. Chem. Phys.,* **62**, 973 (1975).

(40) N. A. Kotov, I. Dékány, J. H. Fendler, *Adv. Mater.,* **8**, 637 (1996).

(41) M. Adachi-Pagano, C. Forano, J.-P. Besse, *Chem. Commun.*, 91 (2000).

(42) R. E. Schaak, T. E. Mallouk, *Chem. Commun.,* **2002**, 706 (2002).

(43) Y. Omomo, T. Sasaki, L. Wang, M. Watanabe, *J. Am. Chem. Soc.,* **125**, 3568 (2003).

(44) W. Sugimoto, H. Iwata, Y. Yasunaga, Y. Murakami, Y. Takasu, *Angew. Chem., Int. Ed.,* **42**, 4092 (2003).

(45) R. Abe, K. Shinohara, A. Tanaka, M. Hara, J. N. Kondo, K. Domen, *Chem. Mater.,* **10**, 329 (1998).

(46) R. Abe, S. Ikeda, J. N. Kondo, M. Hara, K. Domen, *Thin Solid Films,* **343-344**, 156 (1999).

(47) R. Abe, M. Hara, J. N. Kondo, K. Domen, *Chem. Mater.,* **10**, 1647 (1998).

(48) T. Kobayashi, *J-aggregates* (World Scientific Publishing, Singapore, 1996).

(49) N. Miyamoto, K. Kuroda, M. Ogawa, *J. Am. Chem. Soc.,* **123**, 6949 (2001).

(50) M. Ogawa, R. Kawai, K. Kuroda, *J. Phys. Chem.,* **100**, 16218 (1996).

(51) N. Miyamoto, R. Kawai, K. Kuroda, M. Ogawa, *Appl. Clay. Sci.*, **16**, 161 (2000).

(52) N. Miyamoto, K. Kuroda, M. Ogawa, *Appl. Clay. Sci.,* **19**, 39 (2001).

(53) S. Andersson, A. D. Wadsley, *Acta. Crystallogr.,* **14**, 1245 (1961).

(54) C. J. Sandroff, D. M. Hwang, W. M. Chung, *Phys. Rev. B*, **33**, 5953 (1986).

(55) T. Sasaki, M. Watanabe, *J. Phys. Chem. B,* **101**, 10159 (1997).

(56) T. Ishihara, J. Takahashi, T. Goto, *Phys. Rev. B,* **42**, 11099 (1990).

(57) N. Miyamoto, H. Yamamoto, R. Kaito, K. Kuroda, *Chem. Commun.*, 2378 (2002).

CHAPTER 6

MACROSCOPIC AND SOFT ORGANIZATION OF PSEUDOISOCYANINE DYE WITH LYOTROPIC LIQUID CRYSTALS OBTAINED BY EXFOLIATION OF LAYERED NIOBATE

6.1. Formation of Extraordinarily Large Nanosheets from K$_4$Nb$_6$O$_{17}$ Crystals

6.1.1. Introduction

Conversion of inorganic layered materials to nanosheets by exfoliation has attracted keen interests because nanosheets can be used as a component for novel supramolecular assemblies applicable in nanoscience and nanotechnology.[1] Exfoliation of layered crystals means the insertion of an infinite amount of solvent molecules into the interlayer region. Various materials composed of a wide variety of compositions and structures have been synthesized using exfoliated nanosheets. Suspensions or sols containing exfoliated nanosheets can be cast or spin-coated onto substrates to form thin films.[2] A layer by layer method has been utilized for the formation of more complex nanosystems using suspensions of inorganic layered materials.[3] Polymer-clay nanocomposites are a typical example of the use of exfoliated clay minerals.[4]

Exfoliation of layered materials, such as niobate,[5] titanate,[6] zirconium phosphate,[7] has often been studied from photo- and electrochemical viewpoints. The usual synthetic method to induce exfoliation includes ion exchange of interlayer alkali metal ions in these layered materials with protons and the following acid-base reactions of H-type materials with aqueous solutions of organoammonium ions.[8] However, the size of exfoliated nanosheets, reported so far, is limited to about several micrometers. It has been believed that only powder samples can be exfoliated. This chapter describes a successful use of single crystals for exfoliation.

K$_4$Nb$_6$O$_{17}$ (Scheme 1) is synthesized as single crystals by a flux method.[9] K$_4$Nb$_6$O$_{17}$ is quite interesting because it is transparent and semiconducting and the surface can orient dye species in one direction.[10] K$_4$Nb$_6$O$_{17}$•3H$_2$O crystals were allowed to react with propylammonium (PA) ions under hydrothermal conditions to yield exfoliated nanosheets with ultra high aspect ratios if compared with the size of nanosheets reported hitherto. Although an increase in the viscosity of a suspension of

niobate sols prepared by using propylammonium chloride has recently reported,[11] there have been no reports on the size of the nanosheets.
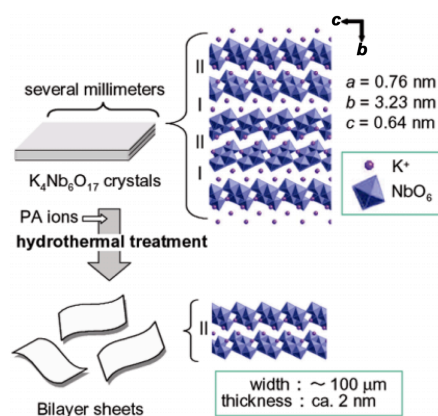
Scheme 1. Schematic image of exfoliation of $K_4Nb_6O_{17}$. $K_4Nb_6O_{17}$ possesses two interlayer environments (interlayer I and II) with different reactivities. Potassium ions in the interlayer I can be easily exchanged while those in the interlayer II are relatively difficult to be replaced.

6.1.2. Experimental

Sample Preparations

n-Propylamine (1.0 ml) and water (20 ml) were added into thin platy transparent crystals of $K_4Nb_6O_{17} \cdot 3H_2O$ (0.10 g) with the size of several millimeters in width.   The mixture was sealed in a Teflon-lined vessel and allowed to stand at 120 °C. The mixture was not stirred to avoid the reduction of the size of exfoliated sheets during the reaction.   After the reaction for 1 day to 3 day, the slurry samples were swiftly and carefully analyzed by powder XRD.   On the other hand, the slurry obtained after the reaction at 120 °C for 1 day was allowed to stand for further one day to separate a supernatant layer and precipitates.   On separation, centrifugation was not used in order to avoid fragmentation.

Characterizations

AFM images of the exfoliated nanosheets were recorded on a Nanoscope E (Digital Instruments) in contact mode (height mode). The TEM image of the exfoliated nanosheet was observed by a JEOL JEM-100CX microscope with an accelerating voltage of 100 kV. The powder XRD patterns of the slurries were recorded on a Mac Science M03XHF[22] diffractometer using Mn-filtered Fe Kα radiation.

6.1.3. Results and Discussion

The powder XRD patterns of the slurries varied with the reaction time (Figure 1). After 1 day, a broad peak at lower than 5° was observed as well as those due to $K_4Nb_6O_{17} \cdot 4.5H_2O$ (2.06 nm, 1.03 nm, and 0.69 nm) and the PA-$K_xNb_6O_{17}$ intercalation compound (2.21 nm, 1.12nm, and 0.76 nm). When the reaction time was extended, the peaks due to both the hydrate and the intercalation compound disappeared and the patterns characteristic to exfoliation[12] were observed in which the baseline increased with lowering the diffraction angles. Consequently, the exfoliation was strongly suggested by intercalation of PA and the subsequent swelling with water to expand the interlayer space to unlimited region.

The AFM image (Figure 2) of the sample in the supernatant clearly shows the presence of very thin nanosheets with the thickness of about 2 nm. The size of the plate direction is several micrometers and very similar to those reported previously using $K_4Nb_6O_{17}$ microcrystals.[13] Mallouk et al. estimated that $K_4Nb_6O_{17}$ nanosheets exfoliated with tetra-n-butyl ammonium (TBA) cations were bilayers.[13] Therefore, the nanosheets obtained here are bilayers where the interlayer I was exfoliated whereas the interlayer II was not affected.
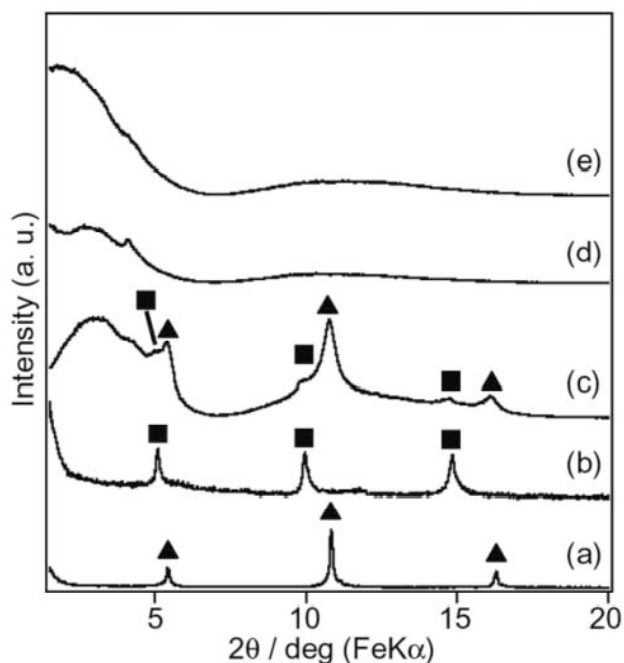
Figure 1. Variation in the powder XRD patterns of the slurries with the reaction time. (a) $K_4Nb_6O_{17} \cdot 4.5H_2O$, (b) PA-$K_xNb_6O_{17}$, the product obtained by hydrothermal treatment for (c) 1 day, (d) 2 days, and (e) 3 days. After the hydrothermal treatment for 1 day, a broad peak at lower than 5° was observed as well as those due to $K_4Nb_6O_{17} \cdot 4.5H_2O$ (▲: d = 2.06, 1.03, and 0.69 nm) and he PA-$K_xNb_6O_{17}$ intercalation compound (■: d = 2.21, 1.12, and 0.76 nm).
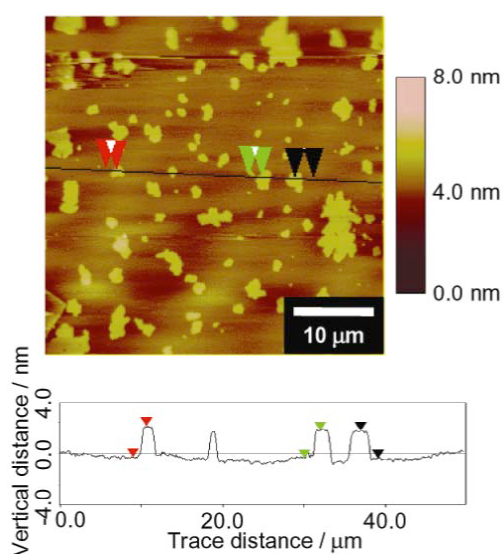
Figure 2. AFM image of the nanosheets in the supernatant.

149

On the other hand, the TEM image of the sample after the dispersion of the precipitates in water shows extraordinarily large nanosheets with several tens of micrometers in width (Figure 3).   The sheet is almost transparent, indicating the exfoliation to a higher degree. The thickness of the large nanosheets was estimated by AFM and the images are shown in Figure 4.   The nanosheets with the size from several tens of micrometers to 100 μm were clearly observed (Figure. 4a).   On the basis of many AFM data, we can state that the distribution of the size mainly varied from 10 μm to ca. 100 μm.   The thickness of the nanosheets was evaluated to be ca. 2 nm by using the image in which one nanosheet was placed on top of the other (Figure 4b).   Thus, the precipitates can also be exfoliated into nanosheets and that the size is much larger than that in supernatant.

When hexylamine (HA) was used instead of propylamine, exfoliation was not realized though an intercalation compound was formed.   HA is relatively hydrophobic and can not entrain water molecules after the intercalation.   TBA cations were also directly reacted with large $K_4Nb_6O_{17} \cdot 3H_2O$ crystals.   However, neither intercalation nor exfoliation was observed.   Accordingly, the selection of PA is quite appropriate for this type of reaction.

Although the present results show that the large nanosheets are prepared, a substantial reduction in size was observed. Nanosheets with the size of 100 μm were obtained though large crystals of several millimeters were used. The AFM image (Figure. 3a) also shows the possible presence of some cracks.   One of the reasons for this reduction in size is the influence of convection in an autoclave at 120 °C.   The other one is possibly due to cleavage by hydration of the crystals during the reaction.
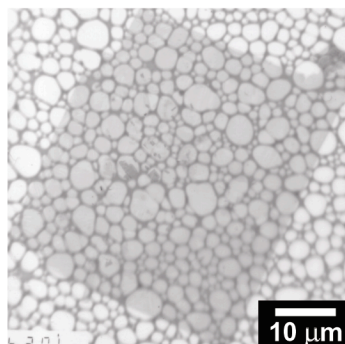
Figure 3. TEM image of the sample after dispersing the precipitates (120 °C, 1 day) in water.
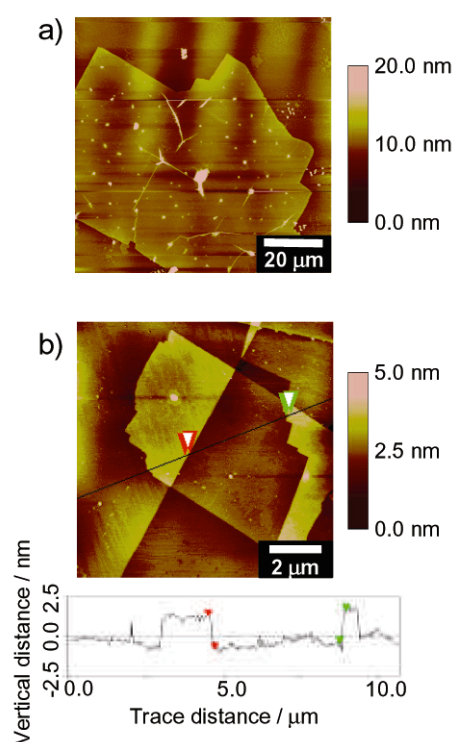
Figure 4. AFM images of the sample on mica surfaces after dispersing the precipitates (120 °C, 1 day) in water. (a) 100 μm × 100 μm and (b) 10 μm × 10 μm.

6.1.4. Conclusion

$K_4Nb_6O_{17} \cdot 3H_2O$ crystals were successfully exfoliated by the reaction with aqueous solution of propylammonium ions under hydrothermal condition. In the supernatant, nanosheets composed of bilayer sheets were formed with several micrometers in size. Nanosheets with 100 μm in size and about 2 nm in thickness were obtained from the precipitates and the size was much larger than those found previously. The research on various properties (electrical property, quantum size effect, and so on) of nanosheets themselves will be very interesting for nanotechnology. Films and nanocomposites using these large nanosheets will also be one of the next steps for applications.

6.1.5. References

(1) D. M. Kaschak, J. T. Lean, C. C. Waraksa, G. B. Saupe, H. Usami and T. E. Mallouk, *J. Am. Chem. Soc.*, **121**, 3435 (1999).

(2) R. Abe, K. Shinohara, A. Tanaka, M. Hara, J. N. Kondo and K. Domen, *Chem. Mater.*, **10**, 329 (1998).

(3) S. W. Keller, H.-N. Kim and T. E. Mallouk, *J. Am. Chem. Soc.*, **116**, 8817 (1994).

(4) T. Lan, P. D. Kaviratna and T. J. Pinnavaia, *Chem. Mater.*, **7**, 2144 (1995).

(5) H. Lee, L. J. Kepley, H. Hong and T. E. Malllouk, *J. Am. Chem. Soc.*, **110**, 618 (1988).

(6) T. Sasaki and M. Watanabe, *J. Am. Chem. Soc.*, **120**, 4682 (1998).

(7) H.-N. Kim, S. W. Keller and T. E. Mallouk, *Chem. Mater.*, **9**, 1414 (1997).

(8) D. M. Kaschak, S. A. Johnson, D. E. Hooks, H.-N. Kim, M. D. Ward and T. E. Mallouk, *J. Am. Chem. Soc.*, **120**, 10887 (1998).

(9) M. Kestigian, F. D. Leipziger, J. R. Carter and F. G. Garabedian, *J. Am. Ceram. Soc.*, **49**, 517 (1966).

(10) N. Miyamoto, K. Kuroda and M. Ogawa, *J. Am. Chem. Soc.*, **123**, 6949 (2001).

(11) T. Nakato and N. Miyamoto, *J. Mater. Chem.*, **12**, 1245 (2002).

(12) P. Joensen, R. F. Frindt and S. R. Morrison, *Mat. Res. Bull.*, **21**, 457 (1986).

(13) G. B. Saupe, C. C. Warasaka, H.-N. Kim, Y. J. Han, D. M. Kaschak, D. M. Skinner and T. E. Mallouk, *Chem. Mater.*, **12**, 1556 (2000).

6.2. Liquid Crystalline Nature of $K_4Nb_6O_{17}$ Nanosheet Sols and Their Macroscopic Alignment

6.2.1. Introduction

Inorganic frameworks with defined nanostructures such as layered solids have been utilized to fabricate nanomaterials by hybridizing various functional organic molecules.[1-3] Among inorganic solids, layered niobates and titanates have attracted interest for their photoactive character[4-6] as well as for intercalating capability.[7-9] Recent studies of the layered niobates and titanates[10-13] have clarified that these materials are exfoliated to provide peculiar inorganic "nanosheets" with the thickness of 1 - 2 nm and lateral dimension of 0.1 - 10 μm; the exfoliated layers retain the properties of the original solid such as defined crystal structure of the oxide layers. The exfoliated nanosheets have been used as, for example, modules to fabricate multi-layered films[14-18] and porous materials,[19, 20] which are applicable as integrated systems for photoenergy conversion. However, nanosheet sols of layered solids including the niobates and titanates, except for the smectite clay minerals, had scarcely been investigated from the viewpoint of colloid chemistry.[21, 22] Nakato and the present author have very recently found unusual pH-induced sol-gel transition of $[Nb_6O_{17}]^{4-}$ nanosheet colloids[23]; nevertheless colloids of smectite clays do not exhibit such behavior. This fact shows peculiarity of the niobate colloids and prompts us to investigate various other properties of the colloidal system.

In this chapter, liquid crystalline nature of the nanosheet colloids, which are prepared from layered niobate $K_4Nb_6O_{17}$, is revealed; the liquid crystalline sol was usable to organize cationic cyanine dye with macroscopic order. Although liquid crystalline properties are expected for the colloidal systems of inorganic nanosheets due to their anisotropic shapes,[24, 21, 22] there are only a few pioneering studies concerning V_2O_5,[25-27] and $H_3Sb_3P_2O_{14}$;[28] the most popular nanosheet colloids, smectite clays, do not behave as liquid crystals except under limited conditions.[29, 28] Due to the large lateral size of $[Nb_6O_{17}]^{4-}$ layers, the colloidal system of niobate nanosheets showed stable liquid crystallinity and unusual macroscopic alignment in cm-scale induced by gravitational

force. A cationic dye was directly immobilized on the mesogenic niobate nanosheets, indicating applicability of the colloidal nanosheets for matrices of functional molecules. The degrees of orientation of the samples were evaluated from dichroism of the aligned dye dipoles.

6.2.2. Experimental

<u>Sample Preparation</u>

$K_4Nb_6O_{17} \cdot 3H_2O$ was prepared by heating a mixture of K_2CO_3 and Nb_2O_5 according to the literature.[30] $K_4Nb_6O_{17} \cdot 3H_2O$ (1 g) was allowed to react with a 0.2 mmol dm^{-3} aqueous solution of propylamine hydrochloride (58 cm^3) at 353 K for 3 d. The reaction product was centrifuged and the deposit was washed twice with water. The obtained wet solid was re-dispersed in water (100–1000 cm^3) to form sols. Dye-modified sols were prepared by adding 0.5 cm^3 of aqueous solution (5 × 10^{-5} mol dm^{-3}) of a cationic cyanine dye salt, 1,1'-diethyl-2,2'-cyanine bromide, to 4.5 cm^3 of the sols with varied $[Nb_6O_{17}]^{4-}$ concentration. The $[Nb_6O_{17}]^{4-}$ concentrations in the sols were finally adjusted to 9.6 × 10^{-4} - 9.6 × 10^{-5} mol dm^{-3} (ca. 0.1-1 in mass %).

<u>Characterizations</u>

The samples were observed with an Olympus BX-50 polarizing microscope attached with a color CCD camera; the setup of a sample cell, polarizers and a wave plate (Olympus U-TP530) are schematically shown in Figure 1d. The photographs of the oriented samples in test tubes were recorded with a digital camera using crossed polarizers and the wave plate. Polarized visible spectra were measured on a JASCO Ubest-55 spectrophotometer placing a polarizer between monochromated light and a sample.

6.2.3. Results and Discussion

Stable Liquid Crystallinity of the Niobate Nanosheet Colloids

The birefringence of the $[Nb_6O_{17}]^{4-}$ nanosheet colloids clearly demonstrated the liquid crystalline nature of the system. Figure 1a shows a typical image of a sol containing 9.6×10^{-3} mol dm^{-3} of $[Nb_6O_{17}]^{4-}$ layers in a 1 mm-thick cell observed with optical microscopy between crossed polarizers. The marble pattern with various interference colors due to birefringence of the sample is characteristic to liquid crystalline phases.[21, 22] Although the type of the liquid crystal has not been identified, lamelar[28] and columnar[31] as well as nematic phases, can occur for the present nanosheet colloid.
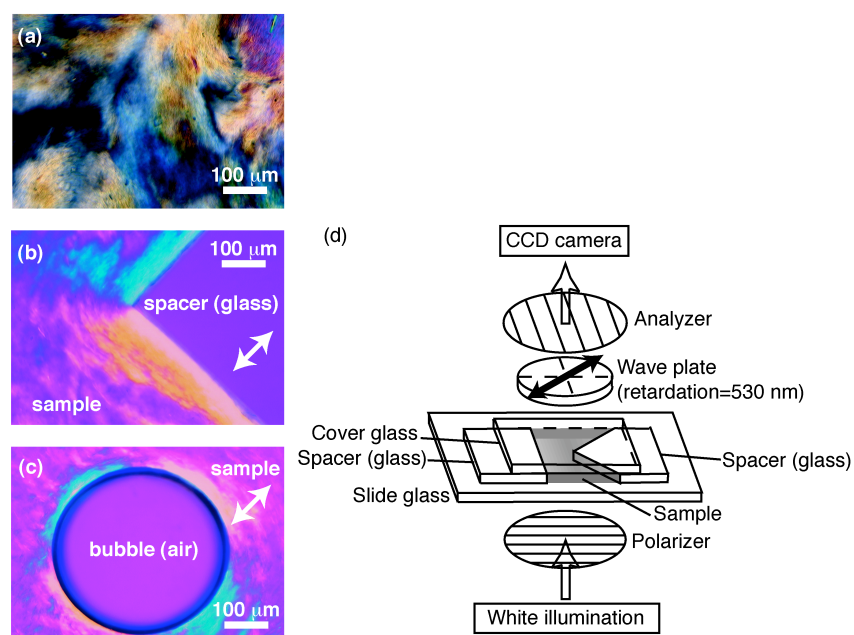
Figure 1. Microscopic images of the sols containing 9.6×10^{-4} mol dm^{-3} of $[Nb_6O_{17}]^{4-}$ placed in a cell with the thickness of (a) 1 mm and (b)(c) 0.2 mm. The images were observed between crossed polarizers whose directions are indicated by double arrows. A wave plate (optical retardation=530 nm) was used for the observations (b) and (c) with the "slow-vibrational direction" of the plate as indicated by bold arrows; schematic illustration used for the observations (b and c) is shown in (d).

The liquid crystalline state of the niobate nanosheets is highly stable.   The colloid kept birefringence even at the concentration of 4×10^{-4} mol dm^{-3} or ca. 0.04 mass % of $[Nb_6O_{17}]^{4-}$ layers.   Although birefringence of the colloidal dispersions of inorganic oxide nanosheets has already been observed for V_2O_5,[25-27] $H_3Sb_3P_2O_{14}$,[28] they show transition to isotropic phases at certain concentrations (e.g. the V_2O_5 system transits to isotropic at < 0.5 mass %).   Colloids of smectite clay minerals show birefringence only under shear[29] or in the state of gel at high concentrations.[28] Whereas there are several liquid crystalline colloidal systems composed of anisotropic inorganic solids other than nanosheets[21, 22] such as boehmite rods[32, 33] and gibbsite plates,[34, 31] they also show transition to isotropic phase at concentrations of around 0.7-10 mass% for the rods and around 16 mass% for the plates, respectively.   Since isotropic phases was not observed in the present system down to ca. 0.04 mass%, the concentration of transition is lower than other systems.

Macroscopic Alignment of the Liquid Crystals

Macroscopic alignment of the liquid crystalline sols in cm-scale was induced by rotating the test tube (1 cm in diameter) filled with a sample for only several seconds. Figs. 2a and 2b show the photographs of an aligned sample (concentration of $[Nb_6O_{17}]^{4-}$ is 9.6×10^{-4} mol dm^{-3}) observed between crossed polarizers.   The aligned domain of the sample appears most bright when the crossed polarizers are set inclined 45° to the ground (Figure 2a), indicating that this is "diagonal position", while it turned dark (Figure 2b) at the "extinction position" (the position turned by 45° from the "diagonal position").   The aligned domain is preferentially observed along the tube wall, indicating that the macroscopic orientation was induced by shear flow of the sol along the wall.

The liquid crystalline sols were aligned even by gravitational force by standing the sample for several minutes.   The alignment was observed not only at the vicinity of the tube wall but over the whole domain of the sample.   Figs. 2c and 2d show the photographs of an aligned sample (concentration of $[Nb_6O_{17}]^{4-}$ is 9.6×10^{-4} mol dm^{-3}) between crossed polarizers.   The whole domain of the sample turns bright

(Figure 2c) and dark (Figure 2d) upon rotation of the crossed polarizers between diagonal and extinction positions, indicating the formation of a macroscopically oriented domain in cm-scale.   There are few reports of liquid crystalline sols of inorganic compounds (nanosheets, rods and plates) aligned in cm-scale.[21, 22]   Even in rare cases, the alignment was achieved by continuous shearing,[25, 28] application of magnetic field[27, 28] and careful gelation.[35]   To our knowledge, the present study is the first example of macroscopic alignment of inorganic colloids by gravitational force.

(a)   (b)   (c)   (d)   (e)   (f)
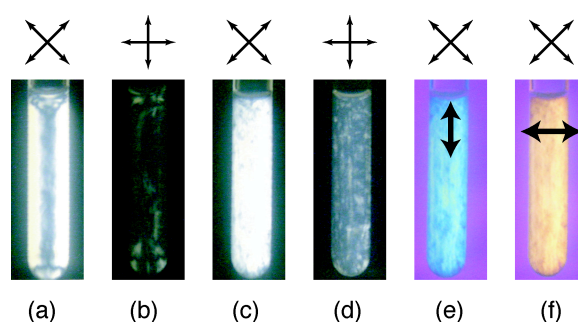
Figure 2.   Photographs of the sols containing 9.6×10^{-5} mol dm^{-3} of $[Nb_6O_{17}]^{4-}$ in a test tube (1 cm in diameter) observed between crossed polarizers whose directions are indicated by double arrows.   The images were taken after several seconds of rotation for (a) and (b) and after standing the sample for 60 minutes for (c)-(f).   A wave plate (optical retardation=530 nm) was used in the observations (e) and (f) setting the "slow-vibrational direction" as indicated by bold arrows.

        The high capability of the present system to form macroscopic ordering, even by gravitational force, was further exemplified by microscopic observations of the sample near interfaces between crossed polarizers with a wave plate.   The wave plate is used to identify the direction of the optic axis of a birefringent domain, because the observation with crossed polarizers alone cannot give the information on the direction of the optic axis.   The plate alone between crossed polarizers appears purple, which is

the interference color at the optical retardation (the product of birefringent index and the thickness of colloid) of the plate (530 nm). When the plate is set with its "slow-vibrational direction" parallel to the optic axis of an oriented domain, the optical retardation due to the domain is added to that given by the plate, so that the domain is observed blue, whereas the interference color turns to yellow when the directions are perpendicular to each other. Figs. 1b and 1c shows a typical image of the sample containing 9.6×10^{-5} mol dm^{-3} of $[Nb_6O_{17}]^{4-}$ placed in a 0.2 mm-thick cell, observed by optical microscope between crossed polarizers with the wave plate. The domains around the water-solid (glass) (Figure 1b) or water-air (bubble) (Figure 1c) interfaces parallel to the "slow-vibrational direction" of the wave plate (indicated by a bold arrow) are observed blue, while the domains around the other side of the interfaces at the perpendicular positions appears yellow. According to the observed interference colors, the optic axes are oriented along the water-solid (glass) (Figure 1b) or water-air (bubble) interfaces (Figure 1c). This result indicates that interfacial tension induced the orientation of the niobate nanosheets over sub-mm domain.

By using the wave plate for macroscopic observation, the optic axis of the sample aligned in a test tube was determined to be vertical to the ground. Figure 2e shows the photograph of the sample between crossed polarizers observed with the wave plate whose "slow vibrational direction" is set vertical to the ground. The sample appears blue over the whole domain in this setup. The relation of the sample color and the direction of the wave plate indicates that the optic axis of the sample is parallel to the slow-vibrational direction of the wave plate, vertical to the ground. When the slow-vibrational direction of the plate was set horizontal to the ground, the sample appeared yellow (Fig 2f), supporting vertical optic axis. This is the first case to determine the optic axis of a macroscopically aligned mineral liquid crystal using a wave plate.

The easily induced macroscopic alignment observed for the liquid crystal of niobate nanosheet sols is rationalized by large lateral size of the $[Nb_6O_{17}]^{4-}$ nanosheets. The mean lateral dimension of exfoliated nanosheets of $K_4Nb_6O_{17}$ observed by AFM or TEM is typically around 1-2 mm.[36] This size is much larger than the dimensions of

ever studied inorganic colloids such as rods of boehmite,[32, 33] plates of gibbsite[34, 31] and nanosheets of smectite clays[29, 28], $H_3Pb_3P_2O_{14}$.[28] and V_2O_5.[25-27]. The high stability of alignment is rationalized by Onsager's theory, which indicates that larger exclusive volume of mesogenic particles serves to orient platy colloidal particles in higher order[24] as well as to stabilize the liquid crystalline state (i.e. to lower the critical concentration of isotropic-to-nematic transition).[24, 37, 38]

Hybridization with a Cationic Dye

The present system can be used as a new-type anisotropic nanohybrid in the form of sol. Nanosheet colloids were hybridized with a dye and the dichroism of the visible absorption spectra of the dye was measured, as the first step of such application. As is established for several layered solids,[39, 9, 40] a cationic cyanine dye was electrostatically adsorbed onto the negatively charged $[Nb_6O_{17}]^{4-}$ nanosheets.[39] Thus, the niobate sheets were hybridized with the dye as the first example of dye-modified mesogenic unit of inorganic liquid crystal. The supernatant after centrifugation (at 11000 rpm for 30 minutes) of the sol added with cyanine dye solution was colorless, indicating that all the dye cations were adsorbed onto the nanosheets. Figure 3 shows the polarized visible spectra of the sample added with the dye. Sharp absorption band (J-band) appeared around 580 nm, showing the presence of cyanine dye J-aggregates formed during adsorption.[39, 9, 40] The presence of the J-aggregates clearly proved the immobilization of the dyes on the nanosheets since only monomers, whose absorption maximum is around 525 nm, were present in the original dye solution.

The degree of orientation of the macroscopically aligned dye-modified sol was estimated by polarized visible spectra. Since the dipoles of J-aggregate of the dye is flat on the niobate layers,[40] the degree of orientation is derived from the dichroic ratio of the J-band is. The J-band measured at the vertical polarization position (Figure 3⊥) showed larger absorbance compared to the band observed at the horizontal position (Figure 3//), indicating that both the dipoles and nanosheets are preferentially aligned along normal of the ground. This direction coincides with the direction of the optic axis determined by using the wave plate. The dichroic ratio of the band became large

with increased concentration of $[Nb_6O_{17}]^{4-}$ (the inset of Figure3).   This result indicates

that the orientation was enhanced at a higher concentration of $[Nb_6O_{17}]^{4-}$.   This finding

coincides with the prediction by Onsager:[24] higher colloid concentration leads to higher

degree of orientation of anisotropic particles in a liquid crystalline state.
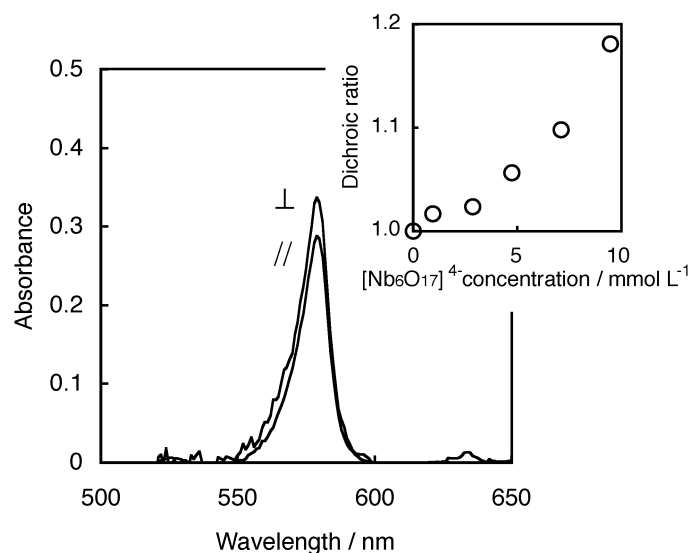
Figure 3.   Polarized visible spectra of the dye-modified sol ($[Nb_6O_{17}]$ = 9.6 × 10^{-4} mol dm^{-3}, [dye] = 5 × 10^{-6} mol dm^{-3}) after relaxation measured at the polarization directions vertical($\perp$) and horizontal(//) to the ground: the spectra shown were obtained after removing background from raw spectra.   The inset shows the relationship between $[Nb_6O_{17}]^{4-}$ concentration and the dicroic ratio(=$A_\perp/A_{//}$), where $A_\perp$ and $A_{//}$ are the absorbances at 580 nm in the polarized spectra.

6.2.4. Conclusions

The liquid crystalline nature of layered niobate nanosheet sols was revealed. The obtained liquid crystal was easily aligned macroscopically in cm-scale by gravitational force as well as by shear flow and interfacial tension. A cationic cyanine dye was immobilized onto the nanosheets and the dye dipoles were macroscopically aligned, showing a potential application of related systems as anisotropic and soft matrices for functional species. Exploitation of semiconducting nature[4-6] and peculiar in-plane organization capability in nanometer-scale[40] of $K_4Nb_6O_{17}$ will lead to unusual materials, which cannot be derived from clays etc. Exfoliation of layered niobates[13] and titanates[11] has recently been vigorously studied. Since these materials can also exhibit liquid crystalline nature (e.g. colloidal sols of $[TiNbO_5]^-$ and $[Nb_3O_8]^-$ were recently found to show liquid crystallinity[41]) the studies with series of the materials may lead to wide variety of future advanced material.

6.2.5. References

(1) M. S. Whittingham, A. J. Jacobson, *Intercalation Chemistry*. M. S. Whittingham, A. J. Jacobson, Eds. (Academic Press, New York, 1982).

(2) G. A. Ozin, *Adv. Mater.,* **4**, 612 (1992).

(3) M. Ogawa, K. Kuroda, *Chem. Rev.,* **95**, 399 (1995).

(4) K. Domen, A. Kudo, M. Shibata, A. Tanaka, K. Maruya, T. Onishi, *J. Chem. Soc., Chem. Commun.*, 1706 (1986).

(5) Y. I. Kim, S. Salim, M. J. Huq, T. E. Mallouk, *J. Am. Chem. Soc.,* **113**, 9561 (1991).

(6) A. Kudo, T. Sakata, *J. Phys. Chem.,* **100**, 17323 (1996).

(7) T. Nakato, K. Kuroda, C. Kato, *Chem. Mater.,* **4**, 128 (1992).

(8) T. Nakato, K. Kusunoki, K. Yoshizawa, K. Kuroda, M. Kaneko, *J. Phys. Chem.*, **99**, 17896 (1995).

(9) N. Miyamoto, K. Kuroda, M. Ogawa, *Mol. Cryst. Liq. Cryst.,* **341**, 259 (2000).

(10) M. M. J. Treacy, S. B. Rice, A. J. Jacobson, J. T. Lewandowski, *Chem. Mater,* **2**, 279 (1990).

(11) T. Sasaki, M. Watanabe, H. Hashizume, H. Yamada, H. Nakazawa, *J. Am. Chem. Soc.,* **118**, 8329 (1996).

(12) Y.-S. Han, I. Park, J.-H. Choy, *J. Mater. Chem.,* **11**, 1277 (2001).

(13) J.-Y. Kim, I. Chung, J.-H. Choy, *Chem. Mater.,* **13**, 2759 (2001).

(14) S. W. Keller, H.-N. Kim, T. E. Mallouk, *J. Am. Chem. Soc.,* **116**, 8817 (1994).

(15) H.-N. Kim, S. W. Keller, T. E. Mallouk, *Chem. Mater.,* **9**, 1414 (1997).

(16) R. Abe, M. Hara, J. N. Kondo, K. Domen, *Chem. Mater.,* **10**, 1647 (1998).

(17) M. Fang, C. H. Kim, G. B. Saupe, H.-N. Kim, C. C. Waraksa, T. Miwa, A. Fujishima, T. E. Mallouk, *Chem. Mater.,* **11**, 1526 (1999).

(18) D. M. Kaschak, J. T. Lean, C. C. Waraksa, G. B. Saupe, H. Usami, T. E. Mallouk, *J. Am. Chem. Soc.,* **121**, 3435 (1999).

(19) R. Abe, K. Shinohara, A. Tanaka, M. Hara, J. N. Kondo, K. Domen, *Chem. Mater.,* **9**, 2179 (1997).

(20) T. Sasaki, S. Nakano, S. Yamauchi, M. Watanabe, *Chem. Mater.,* **9**, 602 (1997).

(21) A. S. Sonin, *J. Mater. Chem.,* **8**, 2557 (1998).

(22) J.-C. P. Gabriel, P. Davidson, *Adv. Mater.,* **12**, 9 (2000).

(23) T. Nakato, N. Miyamoto, *J. Mater. Chem.,* **12**, 1245 (2002).

(24) L. Onsager, *Ann. NY Acad. Sci.,* **51**, 627 (1949).

(25) O. Pelletier, C. Bourgaux, O. Diat, P. Davidson, J. Livage, *Eur. Phys. J. B,* **12**, 541 (1999).

(26) S. Lamarque-Forget, O. Pelletier, I. Dozov, P. Davidson, P. Martinot-Lagarde, J. Livage, *Adv. Mater.,* **12**, 1267 (2000).

(27) H. Desvaux, J.-C. P. Gabriel, P. Berthault, F. Camerel, *Angew. Chem. Int. Ed.,* **40**, 373 (2001).

(28) J.-C. P. Gabriel, F. Camerel, B. J. Lemaire, H. Desvaux, P. Davidson, P. Batail, *Nature,* **413**, 504 (2001).

(29) I. Langmuir, *J. Chem. Phys.,* **6**, 873 (1938).

(30) K. Nassau, J. W. Shiever, J. L. Bernstein, *J. Electrochem. Soc.,* **116**, 348 (1969).

(31) F. M. van der Kooij, K. Kassapidou, H. N. W. Lekkerkerker, *Nature,* **406**, 868 (2000).

(32) P. A. Buining, H. N. W. Lekkerkerker, *J. Phys. Chem.,* **97**, 11510 (1993).

(33) P. A. Buining, A. P. Philipse, H. N. W. Lekkerkerker, *Langmuir,* **10**, 2106 (1994).

(34) F. M. van der Kooij, H. N. W. Lekkerkerker, *J. Phys. Chem. B,* **102**, 7829 (1998).

(35) J.-C. P. Gabriel, C. Sanchez, P. Davidson, *J. Phys. Chem.,* **100**, 11139 (1996).

(36) G. B. Saupe, C. C. Waraksa, H.-N. Kim, Y. J. Han, D. M. Kaschak, D. M. Skinner, T. E. Mallouk, *Chem. Mater.,* **12**, 1556 (2000).

(37) R. Eppenga, D. Frenkel, *Mol. Phys.,* **52**, 1303 (1984).

(38) M. Bates, D. Frenkel, *J. Chem. Phys.,* **110**, 6553 (1999).

(39) M. Ogawa, R. Kawai, K. Kuroda, *J. Phys. Chem.,* **100**, 16218 (1996).

(40) N. Miyamoto, K. Kuroda, M. Ogawa, *J. Am. Chem. Soc.,* **123**, 6949 (2001).

(41) T. Nakato, N. Miyamoto, A. Harada, *Chem. Commun.,* 78 (2004).

6.3. Liquid Crystalline Nanosheet Colloids with Controlled Particle Size Obtained by Exfoliating Single Crystal of Layered Niobate K₄Nb₆O₁₇

6.3.1. Introduction

Exfoliation of inorganic layered materials into their elementary layers has attracted keen interest in the last decade, because the exfoliated inorganic nanosheets with the thickness of several nanometers and width of up to several micrometers are useful modules for constructing novel nanomaterials. In addition to historically studied clay minerals,[1-10] various layered solids have been exfoliated: chalcogenides,[11,12] phosphates,[13-18] graphite oxide,[19] layered double hydroxides,[20] niobates,[14,16,21-27] titanates,[28-37] and other metal oxides.[38,39] The nanosheets obtained have widely been utilized as modules to fabricate solid nanohybrids by reconstructing the exfoliated nanosheets into cast films,[8,12,23,31,40] layer-by-layer self-assemblies,[9,14-16] electrophoretically deposited films,[33,41] porous solids,[24,29] and nanosheet-polymer composites.[34,42,43] In particular, nanosheets of layered niobates exemplified by $K_4Nb_6O_{17}$, $HTiNbO_5$, and $HCa_2Nb_3O_{10}$, have been paid attention, because of the potential application for advanced materials with the use of their photoactive nature[44-46] and capability of organizing guest species on the layer surface.[47]

Chapter 6.2 revealed that the colloids of niobate nanosheets prepared by exfoliation of layered niobate $K_4Nb_6O_{17}$ exhibit peculiar liquid crystalline behavior[48] as well as pH-induced sol–gel transition.[49] The nanosheet of $K_4Nb_6O_{17}$ are also interested due to the coiling behavior, whereas pH-induced sol–gel transition has been reported elsewhere.[50] Liquid crystallinity of the nanosheet colloids of layered $H_3Sb_3P_2O_{14}$ has also been reported a little while before our finding.[18] These findings demonstrate another novel aspect of the nanosheets other than modules of solid materials, and will lead to rediscovery of the colloidally dispersed inorganic layered materials as soft materials. Inorganic nanosheets may be utilized in colloidal states as novel soft materials with macroscopic alignment; they are distinguished from other assemblies of the nanosheets by their orientationally ordered soft structure.

The liquid crystallinity of the dispersed nanosheets is in particular of great interest both from fundamental aspects and for applications as advanced materials.[18,51,52] Liquid crystalline nanosheet colloids are classified into lyotropic liquid crystals of anisotropic particles with relatively large molecular weights, being distinguished from thermotropic liquid crystals. Theoretical[53-57] and simulation[58-61] studies have verified that colloidally dispersed anisotropic particles (rods and plates) generally form lyotropic liquid crystals because of excluded-volume effects working among the particles. The lyotropic liquid crystals of anisotropic particles are potentially applicable as optical, magnetic and electric devices,[27,52,62] templates for porous materials,[50,63] soft matrices of functional molecules,[48] etc.

However, liquid crystallinity of the nanosheet colloids has not been well-understood due to the paucity of systematic studies; only a limited number of colloidal plates have been reported to form liquid crystalline phases, whereas larger number of colloidally dispersed rods have been found to form liquid crystals: e.g., viruses,[64] chain polymers,[55,65] DNA,[66,67] surfactant micelles and inorganic nanoparticles.[51,52,62] Nanosheet colloids of natural and synthetic layered clay minerals[1-7] have been studied for long time, and known to form liquid crystalline phases. Nevertheless, they are observed only with gelation of the colloids; thus details of the clay liquid crystals are still unclear. As another example, colloidally dispersed V_2O_5 nanosheets[68,69] were discovered in 1920's and have been known to show liquid crystallinity; nevertheless, they are recognized as colloids of oblate rods rather than sheets due to the ribbon-like shape with the dimension of e.g. ca. $1 \times 10 \times 1000$ nm^3 of V_2O_5 layers.[70] Recently reported are colloidal plates (not nanosheets) of gibbsite[71,72] and nickel hydroxide,[73,74] characterized by relatively small aspect ratios and low polydispersity; they are used as excellent model systems of theoretical investigations.

This chapter describes the preparation and liquid crystallinity of exfoliated layered niobate $K_4Nb_6O_{17}$ with controlled lateral size and fixed thickness of 1.8 nm; the dependence of the liquid crystallinity on the lateral size and concentration of the nanosheets are demonstrated. The use of $K_4Nb_6O_{17}$ single crystals as the starting material allowed us to control the lateral dimension over an extremely wide range. A

novel fundamental aspect of colloidally dispersed inorganic nanosheets is clarified; it is of significance in manipulating the inorganic layered materials with the delamination technique for constructing various assemblies.

6.3.2. Experimental

Preparation of the Niobate Nanosheet Sols with Controlled Particle Sizes by Exfoliation of K$_4$Nb$_6$O$_{17}$ Single Crystal

Single crystals of K$_4$Nb$_6$O$_{17}$ was used as the starting material in order to obtain large nanosheets by exfoliation.[26]   K$_4$Nb$_6$O$_{17}$ single crystals were prepared by a flux method according to the literature:[75,76] a mixture of K$_2$CO$_3$ and Nb$_2$O$_5$ (1:1.1 in molar ratio) was heated at 1323 K, and then cooled gradually.   The obtained single crystalline K$_4$Nb$_6$O$_{17}$ (2 - 10 mm in width and 1 - 2 mm in thickness, 5 g) were allowed to react with a 0.2 mmol·dm^{-3} aqueous solution of propylamine hydrochloride at 353 K for 9 d. The reaction product was centrifuged and the deposit was washed three times with water.   The obtained wet deposit was redispersed in water (500 dm^3) to form a nanosheet sol ([Nb$_6$O$_{17}{}^{4-}$] = 2.4 × 10^{-2} mol·dm^{-3} or volume fraction ϕ = 6.3 × 10^{-3}).   The volume fraction ϕ of the sol was calculated according to

$$\phi = [\mathrm{Nb_6O_{17}}{}^{4-}]\frac{2acL}{Z}N_A$$

where [Nb$_6$O$_{17}{}^{4-}$] is the molar concentration of the niobate, a and c (= 0.76 and 0.64 nm) the lattice parameters of K$_4$Nb$_6$O$_{17}$, Z (= 4) the number of K$_4$Nb$_6$O$_{17}$ molecules included in its unit cell, L the thickness of nanosheets, and N_A the Avogadro constant. L is estimated as 1.8 nm corresponding to the sum of thicknesses of two [Nb$_6$O$_{17}$]$^{4-}$ layers, because K$_4$Nb$_6$O$_{17}$ has been reported to be exfoliated with every other interlayer spaces to form bilayer nanosheets.[22,26]

The nanosheet sol prepared from the single crystals was ultrasonicated for 0, 10, 50, 90 and 180 min to yield the nanosheets with reduced lateral sizes.   After the ultrasonication, the concentrations of the colloids were adjusted to ϕ = 5.1 × 10^{-6} – 2.8 × 10^{-2} by adding or evaporating water (by heating at 353 K).   A nanosheet sol was also obtained from powders of K$_4$Nb$_6$O$_{17}$,[48] which was prepared by a conventional solid-state

reaction, for comparison of the lateral size and for determining the composition of the exfoliated nanosheets.

Characterization of the Nanosheet Sols

Liquid crystallinity of the nanosheet sols was investigated by observing their birefringent nature. The colloids in a test tube or a glass capillary were observed between crossed polarizers and were recorded on a digital camera. Microscope observations of the colloids were carried out with an Olympus BX-51 optical microscope between crossed polarizers.

Transmission electron microscope (TEM) images of the nanosheets in the colloids were taken by using a Hitachi H-7100 microscope operating at 100 kV. A nanosheet sol was added with methanol (water : methanol = 1 : 9 in volume), and loaded on a grid coated with collodion membrane followed by drying under ambient conditions. When the colloid was loaded without addition of methanol, nanosheets were aggregated on the membrane due to high hydrophobicity of the membrane.

Concentration of the nanosheets was determined by UV spectroscopy using a JASCO Ubest–55 spectrophotometer for concentrated sols obtained after partial evaporation of water. The $[Nb_6O_{17}]^{4-}$ nanosheets showed an absorption band centered at 224 nm with the molar absorption coefficient of 7.6×10^5 mol^{-1} (of $[Nb_6O_{17}]^{4-}$) dm^3 cm^{-1}, being independent on the lateral size of the nanosheets. XRD patterns of the sols after drying on glass plates were recorded on a MAC Science MX Labo diffractometer (monochromatic CuKα radiation; the tube voltage and currents are 40 kV and 30 mA). Composition of the powders obtained by evaporating water from the nanosheet colloid (prepared from powders of $K_4Nb_6O_{17}$) was determined by X-ray fluorescence spectroscopy (XRF) using a Rigaku RIX-3100 wave-dispersed X-ray fluorescence analyzer and CHN analysis. The viscosity of the colloid was measured with Ubbelohde-type viscometers.

6.3.3. Results

Formation of the Nanosheet Sols with Controlled Particle Size

Exfoliation of the single crystal of $K_4Nb_6O_{17}$ yielded large niobate nanosheets. Figure 1a shows a typical TEM image of the nanosheets before sonication. Rectangular plates with the lateral sizes of up to ca. 100 μm are observed. Distribution of D, the lateral size, was estimated as Figure 2a by measuring the lengths of the edges of the plates observed in the TEM images (over 100 edges were measured). Since D obviously has a log-normal distribution, the mean lateral size D_m and polydispersity $\sigma_{(\log)}$ on the logarithmic scale are estimated as $D_m = 10^{<\log D>} = 7.8$ μm and $\sigma_{(\log)} = (<(\log D)^2> - <\log D>^2)^{1/2} / <\log D> = 9.2$ %, respectively. This polydispersity corresponds to –56 % and +128 % on normal scale. In contrast to the nanosheets obtained from single crystal, D_m and $\sigma_{(\log)}$ are estimated as 3.6 μm and 9.8 % for the nanosheets from the $K_4Nb_6O_{17}$ powders (Figure 2f), indicating that the difference in starting $K_4Nb_6O_{17}$ affects the lateral size of the exfoliated nanosheets.

Treatment of the sol prepared from single crystalline $K_4Nb_6O_{17}$ with ultrasonication effectively reduced the lateral sizes of the nanosheets. Figures 1c and d show typical TEM images of the nanosheets obtained by 50 and 180 min of ultrasonication, and Table 1 summarizes D_m and $\sigma_{(\log)}$ of the sonicated sols. The TEM images demonstrate that the nanosheets after sonication possessed rectangular shapes similar to those before sonication, while that the lateral size is reduced with prolonged sonication. Figures 2b, c, d, and e indicate distributions of the lateral size obtained from TEM images for the colloids after 10, 50, 90 and 180 min of sonication, respectively. All the sols give log-normal distributions similar to that for the as-prepared sol, and D_m is reduced from 7.8 μm to 6.2, 1.9, 0.38 and 0.15 μm after ultrasonication for 10, 50, 90 and 180 min, respectively. $\sigma_{\log}$ is kept almost unchanged around 6.8 – 11 %.
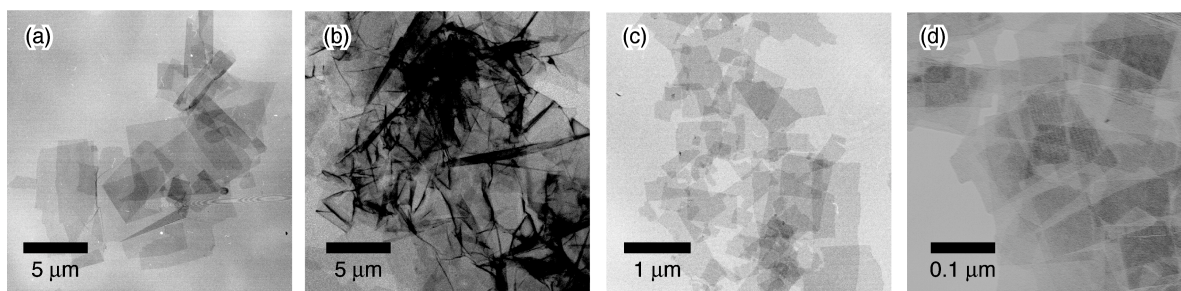
Figure 1. The TEM images of the nanosheets obtained from $K_4Nb_6O_{17}$ single crystals after (a)(b) 0, (c) 50 and (d) 180 min of ultrasonication. For the observation (b), the colloid was loaded on the grid without adding methanol.
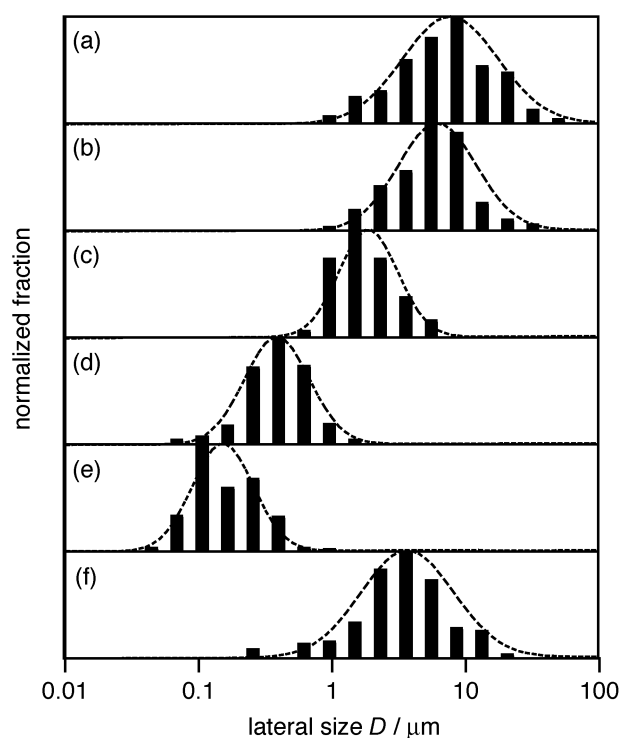
Figure 2. The size distributions of the nanosheets obtained from (a)-(e) single crystals and (f) powders of $K_4Nb_6O_{17}$ with (a) 0, (b) 10, (c) 50, (d) 90, (e) 180 and (f) 0 min of ultrasonication. The dashed lines represent the logarithmic Gaussian distributions with the mean lateral size $D_m = 10^{<\log D>}$ and the polydispersity $\sigma_{(\log)} = <(\log D)^2> - <\log D>^2)^{1/2}$ / $<\log D>$.

Table 1.   The mean lateral sizes and the critical concentrations of phase transitions

ultrasonication / min	D_m / μm	$\sigma_{(log)}$ / %	$\phi_I{}^*$ (vol / vol)	$\phi_{LC}{}^{**}$ (vol / vol)
0	7.8	9.2	$< 5 \times 10^{-6}$	$\sim 3 \times 10^{-3}$
10	6.2	7.7	$< 5 \times 10^{-6}$	$\sim 5 \times 10^{-3}$
50	1.9	6.8	1.9×10^{-3}	1.9×10^{-2}
90	0.38	9.5	7.3×10^{-3}	2.3×10^{-2}
180	0.15	11	1.0×10^{-2}	2.6×10^{-2}
0 (from powder)	3.6	9.8		

*The concentration where the colloid transits from isotropic to biphasic
**The concentration where the colloid transits from biphasic to liquid crystalline

<u>Intrinsic Properties of the Niobate Nanosheets.</u>

The TEM observations also give information on intrinsic properties of the niobate nanosheets, the properties which are independent on their lateral sizes.   Figure 1b exemplifies flexibility of the nanosheets caused by their thinness.   When the sols were mounted on the TEM grids without addition of methanol, the nanosheets are aggregated, bent and crumpled without cleavage, due to high hydrophobicity of the membrane spread on the grid.   The flexibility of the $[Nb_6O_{17}]^{4-}$ nanosheets has already been indicated as their coiling to form nanotubes under lowered pHs.[22,26]   Flexibility of the nanosheets should affect the behavior of the nanosheets in colloidal states.

The uniformly low contrast of the nanosheets observed in TEM images strongly suggests that all the nanosheets are similar in thickness, probably because of entire exfoliation, regardless of their lateral sizes.   In addition, XRD patterns of the films prepared by drying the colloids after 0 and 180 min of the sonication on glass plates (Figure S3) evidence that propylammonium ions are intercalated into every other interlayer space of $K_4Nb_6O_{17}$ to exfoliate the niobate as bilayer nanosheets with the thickness of 1.8 nm.[22,26,77]   The composition of the powders recovered by drying the nanosheet colloid (prepared from powdery $K_4Nb_6O_{17}$) is determined as $K_{3.1}(C_3H_7NH_3)_{0.9}Nb_6O_{17}$, also confirming the bilayer structure.
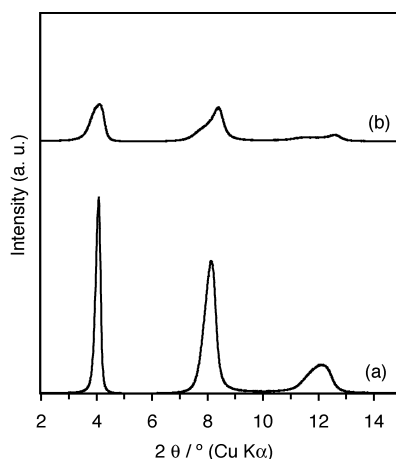
Figure 3. XRD patterns of the colloids dried on a glass plate: D_m = (a) 7.8 and 0.15 µm.

Liquid Crystallinity of the Niobate Nanosheet Sols.

Liquid crystallinity of the as-prepared (before ultrasonication) $[Nb_6O_{17}]^{4-}$ nanosheet sols is confirmed by observing them between crossed polarizers. Figure 4a shows a typical photograph of a nanosheet sol before ultrasonication (D_m = 7.8 µm; ϕ = 6.3 × 10^{-3} vol.-%) observed between crossed polarizers. The sol clearly shows birefringence. The optical microscope image of the same colloid shown in Figure 5a exhibits textures due to birefringent liquid crystalline domains. Resemblance of the textures to those reported for nematic phases of colloidal plates in the literatures[51,52] suggests that the sol forms a nematic phase, whereas formation of lamellar phase is also possible as is observed for nanosheet colloid of $H_3Sb_3P_2O_{14}$.[18] Occurrence of columnar phase is not probable since it only appears in the colloidal disks with small polydispersity in diameter.[78] Further clarification on the structure of the liquid crystalline sols is now underway by using small-angle neutron scattering and will be published elsewhere.

Images of the colloids between crossed polarizers confirm that the colloids after ultrasonication of 50 min (D_m = 1.9 µm) and 180 min (D_m = 0.15 µm) also show liquid crystallinity similar to the colloid before sonication. The observations by naked eyes (Figures 3b and d) clearly prove the birefringence of the sols (D_m = 1.9 µm, ϕ = 6.3

172

$\times$ 10^{-3}; D_m = 0.15, ϕ = 2.8 $\times$ 10^{-2}).   The microscope images (Figures 5b and c) also characterize the liquid crystallinity of the sols.
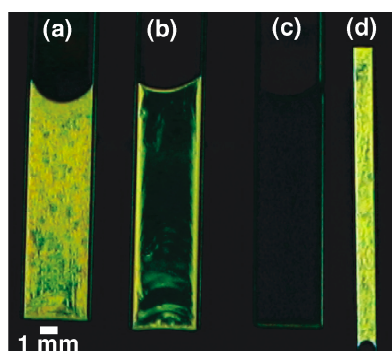
Figure 4.   The photographs of the nanosheet colloids with D_m = (a) 7.8 μm, (b) 1.9 μm, and (c)(d) 0.15 μm, and ϕ = (a)-(c) 6.3 $\times$ 10^{-3} and (d) 2.8 $\times$ 10^{-2}.   The colloids in flat glass capillaries with the thickness of (a)-(c) 0.4 mm and (d) 0.1 mm were observed between crossed polarizers.
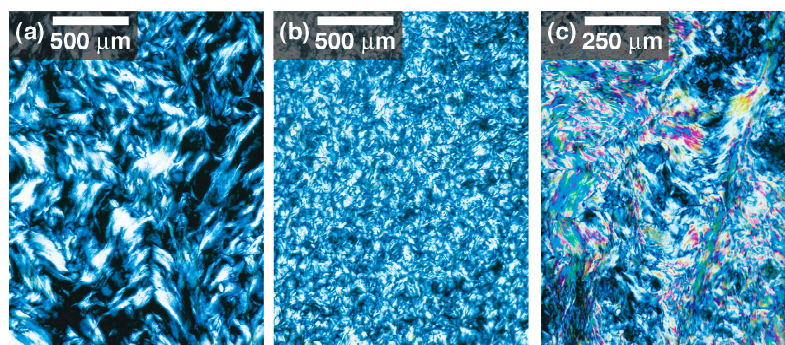
Figure 5.   The microscopic images of the nanosheet colloids with D_m = (a) 7.8 μm, (b) 1.9 μm, and (c) 0.15 μm, and ϕ = (a), (b) 6.3 $\times$ 10^{-3} and (c) 2.8 $\times$ 10^{-2}.   The colloids were observed between crossed polarizers in the flat glass capillaries with the thickness of (a), (b) 0.2 mm and (c) 0.1 mm.

Effect of the Particle Size and Concentration of Nanosheets on Liquid Crystallinity

Liquid crystallinity of the niobate sols becomes weaker for the colloids with smaller particles, when compared at a fixed volume fraction of the nanosheets. Figures 4a-c compare the photographs of the nanosheet colloids with the same ϕ (6.3 × 10^{-3}) and varied D_m observed between crossed polarizers. While the colloid with D_m = 7.8 μm is strongly birefringent (Figure 4a), the sol with D_m = 1.9 μm is only weakly birefringent (Figure 4b). The sample with D_m = 0.15 μm (Figure 4c) appears wholly dark, indicating that the colloid is isotropic.

The concentration (volume fraction ϕ) of $[Nb_6O_{17}]^{4-}$ nanosheets present in the sols also affected the liquid crystallinity. Figure 6 compares the colloid (D_m = 7.8 μm) at various ϕ, and shows that the observed birefringence becomes weaker as ϕ decreases. Similar trend is found for the sols with other D_m values: for example, the colloid with D_m = 0.15 μm is strongly birefringent at $\phi = 2.8 \times 10^{-2}$ (Figure 4d), while the observed interference color becomes weaker with decreasing ϕ, and the colloid is isotropic at $\phi = 6.3 \times 10^{-3}$ (Figure 4c).

The isotropic sols with rather small D_m or ϕ turned to temporarily birefringent by applying shear stress as exemplified in Figure 7. When the glass tube containing an isotropic sol (D_m = 1.9 μm; $\phi = 7.6 \times 10^{-4}$) is rotated, the colloid become bright along the tube wall between crossed polarizers (Figure 7; 0s), indicating that the nanosheets are macroscopically oriented along the shear flow. This birefringence is temporal and gradually disappears after terminating the rotation (Figure 7; 1.5 – 9 s). This result demonstrates that the isotropic phases contain anisotropic particles are potentially aligned macroscopically by weak external stimuli. Observations of some other isotropic samples with different ϕ and D_m confirmed that the returning to the isotropic state was slower for the colloids with larger sizes and higher concentrations of the nanosheets.
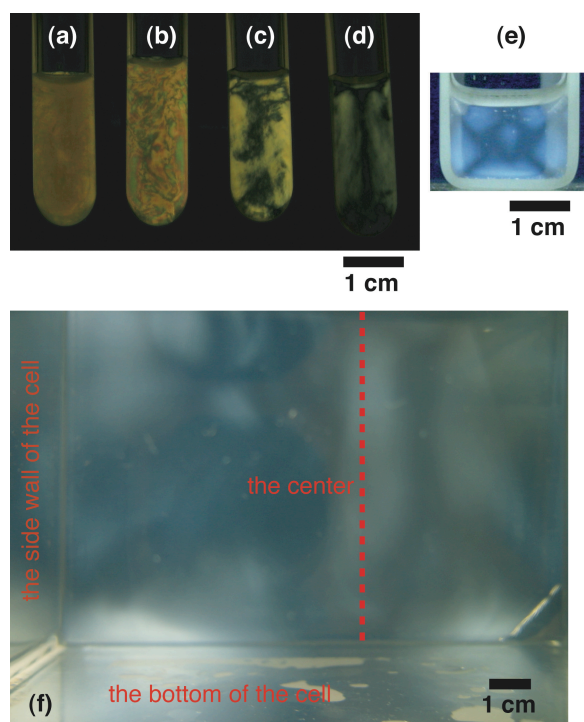
Figure 6. The photographs of the nanosheet colloids (D_m = 7.8 μm) with varied f = (a) 1.5×10^{-3}, (b) 7.6×10^{-4}, (c) 2.5×10^{-4}, (d) 1.3×10^{-4}, and (e)(f) 5.1×10^{-6}. The colloids were observed between crossed polarizers in (a)-(d) a glass tube (1 cm in diameter), (e) a glass cell (10 cm in thickness), and (f) a large glass vessel ($15 \times 15 \times 15$ cm^3).
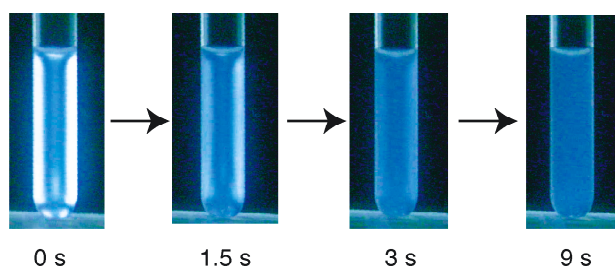
Figure 7. The photographs of the nanosheet colloid (D_m = 1.9 μm, ϕ = 7.6×10^{-4}) in a glass tube (1 cm in diameter) observed between crossed polarizers during the relaxation process of the birefringent state, induced by rotation of the tube at the rate of approximately 1 revolution per second, to isotropic state.

175

Liquid Crystalline–Isotropic Biphasic State

   The weakly birefringent colloids with rather low ϕ and small D_m, such as the one in Figure 4b, were biphasic mixtures of liquid crystalline and isotropic phases. Figures 8a shows the sol (D_m = 1.9 μm, ϕ = 6.3 × 10^{-3}) observed between crossed polarizers before and after phase separation.   The colloid is separated into two phases within a day: the birefringent liquid crystalline phase in the bottom and isotropic phase on the upper side.   After the separation, the volume of the lower phase was kept almost unchanged even after weeks.   Here, the fraction of the birefringent lower phase observed is regarded as the volume fraction of the liquid crystalline phase.   UV spectroscopy confirmed that the niobate nanosheets were present in the upper isotropic phase as well as in the lower liquid crystalline phase; concentrations ϕ of the nanosheets in the lower and upper phases were determined as 7.9 × 10^{-3} and 3.3 × 10^{-3}, respectively, while that of the original colloid was 6.3 × 10^{-3}.   This fact indicates that the observed separation of the colloid is not due simply to settlement nor flocculation of the nanosheets.   Similar phase separation behavior was also observed for the colloids with D_m = 0.38 and 0.15 with intermediate concentrations, while the volume fraction of the liquid crystal domain was varied with D_m and ϕ, as will be shown in the next section. Formation of liquid crystalline–isotropic biphasic states and separation under gravitational field due to the difference in the densities are generally observed in the colloidal systems that undergo isotropic to liquid crystalline[18,78] or crystalline[79] phase transitions.

   In contrast, the colloids of larger nanosheets (D_m = 6.2 and 7.8 μm) showed more complicated behavior.   Figure 8b shows the course of the phase separation of the colloid (D_m = 7.8 μm, ϕ = 1.5 × 10^{-3} vol.-%) observed between crossed polarizers. Although the colloid is separated into the two phases within 1 day, the volume of the lower phase continued to gradually shrink for more than 10 day.   This is probably due to contribution of sedimentation that is not negligible for the colloids of larger nanosheets.[80-82]   The colloid with D_m = 6.2 μm also showed similar behavior, whereas the volume fraction of the liquid crystalline domain was smaller compared with the colloid with D_m = 7.8 μm and the same ϕ.

(a)   (b)
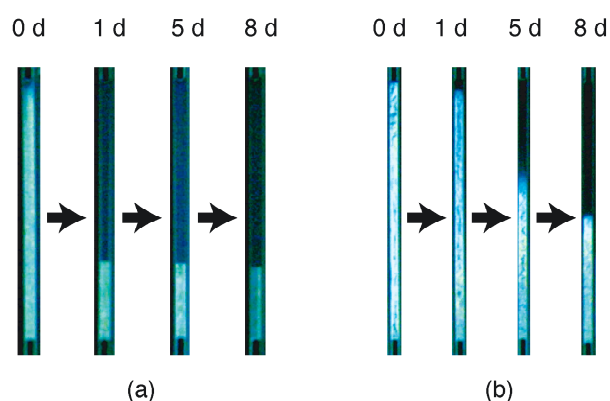
Figure 8.   The course of the colloids with (a) $D_m = 1.9$ μm and $\phi = 6.3 \times 10^{-3}$ and (b) $D_m = 7.8$ μm and $\phi = 1.5 \times 10^{-3}$ in a glass capillary (0.8 mm in diameter) observed between crossed polarizers.

Critical Concentrations of the Phase Transitions

Since the state of the nanosheet colloid varied from isotropic to biphasic, and finally to liquid crystalline as ϕ increased, the critical concentrations of the phase transitions are determined based on the relationship between ϕ and the volume fraction of the liquid crystalline phase.   Figure 9a-c shows the relationship observed for the sols with $D_m = 0.15$, 0.38 and 1.9 μm.   For each D_m, liquid crystalline domain appears above a certain transition concentration, grows with increasing ϕ, and finally covers whole volume of the colloid.   Volume fraction of the liquid crystalline phase is linearly correlated with ϕ.   Fitting the plots with straight lines (as shown by dashed lines in the figure) gives intercepts at the volume fraction of the liquid crystalline phase = 0 and 1. The former corresponds to the critical concentration of the phase transition from isotropic to biphasic, ϕ_I, and the latter indicates that from biphasic to liquid crystalline, ϕ_LC; they are listed in Table 1.   The critical concentrations were lower for the colloids of larger nanosheets, confirming that the colloid of larger nanosheets form more stable liquid crystalline phase.

177

For the colloids of larger nanosheets (D_m = 6.2 and 7.8 µm), the transition concentrations were only roughly determined due to the continuous sedimentation mentioned in the previous section. Figures 9d and e show the relationships between ϕ and the volume fraction of liquid crystalline phase. Here, the results after 5 days is adopted as the data representing the phase-separated state although the fraction of the liquid crystalline phase significantly varied with time. Thus, ϕ_{LC} = 5 × 10^{-3} and 3 × 10^{-3} for the colloids with D_m = 6.2 and 7.8 µm, respectively, whereas ϕ_I is nearly 0 for both the systems; namely these sols hardly become isotropic. Observation of the colloid with D_m = 7.8 µm in a glass cell with a long optical path (10 cm) between crossed polarizers gives a little more information of ϕ_I. Weak birefringence is observed for the colloid with ϕ = 5.1 × 10^{-6} as shown in Figure 6e. The colloid with D_m = 6.2 µm also kept birefringent at this concentration. Hence, $\phi_I < 5.1 × 10^{-6}$ in these systems.

It must be noted that the birefringence observed in these systems is ascribed to permanent liquid crystallinity rather than to temporal ones induced by the gravitational force, interfacial tension, or shear flow. If the nanosheets were oriented along the gravitational force, whole the domain in the vessel should appear bright and dark when the crossed polarizers are set inclined 45° and 0° to the ground, respectively;[48] nevertheless, we did not observe such the phenomenon. By contrast, birefringent domains were oriented along the cell wall (the sides and the bottom) and the liquid surface (Figure 6e). This phenomenon indicates that the orientation of the nanosheets is facilitated at the solid-liquid and air-liquid interfaces. However, observations of the colloids in a large vessel have indicated that the colloids exhibit birefringence without interfacial tension. Figure 6f shows a photograph of a dilute colloid in a large rectangular vessel (15 × 15 × 15 cm^3) between crossed polarizers. Domains at the center of the vessel, i.e. far from the cell wall (liquid–solid interface), are also birefringent without macroscopic orientation. Moreover, the effect of shear flow is also excluded. The liquid crystalline colloids kept birefringence even after standing them for more than 2 h, although the shear-induced birefringence of the isotropic colloids (Figure 6) was easily lost after stopping the flow.
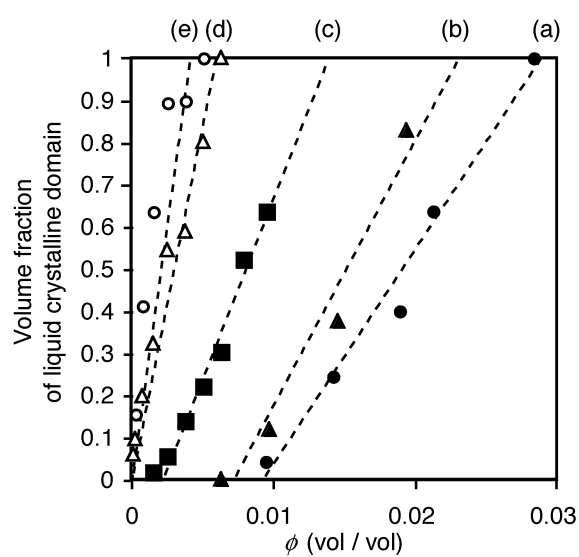
Figure 9. The relationship between colloid concentration ϕ of a colloid and the volume fraction of the liquid crystalline domain to the total volume. The colloids with D_m = (a; open circle) 0.15, (b; open triangle) 0.38 and (c; filled square) 1.9 mm were observed 1 day after preparation, whereas the colloids with D_m = (d; filled triangle) 6.2 and (e; filled circle) 7.8 mm were observed 5 day after preparation.

Fluidity of the Colloids

The liquid crystalline colloids of the niobate nanosheets examined in the present study retained fluidity, in contrast with the colloids of layered clay minerals whose liquid crystallinity was observed only under gelated state.[5,7] Figures 10a and b show the relationship between the concentration of the niobate nanosheets and kinematic viscosity of the colloids with D_m = 7.8 and 0.15 μm. The viscosity of the colloid with D_m = 0.15 μm is as low as the solvent, indicating the high fluidity of the colloid. The viscosity increased at higher concentration and for larger particle size as are generally known behavior of colloidal systems, whereas the colloids here are not gelated over whole the measured concentration range. Eye observation of the sols in a vessel also confirms the fluidity of concentrated colloids; the colloids (e.g. D_m = 7.8 μm, ϕ = 1 × 10⁻²) flowed by tilting the vessel. In contrast, according to the literatures, nanosheet colloid of Laponite[5] is gelated at ϕ = 7.2 × 10⁻³. Thus, the sols of niobate nanosheets are less viscous than other known nanosheet colloids.
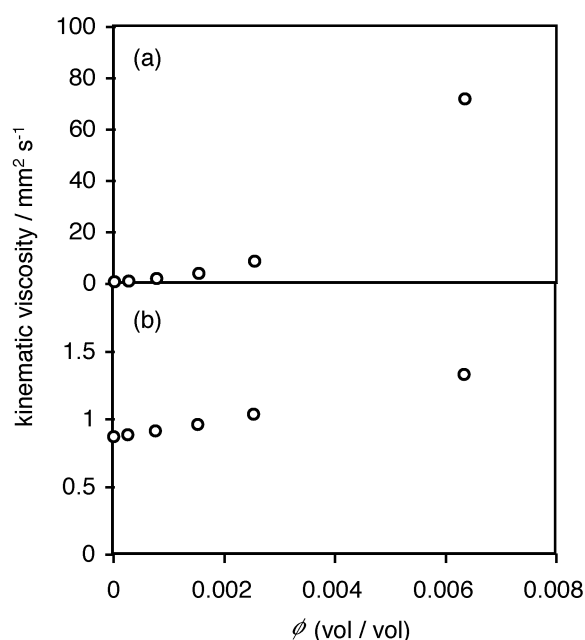
Figure 10. The dependence of kinematic viscosity of the nanosheet colloids with D_m = (a) 7.8 and (b) 0.15 μm on the colloid concentration ϕ.

6.3.4. Discussion

Control of Particle Size by Ultrasonication

This study presents a simple method for controlling the lateral size of inorganic nanosheets prepared by exfoliation of inorganic layered materials. The lateral size of the nanosheets have scarcely been paid attention,[26,35,37] although numerous studies on exfoliation of layered solids have been reported during the last decade. However, the present results demonstrate that the lateral size of the exfoliated niobate layers greatly affects the behavior of colloidally dispersed nanosheets as exemplified by the dependence of the stability of liquid crystalline phase. The lateral size should also be a key factor for controlling optical, electrical and mechanical properties of the nanosheets themselves and the nanohybrid solids obtained by assembling the nanosheets. Since exfoliation of single crystalline $K_4Nb_6O_{17}$ yields large nanosheets, the lateral size of the sheets is easily reduced in a broad range simply by ultrasonication of the as-prepared colloids. This method would be applicable for other layered inorganic materials, whereas polydispersity of the lateral size is still to be controlled.

The distribution of the lateral sizes was log-normal, as commonly found in the size distributions of powder materials.[83] In the present system, this distribution can be explained by a simple model. Supporting Information Figure 11a illustrates the model. If n_i parent sheets having D_i of the edge length are assumed to be broken at the rate of v into $n_{i+1} = 2n_i$ smaller sheets, whose area is half that of the parent sheets, the distribution of D_i vs n_i is estimated as log-normal when $i \gg 0$ and $t \gg 0$ as shown in Figure 11b.

(a)

$n_{(2, 2)}$ $D/2$

$D/2$

$n_{(1, 1)}$ $n_{(1, 2)}$ ...

D

D

$n_{(0, 0)}$ $n_{(0, 1)}$ $n_{(0, 2)}$

$t = 0$ $t = 1$ $t = 2$
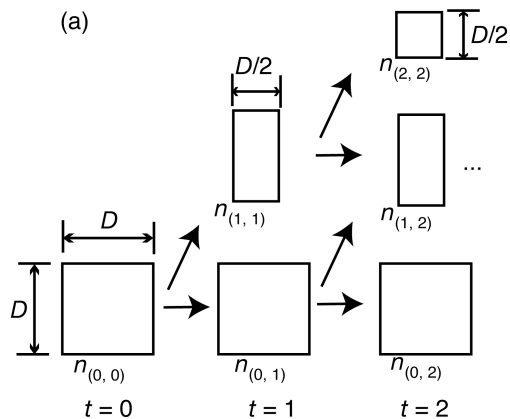
$$n_{(i, t)} - n_{(i, t-1)} = v\,(2n_{(i-1, t-1)} - n_{(i, t-1)})$$

t : time

$n_{(i, t)}$: number of the sheets, whose area is 2^{-i}, at time t

v : the rate (probability) of break down of the sheets

D : edge length

$t = 50,\ 40,\ 30,\ 20,\ 10,\ 0$

(b)

normalized fraction

10^{-7} 10^{-6} 10^{-5} 10^{-4} 10^{-3} 10^{-2} 10^{-1} 1

D
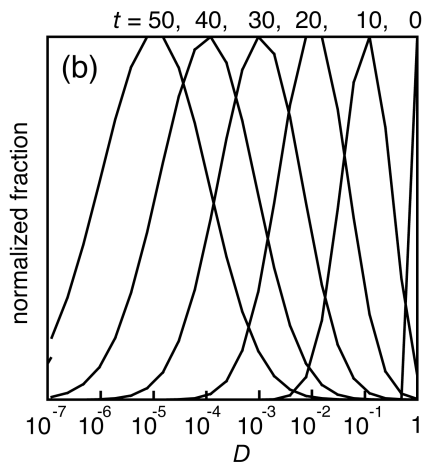
Figure 11. (a) Schematic model of breaking down of the nanosheets and (b) the size distribution numerically calculated on the model.

Origin of the Liquid Crystallinity

The isotropic to liquid crystalline phase transition observed for the niobate nanosheet colloids in the present system is basically rationalized by excluded-volume effect.[53,54] The anisotropic colloids transit from isotropic to liquid crystalline state when the loss of orientational entropy is outweighed by gain in excluded-volume (packing) entropy and, therefore, the liquid crystalline state is favored at higher concentration and larger aspect ratio of the particles.

The origin of the liquid crystallinity is discussed by comparing the concentrations of isotropic to biphasic transition ϕ_I and biphasic to liquid crystalline transition ϕ_{LC} observed for the niobate nanosheet colloids in the present study with those of previously reported colloidal systems of inorganic plates and nanosheets: gibbsite,[71] Laponite,[5,7] and bentonite[7] exhibit isotropic-nematic phase transition, while those $H_3Sb_3P_2O_{14}$[18] and $Ni(OH)_2$[73,74] undergo isotropic-lamellar and isotropic-columnar phase transition. Figure 12 plots ϕ_I and ϕ_{LC} against the aspect ratio of the particles D/L, where D and L are the lateral size and thickness of the inorganic particles, together with the theoretical dependence of ϕ_I and ϕ_{LC} on D/L obtained from the literature[56,57,84] that numerically solved Onsager theory. Except for some cases such as the colloids of niobate with very large D/L ($>10^3$), $H_3Sb_3P_2O_{14}$ and Laponite, the relationship between transition concentrations and aspect ratio is almost in accordance with the theoretical lines for isotropic-nematic transition. This fact demonstrates that the liquid crystalline behavior of the present system as well as the related colloidal nanosheet systems is basically interpreted by the exclude-volume effect, although the structure of the liquid crystalline phase (nematic or lamellar) is unclear at present.

Deviations of the experimental ϕ_I and ϕ_{LC} values from the theoretical lines observed in Figure 12 would be explained by the following factors, by which the theory has been extended to be applicable for experimental systems. First, the original theory is not valid at higher concentrations since it only takes into account interactions between two particles; nevertheless interactions among larger number of particles are not negligible at higher concentrations. The theoretical lines should shift to lower concentrations, if the interactions between many particles are taken into account.[61]

Second, the rather large polydispersity in the lateral size observed in present systems would have large effects on the phase transition. Monte Carlo simulations on polydisperse colloidal disks[61] showed that the gap between ϕ_I and ϕ_{LC} is larger at higher polydispersity. Broadening of the gap was also pronounced in the experimental system, colloidal plates of gibbsite.[72,78] Third, the flexibility of the nanosheet can also affect the liquid crystalline state; theory and experiments on flexible rod (chain polymers) showed that the high flexibility reduce the liquid crystallinity since effective excluded-volume is reduced.[55]
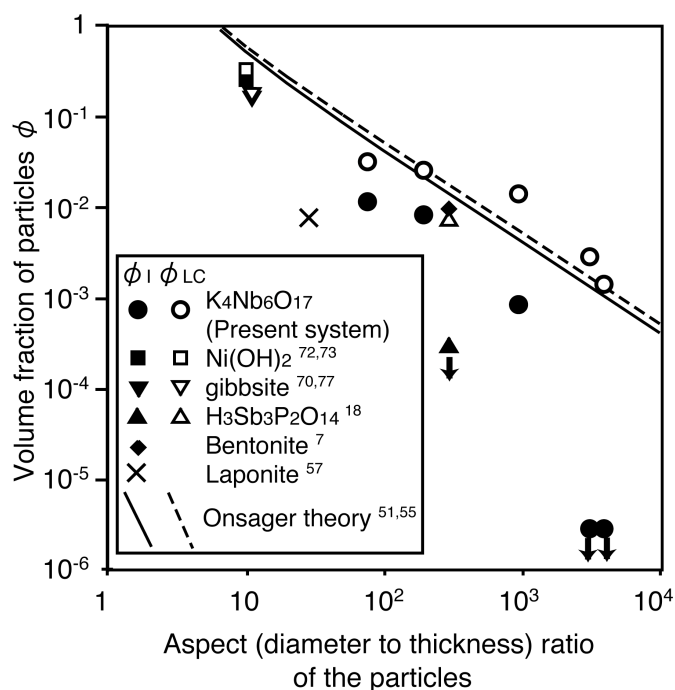
Figure 12. The relationship between diameter to thickness ratio of colloidal disks and the transition concentrations ϕ_I (isotropic to biphasic) and ϕ_{LC} (biphasic to liquid crystalline) observed in the present study and in the literatures. Solid and dashed lines represent the theoretical values numerically calculated based on Onsager's second virial approximation.[53,57] The down arrows indicate that the transition concentration was not determined but is lower than the value indicated by the symbols.

Electrostatic interactions between the nanosheets can also affect the phase behavior; however this is supposedly not important in the present system. Electrostatic repulsion among colloidally dispersed particles increases effective diameter of each particle. This leads to increased effective excluded-volume; hence phase transition concentrations become lower.[53,54] However, this effect is not large for disk-like particles compared with rods. The excluded-volume is almost independent on the thickness of particle, if Debye screening lengths κ^{-1} [53,54] is small enough compared to the dimension of a particle.[53,54] For the present system, if diameter and thickness of the particles are enlarged by 50 nm, the transition concentrations ϕ_I are estimated as 100 %, 98 % and 92 % those of the original particles with $D = 7.8$, 1.9, 0.38 μm, respectively. On the other hand, Debye screening lengths at around ϕ_I of the present systems are estimated as 70, 3.6 and 1.6 nm for the nanosheets with $D = 7.8$, 1.9 and 0.38 μm, respectively.[85] Judging from these calculations, electrostatic interactions between the nanosheets should be negligible.

On the other hand, the present study indicates that ϕ_I of the sols with very large D/L (the colloid with $D_m = 6.2$ and 7.8 μm) is significantly smaller than the theoretical value in the order of 2–3. It is supposed that restricted motion of colloidal nanosheets due to their large lateral size is a reason for the incompatibility; theoretical and experimental studies have shown that diffusion of anisotropic particles is greatly suppressed for large particles and is anisotropic for plates.[81]

The effect of gravity would also affect the orientation of the nanosheets. The observation (Figure 6f) showed that the birefringence observed for dilute colloids of large nanosheets ($D_m = 6.2$ and 7.8 μm) are due to permanent liquid crystallinity rather than due to gravity-induced sedimentation. In contrast, Chapter 6.2 has already revealed that the liquid crystalline domains of the niobate nanosheets obtained from powders ($D_m = 3.6$) are macroscopically aligned by gravity at higher concentrations.[48] This apparent discrepancy would be explained based on the calculation of rotary Péclet number, Pe_R, the dimensionless parameter which indicate the effect of gravity to rotational Brownian diffusion.[80,86,87] Brownian diffusion dominates when $Pe_R \ll 1$, whereas the shear flow affect the orientation of the particle when $Pe_R \gg 1$. Pe_R is

calculated as 0.082, 0.48, and 0.84 for the nanosheets with D_m = 3.6, 6.2, and 7.8 μm, respectively. These values are not so far from 1 and can vary if the nanosheets interacts with themselves at higher concentrations. Thus, the orientation of these large nanosheets is potentially affected by gravity, depending on the conditions such as colloid concentration.

6.3.5. Conclusions

The present study demonstrates characteristic liquid crystallinity of the colloids of niobate nanosheets depending on the lateral size as well as concentration of the nanosheets. Delamination of single crystalline $K_4Nb_6O_{17}$ enables control of the lateral size over wide range, yielding model plate-like particles with very high aspect ratios. The relationship between the aspect ratio and phase transition concentrations (isotropic–biphasic and biphasic–liquid crystalline) indicates that the liquid crystallinity is basically explained by the excluded-volume effect between the nanosheets, being in harmony with Onsager theory of colloidally dispersed anisotropic hard particles. In contrast, the discrepancy between experimental and theoretical phase behaviors at large aspect ratios, probably due to restricted motion of large colloidal particles, represents peculiar behavior of the colloidal systems of the niobate nanosheets.

Because of versatility of liquid crystals, which have been utilized in various areas as, for example, displays, anisotropic reaction media, and templates for ordered nanostructures, liquid crystalline nanosheet colloids will also be applied widely as advanced materials. The high fluidity of the liquid crystals obtained here, in particular for the colloids of large nanosheets which exhibit liquid crystallinity at very low concentrations, distinguishes the present system from conventional liquid crystalline materials; hence, high responsiveness to electric, magnetic and shear stimuli, e.g. gravity induced macroscopic orientation already reported in the previous communication,[48] are expected. Combining the liquid crystallinity with other properties of the layered niobate such as semiconducting nature[44-46] and capability of organizing guest species on the layer surface[47] will lead to integrated materials. Extension of the present methodology to other layered materials such as layered titanates and perovskite-type oxides will provide variety of liquid crystalline colloidal systems which may be useful for both application and fundamental investigations.

6.3.6. References

(1) I. Langmuir, *J. Chem. Phys.,* **6**, 873 (1938).

(2) H. van Olphen, *An Introduction to Clay Colloid Chemistry, 2nd ed.* (Krieger, Malabar, FL, 1977).

(3) K. Inukai, Y. Hotta, M. Taniguchi, S. Tamura, A. Yamagishi, *J. Chem. Soc., Chem. Comm.*, 959 (1994).

(4) E. R. Kleinfeld, G. S. Ferguson, *Science,* **265**, 370 (1994).

(5) M. Ogawa, M. Takahashi, K. Kuroda, *Chem. Mater.,* **6**, 715 (1994).

(6) A. Mourchid, A. Delville, J. Lambard, E. Léolier, P. Levitz, *Langmuir,* **11**, 1942 (1995).

(7) A. Mourchid, A. Delville, P. Levitz, *Faraday Discuss.,* **101**, 275 (1995).

(8) J.-C. P. Gabriel, C. Sanchez, P. Davidson, *J. Phys. Chem.,* **100**, 11139 (1996).

(9) A. Mourchid, E. Lécolier, H. van Damme, P. Levitz, *Langmuir,* **14**, 4718 (1998).

(10) B. J. Lemaire, P. Panine, J. C. P. Gabriel, P. Davidson, *Europhys. Lett.*, **69**, 55 (2002).

(11) D. W. Murphy, G. W. Hull, *J. Chem. Phys.,* **62**, 973 (1975).

(12) I. Lagadic, P. G. Lacroix, R. Clément, *Chem. Mater.*, **9**, 2004 (1999).

(13) G. Alberti, M. Casciola, U. Costantino, *J. Colloid Interface Sci.*, **107**, 256 (1985).

(14) S. W. Keller, H.-N. Kim, T. E. Mallouk, *J. Am. Chem. Soc.*, **116**, 8817 (1994).

(15) H.-N. Kim, S. W. Keller, T. E. Mallouk, *Chem. Mater.,* **9**, 1414 (1997).

(16) D. M. Kaschak, J. T. Lean, C. C. Waraksa, G. B. Saupe, H. Usami, T. E. Mallouk, *J. Am. Chem. Soc.*, **121**, 3435 (1999).

(17) J.-C. P. Gabriel, F. Camerel, B. J. Lemaire, H. Desvaux, P. Davidson, P. Batail, *Nature,* **413**, 504 (2001).

(18) N. Yamamoto, T. Okuhara, T. Nakato, *J. Mater. Chem.,* **11**, 1858 (2001).

(19) N. A. Kotov, I. Dékány, J. H. Fendler, *Adv. Mater.,* **8**, 637 (1996).

(20) M. Adachi-Pagano, C. Forano, J.-P. Besse, *Chem. Commun.*, 91 (2000).

(21) M. M. J. Treacy, S. B. Rice, A. J. Jacobson, J. T. Lewandowski, *Chem. Mater,* **2**, 279 (1990).

(22) R. Abe, K. Shinohara, A. Tanaka, M. Hara, J. N. Kondo, K. Domen, *Chem. Mater.,* **9**, 2179 (1997).

(23) R. Abe, M. Hara, J. N. Kondo, K. Domen, *Chem. Mater.,* **10**, 1647 (1998).

(24) G. B. Saupe, C. C. Waraksa, H.-N. Kim, Y. J. Han, D. M. Kaschak, D. M. Skinner, T. E. Mallouk, *Chem. Mater.,* **12**, 1556 (2000).

(25) R. E. Schaak, T. E. Mallouk, *Chem. Mater.,* **12**, 3427 (2000).

(26) N. Miyamoto, H. Yamamoto, R. Kaito, K. Kuroda, *Chem. Commun.*, 2378 (2002).

(27) F. E. Osterloh, *J. Am. Chem. Soc.,* **124**, 6248 (2002).

(28) T. Sasaki, M. Watanabe, H. Hashizume, H. Yamada, H. Nakazawa, *J. Am. Chem. Soc.,* **118**, 8329 (1996).

(29) T. Sasaki, S. Nakano, S. Yamauchi, M. Watanabe, *Chem. Mater.,* **9**, 602 (1997).

(30) R. Abe, K. Shinohara, A. Tanaka, M. Hara, J. N. Kondo, K. Domen, *Chem. Mater.,* **10**, 329 (1998).

(31) T. Sasaki, M. Watanabe, *J. Am. Chem. Soc.,* **120**, 4682 (1998).

(32) J.-Y. Kim, I. Chung, J.-H. Choy, *Chem. Mater.,* **13**, 2759 (2001).

(33) N. Sukpirom, M. M. Lerner, *Chem. Mater.,* **13**, 2179 (2001).

(34) W. Sugimoto, O. Terabayashi, Y. Murakami, Y. Takatsu, *J. Mater. Chem.,* **12**, 3814 (2002).

(35) N. Sukpirom, M. M. Lerner, *Mater. Sci. Eng. A,* **333**, 218 (2002).

(36) Y. Ide, M. Ogawa, *Chem. Commun.*, 1262 (2003).

(37) T. Tanaka, Y. Ebina, K. Takada, K. Kurashima, T. Sasaki, *Chem. Mater.,* **15**, 3564 (2003).

(38) R. E. Schaak, T. E. Mallouk, *Chem. Commun.,* **2002**, 706 (2002).

(39) Y. Omomo, T. Sasaki, L. Wang, M. Watanabe, *J. Am. Chem. Soc.,* **125**, 3568 (2003).

(40) M. Isayama, K. Sakata, T. Kunitake, *Chem. Lett.*, 1283 (1993).

(41) Y. Matsumoto, A. Funatsu, D. Matsuo, U. Unal, *J. Phys. Chem. B,* **105**, 10893 (2001).

(42) A. Usuki, Y. Kojima, M. Kawasumi, A. Okada, Y. Fukushima, T. Kurauchi, O. Kamigatio, *J. Mater. Res.,* **8**, 1179 (1993).

(43) G. Lagaly, *Appl. Clay Sci.,* **15**, 1 (1999).

(44) K. Domen, A. Kudo, M. Shibata, A. Tanaka, K. Maruya, T. Onishi, *J. Chem. Soc., Chem. Commun.*, 1706 (1986).

(45) Y. I. Kim, S. Salim, M. J. Huq, T. E. Mallouk, *J. Am. Chem. Soc.,* **113**, 9561 (1991).

(46) A. Kudo, T. Sakata, *J. Phys. Chem.,* **100**, 17323 (1996).

(47) N. Miyamoto, K. Kuroda, M. Ogawa, *J. Am. Chem. Soc.,* **123**, 6949 (2001).

(48) N. Miyamoto, T. Nakato, *Adv. Mater.,* **14**, 1267 (2002).

(49) T. Nakato, N. Miyamoto, A. Harada, H. Ushiki, *Langmuir,* **19**, 3157 (2003).

(50) F. Camerel, J.-C. P. Gabriel, P. Batail, *Chem. Commun.*, 1926 (2002).

(51) A. S. Sonin, *J. Mater. Chem.,* **8**, 2557 (1998).

(52) J.-C. P. Gabriel, P. Davidson, *Adv. Mater.,* **12**, 9 (2000).

(53) L. Onsager, *Ann. NY Acad. Sci.,* **51**, 627 (1949).

(54) P. A. Forsyth, S. Marcelja, D. J. Mitchell, B. W. Ninham, *J. Chem. Soc., Faraday Trans 2,* **73**, 84 (1977).

(55) P. A. Forsyth, S. Marcelja, D. J. Mitchell, B. W. Ninham, *Adv. Colloid Interface Sci.,* **9**, 37 (1978).

(56) G. J. Vroege, H. N. W. Lekkerkerker, *Rep. Prog. Phys.,* **55**, 1241 (1992).

(57) T. Sato, A. Teramoto, *Adv. Polymer Sci.,* **126**, 85 (1996).

(58) D. Frenkel, R. Eppenga, *Phys. Rev. Lett.,* **52**, 1089 (1982).

(59) D. Frenkel, B. M. Mulder, *Mol. Phys.,* **55**, 1171 (1985).

(60) J. A. C. Veerman, D. Frenkel, *Phys. Rev. A,* **45**, 5632 (1992).

(61) M. Bates, D. Frenkel, *J. Chem. Phys.,* **110**, 6553 (1999).

(62) L. Li, J. Walda, L. Manna, A. P. Alivisatos, *Nano Lett.,* **2**, 557 (2002).

(63) F. Camerel, J.-C. P. Gabriel, P. Btail, *Adv. Funct. Mater.,* **13**, 377 (2003).

(64) F. C. Bawden, N. W. Pirie, J. D. Bernal, I. Fankuchen, *Nature,* **138**, 1051 (1936).

(65) A. Ciferri, Ed., *Liquid Crystallinity in Polymers* (VCH publishers, Inc., New York, 1991).

(66) T. E. Strzelecka, M. W. Davidson, R. L. Rill, *Nature,* **331**, 457 (1988).

(67) F. Livolant, A. M. Levelut, J. Doucet, J. P. Benoit, *Nature,* **339**, 724 (1989).

(68) V. H. Zocher, *Anorg. Allg. Chem.,* **147**, 91 (1925).

(69) O. Pelletier, C. Bourgaux, O. Diat, P. Davidson, J. Livage, *Eur. Phys. J. B*, **12**, 541 (1999).

(70) P. Davidson, A. Garreau, J. Livage, *Liquid Crystals,* **16**, 905 (1994).

(71) F. M. van der Kooij, H. N. W. Lekkerkerker, *J. Phys. Chem. B,* **102**, 7829 (1998).

(72) F. M. van der Kooij, K. Kassapidou, H. N. W. Lekkerkerker, *Nature,* **406**, 868 (2000).

(73) A. B. D. Brown, S. M. Clarke, A. R. Rennie, *Langmuir,* **14**, 3192 (1998).

(74) A. B. D. Brown, C. Ferrero, T. Narayanan, A. R. Rennie, *Eur. Phys. J. B,* **11**, 481 (1999).

(75) M. Kestigian, F. D. Leipziger, J. R. Carter, F. G. Garabedian, *J. Am. Ceram. Soc.*, 517 (1966).

(76) K. Nassau, J. W. Shiever, J. L. Bernstein, *J. Electrochem. Soc.,* **116**, 348 (1969).

(77) Since $K_4Nb_6O_{17}$ possesses alternating two types of interlayer spaces, it can form two type of intercalation compounds: one accommodates the guest species in every other interlayer space and the other contain them in both spaces. The former type of intercalation compounds yields bilayer nanosheets by exfoliation through infinite swelling of the interlayer spaces with the guests, whereas the latter produces monolayer nanosheets. The thickness of the $[Nb_6O_{17}]^{4-}$ nanosheets obtained by exfoliation with tetrabutylammonium[22] or propylammonium[26] has been estimated by using atomic force microscope as around 1.8 nm, which value corresponds to the thickness of the bilayer nanosheets, i.e., total thickness of two $[Nb_6O_{17}]^{4-}$ layers with K^+ sandwiched in the interlayer space.

(78) F. M. van der Kooij, K. Kassapidou, H. N. W. Lekkerkerker, *Nature,* **406**, 868 (2000).

(79) P. N. Pusey, W. van Megen, *Nature,* **320**, 340 (1986).

(80) H. Brenner, *Int. J. Multiphase Flow,* **1**, 195 (1974).

(81) W. B. Russel, D. A. Saville, W. R. Schowalter, *Colloidal dispersion* (Cambridge University Press, Cambridge, 1989).

(82) F. M. van der Kooij, A. P. Phillipse, J. K. G. Dhont, *Langmuir,* **16**, 5317 (2000).

(83) T. Allen, *Particle Size Measurement* (Chapman and Hall Ltd., London, 1968).

(84) Since the literature gives relationship between the aspect ratio D/L and the reduced

density ρV_{excl}, where ρ is the number density of the particles and V_{excl}, is the

excluded volume per one particle. ρV_{excl} is converted to volume fraction f of the

particles for comparison with experimental values as

$$\phi = (\rho V_{excl}) \frac{V_{core}}{V_{excl}}$$

where V_{excl} between two cylinders with the diameter D and thickness L is

$$V_{excl} = \frac{\pi}{4} D(L^2 + \frac{\pi + 3}{2} LD + \frac{\pi}{4} D^2)$$

and the core volume of a disk V_{core} is

$$V_{core} = \frac{D^2}{4} \pi \cdot L$$
.

At isotropic to biphasic transition, ρV_{excl} is estimated as 3.3 – 5.6 by numerical solution[55,][56] for monodisperse colloidal disks with D / L ranging from ∞ to 0.1.

(85) Debye screening length κ^{-1} is calculated as

$$\kappa^{-1} = \sqrt{\frac{\varepsilon_0 \varepsilon_r k_B T}{e^2 N_A 2I}}$$

where ε_0 is permittivity of vacuum, ε permittivity of solvent, k_B Boltzmann constant, e

the charge of an electron, N_A Avogadro constant, T the temperature, and I the ionic

strength of colloid.   Ionic strength I is

$$I = \frac{1}{2} \sum_i c_i z_i^2 = [Nb_6O_{17}{}^{4-}]$$

where c and z are the molar concentration and the valence of ions, respectively, if

we assume that 1 mol of $[Nb_6O_{17}]^{4-}$ releases 2 mol of monovalent cations (K^+ or

popylammonium).

(86) T. Okubo, *J. Am. Chem. Soc.,* **109**, 1913 (1987).

(87) Pe_R for a very thin circular disk with the radius r is expressed as[80, 86]

$$Pe_R = \frac{\dot{\gamma}}{D_R} = \frac{32 r^3 \eta_0 \dot{\gamma}}{3kT},$$

where $\dot{\gamma}$ is the shear rate, D_R the rotational diffusion constant, η_0 the viscosity of solvent, k Boltzmann constant, and T the temperature. On the other hand, the disk sediments at infinite dilution in the gravitational field at the velocity S of

$$S = \frac{V(\rho - \rho_0)g}{f},$$

where g is the gravitational constant, V ($= \pi r^2 L$; L is the thickness of disk) the volume of the disk, ρ and ρ_0 the densities of the particle and the solvent, and f the friction factor. Since f is given as $f = 6\eta_0(2r)$ for a randomly oriented disk with $2r/L \to \infty$[81] and $\dot{\gamma} = S/(2r)$, we obtain

$$Pe_R = \frac{4\pi r^3 L(\rho - \rho_0)g}{9kT}.$$

CHAPTER 7

LIQUID CRYSTALLINE COLLOIDAL SYSTEM OBTAINED BY MIXING NIOBATE AND ALUMINOSILICATE NANOSHEETS

7. Liquid Crystalline Colloidal System Obtained by Mixing Niobate and Aluminosilicate Nanosheets

7.1. Introduction

Colloids consisting of anisotropic particles show peculiar properties such as liquid crystallinity and unusual rheological properties due to anisotropic interactions between the particles,[1] in contrast to those with spherical particles. Colloids of inorganic platelets with the thickness of around 1 nm, called as "nanosheet colloids" hereafter, can be obtained by exfoliation of various layered inorganic crystals. Whereas this type of colloids is regarded as a fascinating class of such anisotropic colloidal systems, the only well-studied system is colloids of layered clay minerals exemplified by montmorillonite, which are infinitely swelled in water through hydration of interlayer exchangeable cations (mainly Na^+) to give exfoliated aluminosilicate nanosheets. The clay nanosheet colloids have been found to show various peculiar properties such as thixotropy[2] and flow-birefringence.[3] Other layered solids investigated as nanosheet colloids are V_2O_5[4-6] and very recently reported $H_3Sb_3P_2O_{14}$.[7]

A colloidally dispersed system of layered niobate $K_4Nb_6O_{17}$, whose structure is constructed by the $Nb_6O_{17}^{4-}$ niobate layers and interlayer K^+ ions, are regarded as a unique end member of the nanosheet colloids.[8,9] This material is exfoliated through exchange of interlayer K^+ ions for alkylammonium ions and subsequent dispersion in water. The niobate nanosheet colloids exhibit unusual properties of stable liquid crystallinity accompanied by macroscopic (on cm-scale) orientation[8] and pH-induced sol-gel transition.[9] Thus, the niobate nanosheet colloids are applicable as novel soft materials which cannot be prepared from other inorganic colloidal systems.

As a method of such utilization, the niobate nanosheet colloids can be used as "soft matrices" of cationic functional molecules since the negatively charged $Nb_6O_{17}^{4-}$ layers have capability of adsorbing cationic species.[10,11,8] For this purpose, ordering of the soft cavities provided by the niobate nanosheets, i.e. liquid crystallinity of the nanosheets, should play an important role in constructing the hybridized systems consisting of colloidal nanosheets. Addition of other anisotropic inorganic

nanoparticles to the niobate nanosheet colloids can influence both the structure, from molecular arrangement to macroscopic ordering, and properties of the colloidal systems. However, to my knowledge, such attempts have not been reported.

This chapter deals with a colloidal system of inorganic nanosheets obtained by mixing two different kinds of nanosheets, $Nb_6O_{17}{}^{4-}$ and montmorillonite clay. While the niobate nanosheets are characterized by rather large lateral size (< 100 μm)[12,8] and high charge density of oxide layers,[13] the aluminosilicate nanosheets of montmorillonite are small and their charge density is relatively low.[14] Recent theoretical and experimental studies of double-component colloidal systems involving morphologically different inorganic particles, such as rod-plate[15,16] and rod-sphere[17] systems, have revealed unusual behavior exemplified by rich phase behavior which have not been observed for conventional colloids composed of a single dispersed species. Even for the single-component colloids of platelets or rods, difference in polydispersity largely affects the phase behavior.[18,19] Plate-plate mixtures of layered clay minerals with lamellar micelles of surfactants have also been reported to show homogeneously mixed or demixed states depending on the concentration;[20,21] however, the formation-deformation equilibrium of lamellar micelle and possible breakdown of the micelles make the system complicated.

Based on the optical measurements under crossed polarizers, this chapter reveals that the niobate-montmorillonite nanosheet colloids (described as "niobate-clay colloids" hereafter) exhibit liquid crystalline macroscopic ordering similar to the single-component niobate nanosheet colloids. Microscopic environments provided by the colloidally dispersed nanosheets was investigated using a spectroscopic probe; aggregative adsorption of a cationic dye of 1,1'-diethyl-2,2'-cyanine (pseudoisocyanine, abbreviated as PIC hereafter) onto the nanosheets is utilized to probe mass transfer between the niobate and clay nanosheets.

7.2. Experimental

Materials

$K_4Nb_6O_{17} \cdot 3H_2O$ was prepared by heating a mixture of K_2CO_3 and Nb_2O_5 according to the literature.[22] Purified natural montmorillonite (product of Tsukinuno mine, Yamagata, Japan) used as received was a JCSS-3101 reference clay sample supplied from the Clay Science Society of Japan. The cation exchange capacities (CECs) of montmorillonite and $K_4Nb_6O_{17}$ are 119 meq / 100 g clay and 4 eq / 1 mol (or 384 meq / 100 g) $K_4Nb_6O_{17} \cdot 3H_2O$, respectively. 1,1'-Diethyl-2,2'-cyanine bromide (PICBr; purity 99.9 %) was purchased from Hayashibara Biochemical Laboratories Inc. and was used as received.

Preparation of the Colloids

$K_4Nb_6O_{17}$ was allowed to react with a 0.2 mol dm^{-3} aqueous solution of propylamine hydrochloride at 80 ºC for 3 d.[8,9] The product was centrifuged and washed twice with water, followed by re-dispersion in water to form the niobate colloids. Montmorillonite colloids were prepared by dispersing the clay powders in water. Both the colloids were simply mixed to yield niobate-clay colloids. Optical microscope images of the colloids between crossed polarizers were recorded on an Olympus BX-51 polarizing microscope.

Spectroscopic Investigations Using a Cyanine Dye

The niobate or clay colloids were added by an aqueous PIC solution (5×10^{-5} mol dm^{-3}) to form PIC/niobate or PIC/clay colloids. PIC/niobate-clay colloids were prepared by three different methods: (i) addition of a PIC/clay colloid to a niobate colloid, (ii) addition of a PIC/niobate colloid to a clay colloid and (iii) addition of the PIC solution to the niobate-clay colloid. It must be noted that all the dye was adsorbed on or present in the vicinity of the nanosheets, since the supernatants obtained by centrifugation of the PIC-added colloids were colorless.

Visible spectra of the dye-adsorbed colloids were measured with a JASCO Ubest-55 spectrophotometer, using an integrating sphere to lower background signals

due to scattering of the incident beam by the colloid. The spectra shown were measured after equilibrating the samples by standing for over 10 days after preparation. All the spectra were obtained after subtracting their background scattering. Polarized visible spectra were measured by placing a polarizer between the incident light and a sample.

Macroscopically Separated Niobate and Clay Colloids

To obtain information of mass transfer between the niobate and clay colloids, the behavior of PIC dye in the colloids was spectroscopically investigated. A PIC/niobate colloid was poured into a semipermeable cellulose membrane tube with pores of 2.4 nm, and then contacted with a montmorillonite colloid. Change of the visible spectrum of each phase was monitored. Thermogravimetric and differential thermal analyses (TG-DTA) of the powders obtained by evaporating water from the colloids were carried out by using a Seiko TG/DTA6300 analyzer to estimate the organic contents in the samples. X-ray diffraction (XRD) patterns of the dried samples, which were prepared by casting and drying a colloid on a glass substrate, were recorded on a MAC Science MX Labo diffractometer (monochromated CuKα radiation; the tube voltage and current are 40 kV and 30 mA).

7.3. Results

Liquid Crystallinity of the Niobate-Clay Colloids

The niobate-clay colloids were liquid crystalline, similarly to the single-component colloids of the niobate nanosheets.[8] Figures 1a-c show typical optical microscope images of the niobate-clay colloids with different niobate concentrations at a fixed clay content ($[Nb_6O_{17}{}^{4-}]$ = 2.4 × 10^{-2}, 4.8 × 10^{-3}, and 1.9 × 10^{-3} mol dm^{-3} (= 20, 4 and 1.6 g dm^{-3}), [clay] = 20 g dm^{-3}) observed between crossed polarizers. Images of the single-component colloids of Na-montmorillonite ([clay] = 5.0 g dm^{-3}) and the niobate ($[Nb_6O_{17}{}^{4-}]$ = 2.4 × 10^{-2}, 4.8 × 10^{-3}, and 1.9 × 10^{-3} mol dm^{-3}) are shown in Figures 1d and 1e-g, respectively, for comparison. All the present niobate-clay colloids, as well as the single-component niobate colloids of the same $Nb_6O_{17}{}^{4-}$ concentrations, are birefringent in the concentration range of 9.1 × 10^{-4} to 2.4 × 10^{-2} mol dm^{-3} (0.075 to 20 g dm^{-3}) of $Nb_6O_{17}{}^{4-}$; the colloids are liquid crystalline. In contrast, a dark image observed for the single-component montmorillonite colloid indicates that the clay colloid is wholly isotropic. The clay colloids were isotropic in the concentration range of 5.0 to 20 g dm^{-3} of clay. Previous studies have reported that clay nanosheet colloids are present as isotropic phases at concentrations of clay below 20 - 30 g dm^{-3}.[23,24]

The optical microscope observations indicate that liquid crystallinity of the niobate-clay colloids depends on the $Nb_6O_{17}{}^{4-}$ concentration in the colloids, but not on the clay concentration. Weaker interference colors observed for the niobate colloids with lower $Nb_6O_{17}{}^{4-}$ concentrations (Figures 1e-g) indicate decreased liquid crystallinity of the colloids. The interference colors observed in the niobate-clay colloids (Figures 1a-c) are similar to those observed for the corresponding single-component niobate colloids of the same $Nb_6O_{17}{}^{4-}$ concentrations. This fact demonstrates that liquid crystalline ordering of the niobate nanosheets is not disturbed by introducing the clay nanosheets into the system.

Naked eye observations of the niobate-clay colloids in a test tube (diameter = 1 cm) using crossed polarizers (Figures 1i and h) also show liquid crystallinity of the colloids, and this macroscopic observation reveals that the niobate-clay colloids are easily aligned on centimeter scale. A niobate-clay colloid ($[Nb_6O_{17}{}^{4-}]$ = 4.8 × 10^{-3} mol

dm^{-3}, [clay] = 5.0 g dm^{-3}) just after shaking the tube shows bright and dark domains, indicating that the liquid crystalline domain is randomly oriented (Figure 1i) due to the shear flow. After standing the colloid for several minutes, the sample appears almost homogeneously bright between crossed polarizers (Figure 1h); the crossed polarizers are set inclined 45° to the ground for this observation, and the colloids turn wholly dark when the crossed polarizers are set horizontally and vertically to the ground. This fact indicates that the niobate-clay colloids are macroscopically oriented on centimeter scale along the normal to the ground; similar macroscopic alignment of the niobate nanosheets has already been observed for the single-component niobate colloids.[8]

500 μm
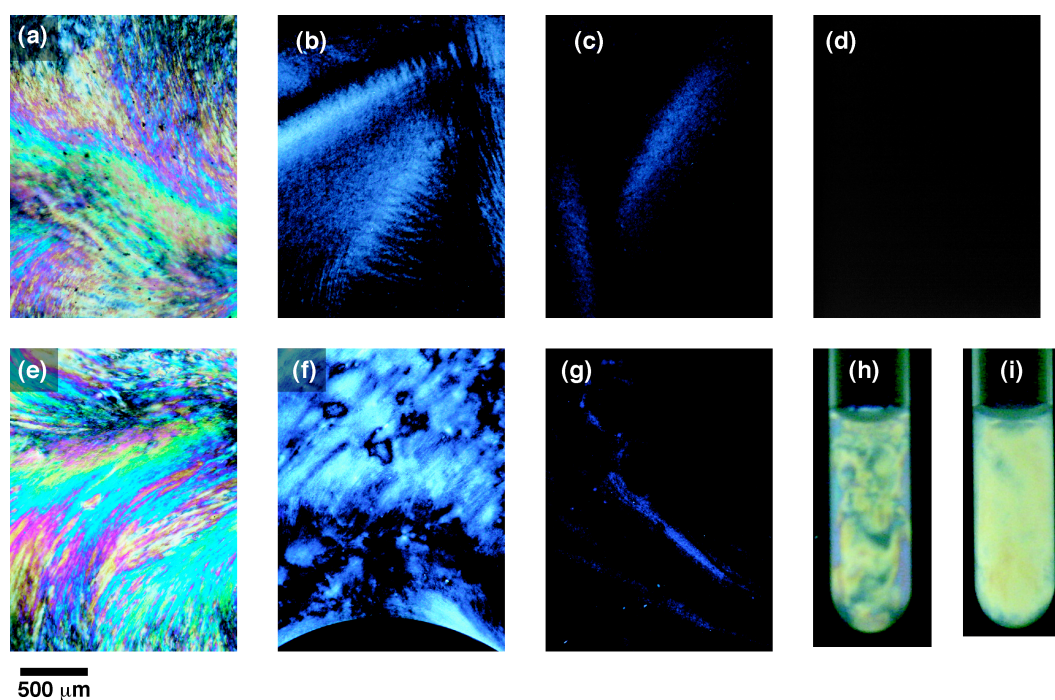
Figure 1. Optical microscope images of the (a)-(c) niobate-montmorillonite colloids, (d) montmorillonite colloid ([clay] = 5 g dm^{-3}), and (e)-(g) niobate colloids placed in a 0.4 mm-thick cell observed between crossed polarizers, and (h)(i) photographs of the niobate-clay colloid in a test tube between crossed polarizers. Concentrations of the niobate nanosheets are [Nb$_6$O$_{17}$$^{4-}$] = 2.4 × 10^{-2} mol dm^{-3} (20 g dm^{-3}) for (a) and (e), 4.8 × 10^{-3} mol dm^{-3} (4 g dm^{-3}) for (b), (f), (h), and (i), and 1.9 × 10^{-3} mol dm^{-3} (1.6 g dm^{-3}) for (c) and (g). Concentrations of the clay nanosheets are [clay] = 20 g dm^{-3} for (a)-(c), and 5 g dm^{-3} for (h) and (i). The pictures of the test tube were taken (h) immediately after shaking the tube and (i) after standing it for 40 min.

Demixing of the Colloids on Microscopic Scale

XRD measurements of dried colloids indicated that the apparently homogeneous niobate-clay colloids are segregated into clay-rich and niobate-rich domains on smaller scale. The cast film obtained from a single-component niobate colloid gave a diffraction peaks at d = 2.1 and 1.0 nm which are ascribed to propylammonium-$K_xNb_6O_{17}$ intercalation compound (Figure 2a), whereas the film prepared from colloidal montmorillonite exhibited a peak at d = 1.3 nm which is assigned to Na-montmorillonite (Figure 2b). The film prepared from a niobate-clay colloid (Figure 2c) gave both the peaks assigned to the propylammonium-$K_xNb_6O_{17}$ intercalation compound and Na-montmorillonite, but no peak ascribable to hetero-stacking of the niobate and clay nanosheets. The variation in mixing ratio only affected the relative intensity of the two peaks, while hetero-stacking was not observable at any mixing ratio. Thus, the niobate-clay colloids are segregated into two phases at a certain stage of evaporating the solvent, i.e. at a certain condensed state. On the other hand, the XRD pattern of a rapidly dried colloid indicates that the niobate and clay are segregated even before condensation. Figure 7d shows the XRD pattern of the colloid cast on a heated glass plate and dried within a second. The peaks due to Na-montmorillonite and niobate are observable similarly to the slowly dried sample.

Figure 2. XRD patterns of the cast films prepared from the (a) PIC/niobate, (b) PIC/montmorillonite, (c) PIC/niobate-montmorillonite colloids, and (d) niobate-montmorillonite colloid. The samples (a)-(c) were prepared by drying the colloid slowly in ambient atmosphere, while the sample (d) was prepared by very rapidly drying the colloid by dropping the colloid onto heated plate.

Selective Adsorption of the Cyanine Dye in the Niobate-Clay Nanosheet Colloid

A novel aspect of the niobate-clay colloids for organizing cationic species was revealed by spectroscopic investigation of the colloids using the probe PIC dye; PIC was selectively adsorbed onto the clay nanosheets rather than onto the niobate. Figure 3 compares a typical absorption spectrum of PIC added to a niobate-clay colloid (prepared by adding PIC to the niobate-clay colloid) with those of PIC added to a single-component niobate and clay colloids. In the single-component colloids, the absorption bands due to PIC are observed at 578 and 564 nm for the niobate (Figure 3a) and montmorillonite (Figure 3b) colloids, respectively. These bands are assigned to the J-aggregates of PIC adsorbed on the niobate and montmorillonite surfaces, being in harmony with the previously reported results.[25,26] The weak bands at 515 nm for the dye/niobate and 500 nm for the dye/montmorillonite are assignable to side bands. In the niobate-clay colloid (Figure 3c), the J-band at 564 nm, assigned to the PIC adsorbed on the clay, is observed, accompanied by monomer bands at 522 and 485 nm. The J-band at 578 nm assignable to the PIC adsorbed on the niobate nanosheets is absent.

The selective adsorption of PIC on the clay nanosheets was also observed for the sample obtained by adding the montmorillonite colloid to the niobate colloid pre-adsorbed by PIC. The absorption spectrum after this treatment (Figure 3d) is almost the same as that observed for PIC added to the niobate-clay colloid; the J-band on niobate observed before the treatment almost disappeared after the mixing. On the other hand, when the niobate colloid was added to the PIC-adsorbed clay colloid, the strong J-band on the clay remains while the monomer bands are observable at 522 and 485 nm (Figure 3e). PIC is transferred from the niobate layers to the clay nanosheets when it was pre-adsorbed on the niobate, while the dye added to the clay colloid stays on the aluminosilicate platelets after the addition of niobate nanosheets.

Figure 3. Visible spectra of the (a) PIC/niobate colloid ($[Nb_6O_{17}^{4-}]$ = 8.3 × 10^{-4} mol dm^{-3} (= 0.69 g dm^{-3})), (b) PIC/montmorillonite colloid ([clay] = 1 g dm^{-3}) and (c)(d)(e) PIC/niobate-montmorillonite colloids ([clay] = 1 g dm^{-3}, $[Nb_6O_{17}^{4-}]$ = 9.6 × 10^{-4} mol dm^{-3} (= 0.80 g dm^{-3})). All the colloids contain 5 × 10^{-6} mol dm^{-3} of the dye. The PIC/niobate-montmorillonite colloids were obtained by adding (c) PIC solution to niobate-montmorillonite colloid, (d) PIC/niobate colloid to montmorillonite colloid, (e) and PIC/montmorillonite colloid to niobate colloid.

Distribution of the Cyanine Dye between Macroscopically Separated Niobate and Clay Phases

The selective adsorption of PIC was further investigated by using a system containing the niobate and clay nanosheet colloids macroscopically separated with a semipermeable cellulose membrane for dialysis. When a PIC/niobate colloid ([PIC] = 1×10^{-5} mol dm^{-3} and [Nb$_6$O$_{17}$$^{4-}$] = 3.8×10^{-3} mol dm^{-3} (or [Nb$_6$O$_{17}$$^{4-}$] = 3.2 g dm^{-3})) was brought in contact with a clay colloid ([clay] = 4 g dm^{-3}) through the cellulose membrane, PIC molecules were transferred to the clay phase. After 1 day of the treatment, the initially colored niobate phase was completely decolorized, while the colorless montmorillonite phase turned to red (the color of PIC). Figures 4a and b show changes in the visible spectra of the niobate and clay phases during the treatment. In the spectrum of the niobate phase (Figure 4a), the absorbance of the J-aggregate on the niobate nanosheets gradually decreases with time whereas the bands assignable to PIC on the clay platelets emerges slowly in the montmorillonite phase (Figure 4b). These results demonstrate transfer of PIC from the niobate phase to the montmorillonite colloid through the semipermeable membrane. In contrast, transfer of PIC in the inverse direction (clay to niobate) was not observed when the clay colloid firstly added by PIC was contacted with the niobate colloid.
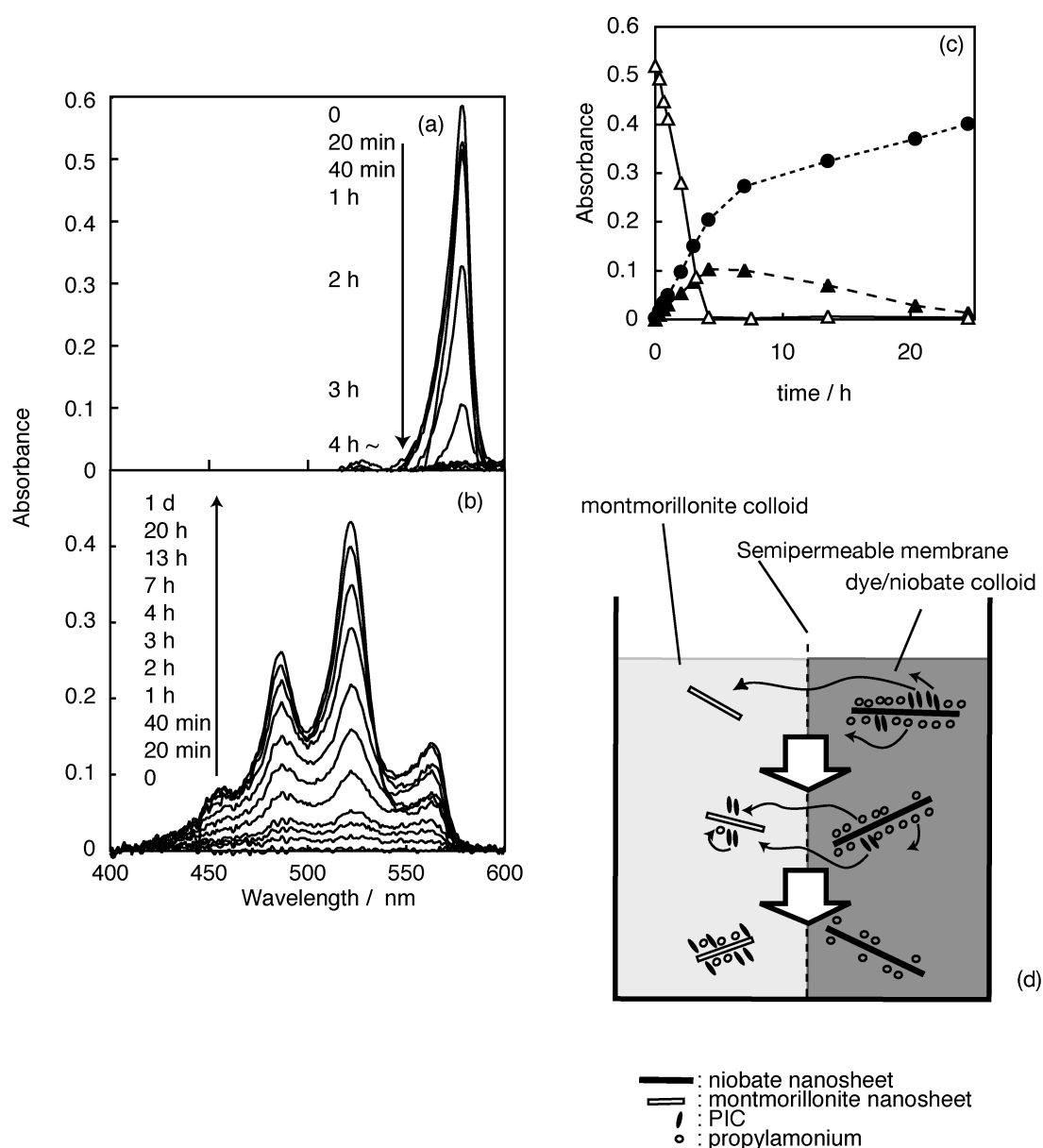
Figure 4. Visible spectra of the niobate and clay nanosheet colloids macroscopically separated by the cellulose membrane: the (a) niobate pre-adsorbed by PIC ([PIC] = 1 × 10^{-5} mol dm^{-3} and [Nb$_6$O$_{17}$] = 3.8 × 10^{-3} mol dm^{-3} (= 3.2 g dm^{-3})) and (b) montmorillonite ([clay] = 4.2 g dm^{-3}) phases.   Variations of the spectra were recorded with time after the two colloidal phases were brought in contact.   (c) Time courses of the absorbances at 578 nm (open triangle) observed for the niobate phase and at 522 (filled circle) and 564 nm (filled triangle) for the clay phase.   (d) Schematic representation of the mass transfer between niobate and montmorillonite when PIC/niobate and montmorillonite colloids were contacted through a semipermeable membrane.

Dissociation of the J-Aggregates of PIC in the Niobate-Clay Nanosheet Colloids

A noticeable effect of the niobate-clay colloids on the behavior of PIC is dissociation of the J-aggregates. Since the niobate and clay nanosheets themselves stably immobilize the J-aggregates, as evidenced by the spectra obtained for the single-component colloids, the dissociation should be caused by other components involved in the niobate-clay colloids. It is supposed that propylammonium ions, which are initially present with the niobate nanosheets, play a crucial role in the dissociation of PIC; propylammonium ions were added as the exfoliating agent at the first step of preparing the niobate nanosheet colloids.

If propylammonium ions were also transferred from the niobate nanosheets to the clay platelets, the dissociation of PIC on montmorillonite can be caused by coadsorption of the alkylammonium ions. The monomer/J-aggregate ratio of PIC in the niobate-clay colloids became larger as the niobate/clay ratio increased, which is deduced from the visible spectra of the colloids with various niobate/clay ratios shown in Figure 5. Greater niobate/clay ratio supplies larger amount of propylammonium ions into the niobate-clay colloid system. On the other hand, visible spectra confirmed that coadsorption of PIC with propylammonium ions on montmorillonite induced dissociation of the J-aggregates. Figure 6 shows the visible spectra of PIC/montmorillonite colloids added with varied amounts of propylammonium. The monomer/J-aggregate ratio is higher when the concentration of propylammonium increases, indicating that coadsorbed propylammonium causes dissociation of the J-aggregates. The dissociation of J-aggregates by coadsorbed species has also been reported for tetramethylammonium-PIC-montmorillonite system.[27] Similar effect of coadsorbed species were also reported for the aggregative dyes, such as g-stilbazolium[28] and spiropyran,[29] coadsorbed on clay minerals with alkylammonium ions.
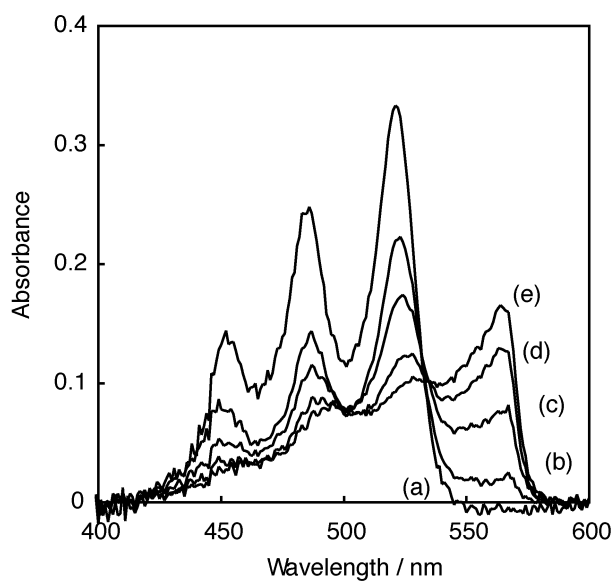
Figure 5. Visible spectra of the PIC/niobate-clay colloids containing 5×10^{-6} mol dm^{-3} of PIC, 1 g dm^{-3} of montmorillonite and (a) 9.1×10^{-3}, (b) 9.1×10^{-4}, (c) 4.6×10^{-4}, (d) 2.3×10^{-4} and (e) 9.1×10^{-5} mol dm^{-3} (or (a) 7.5, (b) 0.75, (c) 0.38, (d) 0.19 and (e) 0.075 g dm^{-3}) of [Nb$_6$O$_{17}{}^{4-}$].
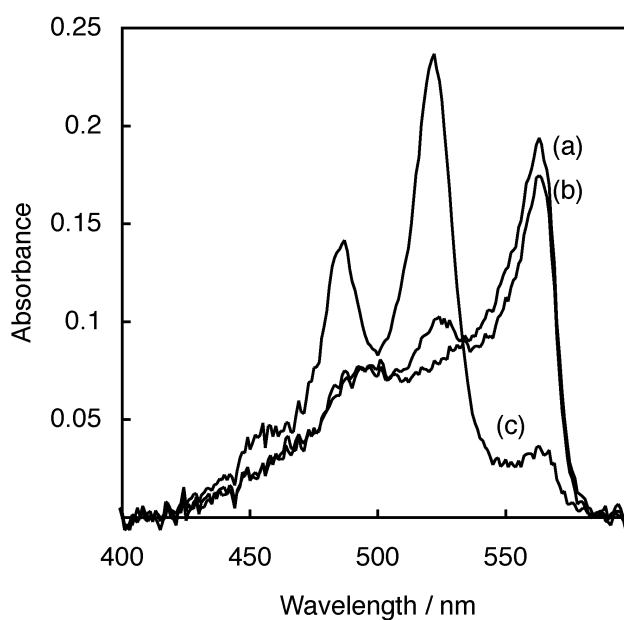
Figure 6. Visible spectra of the PIC/montmorillonite colloids added with propylamine; the colloids contain 5×10^{-6} mol dm^{-3} of PIC, 1.0 g dm^{-3} of montmorillonite and (a) 0, (b) 5 $\times 10^{-4}$ and (c) 5×10^{-3} mol dm^{-3} of propylamine.

Dissociation of the J-aggregates was also observed for the systems of niobate and clay colloids separated by the dialysis membrane.   Figure 4c shows changes of the amount of PIC species involved in this system with time; the quantities of the PIC species are monitored by absorbances at 522 (monomer in the clay phase), 564 (J-aggregate in the clay phase), and 578 nm (J-aggregate in niobate phase).   The J-aggregates on the niobate nanosheets (578 nm) disappear within about 4 h, while the monomer band (522 nm) and J-band (564 nm) emerge in the montmorillonite phase, followed by decrease in the J-band afterward.   The results reveal that the dye molecules are transferred relatively quickly from the niobate phase to the clay phase while that the J-aggregates on montmorillonite were dissociated relatively slowly.   PIC molecules should be at first adsorbed on montmorillonite with partial aggregation due to the tendency of PIC to form J-aggregates, and then the aggregates are dissociated to form monomers by the propylammonium cations which also come from the niobate phase but slowly.   A schematic model of the mass transfer is shown in Figure 4d.

Thermal Analysis of the Solid Samples Recovered from the Colloids

Further evidence for the transfer of propylammonium ions was obtained from the macroscopically separated colloid system by thermal analysis of the powder samples yielded by drying the clay phase where the J-aggregates were dissociated.   DTA curve of Na-montmorillonite (Figure 7a) shows endothermic peaks at around 80 ℃ and 100–800℃ due to elimination of interlayer water molecules and condensation of the aluminosilicate layers, respectively.   In contrast, DTA curve of the sample recovered from the colloid exhibits an exothermic peak around 200 ℃ (indicated by the arrow in Figure 7b) in addition to the endothermic ones observed for Na-montmorillonite.   The exothermic reaction is ascribed to combustion of propylammonium ions, since the amount of PIC added to the colloid is very small (0.001 % of CEC of the clay and 0.1 mass% of the propylammonium ions present in the system) and there are no organic species other than PIC and propylammonium.

The amount of propylammonium ions was estimated from TG analysis based on the interpretation of DTA curves.   The mass losses at 100–900 ℃ observed in the

TG curve of the dried clay sample after the contact with the PIC/niobate nanosheet colloid is ascribed to the sum of combustion of propylammonium and condensation of the silicate layers.　By subtracting the mass loss due to the condensation, the amount of propylammonium ions transferred to the clay phase are estimated as 22 mmol per 100 g of clay for the sample recovered after a day of contacting the clay colloid with the PIC/niobate colloid.　It was also confirmed by similar method that the corresponding amount of propylammonium ions in the niobate phase decreased after a day, supporting the assumption that the niobate phase is the reservoir of the propylammonium ions.
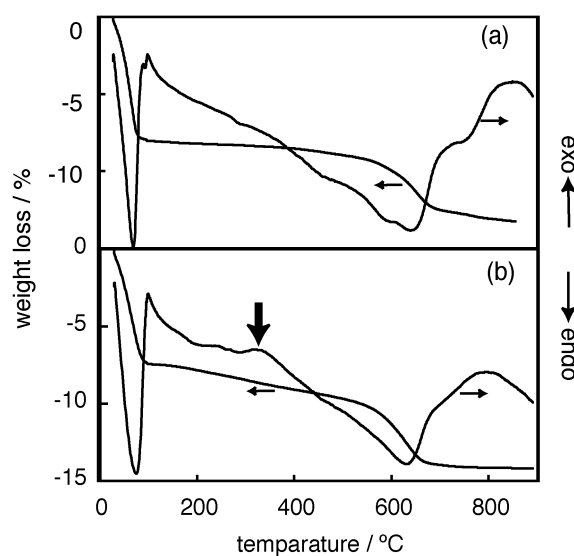
Figure 7.　TG-DTA curves of (a) Na-montmorillonite and (b) the powder sample recovered from the clay phase after the contact with the PIC/niobate colloid for a day. The arrow in (b) indicates the exothermic peak due to propylammonium ions (see the text).

Polarized Spectra on the Dye-Added Niobate-Clay Colloids

It was revealed that orientation of the clay nanosheets in the liquid crystalline niobate-clay colloids was isotropic by using polarized spectroscopy of the adsorbed PIC. Since PIC molecule possesses anisotropic dipole with a flat conformation on the nanosheets, the degree of orientation of the nanosheets can be estimated by using polarized spectra of PIC introduced in the colloids.[8]   Figure 8 shows changes of the dichroic ratio determined by the polarized spectra of PIC present in a niobate-clay colloid with time.   Since PIC is adsorbed only on the clay nanosheets in this system, the dichroic ratio reflects orientation of the clay platelets.   The dichroic ratio is kept around 1 in the niobate-clay colloid system as shown in Figure 8 (filled circle), in contrast with the PIC/niobate system (Figure 8 open circle) where the ratio gradually increased due to ordering of the niobate nanosheets.   Thus, the result confirms the isotropic dispersion of montmorillonite nanosheets in the niobate-clay colloids. Namely, the clay platelets do not contribute to the liquid crystallinity of the niobate-clay colloids but present with random orientations independently on the ordering of the niobate layers; the liquid crystalline ordering is only given by the niobate nanosheets. This result coincides with the observations described above that addition of clay did not affect the liquid crystallinity.

Apparent Homogeneity of the Niobate-Clay Colloids on Macroscopic Scale

The niobate-clay colloids were apparently homogeneous on macroscopic scale, although the demixing of the niobate-clay colloid on nanoscopic scale was indicated by the XRD results.   As already shown in Figures 1h and i, the niobate-clay colloid is regarded as a homogeneously spread liquid crystalline phase.   Even in the optical microscope observation, the colloids are homogeneous without showing any segregated domains, i.e. liquid crystalline and isotropic, or colored and less colored domains; no indication of phase segregation was observed even after days.

Although standing multiphasic colloids under gravitational field generally cause macroscopic phase separation observable by naked eyes because of the difference

in density between the phases, the phenomenon was not observed in the present system due to the sedimentation of the nanosheets themselves.   Both the single-component niobate and clay colloids settled out in the bottom of a vessel in days.   Standing a niobate-clay colloid ([clay] = 1 g dm^{-3}, [Nb$_6$O$_{17}$] = 9.6 × 10^{-4} mol dm^{-3} (= 0.80 g dm^{-3})) added with the dye resulted in the settlement of both the niobate and clay particles to form a deposit of a viscous sol within days.   The deposit was homogeneously colored and liquid crystalline, indicating that niobate and montmorillonite nanosheets, the latter which were adsorbed with the dye, are apparently homogeneously mixed in the deposit. When a thicker niobate-clay colloid ([clay] = 10 g dm^{-3}, [Nb$_6$O$_{17}^{4-}$] = 9.6 × 10^{-3} mol dm^{-3} (= 8.0 g dm^{-3})) was examined, the settlement was slower and took a week.   However, macroscopic phase separation was not observed neither in this case.   In this experiment, the initial colloid was a viscous sol, but not gelated.
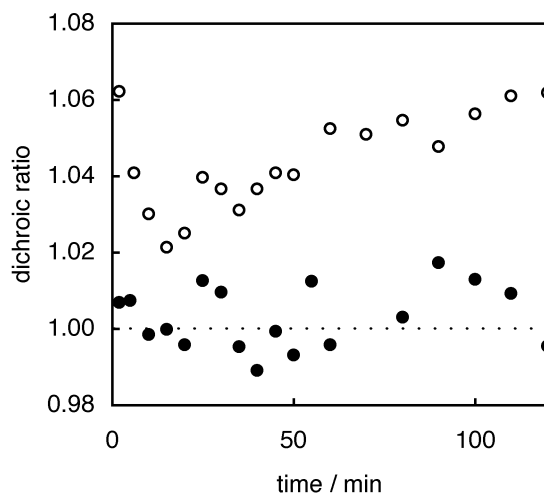
Figure 8.   Changes of the dichroic ratio with time by standing the PIC/niobate ([Nb$_6$O$_{17}$] = 4.8 × 10^{-3} mol dm^{-3} (= 0.80 g dm^{-3}), open circles) and PIC/niobate-montmorillonite ([Nb$_6$O$_{17}$] = 4.8 × 10^{-3} mol dm^{-3} (= 4.0 g dm^{-3}), [clay] = 5 g dm^{-3}, filled circles) colloids containing 2.5 × 10^{-5} mol dm^{-3} of the dye in a quarts cell (thickness of 1 mm).   The dichroic ratios were calculated from the absorption maxima of the polarized spectra at 580 nm and 525 nm, for the PIC/niobate and PIC/niobate-montmorillonite colloids, respectively.

7.4. Discussion

Liquid Crystallinity and Demixing of the Niobate-Clay Colloid

The present niobate-clay colloidal systems are characterized by their liquid crystallinity which is caused by the ordering of only the niobate nanosheets but clay nanosheets. As evidenced by the polarized spectra (Figure 8), only the niobate nanosheets contribute to the liquid crystallinity of the system, while the clay nanosheets are present as isotropic dispersed state. As mentioned in Chapter 6.3., the single-component niobate nanosheet colloids with smaller particle sizes transits from isotropic to biphasic (isotropic and liquid crystalline) and finally to fully liquid crystalline state as the nanosheet concentration increases. Since the microscope images (Figure 1) indicated that the liquid crystallinity of the niobate-clay colloids is similar to that of the single-component niobate colloids, the niobate nanosheets should behave similarly to the single-component system, while clay is only present as isotropic state among the niobate sheets with little effect on liquid crystallinity.

The examined niobate-clay nanosheet colloids should also be characterized by demixing of the niobate and clay nanosheets occurring on microscopic scale. The XRD results strongly suggest that the niobate-clay colloids are always microscopically separated into clay- and niobate-phases but not homogeneously mixed. Spectroscopic observations, indicating that the clay nanosheets do not participate the liquid crystalline ordering of the niobate nanosheets, support demixing of the niobate and clay nanosheets. Demixing of colloidal particles with different size and shape has often been observed for double-component colloidal systems. The colloidal systems containing two morphologically different particles such as rod-plate[15,16] and rod-sphere[17], undergo phase separation due to demixing, for example, into rod-rich and rod-poor phases. Also in the plate-plate mixtures, the mixtures of layered clay minerals with lamellar phases of surfactants, demixed and homogeneously mixed states are observed depending on the concentration of each component.[20,21]

Thus, it is assumed that the system is thermodynamically separated to liquid crystalline (or liquid crystalline plus isotropic) niobate phase and isotropic clay phase; occurrence of the mixed single phase of montmorillonite and niobate is not probable.

However the niobate-clay colloids were apparently homogeneous as evidenced by the optical microscope and naked eye observations. It is supposed that the apparent homogeneity is kinetically retained. The microscopic demixing in the niobate-clay colloids should take place on very small (nm to μm) scale, so that the colloids appear homogeneous on macroscopic scale. Although all the colloids examined were not gelated, thicker colloids or the deposits were viscous sols whose macroscopic segregation should occur slowly. The apparent homogeneity would be simply explained at present by slow diffusion of the niobate and clay nanosheets.

Estimation of the Phase Behavior

The observed liquid crystallinity and demixing of the present niobate-clay colloidal system should be rationalized by entropic basis. Recent theoretical[31] and computer simulation[32] studies showed that, in double-component colloidal systems, the balance among mixing, orientational and packing entropies of the anisotropic particles determines the demixing and mixing of the components as well as isotropic liquid crystalline phase behavior, if electrostatic and steric repulsions are dominant forces between the particles, the case for most of colloids of inorganic particles.

The entropy-based theory predicts that the demixing of the components in a colloid when the loss of mixing entropy is compensated by packing entropy; demixing is favored when the shapes of the two components are largely different. Since the niobate and clay nanosheets are regarded as dissimilar particles because of the differences in charge density and mean lateral size, the demixing in niobate-clay colloids would be rationalized by the entropically driven phase separation.

The theory also predicts that isotropic to liquid crystalline phase transition occurs when the loss of orientational entropy given by aligned particles is overwhelmed by gain in packing entropy. As described in Chapter 6.3., the ordering of the single-component niobate nanosheet colloid is explained semi-quantitatively on that basis.[30] Since addition of the clay nanosheets varies the total colloid concentration and entropy of the system, alteration of the phase behavior, for example the phase transition concentrations, can occur on the clay-added niobate colloids. However, such effects of the clay

nanosheets have not been identified.   This is due to sedimentation of both the niobate and clay particles.   The liquid crystallinity was only roughly evaluated by comparing the interference colors observed by optical microscope under crossed polarizers.   The demixed phases was identified only indirectly by the XRD of dried colloid.   Thus, the present niobate-clay colloids do not give more detailed information of phase behavior such as a multiphase equilibrium of the nanosheets.   Other systems free from the sedimentation would be necessary in order to clarify the phase behavior of niobate-clay system precisely.

The Niobate-Clay Colloids as Novel Soft Matrices of Cationic Species

The spectroscopic results reveal the novelty of the niobate-clay system as a matrix for effectively immobilizing cationic functional molecules exemplified by dyes. The soft matrix provided by the colloidally dispersed niobate-clay nanosheets is characterized by their peculiar microstructure constructed by the liquid crystalline and demixed niobate and clay nanosheets, although its detail is unclear at present. Polarized spectroscopy indicates that the niobate nanosheets are ordered to induce the liquid crystalline state of the colloids, while that the clay nanosheets are present as isotropic among the ordered nanosheets.   The adsorption of cyanine dye selectively onto the clay nanosheets demonstrates unusual microscopically heterogeneous environments given by the colloids.   Since the liquid crystallinity of the niobate-clay colloids is determined only by the niobate nanosheets, dye molecules are introduced into the colloid without influences on the liquid crystalline ordering of the colloids, and, on the other hand, the niobate nanosheets do not spectroscopically affect the dye adsorbed on the clay platelets.   Demixing of the niobate and clay nanosheets indicate that the dye adsorbed on the clay nanosheets can show various properties such as spectroscopic one, independently on the niobate nanosheets.   Hence, the niobate-clay colloid present here will lead to novel heterogeneous, anisotropic and soft hybrids with various functional species.

It is supposed that the observed distribution of the cations between the niobate and clay nanosheets is thermodynamically determined.   Differences in microscopic

environments given by the niobate and montmorillonite nanosheets, e.g. structure, hydrophobicity and density of the negative layer charge, would cause the difference in stability of the adsorbed species. The absorption maximum of the J-band was varied with the kind of nanosheets where PIC is adsorbed (578 and 564 nm for the niobate and clay layers, respectively); it is assumed that the interactions of the dye with montmorillonite are stronger than with the niobate. According to molecular exciton theory,[33] smaller J-aggregates exhibit absorption maximum at shorter wavelengths. Since PIC adsorbed on the clay nanosheets gives the absorption band at the wavelength shorter than that of the dye on the niobate, the PIC molecule forms smaller J-aggregates on the aluminosilicate than on the niobate. Stronger dye-oxide interactions in the clay colloid can result in formation of the smaller aggregates because dye-dye interactions that derive aggregation of PIC become relatively weak under such conditions.

The apparent homogeneity is a noticeable feature of the present system for the use as a matrix. Although the system should be multiphasic mixture, one can practically regard the systems as a homogeneous liquid crystalline sol. The optical property of the sample is macroscopically tuned by utilizing the liquid crystallinity of the niobate, while the state of cationic species is controllable on nanoscopic scale.

7.5. Conclusions

Liquid crystalline double-component nanosheet colloids by mixing the $Nb_6O_{17}{}^{4-}$ and montmorillonite colloids were prepared. The niobate-clay double-component colloid is valuable to heterogeneously organize the cationic functional molecule by taking advantage of the selective adsorption of a dye as was demonstrated by the behavior of the probe cyanine dye added in the niobate-clay colloids. The XRD results on the dried colloids reveal that the colloids are microscopically heterogeneous although they seem macroscopically homogeneous on the observations with microscope as well as naked eyes. Thus, in the niobate-clay nanosheet colloids, the niobate nanosheets work as components which direct the ordering of whole the colloids, while the clay layers are the immobilizing sites for the dye. The double-component nanosheet colloids will be applicable as novel heterogeneous, anisotropic and soft hybrids with various functional species.

7.6. References

(1) L. Onsager, *Ann. NY Acad. Sci.,* **51**, 627 (1949).

(2) H. van Olphen, An Introduction to Clay Colloid Chemistry, 2nd ed. (Wiley-Interscience, New York, 1977).

(3) I. Langmuir, *J. Chem. Phys.,* **6**, 873 (1938).

(4) O. Pelletier, C. Bourgaux, O. Diat, P. Davidson, J. Livage, *Eur. Phys. J. B,* **12**, 541 (1999).

(5) S. Lamarque-Forget, O. Pelletier, I. Dozov, P. Davidson, P. Martinot-Lagarde, J. Livage, *Adv. Mater.,* **12**, 1267 (2000).

(6) H. Desvaux, J.-C. P. Gabriel, P. Berthault, F. Camerel, *Angew. Chem. Int. Ed.,* **40**, 373 (2001).

(7) J.-C. P. Gabriel, F. Camerel, B. J. Lemaire, H. Desvaux, P. Davidson, P. Batail, *Nature,* **413**, 504 (2001).

(8) N. Miyamoto, T. Nakato, *Adv. Mater.,* **14**, 1267 (2002).

(9) T. Nakato, N. Miyamoto, *J. Mater. Chem.,* **12**, 1245 (2002).

(10) G. Lagaly, K. Beneke, *J. Inorg. Nucl. Chem.,* **38**, 1513 (1976).

(11) T. Nakato, K. Kuroda, C. Kato, *Chem. Mater.,* **4**, 128 (1992).

(12) G. B. Saupe, C. C. Waraksa, H.-N. Kim, Y. J. Han, D. M. Kaschak, D. M. Skinner, T. E. Mallouk, *Chem. Mater.,* **12**, 1556 (2000).

(13) M. Gasperin, M. T. L. Bihan, *J. Solid State Chem.,* **43**, 346 (1982).

(14) G. Lagaly, *Clay Miner.,* **16**, 1 (1981).

(15) F. M. van der Kooij, H. N. W. Lekkerkerker, *Langmuir,* **16**, 10144 (2000).

(16) F. M. van der Kooij, H. N. W. Lekkerkerker, *Phys. Rev. Lett.,* **84**, 781 (2000).

(17) M. Adams, Z. Dogic, S. L. Keller, S. Fraden, *Nature,* **393**, 349 (1998).

(18) R. van Roij, B. Mulder, *Phys. Rev. E,* **54**, 6430 (1996).

(19) F. M. van der Kooij, K. Kassapidou, H. N. W. Lekkerkerker, *Nature,* **406**, 868 (2000).

(20) I. Grillo, P. Levitz, T. Zemb, *Langmuir,* **16**, 4830 (2000).

(21) I. Grillo, P. Levitz, T. Zemb, *Eur. Phys. J. E,* **5**, 377 (2001).

(22) K. Nassau, J. W. Shiever, J. L. Bernstein, *J. Electrochem. Soc.,* **116**, 348 (1969).

(23) J.-C. P. Gabriel, C. Sanchez, P. Davidson, *J. Phys. Chem.,* **100**, 11139 (1996).

(24) A. Mourchid, E. Lécolier, H. Van Damme, P. Levitz, *Langmuir,* **14**, 4718 (1998).

(25) M. Ogawa, R. Kawai, K. Kuroda, *J. Phys. Chem.,* **100**, 16218 (1996).

(26) N. Miyamoto, K. Kuroda, M. Ogawa, *J. Am. Chem. Soc.,* **123**, 6949 (2001).

(27) N. Miyamoto, R. Kawai, K. Kuroda, M. Ogawa, *Appl. Clay. Sci.,* **16**, 161 (2000).

(28) H. Usami, K. Takagi, Y. Sawaki, *Bull. Chem. Soc. Jpn.,* **64**, 3395 (1991).

(29) H. Tomioka, T. J. Itoh, *Chem. Commun.,* 532 (1991).

(30) Miyamoto, N.; Nakato, T.; submitted.

(31) H. H. Wensink, G. J. Vroege, H. N. W. Lekkerkerker, *J. Chem. Phys.,* **115**, 7319 (2001).

(32) Z. Dogic, D. Frenkel, S. Fraden, *Phys. Rev. E,* **62**, 3925 (2000).

CHAPTER 8

CONCLUSIONS

8. Conclusions
8.1. Overview

The results of this thesis demonstrated that the model guest species, cyanine dyes, were organized both nanoscopically and macroscopically by hybridizing with inorganic layered solids.   Chapters 2 - 4 elucidated the factors to control nanoscopic organization and orientation of the dye when adsorbed to various inorganic layered solids,   finally   showing   a   new   methodology   to   fabricate   three-dimensional superstructures and an application for light energy conversion and storage systems. Chapters 5 – 7 demonstrated that the cyanine dye is organized on the macroscopic scale by controlling macroscopic morphology of layered solids via exfoliation.   General conclusions obtained from the results are shown below with the brief summaries of the results and future prospects.   The results of this thesis not only offered the general information on organizing aggregative guest species with inorganic layered materials, but also highlighted other important perspectives regarding the chemistry of inorganic layered solids.

8.2. General Conclusions and Future Prospects
Nanoscopic Organization of Aggregative Dyes with Layered Hosts

The   results   of   Chapters   2   -   4   presented   fundamental   information   on organizing aggregative guest species with inorganic layered materials on nanometer scales.   1,1'-Diethyl-2,2'-cyanine did not form aggregates on the smectite clays with smaller particle sizes, indicating that the sufficiently large room is required for the aggregation due to the large dimension of the aggregate.   In contrast, the dye formed J-aggregates when hybridized with clays with large particle sizes (montmorillonite and mica), layered polysilicate magadiite, layered titanates, and layered niobate even at the low loading of the dye.   The variation in the absorption maximum of the J-band observed in the visible absorption spectra indicated that the nanostructure of the dye aggregate is varied depending on the layer charge density and the difference in the interactions between the dye and the layer surface.   Besides, Chapter 3 elucidated that

the adsorbed dye aggregates were uni-axially oriented along the crystallographic axes of $K_4Nb_6O_{17}$ over the whole crystal domain due to the electrostatic interactions between the dyes with regularly and densely arranged ion-exchange sites on the surface of the layered niobate. This result emphasizes that the dye-host interactions are so strong that the orientation of the dye aggregate is directed by the dye-host interactions as well as by the dye-dye interactions.

Thus, inorganic layered materials are good matrixes for organizing supramolecular aggregates with the capability of modifying the microstructure of the aggregates by tuning the host-guest interactions. For optimization of electronic and optical properties of functional organic molecules, the control of molecular arrangements as well as the molecular design is indispensable. An alternative way to control the microstructure by interactions with the surface of layered compounds presented here is of great importance. Although the obtained results are for cyanine dyes, the concept and the basic information obtained will be generalized to other dyes or other functional species.

Macroscopically Oriented Supramolecular Assemblies

The results in Chapter 3 succeeded in fabricating macroscopically ordered supramolecular assemblies by adsorbing the dyes to the single crystal of layered niobate, which possess in-plane anisotropy of the structure. The methodology is generally applicable to organize various molecular and polymer species with useful photochemical properties, etc. into supramolecular architectures with macroscopic ordering by the simple processing. Such the oriented assemblies are useful for fundamental studies of the functional organic molecules or polymers, whose large crystals or oriented domains are not easily obtained.

Further, optimization of the reaction conditions will lead to single crystalline intercalation compounds. Although the characterization of intercalation compounds had been considerably limited due to the fact that the products are, in most cases, obtained in powder forms, single crystals of intercalation compounds are suitable for examining anisotropy of electric properties, photochemical properties, etc.

Fundamental studies with various model dyes and host materials should help to understand the mechanism of the observed macroscopic ordering in more detail. Based on the fundamental information, more precise control of the microstructures and the macroscopic ordering will be possible, leading to future three-dimensional supramolecular devices.

Novel Model Systems of Light-Induced Electron Transfer

The results of Chapter 4 showed that the cyanine dye-layered titanate intercalation compounds undergo visible light induced electron transfer from the intercalated dye aggregates to semiconducting titanate layers, which resulted in very stable charge separated state; these results highlight the potential application of the intercalation compounds for light energy conversion and storage systems with controllable nanostructures. Materials with controlled and defined nanostructures are valuable for fundamental studies of the photo processes in dye-sensitized semiconductor systems to optimize the materials performance. Taking advantage of the further modifiable two-dimensional nanostructure of the intercalation compounds, the present system would be applicable as a good model system for sensitized photoenergy conversion.

Although the samples examined in Chapter 4 were powders, optically transparent oriented films of the composite have also been obtained as described in Chapter 5. Such films are more suitable for detailed photochemical and electrochemical characterizations as well as for optical and electronic devices by taking advantage of their transparency and macroscopic anisotropy compared to the powders.

Liquid Crystals from Inorganic Layered Solids

Chapter 6 highlighted the novel aspect, the liquid crystallinity, of inorganic nanosheets obtained by exfoliating inorganic layered solids, whereas the nanosheets had mostly been regarded as modules for fabricating multi-layered films and porous solids in the previous studies. The results not only revealed the stable liquid crystallinity of the niobate nanosheet sols, but also clarified the effect of the lateral size on the

formation of the liquid crystalline phases. By preparing and examining the nanosheet colloids with controlled lateral sizes over very wide range, it was revealed that the larger lateral size contributes to the formation of more stable liquid crystalline phases. The phase transition concentrations (isotropic-biphasic and biphasic-liquid crystalline) basically agreed with those calculated by Onsager theory. Thus, the systematic study presented here verified the general theory, which is a good fingerpost for designing new liquid crystalline colloidal systems via exfoliation of various inorganic layered solids.

Liquid crystals are currently used for versatile applications for displays, anisotropic reaction media, and templates for ordered nanostructures. The liquid crystalline nanosheet colloids will also lead to a wide variety of advanced materials. The high fluidity of the liquid crystalline nanosheet colloids distinguishes the liquid crystals composed of nanosheets from conventional liquid crystalline materials; high responsiveness to electric, magnetic and shear stimuli are expected. Combining the liquid crystallinity with other properties of the inorganic materials such as semiconducting nature and capability of organizing guest species on the layer surface will lead to integrated materials. Extension of the present methodology to other layered materials will provide a wide variety of liquid crystalline colloidal systems which are useful for both practical applications and fundamental investigations.

Nanosheet Colloids as Anisotropic, Heterogeneous and Soft Matrixes

The results of Chapters 6 and 7 exemplified that the nanosheet dispersions are regarded as anisotropic, heterogeneous and soft matrixes in the form of sol for organizing functional species; such the soft materials should be distinguished form the conventional solid materials due to the high responsiveness to stimuli and high accessibility of various components into the matrixes.

Chapter 6 demonstrated that the liquid crystalline nanosheet dispersions obtained by exfoliating the layered niobate effectively organize the cyanine dye with nanoscopic and macroscopic ordering. The observations showed that a weak stress such as rotational shear, gravity, and interfacial tension largely affected the macroscopic ordering of the nanosheets and therefore of the dyes due to very low viscosity of the

nanosheet sols.   By adding dye to the liquid crystalline nanosheet sol, the cyanine dye was immobilized onto the nanosheets and the dye dipoles were macroscopically aligned due to the macroscopic alignment of the dispersed nanosheets.

Chapter 7 dealt with the double-component nanosheet colloid obtained from montmorillonite and $K_4Nb_6O_{17}$.   The results revealed the perfect selectivity of the dye adsorption onto the montmorillonite rather than to the niobate in the double-component nanosheet colloid.   In addition, the results indicated the possible microscopic phase separation of the double-component colloid into niobate-rich and montmorillonite-rich domains.   It was also found that the double component colloid is liquid crystalline due to ordering of only the niobate nanosheets.   These results will lead to the potential application of the double-component nanosheet colloids as novel heterogeneous, anisotropic and soft hybrids with various functional species.   Further clarification of fundamental properties such as the microstructure of the phase-separated state is necessary for the applications by e.g. using sedimentation-free samples and the characterization using spectroscopic probes.

New Methodologies to Obtain Nanosheets with Controlled Lateral Size

The results in Chapters 5 and 6 revealed the new aspects of chemistry of nanosheets by proposing new methodologies for exfoliating layered materials and controlling the lateral size of the obtained nanosheets.

In Chapter 5, sonication and hydrothermal heating were found to facilitate exfoliation of $Na_2Ti_3O_7$.   Although exfoliation of many layered materials have been reported so far, the layered materials with high charge density such as $Na_2Ti_3O_7$ are generally difficult to be exfoliated.   The present methodologies would be applicable to promote exfoliation of other layered materials that are difficult to be exfoliated by conventional methods.

Chapters 6.1 and 6.3 focused on controlling the lateral size of the nanosheets. The lateral size was effectively varied by using large single crystals of layered niobate as the starting material, followed by breaking down the nanosheets by ultrasonication for varied period.   Although exfoliation of layered materials has been known for long

and extensively studied recently, the control in the lateral size had not been much interested.   This study not only succeeded in controlling the size of the nanosheets but also exemplified the importance of the lateral size on the liquid crystallinity of the nanosheet colloid.   Now, more precise control of the nanosheet morphology is desired. For example, the control of the thickness (the degree of exfoliation) and the polydispersity of the lateral sizes would be important to modify the colloidal properties of nanosheet dispersions.

ACKNOWLEDGMENTS